Chemical differentiation of subduction zone magmas



Beitris Emily Morrison-Evans

Department of Earth Sciences

University of Oxford

This thesis is submitted for the degree of

Doctor of Philosophy

University College

April 2025

Abstract

Arc volcanoes are the product of magmatism at subduction zones. Identifying the origin and evolution of magmas erupted at arc volcanoes is key to understanding where melts are generated, and accumulate, in the underlying crust, and key processes at play in the crustal region. Many volcanoes erupt a limited compositional range of magmas over their lifetime, proposed to reflect the mineralogy of the crystal-rich mush in the source region. La Soufrière volcano, St. Vincent, in the Lesser Antilles is an example of such volcano, erupting predominantly basaltic andesite magmas for hundreds of thousands of years.

Major and trace element geochemistry for lavas and dykes collected from the La Soufrière crater, and western flanks, find magmas to be compositionally homogenous basaltic andesites with rare basalts and andesites. New $^{40}Ar/^{39}Ar$ dates reveal an unconformity in the crater and find magmatism on the western flanks to be very young (≤ 4.4 ± 4.2 ka). Erupted basaltic andesite magmas contain a wide range of crystal cargo, and primitive relict mineral cores support differentiation from a high-magnesium basaltic parent magma. High An plagioclase (≥ An_{85}) is abundant in all samples and indicates a hydrous and oxidising source region.

Near-liquidus multiple saturation experiments find erupted basaltic andesite magmas to originate in the lower crust at 0.6 ± 0.1 GPa, 1020 ± 10ºC, at NNO+2 and with ~ 8 wt. % H_2O in the melt, last equilibrating with an amphibole-gabbro source assemblage. Mineral compositions match erupted crustal xenolith data, and source pressure and temperature estimates agree with geophysical observations and calculated magmatic temperatures for the 2020-2021 eruption at La Soufrière. Oxidation-exsolution textures observed in the 2020-2021 lava dome, but absent from the explosive scoria, are reproduced at ≤ 900ºC and in the presence of air, indicating formation post- or syn-emplacement.

Acknowledgements

I have thoroughly enjoyed my PhD and am thankful to all of the incredible people I have met along this journey. Firstly, thank you to my supervisors Jon and Lena who have taught me so much and who are always inspiring to work with, I am truly grateful. To Richard, Bernie, Julien and Andrew, thank you for welcoming me into the experimental petrology group at the start of my PhD and for your continued help throughout. And to those who have joined the experimental petrology group over the years, thank you for making meetings, pub trips and wine tastings always fun and interesting. To those in the volcanology research group, old and new, thank you for more pub trips and our shared love of all things volcano-related. Thank you also to James and Dave in the workshop, for always being happy to help and for showing me how a piston cylinder is built! Thank you Emily for reviving the geofacilities labs, Hong for help with thin section preparation, Kris for help on the SEM and Andrew and Jon for all of your help on the microprobe, where I felt like I lived a lot of the time! And thank you to my examiners David Pyle and Michel Pichavant for an enjoyable discussion during my viva.

Thank you to all of those who have shared data and helped with analyses, Greg Weber, Holli Frey, Rodrigo Contreras-Arratia, Richie Robertson, Brian Jicha, and Cees-Jan De Hoog. Thank you to the Royal Society for funding this studentship and to University College Oxford for providing funding for conferences and fieldwork. Visiting La Soufrière volcano after the 2020-2021 eruption was an incredible fieldwork opportunity. A huge thank you to Richie for all of the organisation, your wealth of knowledge, and passion for geology and La Soufrière. And thank you to George, Michal, Tyronne, Megan and Lena for making a great fieldwork team. Thank you to all of my incredible office mates over the years: Matthew, Rebecca, Biao, Adewumni, Sharmin, Bing, Rhiannon and Megan. I always enjoy our time spent chatting, ranting, working and going for pizza! And thank you to everyone within the Earth Sciences department who make the cogs turn, especially Jeanette, Ashleigh and Jason.

Nikki, Susie and Emily, thank you for being like family over the last few years and making life at home so much fun. I can’t describe how truly grateful I am to have met you all and am excited

where life will take us next. Thank you Annika and Vikki for all of our amazing adventures, dips in the sea, hikes, climbs, time spent giggling and in awe at cool geology! Thank you Ian, Lot and Charlotte for more geology adventures, wild swims, hosting the best dinner parties and for all of the spontaneous uncontrollable laughter! To the girls from home, thank you for all of your continued love, support and friendship, you all mean the absolute world to me and I think about you all often. Prina and Emily, thank you for being the best uni housemates and friends, for always being there, and for all of the weekends away spent chatting, hiking, playing games, and finding the best vegan food. Thank you Liv for being the best mapping partner and friend, and for always being so motivated and inspirational! Thank you to Jasmin, Manon and Iona for post-Canada adventures; Jess for living the dream in the mountains and always being a joy to see; and Natalia for making visiting London always super fun. To all of the family friends far and wide, I love visiting you all and thank you for all of your support over the years, whether that be dips in the sea in Plymouth or boxes of oranges at christmas time, thank you. And to all of the friends I have made over the years here, thank you for making my time in Oxford so much fun, always being up for a trip to the climbing wall or the pub, and for all of your love and kindness – Rebecca, Sofia, Cathy, Hannah, Toby, Sjef, Jeremy, Malin, Emma, Lauren, Richard, Michal, Maddy, and the many many more people I have probably missed (sorry!).

Thank you to all of my incredible family, Auntie Mel, Auntie Pauline, Uncle Andrew, Grandma Maria, and Uncle James, for always supporting me and having an interest in what I do. And thank you to my cousins Mack and Flo for making me smile so much every Christmas when I visit – I hope that all of my volcano stories inspire you to become a geologist too Mack! And finally, to my mum, dad and Mattea. Thank you for everything, for always being there and supporting me, for encouraging me to follow my love of geology and volcanoes, for believing in me and wanting what's best for me. Words can't describe how grateful I am to have such an amazing family, my number one supporters in everything I do. I love you all so much. Thank you always.

Table of contents

Introduction 1

1.1 Subduction zone magmatism 1

1.2 Multiple saturation experiments as a thermobarometer 3

1.3 Geological setting and eruptive history 4

1.3.1 Tectonic setting 4

1.3.2 St. Vincent 8

1.3.3 La Soufrière 11

1.3.4 Prehistoric eruptions 13

Pre-Somma Lavas 13

Yellow Tuff Formation 14

Crater Lavas 15

Pyroclastic Formation 16

1.3.5 Historic eruptions 16

1.3.6 2020-2021 La Soufrière eruption 18

1.4 Thesis aims and structure 19

Exploring the compositional variability of magmas erupted at La Soufrière volcano, St Vincent, using chemo-stratigraphy and new $^{40}Ar/^{39}Ar$ dates. 21

2.1 Introduction 21

2.1.1 Previous work 22

2.1.2 Fieldwork rationale 24

2.1.3 $^{40}Ar/^{39}Ar$ dating of young volcanic rocks 26

2.1.4 Geochemistry methods 27

Sample preparation 27

Rock powder preparation 28

Analytical methods 29

2.1.5 $^{40}Ar/^{39}Ar$ dating methods 29

Sample preparation 29

Analytical methods 30

2.2 Results 30

2.2.1Field observations and relative age relationships 30

2023: Crater lavas 30

2024: Larikai and Roseau lavas and dykes 32

2.2.2 Whole-rock major element chemistry 35

2.2.3 Trace element chemistry 41

2.2.4 New $^{40}Ar/^{39}Ar$ dates 46

2.3 Discussion 49

2.3.1 Compositional stability of magmas at La Soufrière volcano 49

2.3.2 Differentiation from a basaltic parent magma 50

2.3.3 Low-magnesium basalts of La Soufrière 51

2.3.4 Revised stratigraphic sequence 53

Pre-Somma lavas 53

Somma collapse 53

YTF 55

Crater Lavas 58

Pyroclastic formation and historic lavas 58

2.4 Conclusions 59

A detailed petrological analysis of basaltic andesite magmas erupted at La Soufrière volcano, St Vincent. 61

3.1 Introduction 61

3.1.1 La Soufrière volcano, St. Vincent 63

3.2 Methods 65

3.2.1 Sample preparation 65

3.2.2 Thin section billet preparation 65

3.2.3 Analytical methods 65

3.3 Results 66

3.3.1 Lava petrology 66

Plagioclase 70

Clinopyroxene 71

Orthopyroxene 72

Olivine *75*

Oxides *76*

Glomerocrysts and micro-xenoliths *76*

3.3.2 Mineral chemical compositions 79

Plagioclase *81*

Clinopyroxene *83*

Orthopyroxene *85*

Olivine *87*

Oxides *89*

3.4 Discussion 92

3.4.1 Thermobarometry 92

Clinopyroxene-orthopyroxene *95*

Clinopyroxene-only *95*

MagMaTaB *96*

3.4.2 Oxybarometry 97

3.4.3 Complex crystal cargo of La Soufrière magmas 98

High-An plagioclase *98*

Relict crystals from parent magma *100*

Breakdown textures *102*

Glomerocrysts *104*

3.4.4 Micro-xenolith assemblages as a proxy for arc crust compositions 105

3.4.5 Crystallisation history of La Soufrière basaltic andesite magmas 107

3.5 Conclusions 109

Experimentally-determined lower-crustal origin of calc-alkaline basaltic andesite magmas from La Soufrière volcano, St. Vincent, Lesser Antilles. 111

4.1 Introduction 111

4.1.1 Multiple saturation 112

4.1.2 Calc-alkaline and tholeiitic evolutionary trends 114

4.1.3 Previous basaltic andesite experiments 116

4.1.4 St. Vincent magmas 117

4.1.5 Petrology 118

4.1.6 Xenoliths 121
4.1.7 Melt inclusions 123

4.2 Methods 124

4.2.1 Starting materials 124
4.2.2 One atmosphere experimental setup 126
4.2.3 Piston cylinder experimental setup 127
4.2.4 Analytical methods 130

4.3 Experimental results 131

4.3.1 One-atmosphere experiments 135
4.3.2 Approach to equilibrium in piston-cylinder experiments 135
4.3.3 Volatiles 136
4.3.4 Oxidation state 138
4.3.5 Controlled fO_2 experiments 139
4.3.6 Cooling experiments 141
4.3.7 Phase proportions 143
4.3.8 Phase relationships 144
0.35 GPa 144
0.6 GPa 146
0.8 GPa 147
4.3.9 Phase compositions 148
Glass 148
Plagioclase 151
Clinopyroxene 153
Orthopyroxene 155
Iron-titanium oxides 156
Amphibole 159
Olivine 161

4.4 Discussion 161

4.4.1 Near- and sub-liquidus multiple saturation points 161
4.4.2 Near-liquidus assemblages as a proxy for crustal composition 163
4.4.3 Lower crustal source depth of basaltic andesite magmas at La Soufrière, St. Vincent 168
4.4.4 Calc-alkaline and tholeiitic magmas of St. Vincent 170
4.4.5 Olivine stability in low-magnesium basaltic andesite melts 173
4.4.6 Amphibole-clinopyroxene peritectic 175

4.5 Conclusions **176**

Experimental insight into basaltic andesite lava dome oxidation textures at La Soufrière, St. Vincent. 178

5.1 Introduction **178**

5.1.1 Lava dome petrology 180

Oxidation mechanisms *181*

Iron-Titanium oxides *183*

Olivine *185*

Pyroxene *186*

5.2 Methods and materials **186**

5.2.1 Experimental Methods 186

5.2.2 Analytical Methods 188

5.3 2020-2021 La Soufrière lava dome and scoria petrology **189**

5.3.1 Textural differences 190

5.3.2 Compositional differences 193

5.4 Experimental Results **195**

5.4.1 Textural variations 195

5.4.2 Compositional variations 203

5.5 Discussion **211**

5.5.1 Mechanisms of oxidation 211

5.5.2 Temperature of oxidation 213

5.5.3 Timescale of oxidation 215

5.6 Conclusion **216**

Conclusions 218

6.1 Homogeneity of the basaltic andesite magmas at La Soufrière volcano, St. Vincent **218**

6.2 Evidence for differentiation from a high-magnesium basaltic parent magma **220**

6.3 Origin of erupted basaltic andesite magmas 221

6.4 Magma ascent and crystallisation..... 222

6.5 Lava dome oxidation textures 223

References 224

Appendices 242

List of Figures

Chapter 1

1.1 Map of Lesser Antilles volcanic island arc and geological map of St. Vincent

1.2 Silica versus MgO plot for Lesser Antilles magmas

1.3 Photographs of evolution of La Soufrière crater between 1907 and 2023

Chapter 2

2.1 Map of La Soufrière sample locations

2.2 Photograph of La Soufrière crater lava units

2.3 Photographs of La Soufrière effusive and explosive eruption products

2.4 Total alkali silica (TAS) diagram for La Soufrière magmas

2.5 Major oxides versus MgO for La Soufrière magmas

2.6 REE diagram for La Soufrière magmas

2.7 Eu/Eu* and Dy/Dy* for La Soufrière magmas

2.8 Representative $^{40}Ar/^{39}Ar$ age spectrum plateau diagram and isochron plot

2.9 Schematic of revised eruptive history at La Soufrière

Chapter 3

3.1 Modal proportions of phenocrysts and groundmass

3.2 Photomicrographs of mineral textures

3.3 Photomicrographs of glomerocrysts and micro-xenoliths

3.4 Core and rim compositions for phenocryst mineral phases and calculated Kd values

3.5 Plagioclase core and rim compositions

3.6 Clinopyroxene core and rim compositions

3.7 Orthopyroxene core and rim compositions

3.8 Olivine core and rim compositions

3.9 Magnetite compositions

3.10 Pressure and temperature estimates

Chapter 4

4.1 Photomicrographs of La Soufrière xenoliths

4.2 BSE images of experimental capsules

4.3 BSE images of experimental run products

4.4 Isobaric T-H_2O phase diagrams at 0.35, 0.6 and 0.8 GPa

4.5 Isobaric T-H_2O phase diagram at 0.6 GPa with controlled fO_2 experiments

4.6 Major oxides versus MgO for experimental glass compositions

4.7 FeO versus TiO_2 (wt. %) for experimental glass compositions

4.8 Plagioclase compositional plots
4.9 Clinopyroxene compositional plots
4.10 Orthopyroxene compositional plot
4.11 Magnetite and ilmenite compositional plots
4.12 Amphibole compositional plot
4.13 Near-liquidus P-T phase diagram
4.14 Crustal structure beneath La Soufrière, St. Vincent determined from experiments, petrology and geophysics
4.15 FeO/MgO versus SiO_2 (wt. %) showing calc-alkaline and tholeiitic differentiation at different oxygen fugacities

Chapter 5

5.1 BSE images of the 2020-2021 La Soufrière dome and scoria.
5.2 Experimental T-fO_2 phase diagram of mineral stability fields.
5.3 BSE images of experimental groundmass textures
5.4 BSE images of experimental orthopyroxenes
5.5 BSE images of experimental Fe-Ti oxides
5.6 BSE images of experimental olivines
5.7 Plagioclase and pyroxene microlite compositions as An and Mg# versus fO_2
5.8 Fe-Ti oxide compositions plotted in ternary space

List of Tables

Chapter 2

2.1 New whole-rock data for La Soufrière magmas

2.2 New $^{40}Ar/^{39}Ar$ dates for lavas from La Soufrière

2.3 All K/Ar and $^{40}Ar/^{39}Ar$ dates for La Soufrière and St. Vincent magmas

Chapter 3

3.1 Mineral phase assemblages, proportions and micro-xenolith assemblages

3.2 Temperature, pressure and fO_2 estimates

Chapter 4

4.1 Starting material

4.2 Piston cylinder experiments

4.3 Controlled fO2 experiments

4.3 Cooling experiments

Chapter 5

5.1 Starting material

5.2 Piston cylinder experiments

Chapter 1

Introduction

1.1 Subduction zone magmatism

Arc volcanoes are the surface expression of magmatism at subduction zones. The generation of eruptible magmas at subduction zones begins with partial melting of the peridotite mantle wedge facilitated by fluids derived from the down going slab (Yoder and Tiley, 1962; Kushiro, 1973; Gill, 1981; Grove et al., 2012). The volume and composition of these fluids, along with any sediment fluxed from the subducting slab, controls the composition of the magmas generated (Grove and Baker, 1984; Ulmer, 2001; Gaetani and Grove, 2003). A primary magma is defined as a derivative from the mantle by partial melting, that does not undergo further chemical modification such as fractionation (Grove et al., 2012). Primary magmas rarely erupt at the surface in arc settings as during ascent through the crust, magmas often experience chemical differentiation, magma mixing or crustal assimilation (McBirney, 1980; Hildreth and Moorbath, 1988; Grove et al., 2003; Nandedkar et al., 2014; Stock et al., 2020). In cases where these primary magmas do erupt at the surface (e.g. Tatsumi et al., 1983; Bartels et al., 1991; Melekhova and Blundy, 2024), they can be used to constrain the thermal structure of the mantle wedge and conditions of melting at the base of a magmatic system. Indirect evidence for the existence of such primary magmas feeding arc systems includes phenocryst core compositions in equilibrium with primary magmas or mafic inclusions (Graham and Thirlwall, 1981; Dungan and Davidson, 2004).

Arc volcanoes can erupt a wide range of magma compositions (Ringwood,1974; Grove and Kinzler, 1986) with compositional diversity observed across entire volcanic island arcs, as well as within individual volcanic centres (e.g. Lesser Antilles: Brown et al., 1977, Melekhova et al., 2015, 2017; Japan: Tatsumi et al., 1994; Kamchatka: Churikova et al., 2001, Koulakov et al., 2017). The range of erupted magma compositions at arc settings is thought to reflect polybaric fractional crystallisation, whereby a primary magma produced by partial melting of the mantle wedge undergoes multiple stages of fractionation within the overlying crust (Almeev et al., 2013; Melekhova et al., 2015; Ulmer et al., 2018; Marxer et al., 2022). Understanding where fractionation occurs within the crust and the compositions of melts generated is important in tracking chemical differentiation in magmatic systems. Magmas generated by polybaric fractional crystallisation can be further modified by magma mixing or assimilation (DePaolo, 1981), resulting in an even wider range of compositions erupted at the surface. Conversely, some volcanic centres produce magmas of the same composition (or near enough) throughout their entire lifetime, with examples including Arenal, Costa Rica (Streck et al., 2005; Parat et al., 2014), North Sister and Mt. Rainier, Cascades (Schmidt and Grunder, 2011; Sisson et a., 2014), Calbuco, Chile (Mixon et al., 2021), Klyuchevskoy, Kamchatka (Melekhova and Blundy, 2024), and La Soufrière, St. Vincent (Heath et al., 1998a).

Chemical differentiation in crystal-rich magmatic systems is thought to involve melts percolating through and re-equilibrating with the crystalline mush in a process termed percolative reactive flow (Solano et al., 2014; Jackson et al., 2018; Lissenberg et al. 2018). The ability of magmatic systems to continuously produce near-identical magma compositions is thought to reflect compositional buffering of a melt at its source by the source rock assemblage, which is volumetrically dominant (Sparks et al., 2019; Blundy, 2022). Determining how magmas of the same composition are repeatedly generated is essential to our understanding of chemical differentiation within crystal-rich mushes. Further, locating regions of melt generation and accumulation in the crust could aid our

interpretation of geophysical signals beneath active volcanoes. To test the concept of compositional buffering and locate the source of repeatedly generated magma compositions, I use La Soufrière volcano, St. Vincent, in the Lesser Antilles as an example of a volcano that has continued to erupt basaltic andesite magmas (52 – 57 wt. % SiO_2) throughout its lifetime (over 0.69 Ma; Briden et al., 1979). The compositional homogeneity and crystallisation history of La Soufrière magmas are first explored to establish variability in the system and whether erupted magmas have undergone mixing or assimilation during ascent. I also investigate the alteration textures observed in erupted magmas to determine near-surface residence conditions.

1.2 Multiple saturation experiments as a thermobarometer

Geobarometry and geothermometry are the conventional methods used to derive pressure and temperature estimates of magmas (Powell and Holland, 1994; Powell, 1985), however both require a suitable mineral assemblage and assume the attainment of equilibrium with no further overprinting. Geothermometers can provide temperatures within ~ 40^{o}C of a 900 – 1300^{o}C eruption temperature range (Wells, 1977; Holland and Blundy, 1994; Putirka, 2005, 2008), however geobarometers often have uncertainties of 0.1 – 0.3 GPa, significant when compared to source pressure estimates of, for example 0.7 GPa beneath island arcs (Ballhaus et al., 1991; Ziberna et al., 2017; Weber and Blundy, 2024).

Another method to determine the pressure and temperature a magma formed at is to use experimental petrology. Melting or crystallisation experiments can be carried out to identify where a melt last equilibrated with its source assemblage prior to eruption, by locating near-liquidus multiple saturation (Wyllie, 1984; Asimow and Longhi, 2004). Such experiments were first performed by melting peridotite (mantle source rock) to generate mantle derived magma compositions (Yoder and Tilley, 1962; Kushiro, 1973). Examples

of inverse crystallisation experiments that achieve multiple saturation close to the liquidus include Tatsumi et al. (1983), Pichavant et al. (2002b), Melekhova et al. (2015), Husen et al. (2016), Blatter et al. (2017), Becerra-Torres et al. (2020). In the case of crystallisation experiments, the mineral compositions saturated at the liquidus are compared to natural source assemblages, such as those observed in erupted xenoliths, to ensure experimental data are realistic. The Lesser Antilles volcanic arc is known for its abundance of erupted xenoliths (Arculus and Wills, 1980), of particular interest are the crustal xenoliths that represent the composition of the crust, from which more evolved melts are often derived. Use of near-liquidus multiple saturation experiments as a novel thermobarometer for crustal-derived melts is explored in chapter 4 of this thesis for the frequently erupted basaltic andesite magmas of La Soufrière volcano, St. Vincent.

1.3 Geological setting and eruptive history

1.3.1 Tectonic setting

The Lesser Antilles volcanic island arc (Figure 1.1a) is ~ 750 km long and is the result of the westward subduction of the North and South American plates beneath the Caribbean plate at a relatively slow rate (~ 2 – 4 cm/year; Macdonald et al., 2000). 21 active volcanic centres exist across the arc, between the southern (Grenada to St. Vincent), central (St Lucia to Guadeloupe) and northern (Montserrat to Saba) segments. North of Martinique the arc bifurcates into an active western limb and an extinct eastern limb, with Martinique positioned at the hinge of the volcanic divide. Martinique records this migration in volcanism across the island (Germa et al., 2011), which is thought to be due to the subduction of more buoyant material, such as an aseismic ridge, causing slab-shallowing and a subsequent shift of the arc away from the trench (Boynton et al., 1979; Stein et al., 1982; Bouysse and Westercamp 1990; Cooper et al., 2020).

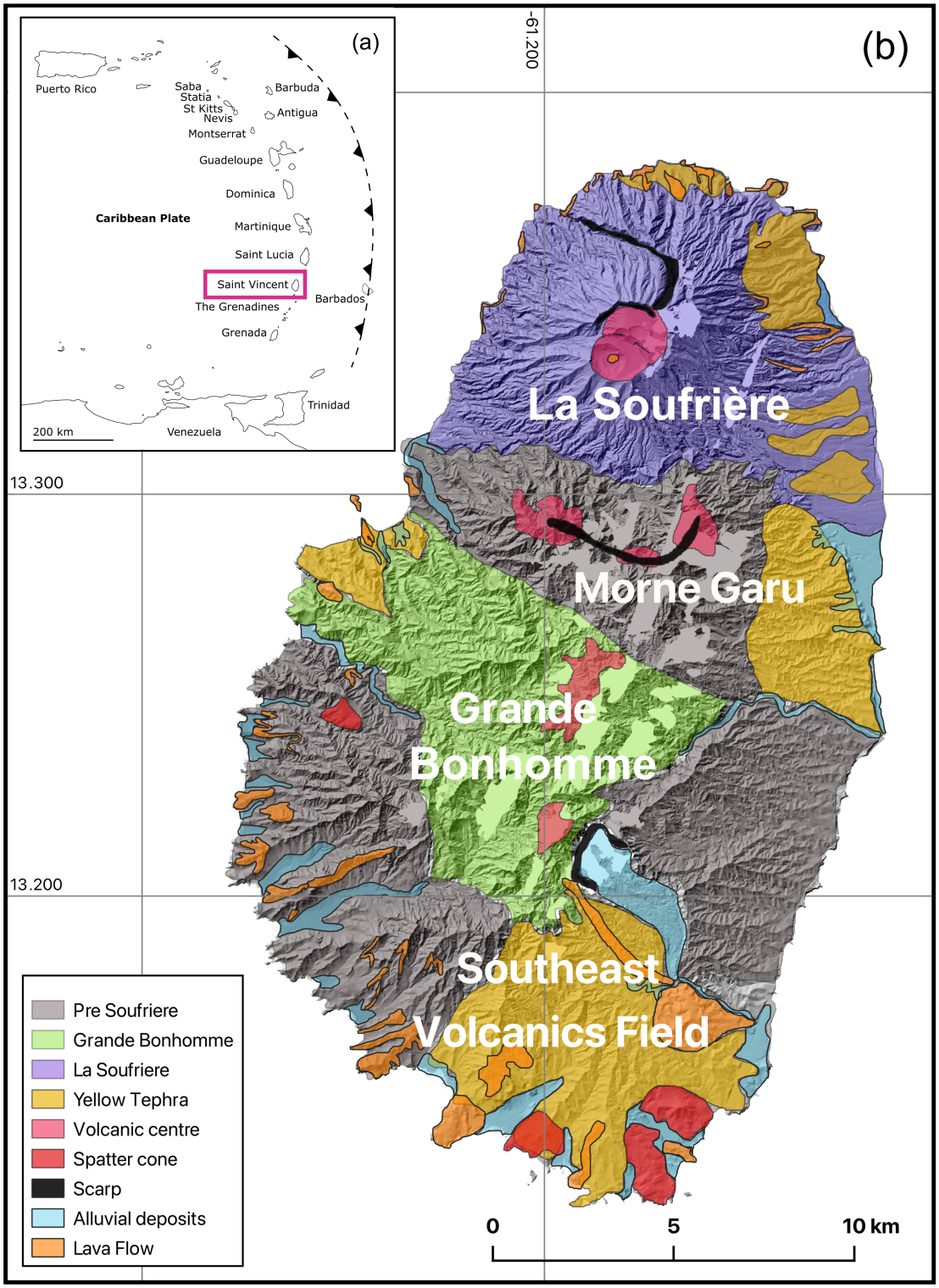


Figure 1.1: Map of **(a)** the Lesser Antilles volcanic island arc and **(b)** the island of St. Vincent. The four volcanic centres present on St. Vincent are labelled, with La Soufrière being the youngest and currently active. Geological units after Fedele et al. (2021) and Robertson (2005). Digital elevation model data from USGS-VDAP.

The Lesser Antilles arc is broadly divided into three compositional groups: the northern islands of Montserrat, St. Kitts and Nevis, St. Eustatius and Saba are classified as tholeiitic (iron-enriched), the central islands of St. Lucia, Martinique, Dominica and Guadeloupe as calk-alkaline (iron-depleted), and the southern islands of Grenada and St. Vincent and the Grenadines produce both calc-alkaline and tholeiitic magmas that are often more mafic and silica undersaturated (Brown et al., 1977). The northern and central islands of the Lesser Antilles produce predominantly andesitic to dacitic magmas, whilst Grenada and St. Vincent and the Grenadines produce more basaltic to basaltic andesite magmas (Macdonald et al., 2000; Brown, 1977). St. Vincent has previously been reported as a compositionally transitional island due to the presence of both calk-alkaline and tholeiitic material (Heath et al., 1998a) and is one of the few islands in the arc (along with Grenada) to erupt primitive high-magnesium basalts (Figure 1.2; Tollan et al., 2012; Pichavant et al., 2002a; Pichavant and Macdonald, 2007; Melekhova et al., 2015). Primitive magmas are defined as magmas with Mg# ≥ 70 (Mg# = 100 * Mg / (Mg + Fe^{2+})) and are in equilibrium with high-forsterite (≥ Fo_{90}) olivine (Grove et al., 2012). High-magnesium basalts in the Lesser Antilles have ≥ 10 wt. % MgO (Pichavant et al., 2002a; Melekhova et al., 2015), with some also containing high chromium contents (≤ 1400ppm; Arculus et al., 1976) indicative of mantle melting (Atlas et al., 2022). Low-magnesium basalts are defined as magmas with 6 – 10 wt. % MgO, and high-aluminium basalts contain ≤ 6 wt. % MgO and ≥ 19 wt. % Al_2O_3 (Melekhova et al., 2015).

Variation in trace element and isotopic abundances and ratios can be diagnostic about sediment input, slab fluid involvement and mantle melting (Hawksworth et al., 1991; Plank and Langmuir, 1993; Thirlwall et al., 1994; Elliot et al., 1997; Elliot, 2003; Plank, 2005; Turner and Langmuir, 2015, 2022; Cooper et al., 2020; Cooper and Inglis, 2022). Trace element concentrations find higher degrees of sediment melting in the northern islands compared to the southern islands (Carpentier et al., 2008; Atlas et al., 2022), whilst enrichment in $\delta^{11}B$ isotopes suggests a greater fluid input in the central arc due to

the subduction of serpentinised fracture zones (Cooper et al., 2020). Over five major faults striking E-W have been identified in the Lesser Antilles region (Schlaphorst et al., 2018; Bie et al., 2020; Braszus et al., 2021), dissecting the subduction zone and providing pathways for fluid and melt (Cooper et al., 2020; Hicks et al., 2023). St. Vincent is unlike neighbouring islands in the Lesser Antilles arc in terms of trace element and isotopic signatures, with little sediment input identified (Hedge and Lewis, 1971; Pushkar, 1973; Atlas et al., 2022), yet considerable fluids (Cooper et al., 2020), suggesting a hydrous and oxidised source region.

Xenoliths are abundant across the Lesser Antilles (Lewis, 1973; Arculus and Wills, 1980; Tollan et al., 2012; Stamper et al., 2014a; Cooper et al., 2016; Camejo-Harry et al., 2018, 2024a; Melekhova et al., 2019, 2022; Brown et al., 2021), and contain varying proportions of plagioclase, clinopyroxene, amphibole, olivine, magnetite, orthopyroxene and some more felsic minerals (Melekhova et al., 2019). Recent work has identified the presence of meta-igneous xenoliths at Petit St. Vincent (Melekhova et al., 2022), suggesting reworking and remelting of the arc crust. Meta-sedimentary xenoliths are identified at numerous volcanoes within the Lesser Antilles and provide insight into the relative contribution from different sedimentary sources and subsequent deformation processes within the crust (Devine and Sigurdsson, 1980; White and Dupre, 1986; Cooper and Inglis; 2022).

Seismic studies exploring the crustal structure beneath the Lesser Antilles arc find considerable variation in crustal density along the arc (Schlaphorst et al., 2018, 2021). A combination of geophysical data and xenolith petrology further constrain the crustal structure beneath the Lesser Antilles arc (Melekhova et al., 2019). At St. Vincent, crustal densities range from 2.88 to 3.93 g/cm^3, with the Moho estimated at ~ 29 km depth (Schlaphorst et al., 2018; Melekhova et al., 2019).

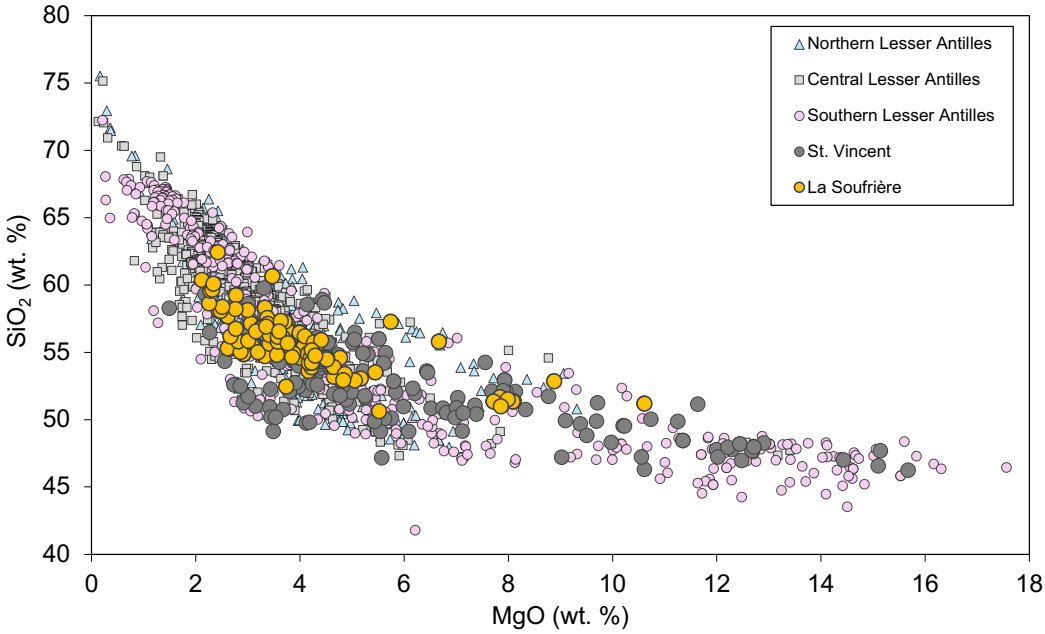


Figure 1.2: Silica versus MgO (wt. %) for Lesser Antilles magmas divided into southern (pink cirlces), central (grey squares) and northern (blue triangles) arc segments. St. Vincent (grey circles) and La Soufrière (yellow circles) magma compositions are plotted separately St. Vincent magma compositions extend to high-magnesium basalts, yet the current active volcanic centre, La Soufrière, has produced a more limited compositional range. Data from GEOROC, Rowley (1978) and Robertson (2002).

1.3.2 St. Vincent

St. Vincent is comprised of four main volcanic centres: the South-East Volcanics, Grand Bonhomme, Morne Garu and La Soufrière (Figure 1.1b). Volcanism on St. Vincent is characterised by alternating periods of effusive and explosive behaviour, ranging from basaltic to andesitic in composition. Thick sequences of interbedded lava and pyroclastic flow deposits are observed across the island suggesting this style of volcanism is typical for St. Vincent. Dykes are identified at all volcanic centres and lava domes are present at the Grand Bonhomme, Morne Garu and La Soufrière volcanic centres (Rowley 1978; Sigurdsson 1981; Robertson, 2002). A small number of spatter cones are found towards the south of the island (Robertson, 2002). Xenoliths at St. Vincent range from olivine gabbros to troctolites to hornblendites (Tollan et al., 2012). Metasediments including calcareous hornfels and norites are also identified at St. Vincent and suggest magmas are sampling the proto-Caribbean limestone crust (Devine and Sigurdsson, 1980).

The South-East Volcanic region is dominated by thick basaltic lava flows, with intruding dykes and numerous late-stage monogenetic spatter cones (Figure 1.1b; Robertson, 2002). The lavas here are dated at 2.74 ± 0.07 to 1.54 ± 0.62 Ma using K-Ar dating (Briden et al., 1979; Robertson, 2005) and are the oldest exposed rocks on St. Vincent. A layer of yellow tuff overlies the deposits from the South-East volcanic zone and is thought to be part of the Yellow Tuff Formation (YTF) eruption from La Soufrière 3.5 – 4.5 ka (Rowley, 1978).

The Grand Bonhomme volcanic centre sits just north of the South-East volcanic zone and covers a large portion of the centre of the island, though is mostly inaccessible (Figure 1.1b). Multiple peaks are identified and considered to be old volcanic plugs or domes responsible for producing lava flows, ash fall deposits, and block and ash flows (Robertson, 2005). Grande Bonhomme produced magmas of basaltic to andesitic composition; lavas on the west and southwest coast are dated at 1.33 ± 0.09 and 1.16 ± 0.18 Ma, respectively (Briden et al., 1979).

Morne Garu is north of Grande Bonhomme and has two volcanic centres, Richmond Peak to the west and Mount Brisbane to the east (Figure 1.1b). These volcanic centres are thought to be the remnants of an old caldera now heavily vegetated and inaccessible. Volcanic products include extensive ash fall deposits, lava flows, volcaniclastics and red scoria bombs (Robertson, 2005). Lavas at Richmond Vale, on the western flank of Morne Garu, are dated at 1.18 ± 0.10 Ma (Briden et al., 1979).

Lavas on the northern flank of La Soufrière are dated at 0.69 ± 0.09, 0.66 ± 0.10 and 0.36 ± 0.07 Ma (Briden et al., 1979), providing the oldest dates for this volcanic centre and supporting a northern migration of volcanism across the island. More recent $^{40}Ar/^{39}Ar$ dating of lavas on the eastern flank of La Soufrière give ages of 0.324 ± 0.015 and 0.291 ± 0.010 Ma (Heath, 1997). Two additional lavas on the eastern flanks of La Soufrière and

Morne Garu, at Black Point (STV301) and Indian Estate (STV345), are younger at 0.180 ± 0.021 and 0.011 ± 0.014 Ma respectively (11 ± 14 ka; Heath, 1997). Whether these lavas originated from Morne Garu or La Soufrière remains debatable due to similarities in lava geochemistry and inaccessibility of the Morne Garu eruptive centres for comparative sampling (Heath, 1997; Robertson 2002). Radiocarbon dating of pyroclastic material and charcoal from La Soufrière date back to ~ 5 ka and are discussed in chapter 2 (Rowley, 1978; Heath, 1997; Robertson, 2005; Cole et al., 2019).

Experimental studies exploring the source of the high-magnesium basalts erupted on St. Vincent propose these magmas are derived from the mantle at 1.0 – 1.6 GPa, 1160 – 1240ºC, with 1.5 – 4.5 wt. % H_2O and at oxygen fugacities between NNO+1 to NNO+2.3, (Pichavant et al., 2002a, Pichavant and Macdonald, 2007, Melekhova et al., 2015), and differentiate to form low-magnesium basalts, high-aluminium basalts, basaltic andesites and andesites. Of these generated melts, basaltic andesites are the most frequently erupted composition at La Soufrière (Rowley, 1978; Heath et al., 1998a), yet their origin in the crust has been little explored.

^{238}U – ^{230}Th mineral isochron ages suggest crustal residence times at La Soufrière are on the order of tens of thousands of years, considerably longer than eruption timescales for the investigated magmas (≤ 4 ka; Heath et al., 1998b). More recent studies propose that long residence times reflect time spent locked up as part of the crystalline mush at temperatures of ≤ 750ºC, and that crystals actually only spend up to a few decades at ≥ 900ºC (Cooper and Kent, 2014). Such findings support the existence of long-lived magma systems, with melts existing only ephemerally. Olivine diffusion chronometry in erupted basaltic andesite magmas at La Soufrière also supports magma mobilisation on decadal timescales prior to eruptions (Camejo-Harry et al., 2025). Understanding where eruptible magmas are generated and reside in the crust prior to eruption is important when considering future eruptions at active volcanoes.

1.3.3 La Soufrière

La Soufrière dominates the northern third of the island of St. Vincent, with a summit elevation of ~ 1178 m (Figure 1.1b). There are three visible eruptive craters at La Soufrière: the Somma crater, the 1812 crater and the currently active La Soufrière crater. The Somma crater is ~ 2.2 km in diameter and is represented by a horseshoe-shaped scarp that opens up to the southwest (SW), with only the northern wall of the crater still standing at ~ 250 m tall (Anderson, 1903; Flett, 1908; Rowley 1978; Robertson 2002, Le Friant et al., 2009). The scarp is indicative of a flank collapse to the SW, removing a large volume of material by debris avalanches (Sigurdsson, 1981; Boudon et al., 2007; Le Friant et al., 2009). The Somma crater crosscuts the Baleine scarp, which opens to the west and likely represents an even larger, earlier flank collapse to the west (Boudon et al., 2007; Le Friant et al., 2009). The La Soufrière crater is located within the old Somma crater, with the 1812 crater situated on its NE rim. After the 2020-2021 eruption and the deposition of a huge volume of pyroclastic material within the La Soufrière crater, the crater is now divided into an inner and outer crater (Figure 1.3a). The inner crater is ~ 0.8 km in diameter and ~ 100 m deep, whilst the outer crater is ~ 1.4 km diameter with the tallest crater walls to the north at ~ 150 m high.

Activity at La Soufrière is dominated by alternating effusive and explosive eruptions. Lava domes, lava flows, ashfall and pyroclastic density current deposits are all identified, though high erosion rates in the tropics act to rapidly remove volcanic deposits simultaneously or sequentially to an eruption (Aspinall et al., 1973; Robertson, 2005). The number of lava domes extruded in the La Soufrière crater remains unknown, as these domes are often destroyed during explosive periods of activity. At least five lava domes have been documented: 1784, 1880, 1971-1972; 1979 and 2020-2021, with the latter three sampled (Aspinall, 1973; Graham and Thirlwall, 1981; Cole et al., 2019; Weber et al., 2024). Compositions of erupted material range from basaltic to basaltic

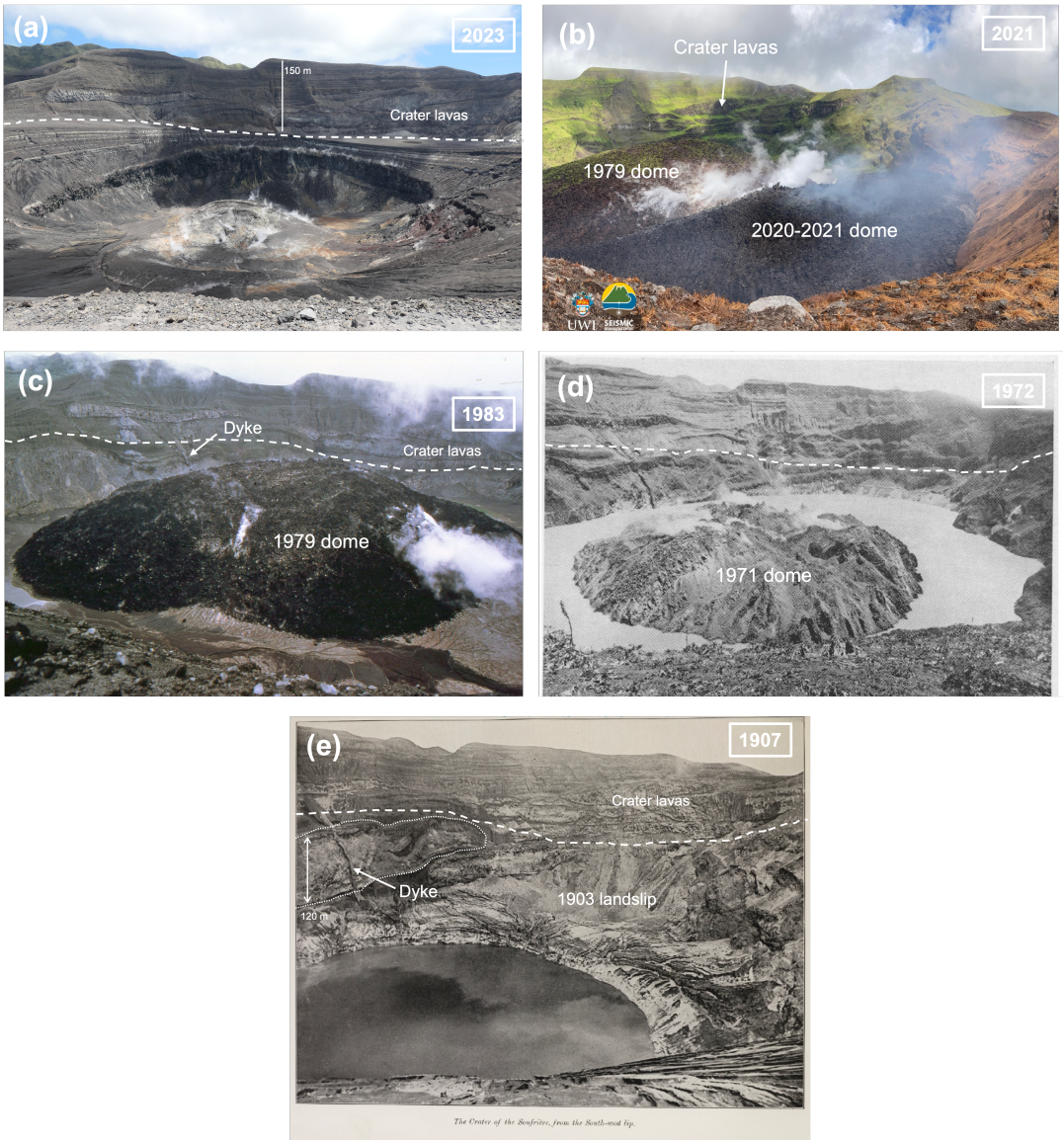


Figure 1.3: Photographs of the La Soufrière crater between 1907 and 2023. **(a)** La Soufrière crater after the explosive phase of the 2020-2021 eruption, exposing the crater walls and infilling the crater with pyroclastic material below the dashed line. Dashed line shown in other images for reference. Photograph taken by George Cooper during fieldwork in 2023. **(b)** La Soufrière crater during the effusive stage of the 2020-2021 eruption, illustrating new dome growth alongside the older 1979 dome. Discolouration of vegetation on crater walls by new activity is clearly observed (green vs orange). Crater lavas in the eastern wall labelled. Photograph from UWI-SRC. **(c)** 1979 dome occupying the crater floor, with small ephemeral crater lake to the east. Lavas in crater walls clearly exposed. 120 m thick lava unit in northern wall now buried by pyroclastic material. Photograph from Fiske in 1983, Smithsonian. **(d)** 1971 lava dome extruding through prominent crater lake. Photograph from Aspinall et al. (1973). **(e)** La Soufrière crater after 1902-1903 explosive eruption. Crater lavas in upper eastern wall clearly exposed. 120 m thick lava flow in northern wall exposed and clearly cross-cut by a dyke. Permanent crater lake at this time. Photograph from Anderson (1908). All photographs taken facing NE and scale as in (e).

-andesite, with rarer andesites and high-magnesium basalts. Fedele et al. (2021) identified abundant micro-xenoliths (≤ 3 cm) in erupted scoria from prehistoric (≤ 1440 CE) and historic (1718 – 1903) eruptions. These micro-xenoliths provide evidence of the crystal-rich mush composition beneath La Soufrière present within the last ~ 400 years, compared to previous xenoliths that could have been erupted up to 0.69 Ma (Briden et al., 1979). Crater lakes have existed in the crater in the past, though often only appear during heavy rainfall. Accumulated water readily evaporates as steam due to high temperatures on the crater floor or when water interacts with hot pyroclastic material in the crater (Sigurdsson, 1981). Today small ephemeral crater lakes sometimes appear on the inner and outer crater floors.

The volcanic deposits of prehistoric La Soufrière have previously been divided up into four main formations: the pre-Somma lavas (PSL), the Yellow Tuff Formation (YTF), Crater Lavas (CL) and Pyroclastic Formation (PF) (Sigurdsson, 1981; Heath et al., 1998a). Six major historic eruptions have since occurred at La Soufrière: 1718, 1812, 1902-1903, 1971-1972, 1979 and 2020-2021.

1.3.4 Prehistoric eruptions

Pre-Somma Lavas

The pre-Somma lavas form the base of the La Soufrière volcanic centre and have been dated at ≤ 0.69 Ma (Briden et al., 1979; Heath, 1997). The name ‘pre-Somma lavas’ originates from the idea that these lavas pre-date the collapse of the Somma edifice, the remnants of which form the Somma scarp to the northwest of today’s current volcanic centre (Figure 1.1b; Heath, 1997). Some refer to these lavas instead as the ‘Somma lavas’ as they built up the Somma edifice (Rowley, 1978), but I use the more widely referred to name of the pre-Somma lavas. The pre-Somma lavas represent a period of predominantly effusive volcanism, dominated by the extrusion of lava flows across the

northern portion of the island. The pre-Somma lavas are generally basaltic in composition and the most primitive material identified from La Soufrière (Heath, 1997). Samples of the pre-Somma lavas have been collected from the Somma caldera wall (NW of the current La Soufrière crater) and along the flanks of the volcano (Rowley, 1978; Heath 1997). The distance from the crater to the coast is ~ 4 km to the west and ~ 6 km to the east, readily achievable by low viscosity magmas. The absence of explosive material during this time is thought to be due to a lack of water interaction, thus no phreatomagmatic eruptions (Sigurdsson, 1981).

The destruction of the southern rim of the Somma crater and formation of the Somma scarp is recorded by the presence of a debris flow unit on the southern edge of the crater over 100 m thick (Sigurdsson, 1981). Dip direction indicates material flowed from the north, supporting the collapse and slumping of the Somma edifice to the south. Basaltic andesite lava blocks up to 1 m in size are identified in the debris flow, and the presence of basaltic andesite lava lenses in deposits to the east suggests that lava extruded simultaneously to the Somma collapse event. Sigurdsson (1981) compares the Somma collapse to the eruptions of Bandai-san in 1888, Bezymianny in 1956, and Mt. St. Helens in 1980, whereby flank collapse or landslides trigger or occur parallel to large explosive eruptions, simultaneously depositing huge debris flows. In the crater, a yellow tuff is deposited on top of the thick debris flow unit (Sigurdsson, 1981).

Yellow Tuff Formation

The Yellow Tuff Formation (YTF), termed the Brown Tuff Formation in Sigurdsson (1981), blankets the entire island of St. Vincent. Deposits are up to 150 m thick in the crater, 50 m thick at Sandy Bay and Jumbly point on the northeast coast, and 5 m thick near Kingstown at the southern end of the island approximately 20 km from the vent (Rowley, 1978). Deposits are comprised of yellow ash, lapilli and black scoria, with up to 110 fall units recognised in a single deposit. The absence of deep weathering or soil horizons

suggests relatively rapid and continuous emplacement (Rowley, 1978). Radiogenic dating (C^{14}) of organic matter in YTF deposits provides age estimates of approximately 3.51 ± 0.065 – 4.335 ± 0.095 ka (Rowley, 1978). An anomalous date of 14 ± 0.15 ka for an airfall deposit at the mouth of the Larikai river isn't considered to be related to the YTF as its stratigraphic position is poorly constrained and the deposit is inferred to have been reworked (Rowley, 1978; Heath, 1997). Within the crater, the yellow tuff formation overlies the Somma collapse debris flows (Sigurdsson, 1981), suggesting the Somma collapse must have occurred at least ~ 4.3 ka. The YTF is basaltic to andesitic in composition, producing some of the most evolved material at La Soufrière, and on St. Vincent. YTF deposits contain blocks of lava, either from older lava flows or lavas erupted simultaneously. Igneous and sedimentary xenoliths are also identified within the YTF deposits.

Crater Lavas

The Crater lavas form the walls of the La Soufrière crater that is active today (Figure 1.3). These lavas likely filled any depressions or topographic lows in the crater formed by the collapse of the Somma edifice and appear to have flowed predominantly to the south and east (Sigurdsson, 1981). This effusive stage of La Soufrière's eruptive history is thought to represent similar conditions to of the emplacement of the pre-Somma lavas, due to the lack of interbedded pyroclastic material, and inferred lack of water-interaction. Sigurdsson (1981) mapped the lavas exposed in the crater walls after the 1979 eruption, identifying the lowest crater lava in the eastern wall (Sample 801; Rowley, 1978), and a 120 m thick lava in the northern wall (Sample 806; Rowley, 1978), both basaltic andesite in composition. The 120 m thick crater lava unit has a steep upper contact with the overlying debris flow and YTF deposits, previously interpreted as unconformable and representative of an old crater wall (Sigurdsson, 1981). The younger crater lavas above this are all thinner (≤ 40 m thick). Jointing and shearing are common features, with lens-

like morphologies indicating discrete flows. Three dykes were identified in the crater that are not visible today, one in the eastern wall and two in the northern wall, one of which cuts the 120 m thick crater lava (Figure 1.3c-e). Pyroclastic deposits overlay the crater lavas thus are inferred to be younger.

Pyroclastic Formation

Pyroclastic and ash fall deposits dominate the crater walls to the SW and blanket the crater lavas to the N and NE (Figure 1.3). Deposits are comprised of lapilli, scoria and lithics; are mostly basaltic andesite in composition; and are thought to be the product of vulcanian explosions and pyroclastic flows (Rowley, 1978; Heath, 1997; Cole et al., 2019). Some lava flows are identified between pyroclastic deposits on the SW flanks (Sigurdsson, 1981), though eruptions appear to be primarily explosive. The pyroclastic formation represents a similar eruptive style to more recent eruptions, predominantly explosive with minor effusive activity. Rowley (1978) likens pyroclastic flows from Overland (SE coast) and Dry Wallibou (SW), dated at 2480 ± 70 and 320 ± 70 years respectively, to the explosive deposits of the 1902 eruption. This style of activity appears to have dominated at La Soufrière for up to ~ 4 ka (post Somma collapse and crater lavas), producing predominantly basaltic andesite composition magmas.

1.3.5 Historic eruptions

Cole et al. (2019) define the historic period at La Soufrière as after 1700 CE, when the Eastern Caribbean was colonised. Six major historic eruptions are known to have occurred during this time: 1718, 1812, 1902-1903, 1971-1972, 1979 and 2020-2021.

The 1718 eruption involved a large explosive eruption after preceding earthquakes. Tephra fallout was reported on ships passing by and on neighbouring islands, reaching up to 20 cm thick on Martinique (Anderson, 1908; Flett, 1908). In 1784 a dome was

identified in the crater, though no age constraints are available for when it formed (Cole et al., 2019). Earthquakes were documented for a year prior to the 1812 eruption, which initiated with a large explosion and PDC's to the SW. Tephra fallout deposits reach ~ 20 cm thickness on the eastern flanks and ashfall was observed on Barbados (Anderson, 1908; Flett, 1908). Today the 1812 crater is still seen on the northeastern rim of the La Soufrière crater (Figure 1.1b).

The 1902-1903 eruption is very well-documented. Fourteen months of earthquakes preceded the initial eruption (Pyle et al., 2018), which occurred in May 1902. A crater lake existed at the time of eruption (Figure 1.3e) resulting in water and steam driven explosions (Cole et al., 2019). Explosions generated numerous PDC's and voluminous ash fallout (Carey and Sigurdsson, 1978; Shepherd et al., 1979), again with ash reported on Barbados. 12 cm of ash fall was noted in Kingstown (Rowley, 1978), greater than all other historic eruptions, but minor compared to the 5 m deposited by the YTF eruption. One particularly large PDC appeared to flow down all flanks of the volcano to the coastline and across the sea for several kilometers, killing 1565 people (Pyle et al., 2018). Explosive eruptions in October 1902 and March 1903 were also significant. The 1902-1903 eruption evolved from basaltic andesite to basaltic in composition (Roobol and Smith, 1975; Cole et al., 2019), unlike all other eruptions that seem to remain homogenous.

The 1971-1972 eruption commenced with steaming of the crater lake and a gradual drop in lake level, indicating an increase in water temperature and evaporation. A basaltic andesite lava dome then extruded as an island through the lake (Figure 1.3d; Aspinall et al., 1973) with no seismic activity detected during either phase (Shepherd et al., 1979). Radial cooling joints and pillow-like textures on the surface of the 1971-1972 dome confirm the likely initial extrusion of magma in water (Aspinall et al., 1973; Sigurdsson, 1981). Six years later, precursory earthquakes hinted at an imminent explosive eruption.

In early 1979, a series of explosive eruptions generated PDC's and mudflows, partly destroying the 1972 dome and completely vaporising the crater lake (Graham and Thirlwall, 1981). Eruption columns, reaching up to 18 km high were reported (Shepherd et al., 1979; Shepherd and Sigurdsson, 1982). Once the explosive activity ended, a basaltic andesite lava dome extruded onto the crater floor, until growth ceased in late 1979 (Figure 1.3c; Huppert et al., 1982). The 1979 eruption produced solely basaltic andesite material, in both effusive and explosive phases (Shepherd et al., 1979; Cole et al., 2019).

1.3.6 2020-2021 La Soufrière eruption

The most recent 2020-2021 eruption at La Soufrière began with the extrusion of a basaltic andesite lava dome adjacent to the remnant 1979 dome, in late December 2020, with minimal precursory seismicity (Joseph et al., 2022). Fresh dome samples were collected by the University of the West Indies Seismic Research Centre (UWI-SRC) team on 16th January 2021, twenty days after the dome first breached the surface. Footprints of the expanding dome illustrate growth of ~ 150 m NW and ~ 100 m SE by the time of sampling (Joseph et al., 2022). By February 2021 the dome had elongated to become a coulee, between the remnant 1979 dome and the SW crater wall (Figure 1.3b).

A series of five explosive phases (U1-U5; Cole et al., 2024) commenced in early April 2021, destroying the 2020 and 1979 domes, and generating numerous PDC's and lahars. Samples of the explosive phase were collected on April 11th from multiple locations on the flanks of the volcano (Cole et al., 2024; Weber et al., 2024). The bulk composition of both the effusive and explosive stages of this eruption are near-identical, with a very similar phenocryst assemblage, but appearing texturally distinct (Weber et al., 2024), investigated in chapter 5. Two-pyroxene thermobarometry indicates magmatic temperatures of 960 – 1020ºC, with scoria temperatures slightly higher than the dome

(Weber et al., 2024). Comparatively, the surface temperature of the dome, measured using a FLIR T65osc thermal camera in January 2021, gave readings of ~ 590ºC, where rockfall had exposed the interior of the dome (Stinton et al., 2024), highlighting a thermal gradient from the centre to the edge of the dome.

The explosive phase of the 2020-2021 eruption exposed the previously heavily vegetated crater walls and infilled the crater with pyroclastic density current deposits, providing access to some of these crater lava units (Figure 1.3a). Today the internal structure of the 1979 dome is exposed in the newly formed inner crater and shows radial columnar joints and discolouring from alteration, likely hydrothermal (Figure 1.3a). New dome growth is observed in the inner crater, with an ephemeral crater lake.

1.4 Thesis aims and structure

In this thesis I use La Soufrière volcano, St. Vincent, Lesser Antilles as an example of a magmatic system that has repeatedly erupted basaltic andesite magmas of nearly the same composition throughout its lifetime. The extent of variability observed in the erupted basaltic andesite magmas is determined by exploring geochemical and petrological trends over time. Mineral compositions and textures provide further details of the crystallisation history and evolution of magmas during ascent, and any interactions with the wider magmatic system. To explore the origin of the frequently erupted basaltic andesite magmas at La Soufrière, near-liquidus high-pressure and high-temperature multiple saturation experiments are performed. Additionally, low-pressure and high-temperature experiments are carried out to investigate the surface processes magmas experience. This thesis explores the origin, evolution and post-eruption processes for basaltic andesite magmas erupted at La Soufrière in the following chapters:

Chapter 2 details fieldwork carried out at La Soufrière volcano and observed stratigraphic relationships. New major and trace element geochemistry data and $^{40}Ar/^{39}Ar$ dates are presented and used to explore the compositional variability of erupted magmas, evidence for differentiation from a parent magma and input from the subducting slab. A revised eruptive history is proposed based on new $^{40}Ar/^{39}Ar$ dates.

Chapter 3 explores the crystallisation history of erupted magmas at La Soufrière volcano and demonstrates the wide range of crystal cargo entrained by magmas. Ascent path conditions are inferred from observed mineral compositions and textures. The origin of antecrystic material and entrained micro-xenoliths are also investigated.

Chapter 4 determines the phase relations of the basaltic andesite magmas erupted at La Soufrière and explores their origin by searching for multiple saturation on the liquidus. Experimental mineral compositions are compared to erupted crustal xenolith compositions to ensure data match natural systems. The conditions of use for multiple saturation as a more precise thermobarometer are established. The role of oxidation state in the formation of calc-alkaline magmas and the stability of amphibole at near-liquidus conditions are also explored.

Chapter 5 uses experimental petrology to determine the conditions and timescales for the formation of alteration textures observed in the basaltic andesite lava dome extruded at La Soufrière in 2020-2021. The lack of such alteration textures in the compositionally identical scoria formed during the explosive phase of the eruption is investigated to determine where magmas may reside prior to the onset of explosive activity.

Chapter 2

Exploring the compositional variability of magmas erupted at La Soufrière volcano, St Vincent, using chemo-stratigraphy and new $^{40}Ar/^{39}Ar$ dates.

2.1 Introduction

La Soufrière is the currently active volcanic centre on the island of St. Vincent in the Lesser Antilles and has been producing basaltic andesite magmas for the last 0.69 Ma (Briden et al., 1979), with rare basalts and andesites. Early volcanism at La Soufrière was dominated by effusive lava flows building the initial Somma edifice (Rowley, 1978; Heath et al., 1998a). La Soufrière experienced a second period of consecutive effusive volcanism during the emplacement of a series of crater lavas from a younger vent. Today activity alternates between explosive pyroclastic density current (PDC) forming eruptions and effusive lava domes refined to the crater, with near-identical compositions (Rowley, 1978; Sigurdsson, 1981; Heath et al., 1998a; Robertson 2005; Cole et al., 2019; Fedele et al., 2021).

The continuous production of magmas with a limited compositional range is not uncommon for arc volcanoes, with other examples including Arenal, Costa Rica (Streck et al., 2002, 2005; Parat et al., 2014); North Sister, Cascades (Schmidt and Grunder, 2011); and Calbuco, Chile (Mixon et al., 2021). Magmatic systems that repeatedly

generate magmas of a similar composition over long periods of time (e.g. thousands of years) are thought to be buffered by the composition of the underlying crust (Hildreth and Moorbath, 1988; Blundy, 2022). These melts are proposed to be in equilibrium with the surrounding crystal-rich mush in their source region and can erupt at the surface, or stall in the shallow crust and evolve (Blundy, 2022), hence producing magmas of more variable compositions. By exploring geochemical and petrological trends in the sequentially emplaced effusive crater lavas at La Soufrière, and in dykes and lava flows on the western flanks of the volcano, I aim to determine whether La Soufrière reflects a long-lived homogenous magmatic system or whether magmas experience significant chemical modification after segregating from their source, such as mixing and differentiation. By dating a selection of these erupted magmas, timings of emplacement can be constrained, furthering our understanding of the eruptive history of La Soufrière.

2.1.1 Previous work

Previous geochemical analyses of the crater lavas found them to be mostly basaltic andesites (52 – 57 wt. % SiO_2) with a small number of andesites (57 – 60 wt. % SiO_2) in the eastern wall, now buried by the 2020-2021 pyroclastic material (Rowley, 1978). Three dykes were previously identified cross cutting the La Soufrière crater lavas (Rowley, 1978; Sigurdsson, 1981), and are also now buried by the pyroclastic deposits. All dykes are andesitic. One of the dykes identified is proposed as a feeder dyke to a crater lava in the northern wall, whilst the other two taper out (Rowley, 1978). Sampling the now accessible crater lava in the northern wall will establish whether the dyke and lava compositions correlate.

The pre-Somma lavas form the base of the La Soufrière volcano and are also predominantly basaltic andesite, though include eight high-magnesium basalts, four low-magnesium basalts and eight andesites of a total of sixty-two lava samples (Rowley

1978, Heath et al., 1998a). The high- and low-magnesium basalts all outcrop along the coastline at the base of the volcano and are inferred to have erupted early-on during building of the old Somma edifice (Heath et al., 1998a). These basalts agree with previous St. Vincent basaltic magma compositions (Robertson, 2002) and illustrate that initial more primitive magmatism ceased over time. The pre-Somma lavas also encompass a small number of andesitic magmas, all found in the Somma crater walls (N of current crater, see section 1.3.4), close to the source of extrusion (Rowley, 1978). These rare basaltic and andesitic magmas reflect small variations in a generally homogenous basaltic andesite magmatic system.

The pre-Somma lavas date back to 0.69 Ma (690 ka; Briden et al., 1979) and continued erupting for over three-hundred thousand years (Heath, 1997). There are large gaps in the eruptive history of La Soufrière between the youngest pre-Somma lavas (~ 291 – 11 ka; Heath, 1997) and ~ 4 ka when explosive activity became more frequent, known from radiogenic dating of pyroclastic deposits (Heath, 1997; Cole et al., 2019). Previously dated pre-Somma lava samples were often collected from coastal exposures. However, their origin is not always conclusively linked to La Soufrière volcano and their stratigraphic position within the Somma crater unknown. Dating the lavas exposed on the western flanks of La Soufrière will provide details of when volcanic activity persisted in this region, whilst dating the upper and lowermost crater lava allows for determination of when this second period of seemingly much briefer effusive volcanism occurred. Links between the emplacement of the crater lavas, the collapse of the Somma edifice, and the large explosive yellow tuff formation (YTF) eruption have previously been determined from field mapping (Sigurdsson, 1981) and dating of the YTF tephra (Rowley, 1978). Dating the crater lavas can provide a better understanding of the volcanic history of La Soufrière.

2.1.2 Fieldwork rationale

After the 2020-2021 eruption, the crater lavas that comprise the eastern crater wall and are usually heavily overgrown, were exposed providing a unique opportunity for sampling. These lavas were emplaced successively, thus preserve the natural relative age order which can be used to determine sequential changes in magma composition and petrology. Rowley (1978) collected rocks from lower down in the sequence, which is now buried by the pyroclastic deposits of the 2020-2021 eruption, but was not able to sample higher up the crater wall. Today the base of the new outer crater allows access to these previously unsampled crater lavas.

Many of the pyroclastic density currents produced by the 2020-2021 eruption funnelled down the western flanks of the volcano, exposing new outcrops and clearing vegetation from river valleys. Larikai valley extends from the base of the volcano to the summit (Figure 2.1). The recent eruption also exposed a dyke outcropping to the NW of the crater in upper Larikai valley not previously observed. Sampling the dyke and comparing whole-rock and mineral compositions to previous La Soufrière data allows me to determine the relationship of the dyke to the current magmatic system, and the role of dykes in feeding the volcano.

Roseau valley, southeast of Larikai valley (Figure 2.1), extends from the base of the volcano (sea level) to ~ 300 m elevation. Roseau has previously only been sampled for tephra (see Cole et al., 2019). Collecting lava samples from Larikai and Roseau valleys allows for comparison of their composition and mineralogy to the crater lavas, providing further insight into the long-term evolution of the La Soufrière magmatic system. The crater lavas and lavas on the western flank of La Soufrière have not previously been dated, thus new age estimates expand our knowledge of the eruptive history of La Soufrière and age of volcanism on the western side of the island

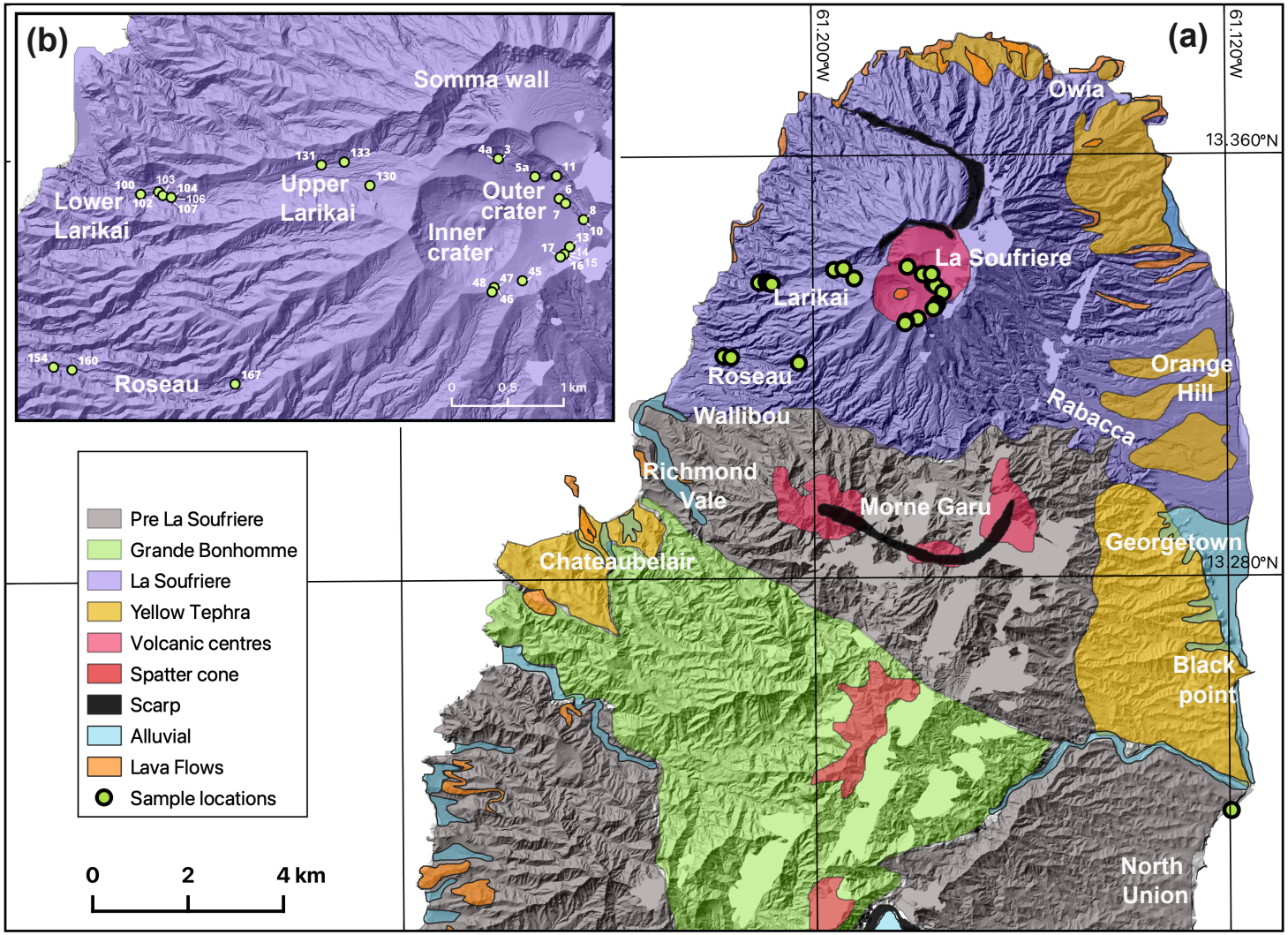


Figure 2.1: (a) Map of St. Vincent after Figure 1.1 with sample locations shown as green circles. Geological units after Fedele et al. (2021) and Robertson (2005). Digital elevation model data from USGS-VDAP. **(b)** Sample numbers and locations in La Soufrière crater and Larikai and Roseau valley, as listed in Table 2.1 (e.g. STV_LS_3 shown as number 3).

In 2023 a small team from the University of Oxford, University of Cardiff, and the University of the West Indies and Seismic Research Centre visited the La Soufrière crater to collect samples of the crater lavas. In 2024 we returned to sample an exposed dyke in upper Larikai valley and lavas from Larikai valley and Roseau valley on the western flanks.

2.1.3 $^{40}Ar/^{39}Ar$ dating of young volcanic rocks

$^{40}Ar/^{39}Ar$ and K/Ar geochronometry can be used to date samples billions of years old down to a few thousand years old (e.g. Lanphere, 2000; Scaillet and Guillou, 2004). These days $^{40}Ar/^{39}Ar$ dating is used more widely than K/Ar dating due to its higher precision and ability to use a smaller sample size.

$^{40}Ar/^{39}Ar$ dating is based on the K/Ar dating system whereby ^{40}K decays to produce radiogenic ^{40}Ar ($^{40}Ar^*$). ^{40}K is present in the atmosphere and naturally incorporated into rocks and minerals, however when the system closes (e.g. when a magma erupts and cools) it is no longer able to exchange with the atmosphere and $^{40}Ar^*$ starts being generated. ^{40}Ar is also present in the atmosphere and incorporated into rocks and minerals, such that an atmospheric correction must be applied to determine the amount of $^{40}Ar^*$ in a sample. In $^{40}Ar/^{39}Ar$ dating, ^{39}Ar is measured as a proxy for ^{39}K, which is used to determine initial ^{40}K from K isotope ratios. ^{39}Ar is not naturally occurring and must be generated from ^{39}K by irradiation which causes a fast neutron reaction (neutron capture, proton emission; n,p). The amount of ^{39}K irradiated is dependent on a number of factors including initial abundance, irradiation length and neutron flux. A standard of known age is irradiated simultaneously as a neutron flux monitor; neutron flux is then extrapolated to sample values and the neutron flux parameter (J) calculated. The sample is incrementally heated to release Ar in numerous stages, which allows for the quality of the data to be assessed, and any alteration detected. The different Ar isotopes are then

analysed using mass spectrometry and their relative abundances used to determine the age of the sample using the equation below:

$$t = \frac{1}{\lambda} \ln \left[\left(\frac{^{40}Ar*}{^{39}Ar} \right) J + 1 \right] \qquad \text{(Equation 2.1)}$$

where t is the age of the sample, λ is the decay constant of ^{40}K, $^{40}Ar^*$ is ^{40}Ar produced by radioactive decay of ^{40}K, ^{39}Ar is produced by irradiation of ^{39}K and J is the neutron flux parameter.

Results are usually displayed as age spectrum diagrams versus cumulative Ar (%), also known as plateau age diagrams, to determine the concordance of the data (Shaen et al., 2020). Some of the criteria for plateau ages include more than 50 % of Ar released agreeing within error of the plateau age; the plateau does not have a slope; and isochrons for all plateau steps used intersect with atmospheric $^{36}Ar/^{40}Ar$. Inverse isochron plots can be used to corroborate the initial amount of trapped atmospheric $^{36}Ar/^{40}Ar$ if data define a strong linear relationship (Shaen et al., 2020).

Some of the caveats of $^{40}Ar/^{39}Ar$ dating are that excess Ar from melt inclusions or xenoliths can result in an overestimate of the dates of samples (i.e. older age). Equally Ar loss due to alteration or high temperature damage can cause an underestimate of the true age (i.e. younger age; Shaen et al., 2020).

2.1.4 Geochemistry methods

Sample preparation

Forty-one samples were prepared for whole-rock major and trace element analysis using the geofacilities laboratories at the Department of Earth Sciences, University of Oxford. These samples include nineteen crater lavas, seven lava blocks recovered from the YTF,

six lava samples from Larikai valley, three lava samples from Roseau valley, five samples from two dykes and one sample of dome-rock.

Rock powder preparation

Lava samples were initially split into smaller fragments (≤ 5 cm^3) and any alteration removed using the stainless-steel rock splitter. Samples were then washed in an ultrasonic bath for 10 minutes and left to dry overnight in a 40ºC oven. Approximately 200 g of the clean sample material was crushed to ≤ 1 mm using the jaw crusher, where a stainless-steel fixed-jaw and removeable-jaw crush the material in one mm intervals, from 5 mm to ≤ 1 mm. The crushed material was then poured through a stainless-steel sample splitter at least three times to ensure a homogenous and representative batch of material.

Grinding of a sample material to a fine powder was carried out using either the agate ball mill or Tema mill. I used both for time efficiency. The ball mill contains four agate holders, each containing 10 agate balls, allowing four samples to be powdered simultaneously. 40 g of sample material was weighed into each agate holder and run at 400 rpm for 20 minutes. The Tema mill contains an inner and outer agate ring. Again 40 g of sample material was added to the agate container and run for 10-20 minutes until a fine powder obtained. Approximately 10 g of each rock powder was weighed into a glass vial and sent to ALS Geochemistry, Loughrea, Ireland for whole-rock major and trace element analysis.

All equipment was cleaned with compressed air and ethanol between each sample, the mills were also run with cleaning silica between samples to reduce contamination. The extractor fan in the preparation laboratory was ran during crushing and cleaning to keep the air clean, and gloves were worn to further reduce contamination.

Analytical methods

Whole-rock major and trace element analyses were performed by ALS Geochemistry, Loughrea, Ireland. Two previously analysed samples were also included (SHKB20 and SHKB51) with the forty-one samples for quality control. Major elements were analysed by x-ray fluorescence (XRF) following a lithium borate fusion. Trace elements were analysed by inductively coupled plasma mass spectrometry (ICP-MS). Precision error reported by ALS is 2 % for major elements and 10 % for trace element measurements; precision error is multiplied by concentration to ascertain the uncertainty of each measurement. Results are reported in Tables 2.1 and S2.2.

2.1.5 $^{40}Ar/^{39}Ar$ dating methods

Sample preparation

Ten lava samples were selected for $^{40}Ar/^{39}Ar$ dating. The criteria for the sample selection included minimal alteration and low vesicularity. Samples were chosen to cover the range of lavas collected from both field campaigns. Samples were shipped to Dr Brian Jicha at the University of Wisconsin-Madison, where they were crushed, sieved and prepared for irradiation at the Oregon State University reactor. Preparation included initial ultrasonic leaching of samples in 3M HCl for 15 minutes, followed by thorough and repeated rinsing with deionised water. Purification of the groundmass by magnetic sorting and hand-picking removed phenocrysts, xenocrysts and any altered material, to leave only fresh groundmass material (180 – 250 μm). Samples were then loaded into aluminium foil packets and irradiated in the cadmium-lined in-core tube at the Oregon State University reactor. A standard is irradiated simultaneously to monitor the neutron flux, the 1.1864 Ma Alder Creek sanidine was used in this case (Jicha et al., 2016).

Analytical methods

Analysis of the irradiated samples was completed at the WiscAr Laboratory at the University of Wisconsin-Madison. Samples were incrementally heated by a CO_2 laser to release the gas trapped in the sample in stages. The gas was then cleaned to remove H_2O, H_2, O_2, CO_2, CH_4, and CO, and analysed on an Isotopx NGX-600 mass spectrometer at 650 μA to determine isotopic abundances. $^{40}Ar/^{39}Ar$ ages were then calculated using equation 2.1, with the decay constants from Min et al. (2000) and an atmospheric correction of $^{40}Ar/^{36}Ar$ of 298.5 ± 0.31 applied, as determined by Lee et al. (2006). Heating steps that caused an increase in mean standard weight deviation (MSWD) ≥ 1.5 were excluded (Powell et al., 2002; Jicha et al., 2016) and are shown in relevant plateau diagrams (Figure 2.8; Figure S2.1). Plateau ages have lower uncertainty thus are used preferentially over isochron ages.

2.2 Results

2.2.1 Field observations and relative age relationships

2023: Crater lavas

Sixteen individual crater lava units in the crater walls (northeast to southeast) were identified (Figure 2.2), with samples collected from fourteen of these units. Relative age order was determined by stratigraphic positioning and the relationship of each unit to adjacent units. The upper crater lavas are assumed to be younger than those lower down in the sequence. Jointing is observed at the top and bottom of all units where exposed, with strong shearing observed in the centre of thicker lava flows (e.g. unit 7; Figure 2.2a). The lavas in the eastern wall have lens-like morphologies and sit directly on top of each other, filling topographic lows with little to no pyroclastic material between units. Red rubbly material is identified between sequential crater lavas, suggesting young hot flows

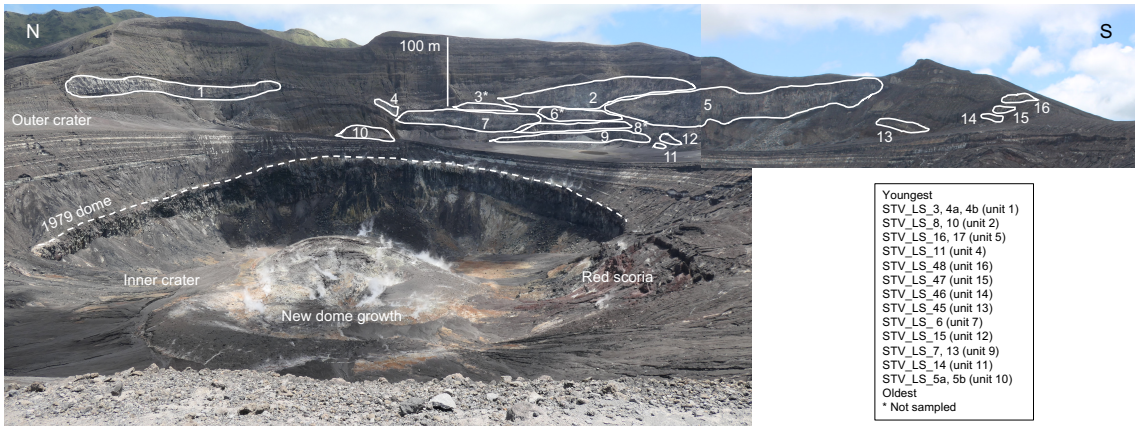


Figure 2.2: La Soufrière crater after the 2020-2021 eruption. Crater lava units labelled and ordered from youngest to oldest based on stratigraphic position. Crater lavas accessed for sampling from the floor of the outer crater. Photograph by George Cooper, 2023.

scorched and oxidised the upper surface of older lavas below. Up to ~ 100 m of pyroclastic material sits on top of the uppermost crater lavas in the eastern wall and can be traced across to the northern crater wall (Figure 2.2). The single crater lava in the northern wall (unit 1) sits sub-horizontal within this thick layer of pyroclastic deposits, meaning it must be younger. Below this unit and now covered by material from the 2020-2021 eruption, a vertical feeder dyke was previously identified (Anderson, 1908; Rowley, 1978; Figure 1.3e).

The 2020-2021 explosive phase of the eruption deposited thick layers of ash and pyroclastic material in the crater itself (Figure 2.2), as well as in both Larikai and Wallibou valleys. Pyroclastic deposits (up to 100 m thick, estimated from previous depth of crater) now fill the crater and cover the base of the crater walls up to unit 9, forming the floor of the outer crater. Blocks of scoria and dense lava scatter the outer crater floor. A small proportion of these loose eruption products are coated with a blue metallic deposit, either covering the entire sample, a single side, or cavities within the sample. These blue rocks are mostly located close to the inner crater rim and considered a product of hydrothermal alteration.

The interior of the 1979 dome, exposed by the 2020-2021 explosive eruptions, displays radial jointing and alteration (likely hydrothermal) as blue to orange discolouration (Figure 2.2). The inner crater is now occupied by a new dome that is actively degassing and shows signs of sagging and deflation. A red scoria unit is visible to the south of the inner crater (Figure 2.2). Active fumaroles and unstable slopes prevented us from entering the inner crater to sample any remaining 1979 dome rock. Abundant crystalline igneous xenoliths and green metasedimentary xenoliths were identified in the crater lavas and loose on the crater floor.

At the coast on the eastern flanks of La Soufrière, a 15 m thick deposit of the YTF is exposed at the side of the road just north of North Union town (Figure 2.1) and contains layers of large lithic blocks embedded in the tuff (≤ 70 cm; Figure 2.3b). Six lava blocks were collected to compare with the composition of the crater lavas to determine if the YTF was emplaced at the same time as some of the crater lavas, or if the lava blocks represent older crater lavas (e.g. pre-Somma lavas). The lava blocks from the YTF appeared rounded and altered.

2024: Larikai and Roseau lavas and dykes

During the 2024 field campaign four lava samples were collected from lower Larikai valley, two lava samples from upper Larikai valley and three lava samples from Roseau valley.

Lava flows in the lower Larikai valley were sampled from the exposed river bed, have smooth weathered upper surfaces (Figure 2.3c) and are interbedded with debris flows. Sample numbers STV_LS_100 and 102 are from the same lava flow ~ 100 m apart. STV_LS_104 could also be the same flow but was difficult to trace due to incomplete exposure. STV_LS_103 is the upper most lava flow sampled and is therefore assumed to be younger than the other lower Larikai lava flows (Figure 2.3d). Shearing and flow



Figure 2.3: (a) Crater lavas in the eastern wall with unit numbers labelled. Lavas display lens-like morphologies and are separated by red rubbly surfaces. Joining observed within all lava flows and shearing at the centre of thicker flows (e.g. unit 7). Pyroclastic unit continues above unit 3. Photography by Elena

Melekhova, 2023. **(b)** YTF deposit displaying containing large lithic lava blocks (≤ 70 cm). **(c)** Extensive lava flow (STV_LS_103) in lower Larikai valley carved out by river and with thick pyroclastic deposits on top. **(d)** Lava flows in lower Larikai valley interbedded with debris flows and cross cut by a vertical dyke. **(e)** Upper Larikai valley with a dyke exposed on the northern side of the valley (circled). Lavas in the background are the pre-Somma lavas comprising the still standing northern Somma crater wall. Thick pyroclastic deposits in the valley (including 2020-2021) make access to lavas difficult. **(f)** Contact between Upper Larikai dyke and lava flow. Upward tilt of lava flow and shearing fractures at the base of the exposure clearly observed. Photograph by Richard Robertson, 2024. **(g)** Thick lava flow in Roseau valley (STV_LS_167) with sheared interior exposed. **(h)** Giant xenolith block found in Roseau valley predominantly composed of interlocking plagioclase, clinopyroxene and olivine crystals. Clusters of different mineral assemblages observed, some displaying layering and banding (circled). (i) In-situ micro-xenolith (≤ 3 cm) in lower Larikai lava STV_LS_100. Contains plagioclase and olivine and displays a recrystallised darker core.

structures, such as elongated and stretched vesicles, and igneous and sedimentary xenoliths are abundant in all lava flows. Xenoliths varied in size from ≤ 3 cm (micro-xenoliths; Figure 2.3i) to ~ 10 – 15 cm. A 15 m tall and 10 m wide dyke was identified cross cutting the lower Larikai lavas (Figure 2.3d). The edge of the dyke is glassy, whilst the centre of the dyke has a high vesicularity. Pyroclastic deposits 20 – 30 m thick sat on top of the lava flows to the sides of the valley.

In the upper Larikai valley, thick pyroclastic flow deposits fill most of the valley with lava flows outcropping at the base and sides (Figure 2.3e). Approximately 300 m below the crater rim to the NW, a lava flow outcropping beneath the pyroclastic flow deposits was sampled (STV_LS_130). A red scoriacious deposit was identified beneath the lava flow. This lava flow contained lots of small igneous and sedimentary xenoliths, sheared vesicles and flow textures, and extended down the valley another ≥ 300 m. The surface of the lava flow was rubbly compared to the smooth weathered surfaces in lower Larikai valley. The second lava flow sampled in the upper Larikai valley (STV_LS_131) was on the northern edge of the valley, however the relationship of this lava flow to the previous flow was unclear. The lava flow follows the topography of the valley. A rubbly surface was observed beneath the flow.

The upper Larikai dyke crosscuts lava flows ~ 100 m upstream from the STV_LS_131 sample site. A sharp contact is observed between the dyke and adjacent lava flow, appearing to uplift the edge of the lava flow it is in contact with (Figure 2.3f). The dyke is ~ 12 – 15 m tall, near vertical and striking 300º (NW). Jointing is observed within the dyke and a region of finer parallel fractures near the base of the exposed dyke curve upwards interpreted as shearing. The upper Larikai dyke cuts into the side of the Somma caldera wall (Figure 2.3e), suggesting it postdates the collapse of the Somma edifice.

Two lava flows in Roseau valley outcropped at the base of the valley, their upper surfaces smooth from weathering and each displaying flow banding structures. These lavas were collected ~ 70 – 100 m apart (STV_LS_154 and 160) and could be from the same flow. The third lava sample was from a lava flow exposed in the valley walls towards the top of the valley (~ 200 m upstream; Figure 2.3g) and on top of the previous flows, thus interpreted to be younger (STV_LS_167). This lava flow is ~ 10 – 15 m thick, strongly jointed, with shearing fractures observed in the centre of the flow and a platy texture observed at the base of the flow (Figure 2.3g). At the sample site the lava flow overlies thick pyroclastic deposits (~ 20 m thick) and debris flows; downstream ~ 2 – 10 m of pyroclastic deposits instead sit on top of the flow.

A ~ 1 m by 1.5 m xenolith block containing inclusions of different xenolith types and textures was located in Roseau valley (Figure 2.3h), evidencing the crystal-rich crust beneath La Soufrière that these magmas must interact with.

2.2.2 Whole-rock major element chemistry

New whole-rock major element data for a total of forty-one samples are reported in Table 2.1. Compositions range from basalt to andesite (49.5 – 57.5 wt. % SiO_2), with the majority of lavas sitting in the basaltic andesite field (Figure 2.4). Three crater lava

Table 2.1. New lava whole rock major element data.

Sample #	Unit	Latitude	Longitude	SiO_2	TiO_2	Al_2O_3	FeO^T	MnO	MgO	CaO	Na_2O	K_2O	P_2O_5	Total	LOI
2023 fieldwork															
STV_LS_3	CL-1	13º20.3333" N	61º10.9004" W	54.79	0.89	18.91	7.89	0.18	4.24	9.01	3.39	0.54	0.13	99.97	-0.35
STV_LS_4a	CL-1	13º20.3334" N	61º10.9005" W	55.20	0.98	18.32	8.13	0.19	3.93	8.45	3.62	0.60	0.14	99.56	-0.20
STV_LS_4b	CL-1	13º20.3334" N	61º10.9005" W	56.03	0.98	18.28	8.09	0.19	3.91	8.45	3.63	0.59	0.14	100.29	-0.33
STV_LS_5a	CL-10	13º20.2465" N	61º10.7236" W	55.80	0.89	18.08	7.61	0.18	4.26	8.35	3.47	0.62	0.13	99.39	-0.19
STV_LS_5b	CL-10	13º20.2465" N	61º10.7236" W	56.22	0.88	18.10	7.50	0.18	4.12	8.28	3.53	0.62	0.13	99.56	-0.23
STV_LS_6	CL-7	13º20.1406" N	61º10.6068" W	54.99	0.93	18.86	7.63	0.17	4.52	8.97	3.40	0.59	0.13	100.19	-0.39
STV_LS_7	CL-9*	13º20.1175" N	61º10.5764" W	50.81	0.86	16.87	8.04	0.17	8.72	10.10	2.70	0.41	0.10	98.78	-0.26
STV_LS_8	CL-2	13º20.0397" N	61º10.49" W	55.49	0.92	18.55	7.73	0.18	4.32	8.67	3.42	0.59	0.13	100.00	-0.36
STV_LS_10	CL-2	13º20.0397" N	61º10.49" W	55.26	0.91	18.54	7.65	0.18	4.28	8.65	3.39	0.59	0.13	99.58	-0.39
STV_LS_11	CL-4	13º20.2497" N	61º10.62" W	54.63	0.93	19.04	7.69	0.17	4.74	9.28	3.46	0.59	0.12	100.65	-0.29
STV_LS_13	CL-9*	13º19.9089" N	61º10.5567" W	51.69	0.88	17.06	8.05	0.17	8.46	10.05	2.78	0.45	0.10	99.69	-0.28
STV_LS_14	CL-11*	13º19.8725" N	61º10.5830" W	52.18	0.89	17.26	8.02	0.17	7.75	9.83	2.87	0.48	0.10	99.55	-0.18
STV_LS_15	CL-12	13º19.8725" N	61º10.5830" W	55.99	0.78	18.68	7.35	0.19	3.44	8.43	3.43	0.55	0.14	98.98	-0.32
STV_LS_16	CL-5	13º19.8725" N	61º10.5830" W	57.34	0.95	17.76	7.43	0.18	3.47	7.60	3.88	0.69	0.15	99.45	-0.33
STV_LS_17	CL-5	13º19.8596" N	61º10.6014" W	57.25	0.94	17.74	7.40	0.18	3.45	7.57	3.91	0.69	0.15	99.28	-0.36
STV_LS_45	CL-13	13º19.7451" N	61º10.7844" W	55.57	0.96	18.09	8.76	0.21	3.77	8.21	3.65	0.57	0.15	99.94	-0.10
STV_LS_46	CL-14	13º19.7120" N	61º10.9211" W	51.74	1.02	18.92	9.10	0.20	4.78	9.91	3.26	0.45	0.12	99.50	-0.41
STV_LS_47	CL-15	13º19.7120" N	61º10.9211" W	51.45	1.02	18.87	9.11	0.20	4.79	9.86	3.23	0.45	0.11	99.09	-0.40
STV_LS_48	CL-16	13º19.6909" N	61º10.9311" W	54.23	0.79	20.29	7.23	0.17	4.02	9.59	3.34	0.55	0.12	100.33	-0.33
STV_LS_18	Dome			55.27	0.98	18.34	8.09	0.19	3.87	8.46	3.59	0.60	0.14	99.53	-0.36
STV_LS_20	YTF	13º13.7491" N	61º07.4935" W	50.62	0.94	19.56	8.54	0.17	5.28	10.55	2.87	0.35	0.10	98.98	0.02
STV_LS_21	YTF	13º14.1291" N	61º07.1822" W	49.44	1.12	20.25	8.94	0.16	5.21	11.25	2.65	0.46	0.08	99.56	0.15

STV_LS_22	YTF	13º14.1291" N	61º07.1822" W	55.15	0.86	18.34	8.28	0.20	3.72	8.00	3.56	0.46	0.15	98.72	0.31
STV_LS_24	YTF	13º14.1291" N	61º07.1822" W	53.62	0.96	19.12	7.80	0.18	3.97	8.30	3.44	0.44	0.14	97.97	0.65
STV_LS_25	YTF	13º14.1291" N	61º07.1822" W	51.83	0.91	20.25	8.06	0.18	4.77	10.15	2.98	0.37	0.11	99.61	-0.21
STV_LS_26	YTF	13º14.1291" N	61º07.1822" W	49.49	1.11	19.82	9.02	0.16	5.72	11.40	2.65	0.46	0.08	99.91	-0.25
STV_LS_27	YTF	13º18.2537" N	61º07.7505" W	52.03	0.91	19.48	7.95	0.17	5.49	9.71	3.02	0.42	0.12	99.30	0.31
2024 fieldwork															
STV_LS_100	LL lava	13°20.1612" N	61°12.6243" W	54.40	0.91	18.14	7.72	0.17	5.24	8.93	3.29	0.59	0.13	99.52	-0.16
STV_LS_102	LL lava	13°20.1735" N	61°12.5384" W	53.79	0.89	17.90	7.65	0.17	5.25	8.82	3.25	0.57	0.12	98.41	-0.21
STV_LS_103	LL lava	13°20.1562" N	61°12.5178" W	53.46	0.88	17.82	7.57	0.17	5.17	8.81	3.23	0.57	0.12	97.80	-0.07
STV_LS_104	LL lava	13°20.1464" N	61°12.4771" W	53.66	0.89	17.92	7.68	0.17	5.29	8.90	3.24	0.57	0.12	98.44	-0.33
STV_LS_130	UL lava	13°20.2040" N	61°11.5197" W	54.27	0.88	18.00	7.69	0.17	5.13	8.90	3.27	0.60	0.13	99.04	0.10
STV_LS_131	UL lava	13°20.3032" N	61°11.7534" W	55.32	0.91	18.43	7.80	0.18	5.15	8.98	3.30	0.60	0.13	100.80	-0.10
STV_LS_154	Roseau lava	13°19.3280" N	61°13.0440" W	55.34	0.90	17.80	7.94	0.18	4.42	8.15	3.57	0.70	0.14	99.14	-0.21
STV_LS_160	Roseau lava	13°19.3144" N	61°12.9554" W	55.12	0.90	17.61	7.87	0.18	4.39	8.07	3.51	0.70	0.14	98.49	-0.27
STV_LS_167	Roseau lava	13°19.2466" N	61°12.1695" W	54.21	0.97	18.22	8.78	0.21	3.98	8.97	3.40	0.50	0.13	99.37	-0.42
STV_LS_106	LL dyke - core	13°20.1464" N	61°12.4771" W	56.29	0.93	18.05	7.86	0.18	3.71	8.12	3.74	0.72	0.14	99.74	-0.19
STV_LS_107	LL dyke - edge	13°20.1464" N	61°12.4771" W	55.96	0.93	17.92	7.87	0.19	3.76	8.07	3.68	0.74	0.14	99.26	-0.02
STV_LS_132	UL dyke	13°20.3174" N	61°11.6433" W	56.84	0.97	17.64	8.31	0.21	3.46	7.76	3.79	0.60	0.14	99.72	-0.46
STV_LS_133	UL dyke	13°20.3174" N	61°11.6433" W	55.85	0.96	17.34	8.36	0.21	3.54	7.80	3.76	0.59	0.14	98.55	-0.39
STV_LS_134	UL dyke	13°20.3174" N	61°11.6433" W	56.87	0.93	17.56	8.11	0.21	3.46	7.80	3.83	0.62	0.14	99.53	-0.40

Coordinate data in decimal degrees minutes; note no data for the dome block as collected loose

Abbreviations include CL - crater lava; YTF - yellow tuff formation; LL - lower Larikai; UL - upper Larikai

* Mafic crater lava unit

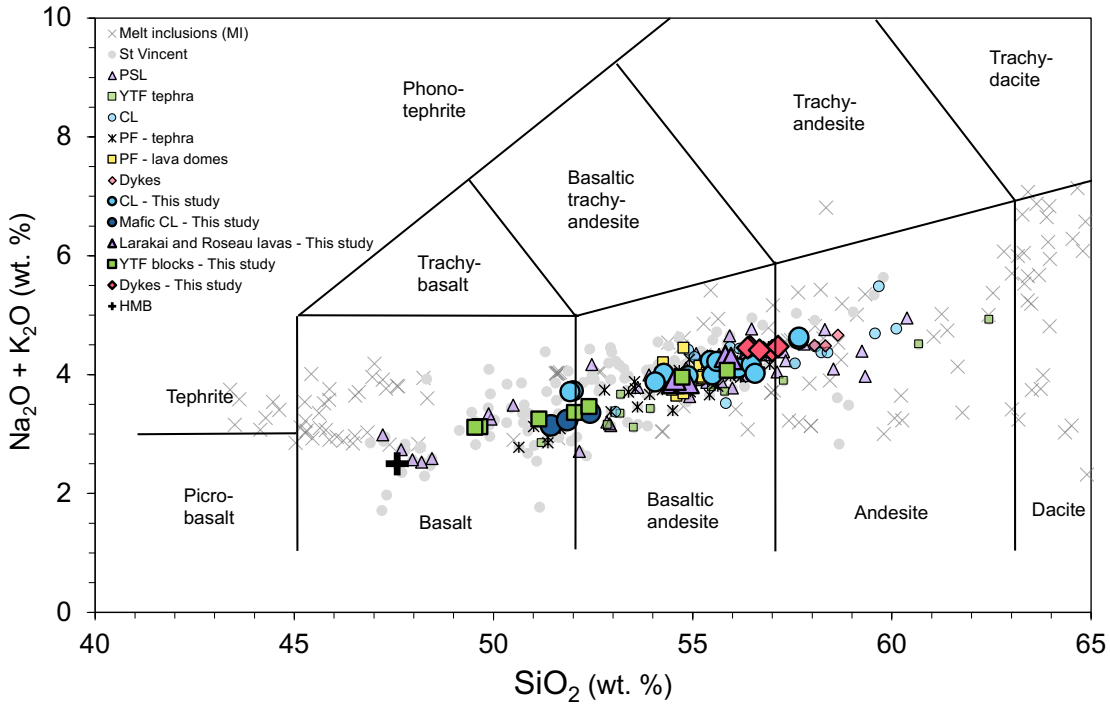


Figure 2.4: Total alkali versus silica (TAS) diagram after Le Bas et al. (1986). Pre-Somma lavas (PSL; including Larikai and Roseau lavas) shown as purple triangles, crater lavas (CL) as blue circles, mafic CL as dark blue circles, yellow tuff formation (YTF) as green triangles, dykes as red diamonds, pyroclastic formation (PF) tephra as stars and historical lava domes as yellow squares. New data for samples analysed in this study are shown as large bold symbols with thick outlines, previous data are shown as smaller faded symbols (Rowley, 1978; Heath et al., 1998a). Previous data for St. Vincent lavas are shown as grey circles and melt inclusions (MI) as crosses (from Robertson 2002 and GEOROC). A high-magnesium basalt (HMB; RSV49; Robertson 2002) is shown as a possible parent melt to La Soufrière magmas (Melekhova et al., 2015).

samples have considerably higher magnesium (~ 8 wt. % MgO) and lower silica (~ 52 wt. % SiO_2) contents (Figure 2.5), and are hereafter referred to as the mafic crater lavas (units 9 and 11 combined). All lava and dyke samples are in good agreement with previous La Soufrière and St. Vincent whole-rock data.

The lava data presented in this study are all calcium and aluminium rich (~ 8 – 11 wt. % CaO; ~ 17 – 20 wt. % Al_2O_3; Figure 2.5b-c), characteristic of the southern Lesser Antilles arc (e.g. MacDonald et al., 2000). High calcium contents denote a delay in clinopyroxene fractionation (Stamper et al., 2014b; Klein et al., 2023), whilst high aluminium contents indicate supressed plagioclase fractionation, often due to high water contents in magmas

(Sisson and Grove, 1993a; Pichavant and Macdonald, 2007). Iron and titanium (7 – 9 wt. % FeO_T; 0.7 – 1.2 wt. % TiO_2) remain fairly constant across different MgO contents. A rapid decrease in iron and titanium in melt inclusion (MI) data at ≤ 2 wt. % MgO is a trend unique to St. Vincent compared to the other islands in the arc (Smith et al., 1980). New data are in good agreement with previous whole rock data and follow typical differentiation trends, decreasing in calcium and iron contents, and increasing in aluminium, sodium and potassium, with decreasing magnesium contents. Conversely, the data presented in Figure 2.5 could be interpreted as lying on a mixing trendline, whereby mafic and silicic melts mix in different ratios to produce observed chemical trends (Eichelberger et al., 2006). Petrological evidence for mixing versus differentiation is explored in Chapter 3.

The mafic crater lava samples have ~ 8 wt. % MgO and are more primitive than all other crater lava compositions. The mafic crater lavas sit with mafic tephra from the pyroclastic formation, mostly from the 1902-1903 eruption (Heath et al., 1998a; Cole et al., 2019), a mafic pumice from the YTF eruption (STV376; Heath et al., 1998a) and two low-magnesium pre-Somma lavas (STV309 and STV315; Heath et al., 1998a; circled Figure 2.5a). The upper and lower Larikai dykes are very similar in composition to each other, but higher in magnesium than previously analysed andesitic dykes in the crater (Rowley, 1978; Heath et al., 1998a). New crater lava and Larikai and Roseau lavas also have higher magnesium contents than previous data. The Larikai and Roseau lavas are similar in composition, though the Larikai lavas contain slightly higher magnesium contents (~ 5 wt. % MgO) than the Roseau lavas (~ 4 wt. % MgO) and plot as two separate clusters in Figure 2.5. The 2020-2021 basaltic andesite lava dome, along with the 1971 and 1979 lava domes and pyroclastic formation tephra, sit with the majority of the new crater lava compositions at 3.5 – 4.5 wt. % MgO (Heath et al., 1998a; Cole et al., 2019; Weber et al., 2024), illustrating the homogeneity of the La Soufrière magmatic system since the Somma collapse.

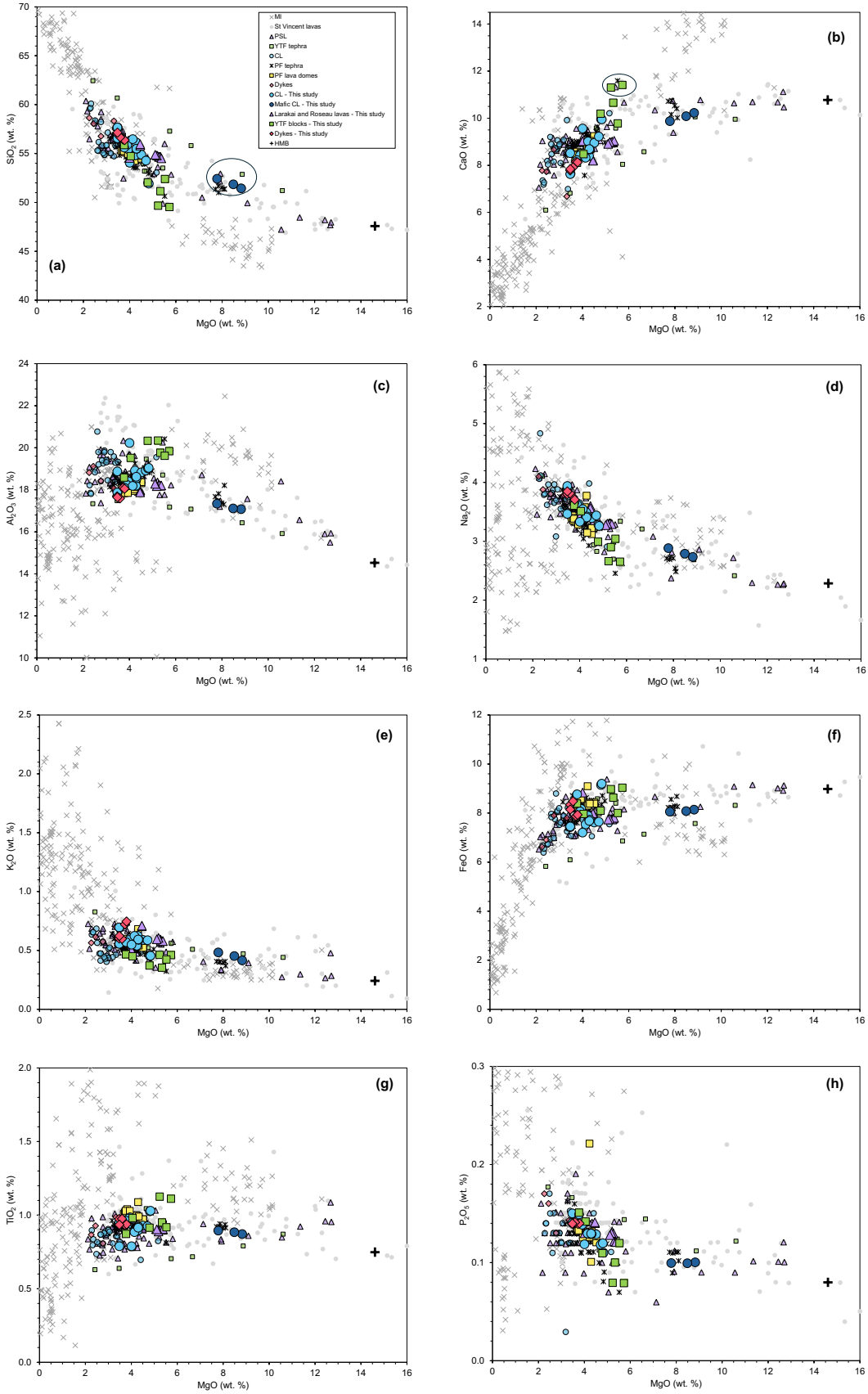


Figure 2.5: Major oxides versus MgO (wt. %). Magmas follow typical differentiation trends. Mafic crater lava unit (STV_LS_7, 13 and 14) circled in (a). High-Ca YTF lava blocks (STV_LS_21 and 26) circled in (b). Symbology and abbreviations as in Figure 2.4.

Five lava blocks from the YTF are high in calcium and aluminium, and low in silica, sodium and potassium compared to the main cluster of new data presented here. Two of these blocks (STV_LS_21 and 26) have the highest calcium, aluminium and titanium contents (~ 11 wt. % CaO; 20 wt. % Al_2O_3; 1 wt. % TiO_2; circled Figure 2.5b), and lowest silica (49 wt. % SiO_2) and are similar in composition to two pre-Somma lavas (STV319 – Heath et al., 1998a; 37166 – Rowley, 1978) sampled on the eastern flank of La Soufrière and tephra from the YTF eruption (SVG14 – Cole et al., 2019). Two lava blocks from the YTF sit with the crater lava cluster (STV_LS_22 and 24) and correlate most closely with crater lava units 1, 10 and 13.

2.2.3 Trace element chemistry

Trace element concentrations and trace element ratios are reported in the appendix (Table S2.2). Rare Earth Element (REE) concentrations normalised to the primitive mantle (Sun and McDonough, 1989) are enriched by approximately one order of magnitude (Figure 2.6). REE patterns appear relatively flat with little variation between lava samples and agree with previous St. Vincent data. The mafic crater lavas have the lowest REE concentrations supporting their more primitive nature. The two basaltic crater lavas (STV_LS_46 and 47) have the lowest La concentrations, bar two YTF lava blocks (seen more clearly in Figure 2.7). Data show a positive Sr anomaly in Figure 2.6 (~ 200 – 250 ppm Sr; Table S2.2), characteristic of arc magmas (Dostal, 1983; Turner and Langmuir, 2022). Two of the YTF lava blocks display significantly higher Sr peaks (460 ppm Sr; STV_LS_21 and 26). Sr readily partitions in plagioclase thus can reflect plagioclase fractionation or accumulation. However, Sr uptake is strongly dependent on anorthite contents and is low in An-rich plagioclase (Duchesne and Demaiffe, 1978; Blundy and Wood, 1991). The An-rich plagioclases (An_{90-95}) typical of the Lesser Antilles would therefore contain only 200 – 600 ppm Sr compared to lower An-plagioclase (An_{80-}

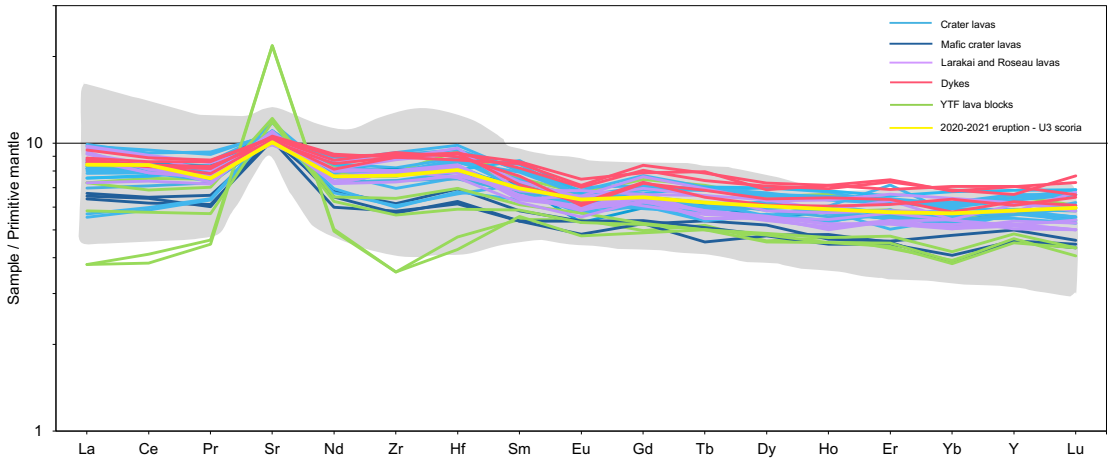


Figure 2.6: REE diagram normalised to the primitive mantle (Sun and McDonough, 1989). Colours as in Figure 2.4. Grey shading represents previous St. Vincent data (GEOROC: Graham and Thirlwall, 1981; Dostal et al., 1983; Bardintzeff et al., 1984; Thirlwall, 1994 Heath et al., 1998a; Plank, 2005; Cole et al., 2019). U3 scoria from 2020-2021 eruption at La Soufrière, average shown as all data near-identical (see Table S2.2).

$_{85}$) that can contain up to 1400 ppm Sr (Duchesne and Demaiffe, 1978; Bindeman and Bailey, 1999), thus not significantly altering Sr concentrations in the magma. Elevated Sr concentrations can also indicate high sediment input, though sediment input is better defined by radiogenic $^{87}Sr/^{86}Sr$ isotopic ratios (Arculus and Johnson, 1980). St. Vincent is known to have low sediment input, with $^{87}Sr/^{86}Sr$ ratios similar to the mantle (0.7040; Pushkar et al.,1973). A previously reported high Sr abundance in one of the pre-Somma magmas was instead considered a product of seawater alteration (Heath, 1997).

A weak negative Eu anomaly is observed in all lavas and dykes (Figure 2.6). Eu has two valence states, Eu^{2+} and Eu^{3+}, of which only Eu^{2+} partitions into plagioclase (Drake and Weill, 1975). In magmas at higher oxidation states less Eu^{2+} is available such that crystallising plagioclase will form only a weak Eu depletion. For example, at ≥ QFM +2 less than 10 % of Eu is thought to be divalent (Aigner-Torres et al., 2007). Eu/Eu* is a measure of Eu depletion relative to adjacent REE's that are most similar in ionic radius, calculated as $Eu^* = Eu_N / \sqrt{Gd_N * Sm_N}$, normalised to the chondritic values of Nakamura (1974), and with Eu /Eu* values < 1 indicative of plagioclase fractionation (Davidson et al., 2013). Eu/Eu* ratios for the La Soufrière magmas range from 0.8 to 1

(Figure 2.7) and tentatively decrease with differentiation, illustrated by increasing La, a LREE that becomes enriched as magmas evolve. This gentle negative relationship is indicative of plagioclase fractionation at oxidising conditions, thus lowering the uptake of Eu^{2+} and weakening the Eu anomaly.

LREE/HREE and MREE/HREE ratios such as La/Yb and Dy/Yb are often used to infer garnet, amphibole and clinopyroxene fractionation (Davidson et al., 2007a). Dy/Dy* measures the depletion of Dy relative to adjacent REE's and can distinguish between garnet fractionation, that preferentially uptakes HREE, from amphibole or clinopyroxene fractionation that prefer MREE (Davidson et al., 2013). Dy/Dy* is calculated as $Dy^* = Dy_N / \sqrt{Gd_N^{4/13} * Sm_N^{9/13}}$ after Davidson et al. (2013). Values range from 1.4 to 1, are positively correlated with Dy/Yb and decrease with differentiation (Figure 2.7). The negative relationship between Dy/Dy* and La suggests more evolved magmas experience more amphibole (or clinopyroxene) fractionation. Amphibole fractionation is assumed at St. Vincent, rather than clinopyroxene, due to the abundance of amphibole and plagioclase rich cumulates (Tollan et al., 2012).

Chromium contents are generally low (≤ 50 ppm Cr), except in the Larikai lavas and a singular lava block from the YTF that contains ~ 140 ppm Cr, and the mafic crater lavas that contain 320 – 410 ppm Cr (Table 2.2). Cr is positively correlated with MgO, such that more primitive magmas have higher Cr contents. Cr readily partitions into early crystallising phases such as spinel, olivine and clinopyroxene (Huebner et al., 1976; Spandler and O'Neill, 2010). Vanadium also has a positive correlation with MgO content, plateauing at ~ 300 ppm. This trend is similar to FeO and TiO_2 Harker diagrams (Figure 2.5), likely due to V readily partitioning into Fe-Ti oxides (Dostal et al., 1983; Toplis and Corgne, 2002; Righter et al., 2006). V also partitions into clinopyroxene (Toplis and Corgne, 2002) and olivine (Shearer et al., 2006; Mallman and O'Neill,

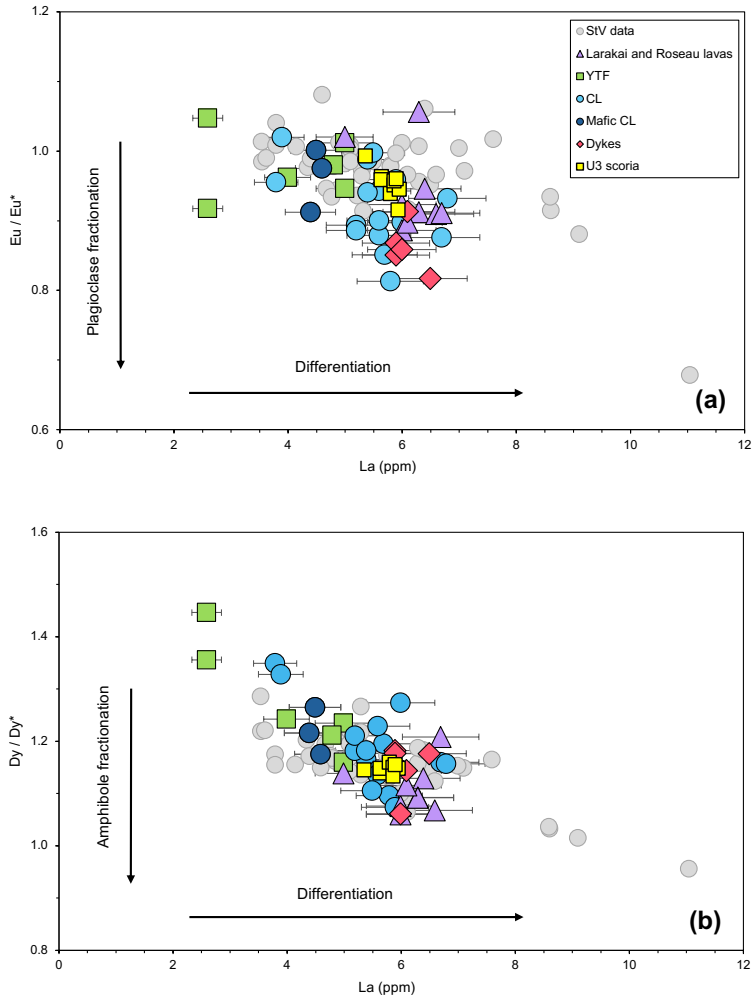


Figure 2.7: Lanthanum (La) versus **(a)** Eu/Eu* to determine the degree of plagioclase fractionation and **(b)** Dy/Dy* to determine the degree of amphibole fractionation experienced by magmas. Eu/Eu* calculated as interpolation between Sm and Gd (see text) and Dy/Dy* calculated after Davidson et al. (2013).

2013). The behaviour of Cr and V are strongly controlled by fO_2 due to their multiple valence states (Cr^{2+}, Cr^{3+}, V^{2+}, V^{3+}, V^{4+} and V^{5+}). Dostal et al. (1983) identified relatively high abundances of Cr in St. Vincent cumulate clinopyroxene and oxides, and V in amphibole, clinopyroxene and oxides, with low concentrations in olivine. The generally low Cr contents of La Soufrière magmas supports clinopyroxene and Fe-Ti oxide fractionation during differentiation of a more primitive parent melt. Yb and Zr concentrations are high whilst Ba, Rb and Sr contents are relatively low in comparison to the rest of the Lesser Antilles islands.

Th/Nb and La/Sm ratios can be used as a proxy for sediment input and enrichment (Elliot et al., 1997). La Soufrière magmas have low Th/Nb (≤ 0.5) and La/Sm (≤ 2.2) ratios (Table S2.2), in agreement with previous St. Vincent data and lower in comparison to other islands in the Lesser Antilles arc (Atlas et al., 2022). Ba/Th reflects fluid addition from slab dehydration (Elliot, 2003; Atlas et al., 2022) as Ba is highly incompatible and readily partitions into a fluid or melt phase. La Soufrière magmas have high Ba/Th ratios (~ 87 to 161; Table S2.2) in good agreement with previous St. Vincent data and signifying high fluid input.

U and Th are both immobile and geochemically tend to behave similarly. At more oxidising conditions U^{4+} oxidises to U^{6+} which readily partitions into the fluid or melt (Brenan, 1995; Elliot et al., 1997; Ague, 2017), whilst Th is only added to arc magmas via sediment from the subducting slab (Hawksworth et al., 1997). The high U/Th ratios (≥ 0.41) but low Th concentrations (≤ 1.41 ppm) of La Soufrière samples further support fluid addition with little sediment input, with the lowest U/Th ratios in the mafic crater lavas. Previous studies have also attributed high $\delta^{11}B$ isotope ratios to elevated fluid input at St. Vincent (Cooper et al., 2020). La Soufrière magmas have low Th/Yb and Ce/Yb ratios (Th/Yb ≤ 0.6, Ce/Yb ≤ 6; Table S2.2). Values are considerably lower than other Lesser Antilles islands (Hawksworth et al., 1991), with low ratios indicative of a simple magmatic system and higher ratios indicating more complex tectonics with elevated sediment input (Hawksworth et al., 1991, Plank and Langmuir, 1993).

Limited trace element data exist for previous YTF tephra and pre-Somma lava samples (Rowley, 1978; Heath et al., 1998a), making geochemical comparisons between units difficult. Rb. Ba, Sr, Zr and Y concentrations in the mafic YTF tephra and low-magnesium basalt pre-Somma lavas (Heath et al., 1998a) generally agree within error with the mafic crater lava unit. The mafic YTF tephra has higher Nb (~ 1 ppm) and Cr (≥ 150 ppm) than the mafic crater lavas. The low-magnesium basaltic pre-Somma lava STV315 has lower

La (≤ 1.5 ppm), Ce (≤ 3 ppm) and Cr (≤ 100 ppm) and STV309 has low V (≤ 90 ppm) compared to the mafic crater lavas. Trace element data available for recent pyroclastic deposits (Cole et al., 2019) finds the mafic 1902-1903 tephra are in very good agreement with the mafic crater lava trace element concentrations. The mafic 1902-1903 tephra are slightly elevated in LREE (e.g. 5.5 ppm versus 4.6 ppm La) and vary in V and Cr concentrations (≤ 50 ppm higher V and ≤ 140 ppm higher Cr in mafic crater lavas). Cr varies within the mafic crater lava samples by ~ 90 ppm, possibly reflecting Cr-spinel fractionation or other Cr-rich mineral phases such as olivine and clinopyroxene (Barnes and Roeder, 2001).

Two lava blocks from the YTF (STV_LS_22 and 24) are lower in Rb (≤ 7 ppm difference), Ba (≤ 55 ppm), V (≤ 80 ppm), compared to crater lava units 1, 10 and 13 previously found to be similar in major element geochemistry. YTF lava blocks STV_LS_21 and 26 that are compared to pre-Somma lavas STV319 (Heath et al., 1998a) and 37166 (Rowley, 1978) are lower in Sr (≤ 200 ppm), Zr (≤ 30 ppm), V (≤ 180 ppm), and higher in Rb (≤ 5 ppm), Cr (≤ 150 ppm), Cs (≤ 0.3) and Th (≤ 0.6).

2.2.4 New $^{40}Ar/^{39}Ar$ dates

New $^{40}Ar/^{39}Ar$ dates for seven lava samples from La Soufrière are reported in Table 2.2 and compared to previous data in Table 2.3. Figure 2.8 illustrates a representative $^{40}Ar/^{39}Ar$ plateau age and inverse isochron age for sample STV_LS_5a, the results for all other samples are presented in the appendix. Dates agree with estimated stratigraphic positions from field observations. Three of four crater lavas were successfully dated, with one crater lava (STV_LS_ 11; units 4) close to the top of the crater lava sequence giving a negative age due to its very young formation (likely ≤ 4 ka). Crater lava STV_LS_3 (unit1) was also sent for dating but sits stratigraphically above the sample that gave a negative age so was not dated. Crater lava STV_LS_46 (unit 14)

Table 2.2. New $^{40}Ar/^{39}Ar$ data for La Soufrière

		Isochron							Plateau	
Sample #	Location	$^{40}Ar/^{36}Ar_i$ ± 2s		Age (ka) ± 2s		N	^{39}Ar %	MSWD	Age (ka) ± 2s	
STV-LS-6	Crater	296.5	± 3.7	16.4	± 19.8	11/16	90.5	0.92	5.7	± 4.4
STV-LS-46	Crater	298.2	± 1.3	12.3	± 18.9	13/14	98.3	0.46	7.9	± 7.7
STV-LS-5a	Crater	299.2	± 1.7	21.6	± 11.0	16/17	99.7	0.59	25.2	± 3.8
STV-LS-103	Lower Larikai	298.4	± 2.2	5.4	± 13.7	12/18	91.4	0.56	4.4	± 4.2
STV-LS-100	Lower Larikai	299.3	± 0.9	22.6	± 15.5	15/18	95.5	0.36	33.7	± 8.0
STV-LS-167	Roseau	298.5	± 2.3	14.7	± 7.9	14/18	95.0	1.03	14.5	± 3.1
STV-LS-154	Roseau	298.5	± 1.3	31.9	± 8.9	15/19	90.7	1.01	31.5	± 4.0

in the southern crater wall is dated at 7.9 ± 7.7 ka, and STV_LS_6 (unit 7) in the eastern crater wall is 5.7 ± 4.4 ka (Figure 2.2). The high uncertainty associated with these young dates means determining the exact order of emplacement of the crater lavas and drawing conclusions about the morphology of the crater is not possible but does confirm their young age. The oldest crater lava (STV_LS_5a) is dated at 25.2 ± 3.8 ka and sits at the base of the new outer crater in the northern wall (Figure 2.2). Previously the crater lavas had been estimated at ~ 4 ka by association with the YTF eruption (Rowley, 1978; Heath, 1997; Robertson 2002). These new dates find the lowermost crater lava to be significantly older.

New dates for the lavas in Larikai valley range from 33.7 ± 8.0 to 4.4 ± 4.2 ka and in Roseau valley from 31.5 ± 4.0 to 14.5 ± 3.1 ka (Table 2.2). These dates are considerably younger than previously dated pre-Somma lavas on the eastern flanks (Table 2.3), though overlap with a lava from the southeast that could have originated from either Morne Garu or La Soufrière (11 ± 14 ka, Table 2.3; Heath, 1997; Robertson 2005). These new dates indicate that La Soufrière continued to produce extensive lava flows down the western flanks in the late pre-Somma and possibly coeval to the emplacement of the crater lavas (~ 4 ka). The youngest lower Larikai lava (4.4 ± 4.2 ka; STV_LS_103) is cross-cut by a dyke (Figure 2.3d), meaning effusive activity continued on the western

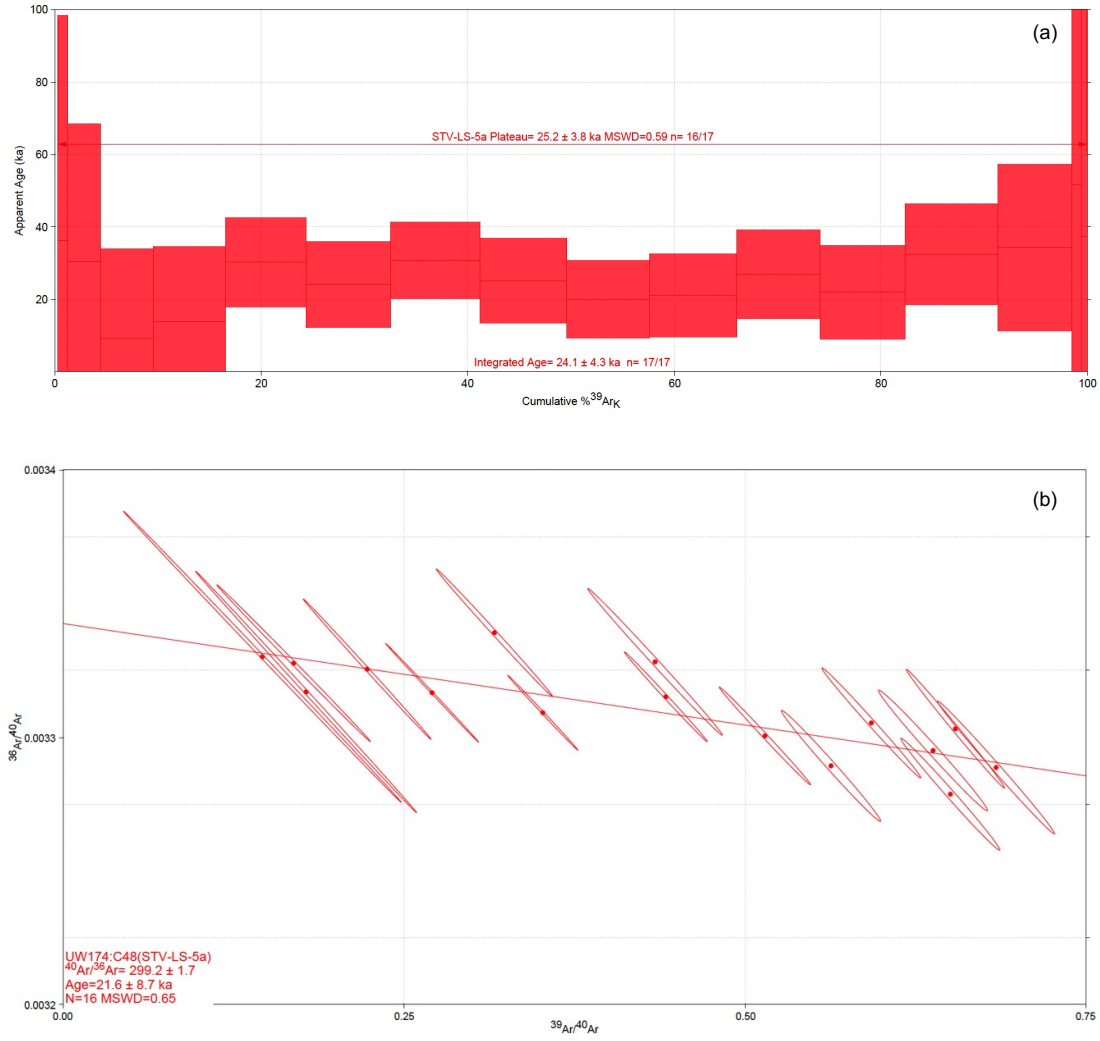


Figure 2.8: Representative $^{40}Ar/^{39}Ar$ dataset. **(a)** Apparent age versus cumulative ^{39}Ar released during n number of heating steps. Heating steps that caused an increase in mean standard weighted deviation (MSWD) ≥ 1.5 are excluded from the calculated plateau age after Powell et al. (2002) and Jicha et al. (2016). **(b)** Inverse isochron plot of $^{36}Ar/^{40}Ar$ versus $^{39}Ar/^{40}Ar$ for each heating step. Ellipsoid represents error associated with each data point. y-axis intercept is within uncertainty of atmospheric value ($^{40}Ar/^{36}Ar$ = 298.5 ± 0.5; Lee et al., 2006). Data gathered and plotted by Dr. Brian Jicha at the University of Wisconsin-Madison.

flank after the young lava flow. The large uncertainty associated with this young date, means that the lava flow could be up to 8 ka, thus pre-dating the crater lava period.

Further work is needed to constrain the relationship between the younger lower Larikai lava flow, the cross-cutting dyke and the emplacement of the crater lavas. The Upper Larikai dyke was also sent for sampling but gave a staircase upwards plateau spectrum indicative of excess ^{40}Ar, likely from alteration (Schaen et al., 2020).

2.3 Discussion

2.3.1 Compositional stability of magmas at La Soufrière volcano

New major element geochemistry for lavas and dykes erupted from La Soufrière finds magmas are predominantly basaltic andesites (Figure 2.4). Dykes display the most restricted compositional range and sit with the majority of the crater lavas, lavas from Larikai and Roseau valley and recent historical dome compositions. The limited variation in major and trace element compositions attests to a homogenous magmatic system. No sequential geochemical trends are observed in the crater lavas suggesting magmas could have last equilibrated with the crust at similar physico-chemical conditions prior to eruption (e.g pressure, temperature, water content), thus be sourced from a similar location within the crust (Wyllie, 1984; Reiners, 2002; Sisson et al., 2005). During the pre-Somma period, La Soufrière produced basaltic andesite magmas repeatedly for hundreds of thousands of years, with more primitive basalts only found to erupt during the early stages of pre-Somma volcanism and becoming rarer over time (e.g. no primitive basalts younger than~ 180 ka (Heath, 1997)). La Soufrière has since continued to erupt basaltic andesite magmas for thousands of years during the emplacement of the crater lavas and in historic eruptions observed today. Previous studies exploring the formation of monotonous basaltic andesites erupted from Arenal volcano, suggest a balance of mixing, recharge and ascent rate produces the compositionally identical magmas (Parat et al., 2014), however it is more likely the melt composition is buffered by the underlying crust (Sparks et al., 2019; Blundy, 2022) and magmas are continuously sourced from the same region of the crust. Small variations in composition are accounted for by minor differences in melting and crystallisation (Annen et al., 2006).

2.3.2 Differentiation from a basaltic parent magma

Previous studies suggest the basaltic andesite magmas of St. Vincent are generated by polybaric differentiation of a high-magnesium basaltic parent melt (Melekhova et al., 2015), similar to some of the high-magnesium basalt pre-Somma lavas (e.g. STV301; Heath et al., 1998a). The basaltic parent melt is found to have last equilibrated with the mantle at 1.3 – 1.6 GPa at ~ 1180ºC with 4.5 wt % H_2O at ~ NNO +2.3 (Pichavant et al., 2002a; Melekhova et al., 2015). Basaltic andesite magmas are then inferred to be generated at 0.7 – 1.0 GPa and ~ 1050ºC from wet parent magmas (Melekhova et al., 2015). Low-magnesium basalts, similar in composition to the mafic crater lava, are also found to be generated from the same wet parent magma but slightly deeper and hotter at ~ 1 – 1.3 GPa and 1050 – 1100ºC.

The relatively flat and enriched REE patterns observed for the La Soufrière basaltic andesite magmas, with respect to the primitive mantle, support a small degree of coherent differentiation from a mantle-derived parent. Eu/Eu* and Dy/Dy* ratios decrease with differentiation (Figure 2.7) and support plagioclase and amphibole fractionation, respectively (Davidson et al., 2013). The trend is only weakly defined for plagioclase fractionation; likely a consequence of the strong fO_2 control on Eu^{2+} uptake into plagioclase (Drake and Weill, 1975), suggesting fractionation at oxidising conditions. High water contents can create more oxidising conditions and are required to form the high-An plagioclase ubiquitous in erupted cumulates from St. Vincent (Sisson and Grove, 1993a; Tollan et al., 2012) and in the wider Lesser Antilles (Arculus and Wills, 1980). St. Vincent magmas are known to be fluid-rich based on H_2O contents and $\delta^{11}B$ compositions in mineral hosted melt inclusions (Bouvier et al., 2008; Cooper et al., 2020) and high Ba/Th ratios (Atlas et al., 2022). Further, previous experimental studies support a hydrous and oxidised source for the parent melt (Pichavant et al., 2002a; Melekhova et al., 2015). Amphibole fractionation is inferred from decreasing Dy/Dy* ratios with

differentiation (Davidson et al., 2013) and is supported by the abundance of amphibole in St. Vincent xenoliths (Tollan et al., 2012). Amphibole is absent from the phenocryst assemblage in La Soufrière magmas, as is common in many volcanoes undergoing cryptic amphibole fractionation (Davidson et al., 2007a). Amphibole is only stable at high water contents (Krawczynski et al., 2012) providing further evidence for a hydrous source region. Trace element ratios (e.g. Th/Nb, La/Sm, Th/Yb) also attest to low sediment input and little crustal contamination (Hawksworth et al., 1991, Plank and Langmuir, 1993; Elliot, 2003; Atlas et al., 2022), suggesting erupted basaltic andesite melts represent true liquids in equilibrium with the crystalline mush extracted from the crust.

2.3.3 Low-magnesium basalts of La Soufrière

A mafic low-magnesium basalt (~ 8 wt. % MgO) crater lava is identified close to the base of the current crater floor (units 9 and 11; Figure 2.2), anomalous to all other crater lava compositions. This is the only mafic effusive magma to be identified in the current La Soufrière crater, as previous compositionally similar low-magnesium basaltic pre-Somma lavas are all identified on the flanks (Heath et al., 1998a). The mafic crater lava is also geochemically similar in major and trace elements to a small number of mafic tephra identified in the YTF and 1902 eruption deposits (also with ~ 8 wt. % MgO; Figure 2.5; Heath et al., 1998a; Cole et al., 2019). The mafic crater lava unit cannot be related to the 1902-1903 eruption since it is overlain by crater lavas dated at 5.7 ± 4.4 ka (Figure 2.2) but could be linked to the mafic YTF pumice that forms part of a mixed fall unit (Heath et al., 1998a).

These mafic magmas support the presence of more primitive, basaltic material at depth. Large explosive eruptions can be caused by injection of more primitive material into the system (Sparks et al., 1977; Murphy et al., 2000; Cassidy et al., 2018), or rapid depressurisation (e.g. flank collapse; Alidibirov and Dingwell, 1996) causing deeper more

primitive magmas to be erupted during emptying of the magmatic system (Manconi et al., 2009). The 1902-1903 eruption is the largest historically reported eruption at La Soufrière, generating large eruption columns, PDC's and ashfall (Carey and Sigurdsson, 1978; Shepherd et al., 1979), with 12 cm of ash deposited in Kingstown 20 km south of the vent (Rowley, 1978). There was no effusive counterpart to this eruption, and the eruption evolved from basaltic andesite to basaltic. The presence of two discrete magma compositions within the 1902-1903 eruption has previously been interpreted as the emptying of a zoned magma chamber (Roobol and Smith, 1975), today considered a zoned crystalline mush or melt lens (Edmonds et al., 2019); or to reflect mafic injection possibly responsible for triggering the eruption (Cole et al., 2019). The 1902-1903 eruption has many similarities to the YTF eruption and could represent a smaller version of the YTF eruption.

A single mixed fall deposit, single basaltic lapilli unit of the YTF, and the absence of reversely zoned phenocrysts have previously been interpreted as evidence that magma mixing was insignificant during the YTF eruption and at La Soufrière in general (Heath et al., 1998a). The YTF eruption is instead linked to the collapse of the Somma edifice by stratigraphic correlations (see section 1.3.4). Collapse of the Somma crater wall could have caused a major depressurisation of the system and evacuation of large volumes of magma. If the mafic crater lava is linked to the YTF eruption, it could represent the final stages of the eruption whereby deeper, more primitive magma is extruded (Manconi et al., 2009; Cassidy et al., 2015), anomalous to La Soufrière's usual basaltic andesites. The crater lavas below the mafic unit (~ 8 wt. % MgO) and now buried by the 2020-2021 pyroclastic deposits, were previously sampled by Rowley (1978) and found to be basaltic andesites and andesites (55 – 60 wt. % SiO_2). All crater lavas above the mafic unit are near-identical basaltic andesites (~ 4 wt. % MgO), suggesting the La Soufrière system then returned to producing its normal basaltic andesite magmas. Such chemical variation followed by stabilisation of the magmatic system is often driven by flank collapse and

has previously been reported across the Lesser Antilles, including on Montserrat (Cassidy et al., 2015), St. Eustatius (Roobol and Smith, 2005), and St. Lucia (Boudon et al., 2008), though post-flank collapse magmas were more evolved on St. Lucia.

2.3.4 Revised stratigraphic sequence

Pre-Somma lavas

The pre-Somma lavas are the oldest (0.69 Ma) and compositionally most diverse magmas erupted from La Soufrière, including early primitive high-magnesium basalts at the base of volcano. The more evolved andesitic pre-Somma lavas are instead refined to the caldera walls due to their much higher viscosity and inability to flow long distances (Rowley, 1978). The youngest pre-Somma lavas known to have originated from La Soufrière were previously dated at 291 ka (Table 2.3; Heath, 1997). New dates for the Larikai and Roseau lavas on the western flanks find that the pre-Somma activity (defined as lavas erupting prior to the collapse of the Somma edifice) continued until ≤ 14.5 ± 3.1 ka. Previous studies debated the origin of a lava on the eastern flanks of La Soufrière and Morne Garu dated at 11 ± 14 ka (Indian estate; Heath, 1997, Robertson, 2005). New $^{40}Ar/^{39}Ar$ dates find that La Soufrière was actively producing lava flows on its western flanks around this time. Thus, it is more likely the ~ 11 ka lava flow on the eastern flanks also originated from La Soufrière rather than Morne Garu

Somma collapse

The lowermost crater lava (unit 10; Figure 2.2) identified in this study is dated at ~ 25 ka, considerably older than previous estimates for the crater lavas (~ 4 ka; Heath, 1997) and new dates for the upper crater lavas (5.7 – 7.9 ka; Table 2.3) emplaced ≤ 20 m above.

Table 2.3. K/Ar, and $^{40}Ar/^{39}Ar$ dates for St. Vincent lavas in age order.

Volcanic centre	Location	Sample #	Reference	Method	Age
La Soufrière	**Lower Larikai lava**	**STV_LS_103**	**This study**	**^{40}Ar / ^{39}Ar**	**4.4 ± 4.2 ka**
La Soufrière	**Crater lava (unit 7)**	**STV_LS_6**	**This study**	**^{40}Ar / ^{39}Ar**	**5.7 ± 4.4 ka**
La Soufrière	**Crater lava (unit 14)**	**STV_LS_46**	**This study**	**^{40}Ar / ^{39}Ar**	**7.9 ± 7.7 ka**
Morne Garu / La Soufrière	Indian Estate	STV 345	Heath 1997	^{40}Ar / ^{39}Ar	11 ± 14 ka
La Soufrière	**Roseau lava**	**STV_LS_167**	**This study**	**^{40}Ar / ^{39}Ar**	**14.5 ± 3.1 ka**
La Soufrière	**Crater lava (unit 10)**	**STV_LS_5a**	**This study**	**^{40}Ar / ^{39}Ar**	**25.2 ± 3.8 ka**
La Soufrière	**Roseau lava**	**STV_LS_154**	**This study**	**^{40}Ar / ^{39}Ar**	**31.5 ± 4.1 ka**
La Soufrière	**Lower Larikai lava**	**STV_LS_100**	**This study**	**^{40}Ar / ^{39}Ar**	**33.7 ± 8 ka**
Morne Garu / La Soufrière	Black Point	STV 301	Heath 1997	^{40}Ar / ^{39}Ar	180 ± 21 ka
La Soufrière	South Sandy Bay	STV 323	Heath 1997	^{40}Ar / ^{39}Ar	291 ± 10 ka
La Soufrière	Chain Spout / Rabacca River	STV 358	Heath 1997	^{40}Ar / ^{39}Ar	324 ± 15 ka
La Soufrière	Commantawana Bay	683755	Briden et al., 1979.	K-Ar	0.36 ± 0.07 Ma
La Soufrière	Porter Point	683740	Briden et al., 1979.	K-Ar	0.66 ± 0.10 Ma
La Soufrière	Rouges Hill (Owia Bay)	683756	Briden et al., 1979.	K-Ar	0.69 ± 0.09 Ma
Grande Bonhomme	Lowmans Leeward	683741	Briden et al., 1979.	K-Ar	1.16 ± 0.08 Ma
Morne Garu	Richmond Vale	683747	Briden et al., 1979.	K-Ar	1.18 ± 0.10 Ma
Grande Bonhomme	Coulls Hill	683749	Briden et al., 1979.	K-Ar	1.33 ± 0.09 Ma
SE volcanics	Arnos Vale	SV-18	Geothermica Italia / Robertson 2005	K-Ar	1.54 ± 0.62 Ma
SE volcanics	Kingstown / Cane Garden road	683763	Briden et al., 1979	K-Ar	1.65 ± 0.18 Ma
SE volcanics	Villa dyke	SV-29	Geothermica Italia / Robertson 2005	K-Ar	2.50 ± 1.40 Ma
SE volcanics	Calliaqua	683762	Briden et al., 1979	K-Ar	2.49 ± 0.07 Ma
SE volcanics	Windward highway / Prospect corner	683761	Briden et al., 1979	K-Ar	2.74 ± 0.11 Ma

Previous mapping in the crater hinted at an unconformity above this 'old' crater lava unit due to a steep upper contact with debris flow and YTF deposits in the NW wall of the current crater (Figure 2.1; to the left and above the 120m thick unit in Figure 1.3e; Sigurdsson, 1981). The age of this lava supports the presence of an unconformity, with the ~ 25 ka lava instead likely from the Somma crater wall. Collapse of the Somma edifice to the south, evidenced by 100 m thick debris flow deposits and the remnant northern Somma crater wall (see section 1.3.4; Sigurdsson, 1981), could have resulted in sections of the old crater walls slumping into the new crater (Figure 2.9). The collapse of material into the new crater would have also blocked the existing vent, causing magmas to find a new route to the surface, as is common at volcanoes that experience repetitive edifice or flank collapse (Maccaferri et al., 2017).

The ~ 25 ka crater lava (unit 10) is similar in major element geochemistry to a number of pre-Somma lavas including STV314, 316 and 323 sampled from the flanks (Heath et al., 1998a) and sample 826 (Rowley, 1978) sampled directly from the Somma crater wall. STV323 was dated by Heath (1997) at 291 ± 10 ka, therefore cannot be related to this lava, but similarities to a number of pre-Somma lavas is supportive that the anomalously old crater lava unit could be sourced from the Somma crater. However, unit 10 also sits compositionally with the main cluster of younger crater lavas. The geochemical similarities between a large number of pre-Somma lavas and crater lavas makes correlating units difficult but does support the long-lasting homogeneity of the La Soufrière magmatic system.

YTF

The collapse of the Somma crater has previously been linked to the YTF eruption due to YTF deposits immediately overlying the Somma collapse debris flow deposits, with no

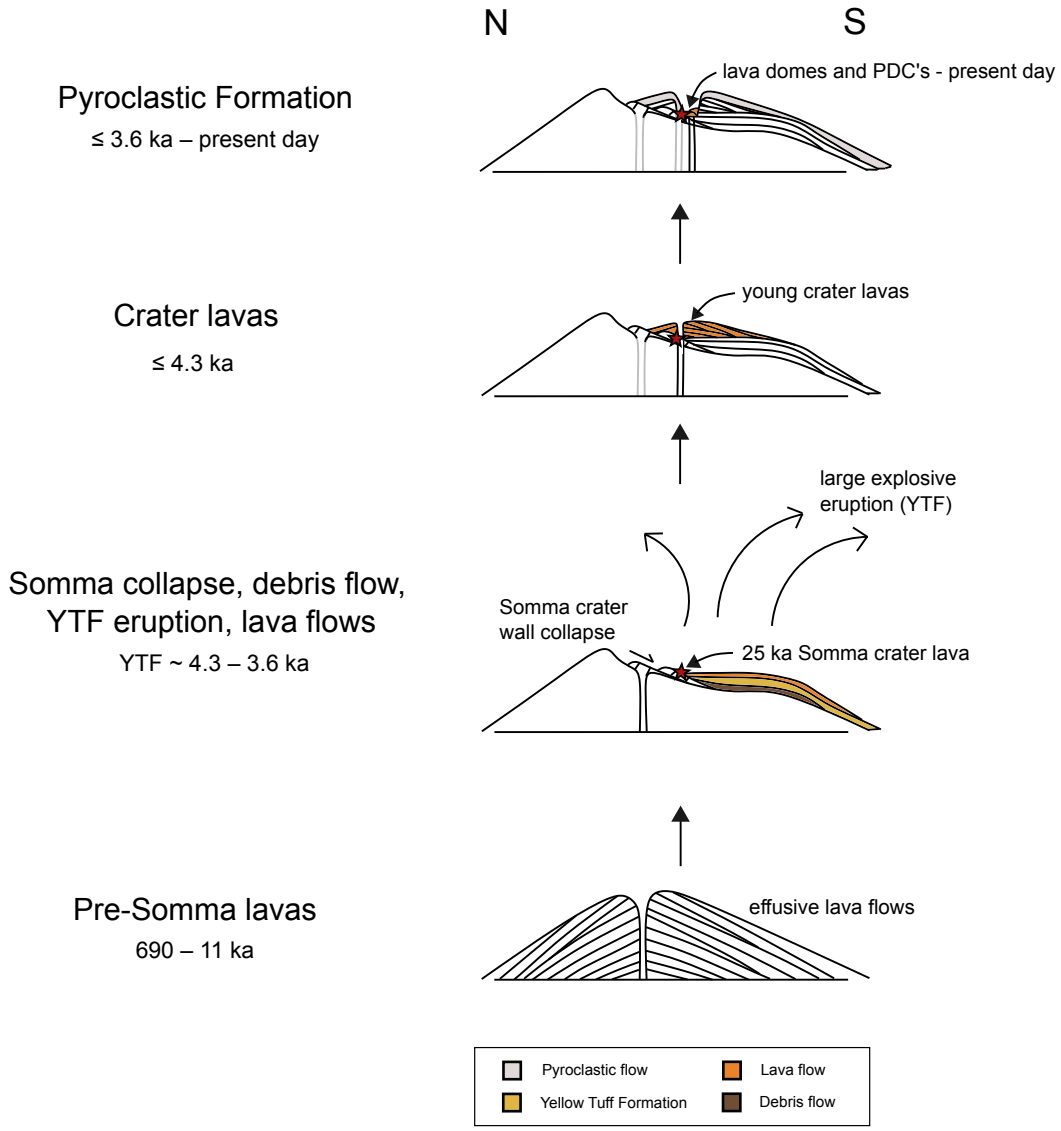


Figure 2.9: Schematic of revised eruptive history at La Soufrière. Pre-Somma lavas date back to 690 ± 90 ka (Briden et al., 1979). The youngest pre-Somma lavas are thought to be 11 ± 14 ka on the eastern flank (Heath, 1997) and 14.5 ± 3.1 ka on the western flank (new $^{40}Ar/^{39}Ar$ dates this study). Collapse of the Somma edifice to the south generated voluminous debris flows and parts of the crater walls likely slumped into the crater (e.g. 25.2 ± 3.8 ka crater lava depicted by a red star). The Somma collapse is also linked to the large explosive YTF eruption and possible outpourings of lava (Sigurdsson, 1981). Radiogenic dates of pyroclastic deposits constrain the YTF eruption to between 4.3 and 3.6 ka (Rowley, 1978). The crater lavas overlie the YTF deposits in the crater therefore must be younger. New $^{40}Ar/^{39}Ar$ dates have large uncertainty but give ages of 7.9 ± 7.7 ka and 5.7 ± 4.4 ka. The pyroclastic formation incorporates all volcanism after the crater lavas and YTF eruption including present day eruptions. Explosive eruptions excavate new craters and deposit thick pyroclastic units whilst effusive volcanism is restricted to within the crater.

evidence of erosion (Rowley, 1978; Sigurdsson, 1981). Additionally, such a large collapse, illustrated by the tall remnant northern crater wall and inferred material removed would have likely resulted in considerable depressurisation of the system and triggered a large explosive eruption (Manconi et al., 2009; Cassidy et al., 2018) as is observed for the YTF eruption (~ 150 m thick deposits in the crater and ≤ 5 m thick deposits in Kingstown 20 km from the crater). Rowley (1978) dated two pyroclastic flows that overlie and underlie the YTF, constraining the age of the eruption to be between 4335 ± 95 yrs and 3590 ± 70 yrs old. These dates coincide with the onset of the extrusion of the crater lavas.

Lava blocks collected from a 15 m thick YTF pyroclastic deposit on the east coast were compared to the crater lavas to determine their relationship. Two of the YTF lava blocks (STV_LS_22 and 24) are geochemically similar to the crater lava units 1, 10 and 13, though are ≥ 0.1 wt. % higher in K_2O and lower in Rb, Ba, Sr and V making them unlikely corresponding units. The other YTF lava blocks are instead distinct to the majority of La Soufrière magmas, correlating with two high aluminium and high calcium pre-Somma lavas (STV319 – Heath et al., 1998a; 37166 – Rowley, 1978). The distinct geochemistry of these lava blocks suggest they could represent these pre-Somma lavas, however they have differences of 0.1 wt. % in K_2O and TiO_2 contents and vary considerably in trace element concentrations (e.g. ≥ 100 ppm lower Sr, 200 ppm lower V). The narrow compositional diversity of La Soufrière magmas and limited trace element data from Rowley (1978) and Heath et al. (1998a) makes correlating units difficult. The similarity of these few YTF blocks to the crater lavas and pre-Somma lavas does suggest the explosive YTF eruption sampled parts of the older crater wall, as well as potentially new extruding magmas in the crater. As discussed above, the mafic crater lava unit could also be related to the YTF eruption.

Crater Lavas

New $^{40}Ar/^{39}Ar$ dates for two crater lavas (5.9 ± 4.4 and 7.9 ± 7.7 ka) and a negative age for one of the youngest crater lavas (≤ 4 ka) agrees with previous estimates that the crater lavas are young in the eruptive history of La Soufrière, and overlap with YTF eruption ages (≤ 4.3 ka; Rowley, 1978; Sigurdsson, 1981; Heath, 1997). Previous eruptive histories propose the emplacement of the crater lavas was constrained to the crater, however the young lava flow in Larikai valley (4.4 ± 4.2 ka) could suggest otherwise. Sigurdsson (1981) also identified a few thin lenses of lava flows between debris flows to the south of the crater, however was unable to correlate them to during or after the YTF eruption. The young Larikai lava flow sits on top of a debris flow and is cross cut by a dyke (Figure 2.3d), implying volcanism on the western flank of La Soufrière was still occurring until much more recently than previously thought (even at its maximum age of ~ 8 ka). The crater lavas exposed today comprise the eastern wall of the current crater, suggesting there must have been an opening for the lavas to flow down at the time. The shape of the crater has a strong control on where magmas are emplaced and flow; if lavas did flow down the western flanks during the crater lava period, then this could imply a more open crater morphology than previously thought.

Pyroclastic formation and historic lavas

The pyroclastic formation of La Soufrière's volcanic history is comprised of alternating explosive and effusive eruptions, depositing thick pyroclastic deposits that overlay the crater lavas and dominate the northern and southern crater walls. Previous radiocarbon dating finds a gap in pyroclastic flow deposit ages between 3.5 and 2.7 ka interpreted as a quiescence period (Heath, 1997), or could represent a time when effusive volcanism dominated and the crater lavas were emplaced. Pyroclastic activity then rejuvenated and has been recorded on timescales of approximately every 40 – 100 yrs leading to present day (Heath, 1997; Robertson, 2005; Cole et al., 2019). Historical eruptions have mostly

encompassed both effusive and explosive volcanism (except the 1902-1903 eruption). The effusive volcanism associated with these eruptions is confined to the crater, today defined by a 100 – 200 m deep depression, and often involved the extrusion of relatively small viscous lava domes. It is unclear when effusive magmatism evolved from voluminous fluid lava flows to small viscous lava domes, as compositionally these magmas are identical. The change could represent a difference in volume of material available, magma ascent rate or viscosity (Cassidy et al., 2018). The explosive eruptions during the pyroclastic formation phase are likely responsible for forming the general crater morphology observed today and carving out the vent magmas erupt from.

2.4 Conclusions

Major and trace element geochemistry finds the majority of recent magmas erupted from La Soufrière to be basaltic andesites with very limited compositional variation. Elevated REE concentrations and trace element ratios find these magmas to have experienced a small degree of coherent differentiation, fractionating plagioclase and amphibole at hydrous and oxidising conditions, implied by low Sr and Eu uptake into plagioclase. These observations agree with previous experimental studies that found basaltic andesite magmas on St. Vincent to be generated by differentiation from high-magnesium basaltic parent magmas (Melekhova et al., 2015). Erupted basaltic andesite magmas at La Soufrière therefore represent melts generated within the crust. Trace element ratios suggest low sediment or crustal input into the magmas, supporting erupted magmas as true liquids.

A single mafic, low-magnesium basalt (~ 8 wt. % MgO) crater lava unit is identified and is more primitive than all other crater lavas. This mafic unit is instead geochemically similar to a small number of previously reported mafic tephra in the YTF and 1902 deposits, and the low-magnesium basaltic pre-Somma lavas. These rare mafic

pyroclastic products correlate with two of the largest explosive eruptions at La Soufrière. The mafic crater lava is stratigraphically older than the 1902-1903 eruption, however could be related to the YTF eruption. Collapse of the Somma edifice likely triggered the YTF eruption by rapid depressurisation of the magmatic system. Such large-scale eruptions can result in deeper more primitive magmas being erupted overtime (Manconi et al., 2009), as was observed in the 1902-1903 eruption (Roobol and Smith, 1975). Further work is required to establish the link between the mafic crater lava, YTF eruption and Somma collapse.

New $^{40}Ar/^{39}Ar$ dates for lavas erupted from La Soufrière reveal two key findings. Firstly, an unconformity is identified in the northern wall of the current crater whereby the oldest crater lava (25.2 ± 3.8 ka) is overlain by crater lavas that are considerably younger (7.9 ± 7.7 and 5.7 ± 4.4 ka). The anomalously old crater lava could represent part of the Somma crater wall that slumped into the current crater during the Somma collapse. Secondly, dates for lavas exposed on the western flanks of La Soufrière (Larikai and Roseau) range from 33.7 ± 8 ka to 4.4 ± 4.2 ka. The youngest lava flow is in the lower Larikai valley and is cross cut by a dyke, suggesting volcanism on the western flank of La Soufrière continued until more recently than previously thought, possibly coeval with the emplacement of the crater lavas. Effusive volcanism since then has produced lava domes refined to the crater.

Chapter 3

A detailed petrological analysis of basaltic andesite magmas erupted at La Soufrière volcano, St Vincent.

3.1 Introduction

Erupted magmas preserve a mineralogical record of their journey through the crust, providing information about the source region, changes in physicochemical conditions during ascent, and any interactions with the wider magmatic system. Crystallisation conditions can be estimated using the composition of mineral phases assumed to be in equilibrium and applying an appropriate geothermobarometer (Powell, 1985; Putirka, 2008). Subsequent changes in the pressure (P), temperature (T), composition (X), and water content (H_2O) of a magma can then be tracked by variations in mineral compositions and mineral textures such as zoning, resorption and breakdown (Davidson and Tepley, 1997; Jerram and Martin, 2008; Streck, 2008). Phenocrysts (or autocrysts, grown from the host melt) primarily record these processes, but other crystal types such as glomerocrysts (crystal clusters), antecrysts (crystals picked up by the melt from the same magmatic system), xenocrysts (crystals foreign to the magmatic system), and xenoliths (fragments of the crystal-rich mush) also provide information about a magmas ascent through the broader magmatic system (D'Mello et al., 2023; Zellmer et al., 2024). Studying the crystal cargo of an erupted magma deepens our understanding of the magmatic architecture beneath volcanoes and could help to constrain depths of magma generation, residence, and crystallisation prior to eruption.

Geothermobarometers rely on the attainment of equilibrium between co-existing phases (e.g. minerals or melt) in order to derive pressure and temperature conditions. Examples of phase pairings include amphibole-plagioclase (Holland and Blundy, 1994), two-pyroxene (Putirka, 2008), pyroxene-liquid (Higgins et al., 2022; Ágreda-López, 2024), olivine-spinel-orthopyroxene (Ballhaus et al., 1991), whole-rock (Weber and Blundy, 2024) and many more. The use of a certain thermobarometer is dependent on the mineral assemblage and stability of different mineral phases in erupted magmas (Powell et al., 2002; Putirka, 2008). Mineral assemblages and compositions are also used to estimate the P-T conditions of crystallisation (O'Hara, 1968; Green, 1971), as well as water content (Gaetani et al., 1994; Grove et al., 2002, 2012) on the basis of experimental phase equilibria. Crystal abundance can be used to infer the crystallisation order and ascent rate (Geschwind and Rutherford, 1994; Blundy and Cashman, 2008; Cassidy et al., 2015). Zoning patterns in minerals evidence crystal growth during ascent (Vance, 1969; Humphreys et al., 2006b; Ginibre et al., 2007), whilst resorption textures indicate mineral instability (Tsuchiyama, 1985; Nelson and Montanna, 1992; Cashman and Blundy, 2013). Changes in the mineral assemblage, such as the breakdown of olivine at low pressures to form orthopyroxene (Grove and Baker, 1984; Gaetani et al., 1994; Coombs and Gardner 2004), or amphibole at low water contents to form clinopyroxene (Rutherford and Hill, 1993; Davidson et al., 2007a; Krawczynski et al., 2012), reflect the P-T-H_2O path of a magma. Additionally, assimilation of crustal material or magma mixing modifies the composition of a magma; the injection of magmas hotter than the host can also cause an increase in temperature (Sparks et al., 1977; Hort, 1998; Ruprecht and Bachmann, 2010; Eichelberger et al., 2006; Schmidt and Grunder, 2011). These changes are recorded by sudden changes in mineral compositions, reverse zoning and even whole-rock trace element concentrations (Gerlach and Grove, 1982; Leeman and Hawkesworth, 1986; Nakamura, 1995; Humphreys et al., 2006b; Bezard et al., 2015).

Some volcanoes continuously erupt magmas of the same composition throughout their lifetime. In the previous chapter, I established that La Soufrière volcano, St. Vincent is an example of such. Studying the mineralogical record at these volcanoes and identifying petrological similarities and differences between erupted units, can help us to understand the origin and crystallisation history of compositionally homogenous magmas. Previous studies have proposed that the homogenous magmas erupted at Arenal volcano, Costa Rica represent identical crystallisation and mixing ratios prior to eruption (Streck et al., 2005). However, if mineral compositions and textures are always the same, this could also imply that magmas are repeatedly generated at the same P-T-H_2O conditions and follow a similar ascent path to the surface every time. In this chapter I use the compositionally homogenous basaltic andesites erupted at La Soufrière volcano, St. Vincent to test mineralogical variability, look for evidence of magma mixing and track any changes in the crystallisation history of these magmas over time. By applying a number of geothermobarometers suitable to the mineral assemblages observed, I estimate crystallisation pressures and temperatures for the La Soufrière magmas, and assess whether magmas could be generated at the same conditions.

3.1.1 La Soufrière volcano, St. Vincent

Previous petrological studies on St. Vincent found basaltic andesite mineral assemblages to be dominated by plagioclase (Graham and Thirlwall, 1981; Heath et al., 1998a; Weber et al., 2024), followed by clinopyroxene, orthopyroxene, Fe-Ti oxides and rarer olivine. High An plagioclase cores are common (≥ An_{90}; Rowley, 1978; Heath et al., 1998a) and are also found in erupted xenoliths (Lewis, 1973; Arculus and Wills, 1980; Tollan et al., 2012) indicative of hydrous crystallisation conditions (Sisson and Grove, 1993a). Olivine is often corroded or overgrown with orthopyroxene, and high Fo cores, along with high Mg# clinopyroxene cores, are attributed to differentiation from a parent magma (Graham and Thirlwall, 1981; Heath et al., 1998a). Previous geothermometry

estimates for the basaltic andesite magmas at La Soufrière find magmatic temperatures to be between 960 – 1050ºC (Heath et al., 1998a; Weber et al., 2024). Limited geobarometers are available for typical basaltic andesite mineral assemblages (plag + cpx + opx + ox) meaning source pressures are poorly constrained and generally have high uncertainly. Clinopyroxene-only barometry estimates give crystallisation pressures of ~ 0.25 – 0.4 GPa (~ 8 – 13 km; Weber et al., 2024). Experimental studies instead propose basaltic andesite magmas at St. Vincent are generated at higher pressures of 0.7 – 1 GPa and ~ 1050ºC by differentiation from a high-magnesium basalt parent with 4.5 wt.% H_2O (Melekhova et al., 2015).

During fieldwork to St. Vincent in 2023 and 2024, lava samples were collected from the La Soufrière crater and two valleys on the western flanks of the volcano (lower and upper Larikai valley and Roseau valley). Two dykes were also sampled from Larikai valley. The relative ages of the lavas and dykes are determined from stratigraphic positioning and new $^{40}Ar/^{39}Ar$ dates (see section 2.2.4). The crater lavas represent a series of sequentially emplaced lava flows, with the oldest at the bottom and youngest at the top, and are the youngest lavas analysed here. Lavas from Larikai and Roseau are the oldest at ~ 30 ka, followed by the lowermost crater lava at ~ 25 ka. Younger lavas from Larikai and Roseau are ~ 4 and ~ 14 ka respectively, followed by the youngest crater lavas at 5 – 8 ka. The ages of the upper Larikai lavas could not be constrained, nor their stratigraphic position relative to other lavas, so are placed at the bottom where results are presented in stratigraphic order. Petrological analyses of these units, in the form of textural and compositional descriptions and comparisons are presented in the work below, followed by a discussion of the findings and their implication.

3.2 Methods

3.2.1 Sample preparation

Ninety samples were prepared for thin section using the geofacilities laboratories at the Department of Earth Sciences, University of Oxford. These samples include the forty-one samples prepared for whole-rock analysis (discussed in section 2.1.4) and an additional forty-eight igneous and meta-igneous xenoliths.

3.2.2 Thin section billet preparation

For samples that were also powdered for whole-rock analysis, samples were initially split into smaller fragments and material for powdering separated. Thin section preparation came afterwards as the fluids used to lubricate and cool the diamond saws can result in rock powder contamination. Samples were cut to blocks 10 – 15 mm thick using a vertical or horizontal diamond saw, depending on sample size. A 27 x 46 mm rectangle was then drawn on each sample and cut to size using the vertical diamond saw. Samples were washed with water, left to dry overnight, and then the sample number written on the back of the billet. Some xenolith samples were impregnated with epoxy to hold them together; both Kemet and Logitech epoxy resin and hardener were used. Both epoxies required 24 hours of drying before they could be cut into. For certain meta-igneous xenoliths, multiple thin section billets were prepared to represent different parts of the sample. Thin section billets were sent to Spectrum Petrographics Inc., Vancouver, Washington to be made into thin sections for petrological analysis.

3.2.3 Analytical methods

Thin sections were analysed using the Cameca SX-5 FE electron microprobe at the University of Oxford. Silicate minerals and oxides were analysed with a focused beam

(1 – 2 μm) at 15 kV and 10 nA. Na and K were analysed first, with lower counting times (20s rather than 30s) to reduce alkali loss. Total iron was determined as Fe^{2+} (FeO^{T}). Secondary standards include St. Johns Island (SJI) olivine and labradorite and are reported in the appendix (Table S4.2).

Mineral proportions (vol. %) were determined by point counting using Jmicrovision. 500 – 700 points were counted for each sample (Table 3.1) in a recursive grid pattern, with crystals ≤ 100 μm included as the matrix. Vesicles were identified in five samples and were counted as a separate phase to determine vesicularity. Photomicrographs were taken in plane- and cross-polarised light using the Leica LAS-X software, to highlight key textures observed within samples.

3.3 Results

3.3.1 Lava petrology

In total thirty-one thin sections of lava and dyke samples from La Soufrière were analysed on the electron microprobe (epma) for petrological study. Mineral assemblages and proportions are reported in Table 3.1, and mineral compositions in Table S3.1. All lavas are porphyritic with typically 40 – 55 vol. % crystals (normalised without vesicularity). Crater lava STV_LS_6 has the lowest crystal volume of 36 vol. % and the lower Larikai dyke edge sample (STV_LS_107) has the highest crystal volume of 63 vol. %. Phenocryst (≥ 500 μm) and microphenocryst (100 – 500 μm) assemblages include plag + cpx + mt ± opx ± ol (Figure 3.1). Plagioclase is the dominant mineral phase in all samples (22 – 48 vol. %). Clinopyroxene is next most abundant (6 – 10 vol. %) followed by Fe-Ti oxides (1 – 6 vol. %). Orthopyroxene is present in all samples (≤ 8 vol. %) except one of the mafic crater lava samples STV_LS_7, and is only found as a core mineral phase rimmed by cpx in crater lavas STV_LS_46 and 47. Olivine is absent from the

Table 3.1. Mineral phase assemblages, proportions and included micro-xenolith assemblages of new lava and dyke samples in age order as determined by stratigraphy and new $^{40}Ar/^{39}Ar$

Sample Number	Unit	$^{40}Ar/^{39}Ar$ age* (ka)	Phase assemblage	Mineral proportions (vesicle-free)								Xenolith assemblage	Xenolith name
				matrix	plag	ol	cpx	opx	ox	v	*n*		
Crater Lavas													
STV_LS_3	CL-1		plag+cpx+opx+ol+mt	45	37	3	7	3	5		*591*	plag+ol±ox	troctolite
STV_LS_4b	CL-1		plag+cpx+opx+ol+mt	45	36	0	8	4	6		*617*	cpx+ox±plag±ol±opx	clinopyroxenite **
STV_LS_8	CL-2		plag+cpx+opx+ol+mt	51	37	1	4	5	3		*741*		
STV_LS_10	CL-2		plag+cpx+opx+ol+mt	52	38	1	5	3	2		*720*	plag+cpx+ol	ol-gabbro
STV_LS_17	CL-5		plag+cpx+opx+mt	55	26	0	7	7	5		*683*	plag+cpx+opx+ox	gabbro **
STV_LS_16	CL-5		plag+cpx+opx+mt	50	35	0	7	6	2		*708*		
STV_LS_11	CL-4		plag+cpx+opx+ol+mt	55	31	1	7	4	2		*652*		
STV_LS_48	CL-16		plag+cpx+opx+ol+mt	52	34	3	6	1	2		*561*		
STV_LS_47	CL-15		plag+cpx+ol+mt±opx	50	35	5	7	1	3		*710*		
STV_LS_46	CL-14	7.9 ± 7.7	plag+cpx+ol+mt±opx	50	37	4	7	0.1	2		*736*		
STV_LS_45	CL-13		plag+cpx+opx+mt±ol	47	36	1	6	5	4		*758*		
STV_LS_6	CL-7	5.7 ± 4.4	plag+cpx+opx+mt±ol	64	25	0.1	4	4	2		*736*		
STV_LS_15	CL-12		plag+cpx+opx+ol+mt	56	32	1	5	4	1		*712*		
STV_LS_7	**CL-9**		plag+cpx+ol+mt+ilm	52	34	4	9	0	1		*723*		
STV_LS_13	**CL-9**		plag+cpx+opx+ol+mt+ilm	41	36	6	10	3	4		*683*	plag+opx+ox	gabbro
STV_LS_14	**CL-11**		plag+cpx+ol+mt±opx±ilm	42	39	4	10	1	3		*696*		
STV_LS_106	LL dyke - core		plag+cpx+opx+ol+mt	46	37	1	7	7	2	13	*806*		
STV_LS_107	LL dyke - edge		plag+cpx+opx+ol+mt	37	48	1	6	5	2	3	*746*		
STV_LS_132	UL dyke		plag+cpx+opx+mt±ol	54	30	0.3	8	6	2		*735*		

STV_LS_133	UL dyke		plag+cpx+opx+mt	58	24	0	8	7	3		*757*	plag+cpx+mt	gabbro **
STV_LS_134	UL dyke		plag+cpx+opx+mt	55	32	0	6	5	3		*839*		
STV_LS_103	LL lava	4.4 ± 4.2	plag+cpx+opx+ol+mt	52	31	2	8	4	2		*653*		
STV_LS_167	Roseau lava	14.5 ± 3.1	plag+cpx+opx+mt±ol	51	33	1	9	4	3		*768*		
STV_LS_5a	CL-10	25.2 ± 3.8	plag+cpx+opx+ol+mt	54	29	2	6	5	4		*739*	cpx+opx+plag+ox	gabbro
STV_LS_154	Roseau lava	31.5 ± 4.0	plag+cpx+opx+ol+mt±ilm	49	33	4	6	5	3		*679*		
STV_LS_160	Roseau lava		plag+cpx+opx+ol+mt±ilm	56	27	3	8	4	3		*712*		
STV_LS_100	LL lava	33.7 ± 8.0	plag+cpx+opx+ol+mt±sp	50	29	1	9	8	3	5	*684*		
STV_LS_102	LL lava		plag+cpx+opx+ol+mt±ilm±sp	53	27	4	8	5	3		*715*	plag+cpx+opx+ol+mt	ol-gabbro
STV_LS_104	LL lava		plag+cpx+opx+ol+mt±sp	55	25	2	9	6	3		*695*	plag+cpx+ol+mt±sp	ol-gabbro
STV_LS_130	UL lava		plag+cpx+opx+ol+mt	59	24	2	7	7	2	9	*735*	plag+cpx+ol+mt	ol-gabbro
STV_LS_131	UL lava		plag+cpx+opx+ol+mt±sp	57	22	2	8	8	2	7	*737*		

* $^{40}Ar/^{39}Ar$ dates from Dr Brian Jicha, University of Wisconsin-Madison (see section 2.2.4)

** recrystallised micro-xenoliths

Bold indicates mafic crater lava units (MgO ~ 8 wt. %; Table 2.1)

mineral proportions are calculated vesicle-free and vesicle percentages (v) reported separately

n is the number of points counted in Jmicrovision

Abbreviations include CL - crater lava; YTF - yellow tuff formation; LL - lower Larikai; UL - upper Larikai; plag - plagioclase; cpx - clinopyroxene; opx - orthopyroxene; ol - olivine; mt - magnetite; ilm - ilmenite; sp – Cr-rich oxide (see text)

upper Larikai dyke and andesitic crater lavas STV_LS_16 and 17, and is only found in trace amounts in all other samples. The mafic crater lava samples contain the highest volume of olivine (≤ 6 vol. %).

The groundmass in all samples is microcrystalline, except in the lower Larikai dyke edge sample (STV_LS_107), where the groundmass is a dark brown aphyric glass (Figure 3.2b). The groundmass is comprised predominantly of plagioclase, as well as pyroxenes and oxides, with crystal size variable between samples (Figure 3.2a vs 3.2d). Trachytic textures are observed in some lavas (e.g. STV_LS_45) in both the groundmass and phenocrysts. Glomerocrysts, defined as crystal clusters (Zellmer, 2021) are ubiquitous in all samples. Antecrysts or xenocrysts, defined as crystals entrained in the melt from either the same or a different magmatic system, respectively, are identified in several lava samples. Distinguishing between antecrysts and xenocrysts often requires crystal-scale trace element or isotopic analysis (Davidson et al., 2007b; Shane et al., 2019; Camejo-Harry et al., 2025). Here xenocrysts are identified by their anomalously large crystal size (e.g. ≥ 6 mm) and unzoned cores, and antecrysts by their similar mineral chemistry to older crystals from the St. Vincent system. Micro-xenoliths (≤ 3 cm) are common with adcumulate textures and sometimes appearing recrystallised (Figure 3.3d). Micro-xenolith assemblages are reported in Table 3.1 and briefly discussed below. The lower Larikai dyke was sampled both at the centre of the dyke and at its quenched margin, adjacent to the lower Larikai lavas (Figure 2.2d), with an increase in vesicularity observed towards the core from 3 to 13 vol. % determined by point counting. Vesicles were otherwise only observed in the upper Larikai lavas and one of the lower Larikai lavas.

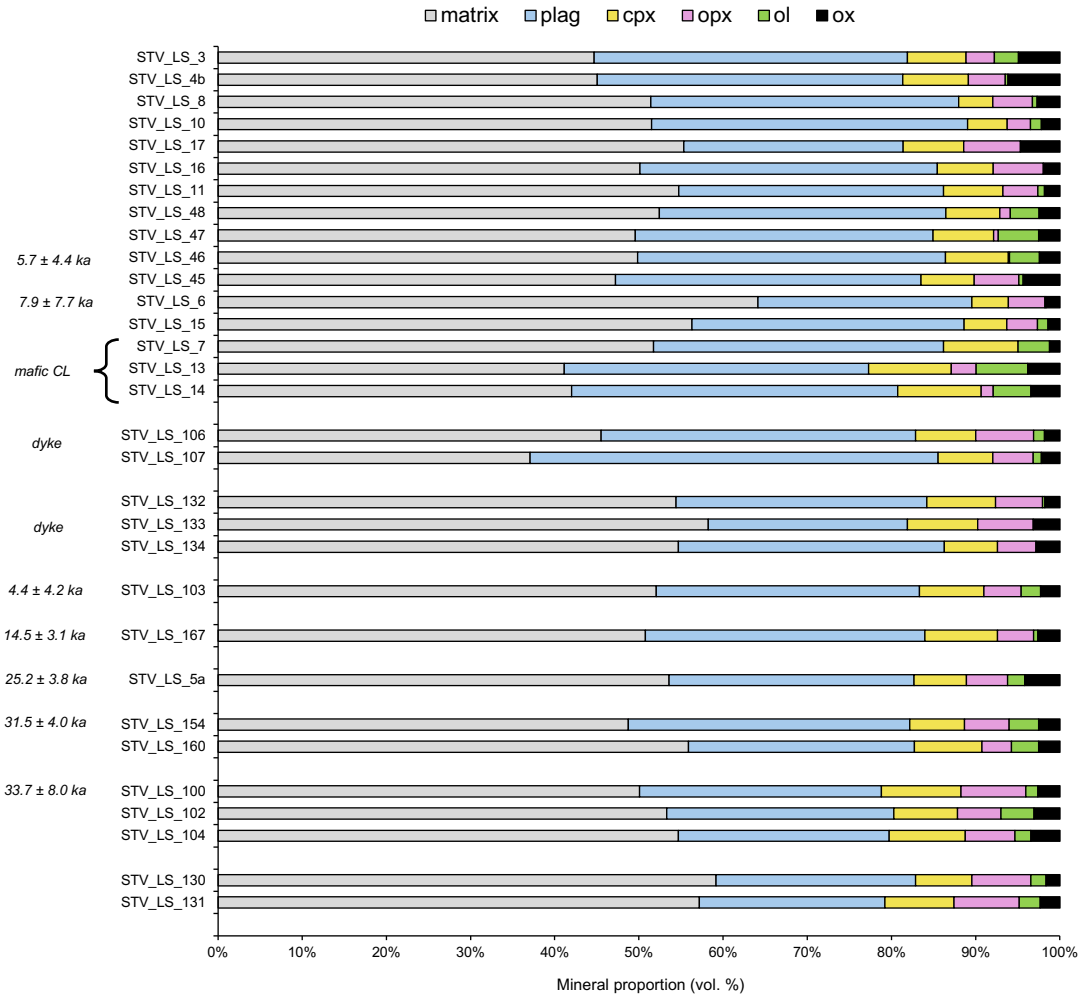


Figure 3.1: Modal proportions of phenocrysts and groundmass in lava and dyke samples from La Soufrière, calculated as a volume percentages and excluding vesicles. Samples are listed in age order from youngest at the top to oldest at the bottom using $^{40}Ar/^{39}Ar$ dates and stratigraphic positioning as reported in chapter 2 and discussed in the text. Abbreviations include plag - plagioclase, cpx - clinopyroxene, opx - orthopyroxene, ol - olivine, ox - Fe-Ti oxides.

Plagioclase

Plagioclase is the most abundant mineral phase in all lava samples (22 – 48 vol. %; Figure 3.1) and often appears as euhedral tabular or acicular laths. Crystal size varies from ≤ 100 – 200 μm in the groundmass; to ~ 200 μm – 4 mm microphenocrysts and phenocrysts; to ≥ 7 mm xenocrysts. Plagioclase also occurs in polymineralic and monomineralic glomerocrysts (Figure 3.3) and is the dominant groundmass phase. Sieve texturing in phenocryst cores is common and is also identified towards the rims of crystals (Figure 3.2a,b). Deformation twinning, sometimes referred to as mechanical

twinning and identified by its tapering appearance (Brown and Macaudière, 1986; Holness, 2018), is ubiquitous in microphenocrysts and most phenocrysts. Concentric and oscillatory zoning is mostly observed in phenocrysts but also present in some microphenocrysts. Zoning is predominantly normal, with reverse zoning identified in only five samples. Some crystals display patchy cores.

Plagioclase phenocrysts rarely contain mineral inclusions, though inclusions of clinopyroxene, orthopyroxene, olivine and Fe-Ti oxides are observed. Plagioclase inclusions within other mineral phases are instead more common, particularly in clinopyroxene and orthopyroxene, as well as in some olivine and Fe-Ti oxides, indicating early crystallization of plagioclase relative to other minerals. Plagioclase inclusions have anorthite contents that span the entire compositional range of each sample (e.g. An_{66} to An_{93} in cpx ($Mg\#_{69}$ to $Mg\#_{78}$) in STV_LS_106; An_{71} to An_{84} in cpx ($Mg\#_{69}$ to $Mg\#_{74}$) in STV_LS_48). The highest anorthite plagioclase inclusions are found in the highest magnesium number clinopyroxenes.

Plagioclase xenocrysts, identified by their considerably large crystal sizes (e.g. ≥ 7 mm), extensive Ca-rich unzoned cores (≥ An_{90}), and very thin low-An rims (e.g. An_{67} for a 0.1 mm rim of a 6 mm crystal; STV_LS_48), are present in three crater lavas, the upper Larikai dyke and one of the Roseau lavas. These crystals unlikely grew from the host melt and instead appear to have been entrained prior to eruption.

Clinopyroxene

Clinopyroxene is the second most abundant mineral phase (6 – 10 vol. %) and is present in all samples as euhedral to subhedral crystals. Phenocrysts range from a few hundred micro-meters to ~ 3 mm; xenocrysts are ≥ 6 mm and identified in two lava samples (STV_LS_11 and 102). Clinopyroxenes are most commonly found as glomerocrysts and are often pitted with oxide inclusions, individual crystals are also present but less

abundant (Figure 3.2). Clinopyroxenes appear pale green to pale pink in plane-polarised light (PPL), typical of calcic compositions. Most clinopyroxenes are unzoned or display weak normal zoning with only a subtle decrease in Mg# towards the rim. Reverse zoning is identified in nine samples. Sieve texturing is uncommon, though is observed towards the rim of the clinopyroxene xenocrysts. Simple twinning is observed in some crystals.

Clinopyroxene phenocrysts tend to contain inclusions of, or are closely associated with Fe-Ti oxides (Figure 3.2c) and plagioclase, suggesting coeval or early oxide and plagioclase crystallisation. Plagioclase An content in inclusions correlates with host clinopyroxene Mg# (see above). Clinopyroxene is rarely found as an inclusion within other mineral phases. For example, clinopyroxene is identified in a plagioclase xenocryst in mafic crater lava STV_LS_14, and as micro-inclusions in two unusual rounded oxide phenocrysts in the lower Larikai lavas, that also contain orthopyroxene inclusions (Figure 3.2g).

Breakdown and disaggregation textures are observed in clinopyroxene crystals in samples from both the upper and lower Larikai dykes (STV_LS_107 and 132; Figure 3.2h) and in one of the lower Larikai lavas (STV_LS_103). Clinopyroxene breaks down to form low An plagioclase and Fe-Ti oxides, with some orthopyroxene present. Clinopyroxene is also found on the rim of orthopyroxene crystals (e.g. Figure 3.2d; discussed below).

Orthopyroxene

Orthopyroxene is present in all samples except mafic crater lava sample STV_LS_7 (Figure 3.1). Its abundance is negatively correlated with the presence of olivine and extends up to 8 vol. %. Only trace amounts of orthopyroxene are identified in crater lava samples STV_LS_46 and 47, where orthopyroxene is a crystal core with a clinopyroxene rim (e.g. Figure 3.2d). Orthopyroxene phenocrysts range from a few hundred micro-

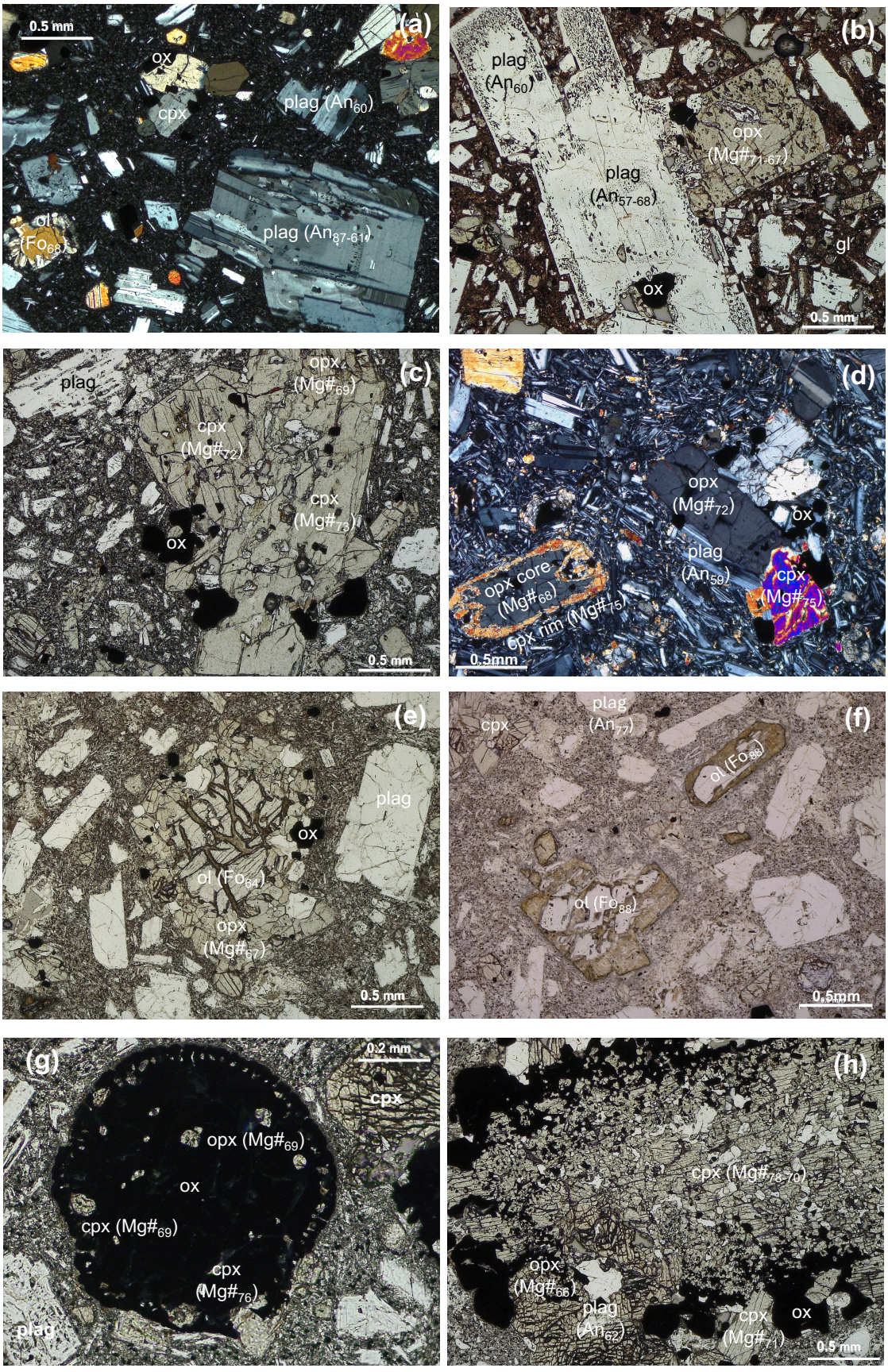


Figure 3.2: Photomicrographs of lava and dyke mineral textures. **(a)** Typical zoned and sieve textured plagioclase phenocryst, twinned plagioclase microphenocryst and olivine microphenocryst rimmed with orthopyroxene. Fine microcrystalline groundmass. (STV_LS_4b; XPL) **(b)** Reversely zoned plagioclase

crystal with a second plagioclase crystal adjoined to the top left corner and orthopyroxene to the right. Sieve texturing is strong at the rim of the plagioclase crystals and weak in the core. Orthopyroxene crystal also display sieve texturing. Brown matrix glass. (STV_LS_107; PPL) **(c)** Cluster of orthopyroxene, clinopyroxene and Fe-Ti oxide crystals. Pyroxenes are pitted with inclusions of plagioclase and oxides. (STV_LS_102; PPL). **(d)** Resorbed orthopyroxene crystal with clinopyroxene rim. Cluster of low anorthite plagioclase, clinopyroxene, orthopyroxene and oxides. Coarsely crystalline groundmass. (STV_LS_11; XPL). **(e)** Heavily cracked olivine with coarse reaction rim comprised of orthopyroxene, plagioclase and oxides. (STV_LS_5a; PPL) **(f)** Resorbed olivine crystals with thick iddingsite rims. (STV_LS_5a; PPL). **(g)** Round oxide crystal with inclusions of orthopyroxene and clinopyroxene, with inclusions prominent along the rim. Note the difference in scale. (STV_LS_102; PPL). **(h)** Unstable clinopyroxene crystal displaying significant breakdown textures. Rim comprised of plagioclase, orthopyroxene and Fe-Ti oxides. (STV_LS_132; PPL). Abbreviations as in Figure 3.1, as well as XPL - cross-polarised light; PPL - plane-polarised light. See text for how An, Mg# and Fo values calculated, An_{87-61} represents core-rim compositions.

meters to ~ 3 mm, with no orthopyroxene xenocrysts identified. Orthopyroxenes are generally euhedral to subhedral, and are present as individual crystals and in glomerocrysts. In PPL orthopyroxenes often appear cream to pale grey/yellow and tend to be more elongated than co-existing clinopyroxenes. Most orthopyroxenes are unzoned or show weak normal zoning at the rim. Reverse zoning is observed in a total of eight samples. Sieve texturing and resorption is uncommon and observed in only a few samples (e.g. Figure 3.2b).

Similar to clinopyroxene, though less frequent, orthopyroxenes can contain Fe-Ti oxide and plagioclase inclusions. Orthopyroxene inclusions within other mineral phases are generally rare, though have been identified in all other phenocryst phases, for example in two plagioclase phenocrysts (An_{55-55}; STV_LS_106 and An_{84-71}; STV_LS_8), one clinopyroxene ($Mg\#_{75-71}$; STV_LS_106), one olivine (Fo_{80}; STV_LS_103), and two rounded oxide phenocrysts (STV_LS_102 and 103; Figure 3.2g).

In five crater lavas orthopyroxene is present as resorbed crystal cores with overgrown clinopyroxene rims (Figure 3.2d). Fe-Ti oxides and low An plagioclase are also found on the rims of such grains. Orthopyroxene is also a common breakdown product on the rim of unstable olivine phenocrysts and microphenocrysts (Figure 3.2a and e).

Olivine

Olivine is present in all samples except three crater lavas (STV_LS_6, 16 and 17) and the upper Larikai dyke (Table 3.1). Olivine abundance extends up to 6 vol. % in the mafic crater lavas. Olivines are subhedral to anhedral microphenocrysts and phenocrysts (200 – 300 μm to 2.5 mm). No olivine xenocrysts are identified. Cracking is common, and most crystals are unzoned or display weak normal zoning at the rim. Reverse zoning is rare and only observed in two samples. All olivine phenocrysts and microphenocrysts have a reaction rim, primarily composed of orthopyroxene, with plagioclase and Fe-Ti oxides present occasionally (Figure 3.2e). Two crater lavas contain heavily iddingsitised olivines (STV_LS_5a and 45; Figure 3.2f). The extent of olivine breakdown varies between samples and does not appear to be correlated with Fo content.

Olivine is found as an inclusion in clinopyroxene and plagioclase in three crater lava samples. Olivine inclusions in the mafic crater lava sample STV_LS_7 (Fo_{74} and Fo_{72}) are hosted in early crystallising clinopyroxene ($Mg\#_{85-78}$) and plagioclase (An_{91-81}), respectively, and are in good agreement with olivine rim and microphenocrysts values for this sample, suggesting early olivine crystallisation. Olivine is rare in STV_LS_45 and only found as a heavily iddingsitised inclusion (Fo_{75}) in a high An plagioclase (An_{94}). Olivine inclusions in STV_LS_47 (Fo_{62} and Fo_{67}) are hosted in normally and reversely zoned clinopyroxenes ($Mg\#_{72-74}$; $Mg\#_{75-71}$), respectively, with Fo contents again in agreement with olivine rim and microphenocrysts values. Olivine phenocrysts rarely contain mineral inclusions themselves; only a few high Fo olivines in the lower Larikai lavas contain small oxides (≤ 10 μm). For example, magnetite is found in olivine (Fo_{89}) in STV_LS_104, and Cr-rich magnetite is found in olivine phenocrysts in STV_LS_100 (Fo_{80}) and STV_LS_102 (Fo_{91-75}). The high Fo contents of these olivines suggests early co-crystallisation of olivine and oxides.

Oxides

Oxides (predominantly magnetite and discussed below in section 3.3.2) are present in all samples, with abundances ranging from 1 – 6 vol. %. Most oxides are microphenocrysts (≤ 300 μm), though oxides in the upper Larikai dyke tend to be larger (~ 500 μm), and some phenocrysts are present and extend up to ~ 1 mm. Oxides tend to be anhedral to euhedral and in close association with, or found as inclusions within, other mineral phases (Figure 3.2). Oxides are also common in the groundmass. Two unusually round phenocrysts are identified in the lower Larikai lavas (STV_LS_102 and 103; Figure 3.2g) and contain inclusions of clinopyroxene and orthopyroxene. Oxides are usually found as an inclusion phase within other mineral phases, and are identified in olivine, plagioclase, clinopyroxene and orthopyroxene phenocrysts, suggesting early or coeval crystallisation.

Oxides are often involved in mineral breakdown reactions and are found on the rim of unstable olivine and clinopyroxene crystals (e.g. Figure 3.2h). In the mafic crater lavas, some oxides are found to exsolve a second Fe-Ti oxide phase (see below), and symplectitic oxides are identified within a plagioclase xenocryst and in micro-xenoliths.

Glomerocrysts and micro-xenoliths

Glomerocrysts are ubiquitous in all samples studied here and have previously been reported as abundant (Fedele et al., 2021; Weber et al., 2024). Typical polymineralic glomerocrysts contain plag ± cpx ± ox ± opx ± ol (e.g. Figure 3.3), though olivine is a rare glomerocryst phase. Monomineralic glomerocrysts of plagioclase and clinopyroxene are also observed (e.g. Figure 3.3b). Crystal size and the degree of nucleation varies within and between samples. Glomerocrysts minerals also exhibit zoning, sieve texturing and contain inclusions, mirroring the phenocryst population.

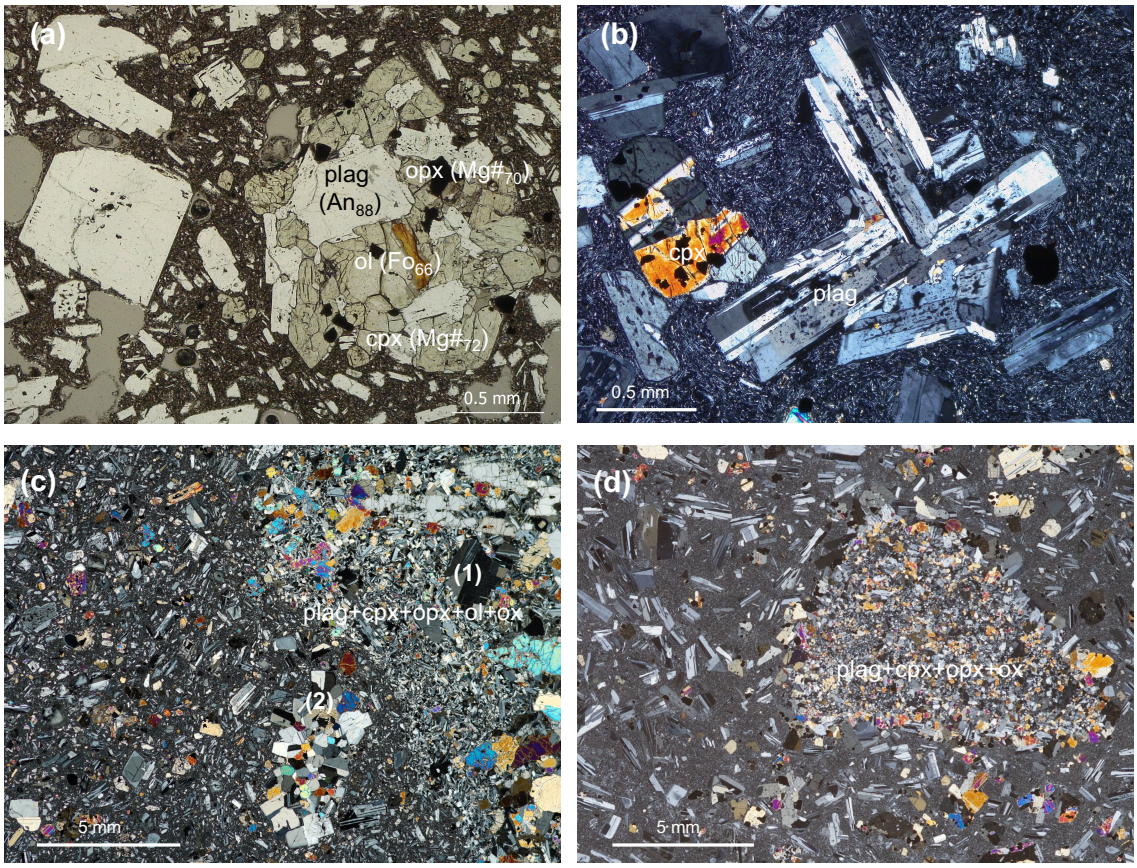


Figure 3.3: Photomicrographs of glomerocrysts and micro-xenoliths in lavas and dykes at La Soufrière. **(a)** Polymineralic glomerocryst with rounded appearance and comprised of interlocking crystals of plagioclase, olivine, clinopyroxene, orthopyroxene and Fe-Ti oxides. (STV_LS_130; PPL) **(b)** Monomineralic glomerocryst of zoned and twinned plagioclase crystals with sieve textured cores. Crystals protrude into the groundmass. Alignment of plagioclase in fine microcrystalline groundmass. (STV_LS_3; PPL) **(c)** Two olivine gabbro micro-xenoliths. (1) displays meso- to adcumulate texture at the core to orthocumulate texture at the rim with increasing interstitial plagioclase. Some resorbed elongated olivines are poikilitic. (2) displays adcumulate equigranular texture (STV_LS_104; XPL) **(d)** Recrystallised gabbro micro-xenolith with adcumulate texture. Coarser crystal sizes are observed around the rim. (STV_LS_17; XPL). Note the scale difference in c and d.

Some lavas contain micro-xenoliths (≤ 3 cm) with compositions including gabbros, ol-gabbros, ol-anorthosites and clinopyroxenites (Table 3.1; Figure 3.3). All micro-xenoliths display adcumulate textures unless stated otherwise. The ol-anorthosite in STV_LS_3 is predominantly large euhedral plagioclases with some smaller rounded olivines. The clinopyroxenite in STV_LS_4b contains large resorbed clinopyroxenes with bands of smaller clinopyroxene and olivine crystals running through the centre of the xenolith and around the rim. Oxides only occur in the recrystallised rim. The olivine gabbro in STV_LS_10 contains large euhedral plagioclases with smaller rounded clinopyroxenes

and olivines. In STV_LS_102 the olivine gabbro micro-xenolith has a meso- to adcumulate textures with small (≤ 700 μm) interlocking euhedral plagioclase, clinopyroxene and orthopyroxene crystals, and a large (~ 1.5 mm) resorbed olivine grain. STV_LS_104 contains two olivine gabbro micro-xenoliths (Figure 3.3c). The first is small (≤ 0.5 cm) and contains equigranular and equicrystalline plagioclase, clinopyroxene and olivine. The second is much larger (~ 3 cm) and is comprised of coarse resorbed olivine, clinopyroxene and plagioclase crystals at the core with a meso- to adcumulate texture. Some olivines are elongated and poikilitic. Towards the rim the texture becomes orthocumulate with the volume of interstitial plagioclase increasing and becoming dominant, resembling quench crystallisation. The olivine gabbro in STV_LS_130 contains two populations of plagioclases, coarse euhedral grains around the rim and smaller equigranular crystals in the centre. Clinopyroxene is poikilitic containing chadacrysts of plagioclase. Olivine is present as an interstitial phase. Gabbro micro-xenoliths in STV_LS_5a and 13 contain euhedral interlocking plagioclase and pyroxene crystals, with rounded oxides. Gabbro micro-xenoliths in STV_LS_17 and 133 instead appear recrystallised with equigranular plagioclase and pyroxenes. The micro-xenolith in STV_LS_17 (Figure 3.3d) has a coarser crystalline rim, with oxides only present in the rim.

Large xenocrysts (≤ 1 cm) are identified in a total of seven samples. STV_LS_11 and 102 contain clinopyroxene xenocrysts ($Mg\#_{78\text{-}73}$ and $Mg\#_{81\text{-}73}$) with plagioclase, olivine and oxide inclusions. STV_LS_14 contains a plagioclase xenocryst ($An_{94\text{-}88}$) with inclusions of clinopyroxene ($Mg\#_{78}$), olivine (Fo_{73}) and a symplectitic oxides; STV_LS_46, 48, 134 and 154 all contain plagioclase xenocrysts with extensive high An cores (≥ An_{90}) and a thin low anorthite rim (~ An_{59}).

3.3.2 Mineral chemical compositions

Mineral compositions are shown in Figures 3.4 to 3.9. An content is calculated as molar Ca / (Ca+Na); Fo content as molar Mg / (Mg+Fe+Mn) and Mg# as molar Mg / ($Mg+Fe^{2+}$), with Fe^{2+} calculated by stoichiometry. Phenocryst core and rim compositions observed within each sample are shown in Figure 3.4 in relative age order according to Figure 3.1. Core-rim compositions are written as An_{95-60} corresponding to an An_{95} core and An_{60} rim, and compositional ranges are written as An_{95} to An_{60}.Two distinct plagioclase core populations are identified. All samples contain high An plagioclase cores and some samples also contain low An plagioclase cores (Figure 3.4a). Mg-rich olivine, clinopyroxene and orthopyroxene cores are only observed in small number of samples and are highlighted in Figures 3.4b-d. Grey shading illustrates mineral compositional ranges calculated to be in equilibrium with the bulk magma determined using Kd values from Putirka (2008) for olivine (0.3 ± 0.03), clinopyroxene (0.28 ± 0.08), and orthopyroxene (0.29 ± 0.06). The Kd for plagioclase is found to increase significantly with water content (Sisson and Grove, 1993a). Magmas with ~ 2 wt. % H_2O have Kd values of 1.3 – 1.7 (Baker and Eggler, 1987; Sisson and Grove, 1993a). For H_2O saturated magmas (~ 6 wt. % H_2O at 2 kbar) the Kd value is ~ 5.5 with pressure having little effect (Sisson and Grove, 1993a). Extrapolation of the relationship between Kd and water contents identified by Sisson and Grove (1993a) finds more primitive hydrous magmas with ~ 10 wt. % H_2O (Annen et al., 2006) to have a calculated Kd value of ~ 9.3. Figure 3.4a shows estimated An values using a Kd for magmas with ~ 2 wt. % H_2O (light grey) and 6 – 10 wt. % H_2O (dark grey). In general, most natural data core compositions overlap with calculated equilibrium values, except Mg#'s in natural orthopyroxene crystals which tend to be consistently lower than Kd estimates. Olivine Fo contents and orthopyroxene Mg# are highest in the older Roseau and Larikai lavas and in the mafic crater lavas. The upper and lower Larikai dykes tend to have more restricted compositional ranges for olivine, clinopyroxene and orthopyroxene.

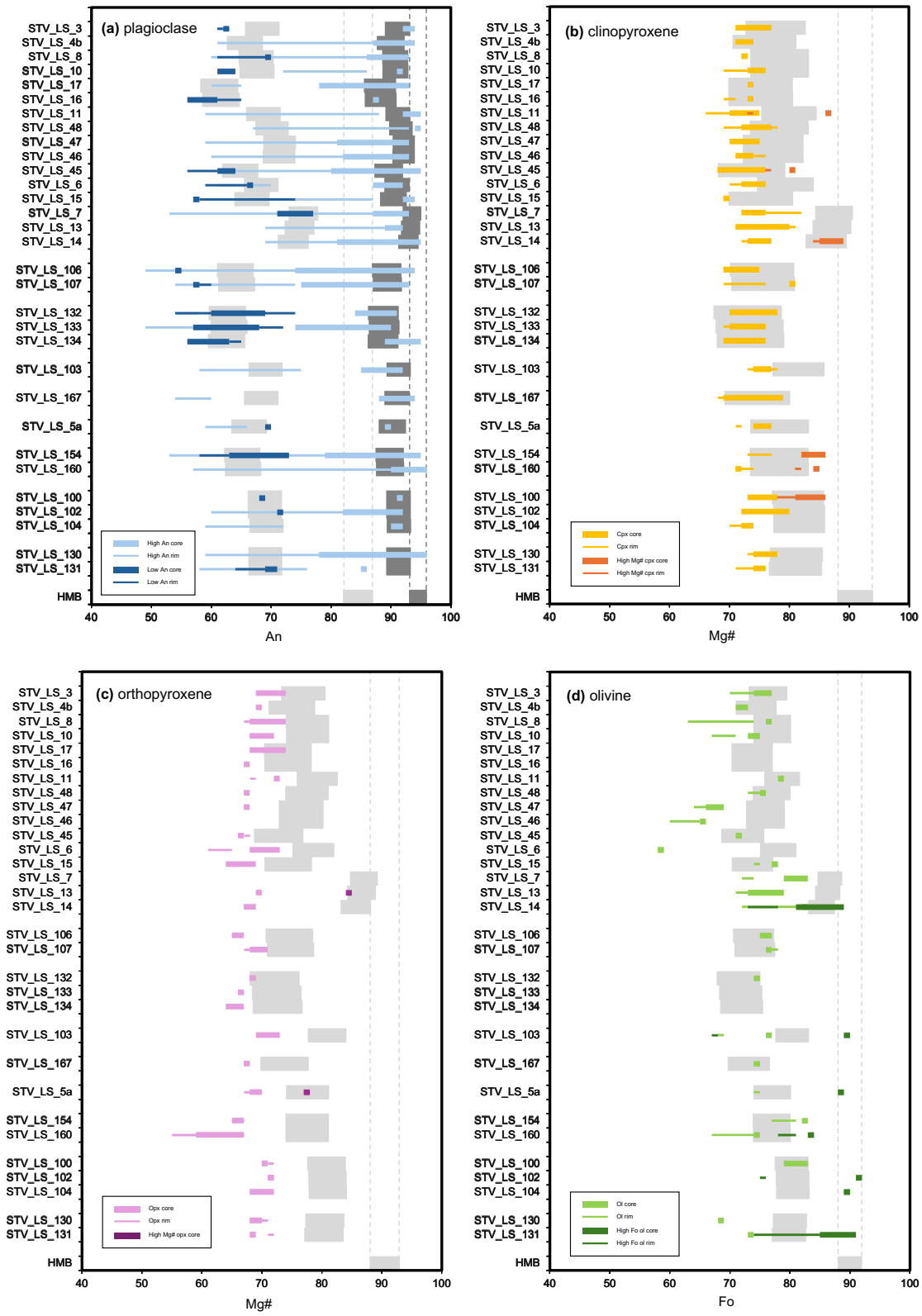


Figure 3.4: Core and rim compositions for **(a)** plagioclase, **(b)** clinopyroxene, **(c)** orthopyroxene, and **(d)** olivine. Lava and dyke samples are listed in age order as in Figure 3.1. Core compositional ranges are shown as thick boxes, and associated rim compositions as thin boxes. Where two coloured boxes are shown this represents two populations of core and rim compositions. Grey shading illustrates calculated mineral compositions in equilibrium with the bulk magma using Kd values from Puritka (2008) and Sisson and Grove (1993a). See text for details. The light grey shading in (a) illustrates the Kd values for magmas with relatively

low water contents (~ 2 wt. % H_2O; Sisson and Grove, 1993a) and the dark grey shading for more hydrous magmas with 6 – 10 wt. % H_2O (Sisson and Grove, 1993a; Annen et al., 2006). See text for details. Estimated mineral compositions in equilibrium with parent high-magnesium basalts (HMB; Pichavant et al., 2002a; Melekhova et al., 2015) are shown as dashed lines.

In this next section, all newly acquired data are compared to previously reported phenocryst and xenolith data for St. Vincent and La Soufrière. Phenocryst data are from Heath et al., (1998a), Robertson (2002) and Weber et al., (2024). Xenolith data are from Robertson (2002), Tollan et al. (2012), Fedele et al., (2021) and previously unpublished data (Table S3.2; appendix). All data were measured on an electron microprobe except the Fedele et al. (2021) micro-xenoliths that were measured using EDS on an SEM.

Plagioclase

Anorthite contents in plagioclases range from An_{49} to An_{96} in good agreement with phenocryst and xenolith data (Figure 3.5). This broad range is typical for Lesser Antilles magmas (Camejo-Harry et al., 2018; Cooper et al., 2016; Arculus and Wills, 1980). Two populations of plagioclase compositions are identified: high-An cores (An_{85} to An_{96}) and low-An cores and rims (~ An_{55} to An_{75}). High-An cores are in good agreement with St. Vincent xenolith compositions (An_{90} to An_{95}) and high H_2O Kd values (e.g. 6 – 10 wt. % H_2O; Figure 3.4a). Low-An phenocryst cores, identified in all dyke samples and in twelve lavas, agree with rim compositions and are in equilibrium with low H_2O Kd values (~ 2 wt. % H_2O; Figure 3.4a). Micro-xenoliths from both this study and Fedele et al. (2021) show a wide range of An contents, along with microphenocrysts and glomerocrysts (An_{52} to An_{96}; Figure 3.5).

Plagioclases tend to be normally zoned with calcium-rich cores (≥ An_{80}) and more sodic rims (An_{50} to An_{70}; Figure 3.2a); the largest decrease in anorthite contents recorded is 40 % An (e.g. $An_{93\text{-}53}$ in STV_LS_7). Low-An cores display both normal and reverse zoning. Reverse zoning is only observed in two crater lavas and the upper Larikai dyke, with typical increases in anorthite contents of ≤ 5 % An (e.g. $An_{69\text{-}74}$ in STV_LS_132). In crater

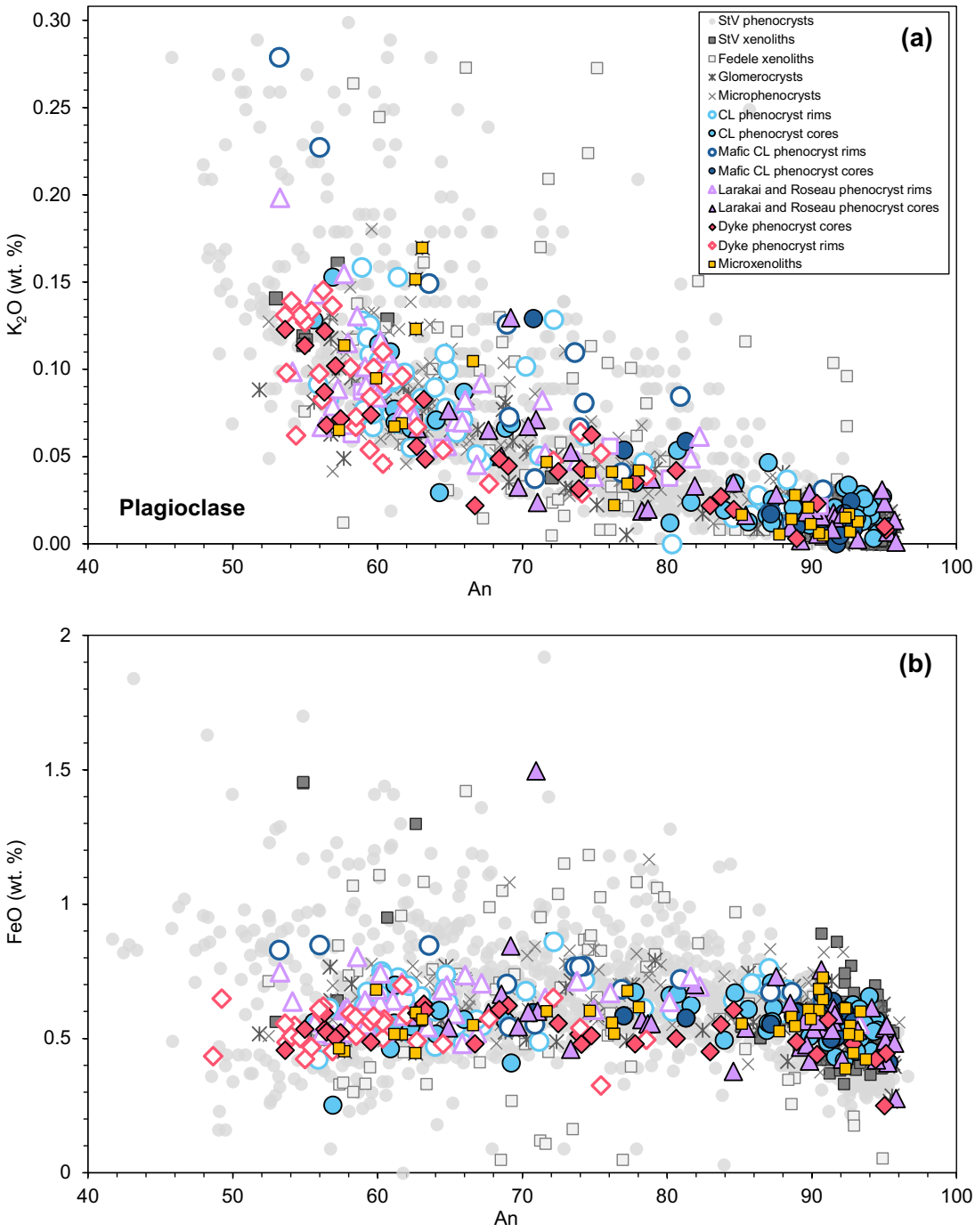


Figure 3.5: Plagioclase core and rim compositions plotted as anorthite content (An) versus **(a)** K_2O (wt. %) and (b) FeO (wt. %). The crater lava (CL; light blue circles), mafic CL (dark blue circles), Larikai and Roseau lava (purple triangles), and dyke (red diamonds) core compositions are shown as filled symbols and rim compositions as open symbols. Microphenocryst compositions for all samples are shown as crosses and glomerocrysts as stars. Grey circles are previous phenocryst data from St. Vincent (Heath et al., 1998a; Robertson, 2002; Weber et al., 2024). Dark grey squares are xenoliths from Robertson (2002), Tollan et al. (2012) and Table S3.2 (appendix); pale grey squares are micro-xenoliths from Fedele et al. (2021); yellow squares are micro-xenoliths from this study.

lava STV_LS_15, a much larger increase in An contents is observed from An_{57} to An_{74} (17% An increase) in a single plagioclase crystal. This plagioclase has an unzoned core but is resorbed with a ~ 250 μm thick sieve textured rim. In lower Larikai dyke sample STV_LS_107 (Figure 3.2b) a rimward increase of 11 % An is observed, again this mineral appears resorbed and has a sieve textured core and rim. Both high-An and low-An, normally and reversely zoned phenocrysts display sieve texturing, oscillatory zoning and deformation twinning, thus it is difficult to distinguish different plagioclase populations based on texture alone. Unzoned plagioclases are also present.

K_2O contents are generally low (≤ 0.18 wt. % K_2O), and increase with decreasing An contents (Figure 3.5a). Some of the lowest An rims contain up to 0.62 wt. % K_2O. FeO contents in plagioclase are generally between 0.25 - 0.85 wt. % FeO (Figure 3.5b). Plagioclases with higher FeO contents also tend to have high TiO_2 contents, indicative of contamination by nearby or included Fe-Ti oxides.

Clinopyroxene

Clinopyroxenes have compositions in the range $Wo_{35-51}En_{36-49}Fs_{6-21}$ and $Mg\#_{66}$ to $Mg\#_{89}$, generally clustering between $Mg\#_{70}$ and $Mg\#_{80}$ (Figure 3.6). The highest Mg# clinopyroxenes (≥ $Mg\#_{80}$) are found in the mafic crater lava, the lower Larikai and Roseau lavas and crater lava STV_LS_11 (Figure 3.4b and 3.6). All new data overlap with previously reported phenocryst and xenolith data. St. Vincent xenolith clinopyroxenes cluster between $Mg\#_{76}$ and $Mg\#_{81}$, whilst the Fedele et al. (2021) micro-xenolith clinopyroxenes show a wider spread of values extending up to $Mg\#_{88}$. These high Mg# clinopyroxenes are present in two olivine-gabbro samples. The high Mg# micro-xenolith clinopyroxenes reported in this study ($Mg\#_{83}$ to $Mg\#_{89}$) are from a recrystallised clinopyroxenite micro-xenolith in crater lava STV_LS_4b. Microphenocrysts have compositions mostly between $Mg\#_{67}$ to $Mg\#_{78}$, with a small subset of microphenocrysts displaying compositions between $Mg\#_{82}$ and $Mg\#_{86}$. These

Mg-rich microphenocrysts are again found in the mafic crater lavas, lower Larikai and Roseau lavas, like the high Mg# phenocrysts. Glomerocrysts generally have compositions between $Mg\#_{70}$ and $Mg\#_{78}$, overlapping with the majority of phenocryst and St. Vincent xenolith data.

Normal zoning is common in clinopyroxene phenocrysts and is typically on the order of a rimward decrease in Mg# of ≤ 4 %. The largest decrease in Mg# observed is 9 % in the Roseau lavas. Reverse zoning is identified in three crater lavas, the mafic crater lava, an upper Larikai dyke and lava sample, and one of the Roseau lavas. Rimward increases in Mg# are usually ≤ 4 % Mg#. The largest increase in Mg# is 12 % is in the mafic crater lava sample STV_LS_7, which interestingly does not contain any normally zoned clinopyroxenes, unlike all other samples.

Between clinopyroxenes with ≤ $Mg\#_{82}$ and those with the highest Mg#'s there appears to be a compositional gap in the data presented here (Figure 3.6). Some previously reported phenocryst data do sit in this gap but are scarce. The St. Vincent phenocrysts with ≥ $Mg\#_{82}$ are generally from primitive basaltic magmas (Robertson, 2002), though some are also reported in the more evolved basaltic andesite and andesite magmas. The crater lavas, both the upper and lower Larikai dykes, and the majority of all other lavas contain much lower magnesium cores and rims (≤ $Mg\#_{78}$). The dykes show a particularly narrow compositional range. These observations suggest that clinopyroxenes with ≥ $Mg\#_{82}$ are inherited from an earlier episode of more mafic magmatism.

CaO contents range from 17 – 24 wt. % CaO and increase with increasing Mg#. TiO_2 contents are low (0.2 –1.4 wt. % TiO_2) and show no trend with Mg#. Al_2O_3 contents range from 0.8 – 8 wt. %, correlating to tetrahedral aluminium (Al^{IV}) contents of 0.03 – 0.25 atoms per formula unit (apfu; calculated on a 6 O basis), and generally decrease with

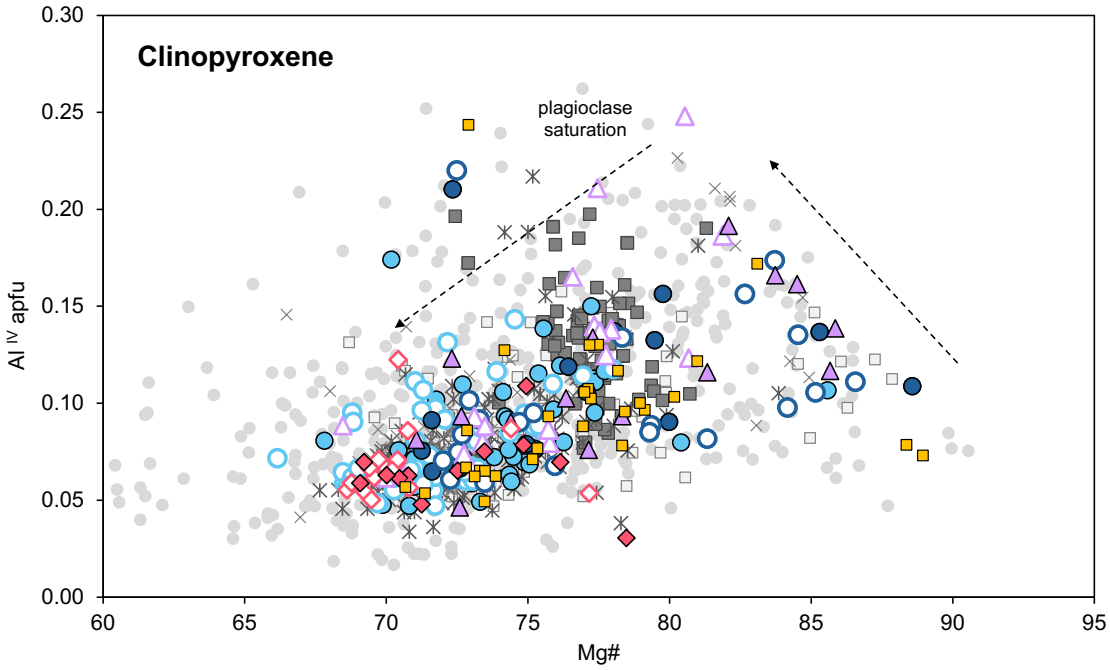


Figure 3.6: Clinopyroxene core and rim compositions plotted as tetrahedral aluminium (Al ^{IV}) as atoms per formula unit (apfu) versus magnesium number (Mg#). Symbols as in Figure 3.5. Note the high Mg# cores in the mafic CL, Roseau lavas and micro-xenoliths.

falling Mg#. However, near $Mg\#_{82}$ there appears to be a change of slope. The high Mg# clinopyroxenes instead increase in Al^{IV} with decreasing Mg#, suggesting crystallisation before plagioclase in more mafic magmas, and hence more Al in the melt. The peak in Al^{IV} denotes the point of plagioclase saturation (Figure 3.6).

Orthopyroxene

Orthopyroxene compositions range from $Wo_{2\text{-}14}En_{54\text{-}81}Fs_{15\text{-}43}$ and $Mg\#_{55}$ to $Mg\#_{84}$, though tend to cluster between $Mg\#_{64}$ and $Mg\#_{74}$ (Figure 3.7). The highest Mg# reported is from a resorbed phenocryst core in mafic crater lava sample STV_LS_13 ($Mg\#_{84}$; Figure 3.4c) and is considerably more Mg-rich than all other orthopyroxenes analysed in this study (≤ $Mg\#_{77}$), and previous studies (≤ $Mg\#_{75}$). Such high Mg# compositions are found in meta-igneous xenoliths on Petit St. Vincent ($Mg\#_{82\text{-}84}$; Melekhova et al., 2022), illustrating that high Mg# orthopyroxenes do exist within the Lesser Antilles, but have not previously been reported for St. Vincent. In general, orthopyroxene compositions reported here are

in good agreement with previous St. Vincent phenocryst and xenolith data. St. Vincent xenolith orthopyroxenes are uncommon, with compositions ranging between $Mg\#_{68}$ and $Mg\#_{72}$. Orthopyroxene is more abundant in the La Soufrière micro-xenoliths (Fedele et al., 2021) and shows a similar range in Mg# ($Mg\#_{66}$ to $Mg\#_{73}$).

Microphenocryst, glomerocryst and micro-xenolith compositions from this study match those of phenocryst core and rim values, though micro-xenoliths display a narrower range (e.g. $Mg\#_{67}$ to $Mg\#_{73}$). Some microphenocrysts have elevated Al_2O_3 contents (≥ 1.5 wt. %), these crystals often found on the rim of olivine or clinopyroxene phenocrysts. Both upper and lower Larikai dykes contain lower and more restricted magnesium (≤ $Mg\#_{68}$) and titanium contents (≤ 0.28 wt. % TiO_2). The lowest Mg# orthopyroxene ($Mg\#_{59-55}$, core-rim) is a euhedral phenocryst (~1.5 mm) analysed in one of the Roseau lavas (STV_LS_160; adjacent to an Fo_{84-78} subhedral olivine) and sits apart from the majority of all other orthopyroxenes (≥ $Mg\#_{64}$). Orthopyroxene compositions tend to be lower in magnesium contents than compositions calculated to be in equilibrium with the host rock (Figure 3.4c).

Unzoned or weak normally zoned orthopyroxenes are common. Normal zoning is typically on the order of a ≤ 4 % Mg# decrease rimward. The largest decrease in Mg# is 8 % ($Mg\#_{73-65}$) in crater lava STV_LS_6. Reverse zoning is observed in one crater lava, all Larikai lavas and one upper Larikai dyke sample (STV_LS_134; the same sample that also exhibits clinopyroxene and plagioclase reverse zoning). Reverse zoning typically involves a 1 – 3 % increase in Mg#; the largest increase in Mg# is 8 % ($Mg\#_{65-73}$) in a microphenocryst in lower Larikai lava STV_LS_100.

CaO and Al_2O_3 contents are low and show no correlation with Mg# (1 - 2 wt. % CaO; 0.5 – 1.8 wt. % Al_2O_3). These Al_2O_3 wt. % values correspond to 0.02 – 0.07 tetrahedral aluminium (Al^{IV}) and are shown in Figure 3.7. The highest Mg# clinopyroxenes sit apart

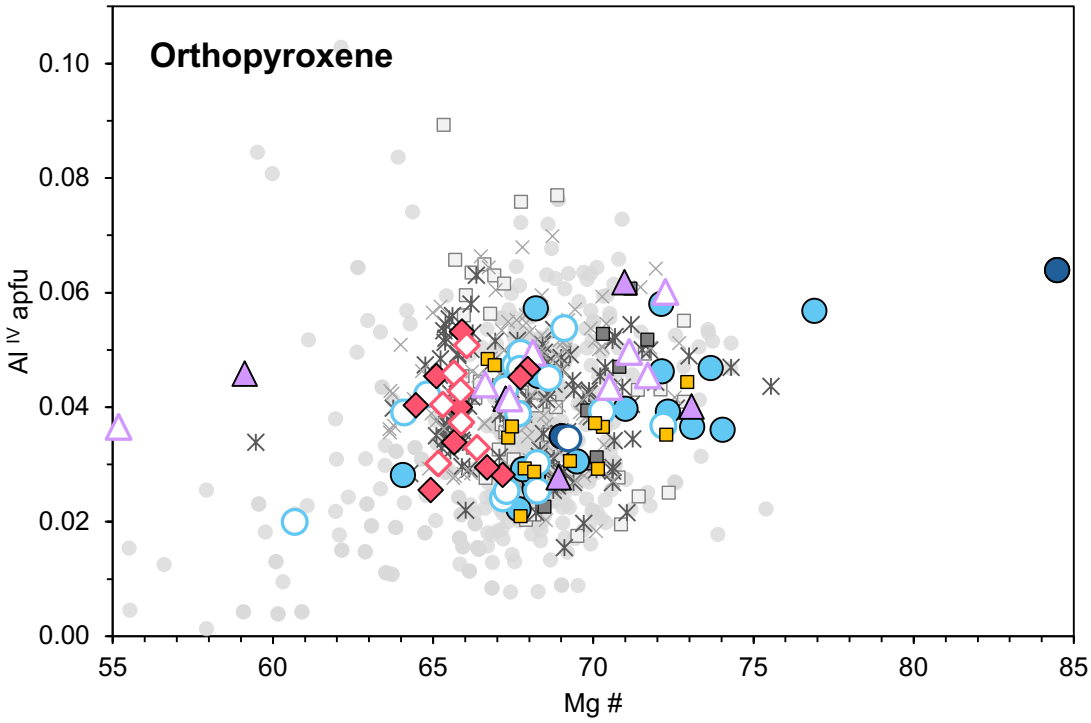


Figure 3.7: Orthopyroxene core and rim compositions plotted as TiO_2 (wt. %) versus magnesium number (Mg#). Symbols as in Figure 3.5. Note the lack of data for mafic CL and abundance of glomerocryst values.

from all other data. TiO_2 contents are also low and mostly sit between 0.14 – 0.4 wt. % TiO_2 (0.004 – 0.012 Ti (apfu)) except the highest Mg# orthopyroxene ($Mg\#_{84}$) that contains 1 wt. % TiO_2. Tetrahedral aluminium (Al^{IV}) increases with increasing Ti (apfu), as in clinopyroxene, and is a function of temperature (Melekhova et al., 2022).

Olivine

Olivine compositions range from Fo_{56} to Fo_{91}, clustering between Fo_{71} and Fo_{78}, and are in good agreement with previous phenocryst and xenolith data (Figure 3.8). The highest Fo contents (≥ Fo_{80}) are found in phenocrysts, glomerocrysts and microphenocrysts in the mafic crater lavas, Roseau and Larikai lavas. The oldest crater lava (STV_LS_5a) contains unusually high Fo olivine crystals (Fo_{88}), that appear heavily iddingsitised (e.g. Figure 3.2f). All other crater lava phenocrysts have Fo contents of ≤ Fo_{78}. The micro-xenolith with high Fo olivine (Fo_{86}) also contains high Mg# clinopyroxene (≤ $Mg\#_{89}$) in crater lava STV_LS_4b. The St. Vincent xenoliths cluster at Fo_{71} to Fo_{77}, whilst the

Fedele et al. (2021) micro-xenoliths range from Fo_{67} to Fo_{85}. Olivine is absent in the upper Larikai dyke, besides two microphenocrysts (Fo_{74} and Fo_{76}). The lower Larikai dyke contains traces of olivine (≤ 1 vol. %; Table 3.1), with a very limited Fo range of Fo_{74} to Fo_{77}. The lowest Fo olivine phenocryst cores and rims are in the crater lavas, predominantly in lava STV_LS_46 that only contains olivine ≤ Fo_{66}, suggesting late crystallisation. Microphenocryst and glomerocryst compositions match those of phenocryst core and rim values. All glomerocrysts with ≤ Fo_{63} are from crater lava STV_LS_46, with all low Fo microphenocrysts in the crater lavas.

Most olivine phenocrysts are unzoned or weakly normally zoned at the rim with a decrease in Fo contents of ≤ 6 %. A reduction in Fo content of 9 – 11 %, and 16 – 22 % is observed in the mafic crater lava and lower Larikai lava olivines, respectively. Reverse zoning is rare and only observed in mafic crater lava sample STV_LS_14 (Fo_{82-84}), and in the lower Larikai dyke STV_LS_107 (Fo_{76-77}).

CaO contents range from 0.02 – 0.25 wt. % CaO in the data reported here and extend up to 0.5 wt. % in previously analysed xenoliths (Robertson, 2002; Fedele et al., 2021). Figure 3.8 shows two trends, one with low CaO contents that the data presented in this study follow, and one with a steeper increase in CaO contents that some of the Fedele et al. (2021) micro-xenoliths and phenocrysts from high-magnesium basalts (Robertson, 2002) follow. The high-CaO trend indicates crystallisation before clinopyroxene (and plagioclase) saturation, which act to bring down the melt CaO contents (Klein et al., 2023). Clinopyroxene saturation is found to be delayed at low pressures (Stamper et al., 2014b), resulting in higher CaO in the melt, and consequently in the olivine crystallising from it. MnO contents range from 0.1 – 0.8 wt. % MnO, displaying a strong negative correlation with Fo contents. NiO_2 (wt. %) increases with Fo content and extends up to 0.46 wt. % NiO_2. Cr_2O_3 concentrations are generally low (≤ 0.04 wt. % Cr_2O_3) and show

a gentle increase with increasing Fo content. The Fedele et al. (2021) micro-xenoliths that follow the high-CaO trend also tend to have elevated Cr_2O_3 and MnO contents.

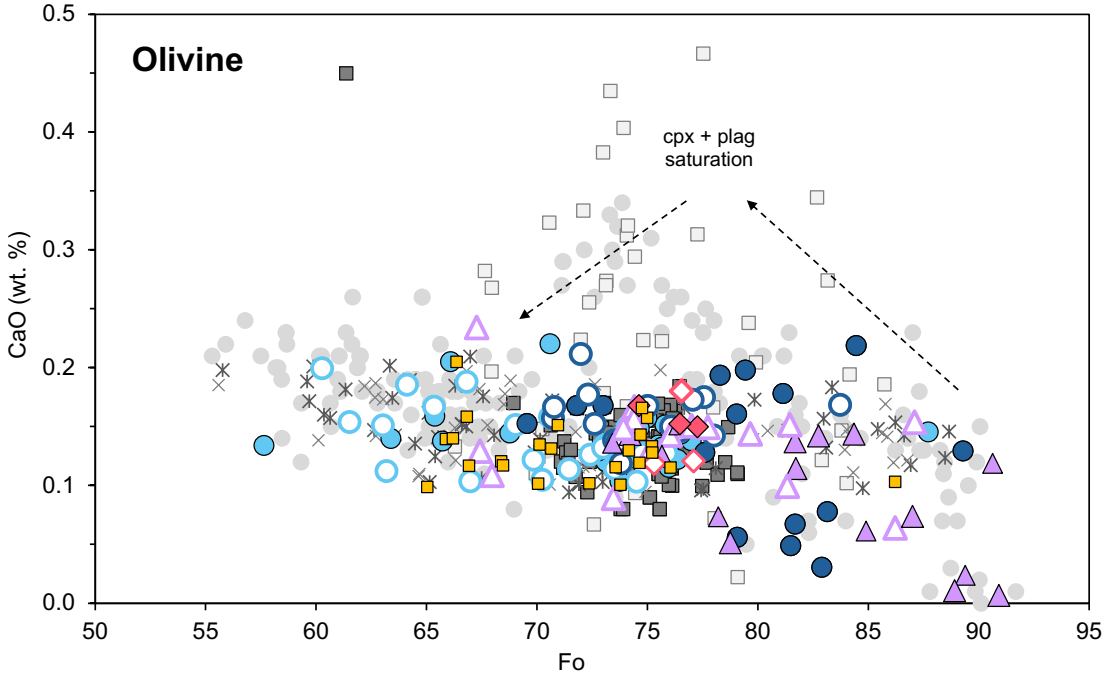


Figure 3.8: Olivine core and rim compositions plotted as CaO (wt. %) versus forsterite content (Fo). Symbols as in Figure 3.5. Note the high Fo cores in the Larikai and Roseau lavas, mafic CL and micro-xenoliths.

Oxides

The majority of the oxides analysed in this study have a cubic spinel structure (AB_2O_4) and classify as titanomagnetites due to their high iron (68 – 80 wt. % FeO^T) and titanium (6 – 16 wt. % TiO_2) contents. Ferric iron contents are determined using charge balance and stoichiometry. Fe^{3+}# is calculated as molar Fe^{3+} / (Fe^{3+}+ Al^{3+}) and Fe^{2+}# as Fe^{2+}/ (Fe^{2+}+ Mg^{2+}). Minor concentrations of magnesium, aluminium and chromium are also present in all oxides (≤ 5 wt. % MgO, ≤ 9 wt. % Al_2O_3, and ≤ 4.5 wt. % Cr_2O_3). All magnetite compositions agree with previous St. Vincent phenocryst data and sit along the spinel-magnetite exchange vector (Figure 3.9a). Fe^{3+} # and Fe^{2+} # are positively correlated, with high iron numbers closer to a magnetite composition and lower iron numbers richer in aluminium and magnesium and closer to a spinel composition. Five titanomagnetites have an Fe^{3+}# < 0.80 and are found either on the rim of breaking down

olivine grains or as inclusions within olivine or clinopyroxene. Oxide compositions primarily overlap with the Fedele xenolith oxides. The St. Vincent xenolith titanomagnetite compositions tend to be more Mg-rich (lower Fe^{2+}#), Al-rich (lower Fe^{3+}#) and Ti-poor (≤ 10 wt. % TiO_2), sitting further away from the magnetite end member (where Fe^{3+}# and Fe^{2+}# equal 1). The micro-xenolith oxide compositions analysed in this study overlap with the microphenocryst (and phenocryst) data reported. The upper and lower Larikai dykes have narrower compositional ranges compared to the lavas (e.g. 11 – 17 wt. % TiO_2; ≤ 2.5 wt. % MgO; Fe^{2+} $\#_{0.90.}$ to Fe^{2+} $\#_{0.97}$).

A small population of xenolith data from two discrete xenolith samples (a dunite (SVG44), Fedele et al., 2021; and a hornblendite (VS18), Tollan et al., 2012 and Table S3.2) have Fe^{2+}# and Fe^{3+}#'s < 0.6 and are Cr-spinels. These oxides have high Cr_2O_3 and Al_2O_3 contents (4 – 25 wt. % Cr_2O_3; 8 – 48 wt. % Al_2O_3), and low FeO contents (30 – 55 wt. % FeO). Most oxides analysed in the La Soufrière lavas and dykes have much lower chromium contents (≤ 0.8 wt. % Cr_2O_3; ≤ $Cr\#_{25}$), except in the mafic crater lava where oxides contain up to 4.5 wt. % Cr_2O_3 (~ $Cr\#_{65}$) and in the Larikai lavas where oxides contain 13 – 14 wt. % $Cr_2O_{3.}$ (green circles in Figure 3.9b; $Cr\#_{52}$ to $Cr\#_{65}$). These oxides have high iron and titanium contents (59 – 66 wt. % FeO; 8 – 9 wt. % TiO_2) and low aluminium (5 – 8 wt. % Al_2O_3), suggesting they are Cr-rich magnetites, with Cr^{3+} replacing Fe^{3+} rather than Al^{3+} in Cr-spinels. These Cr-rich magnetites are found as inclusions in olivine and in a micro-xenolith in STV_LS_104 (Figure 3.3c). The Cr-rich oxide in the upper Larikai lava is found on the rim of an olivine phenocryst and contains the highest concentration of chromium with 32 wt. % Cr_2O_3 ($Cr\#_{74}$; Figure 3.9b), only 7 wt. % Al_2O_3 and 50 wt. % FeO, suggesting it is instead closer to chromite in composition ($FeCr_2O_4$).

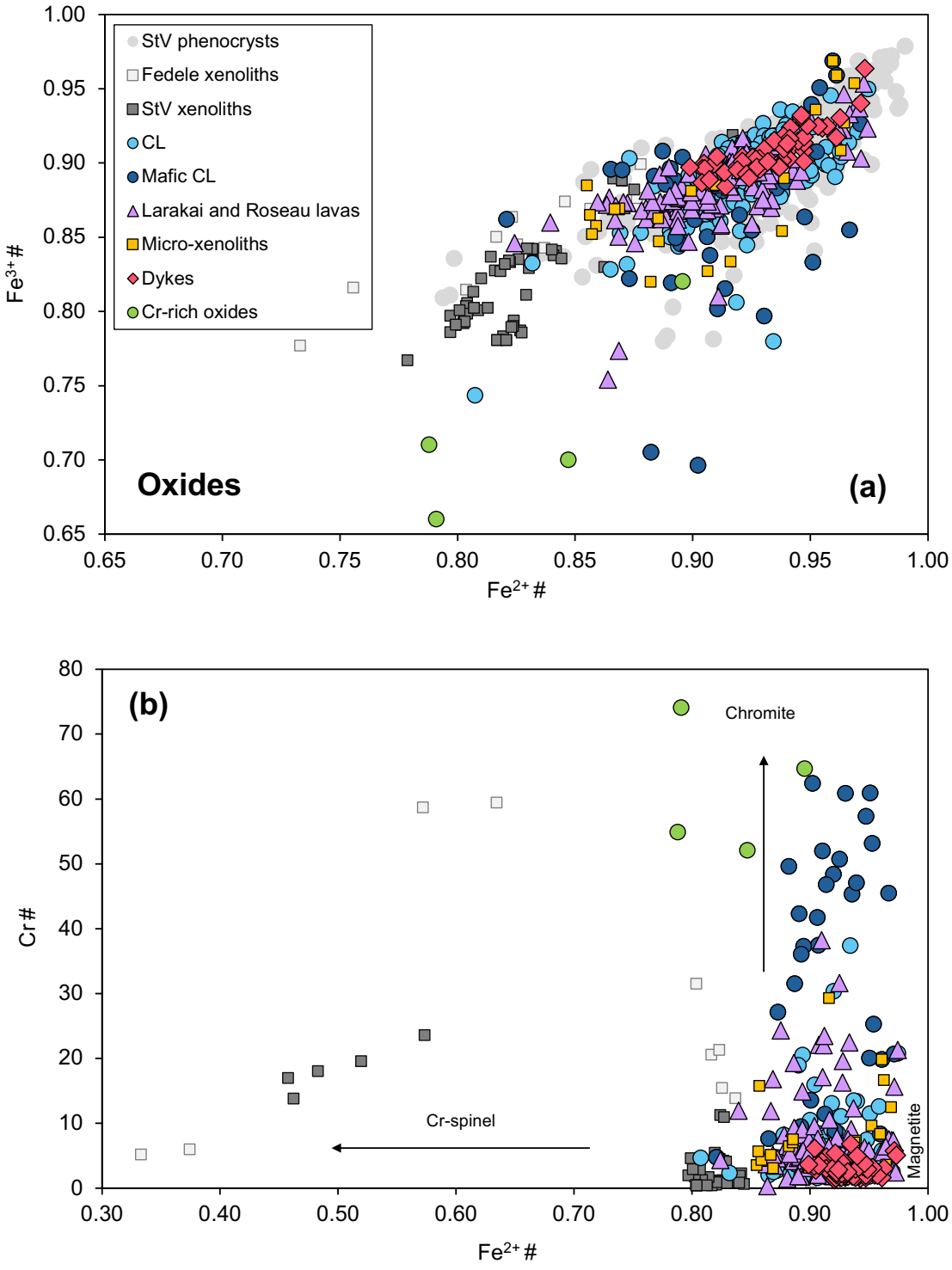


Figure 3.9: Magnetite compositions plotted as Fe^{2+} # versus **(a)** Fe^{2+} # and **(b)** Cr#. Symbols as in Figure 3.5 but all with solid fill as there is little variation between core and rim values. A small number of Cr-rich (13 – 33 wt. % Cr_2O_3) magnetites were identified in the Larikai and Roseau lavas and are shown as green filled circles.

A third Fe-Ti oxide phase with a rhombohedral structure (ABO_3), termed ilmenite, is identified in five lava samples (Table 3.1). Iron and titanium contents range from 43 – 52

wt. % FeO and 37 – 49 wt. % TiO_2. Magnesium, aluminium and chromium concentrations are all low (≤ 6 wt. % MgO, ≤ 1 wt. % Al_2O_3, and ≤ 1.5 wt. % Cr_2O_3). Ilmenite occurs as an exsolution phase in magnetite, or on the rim of unstable olivine grains, in the three mafic crater lava samples. Ilmenite is also found as an inclusion phase within a clinopyroxene xenocryst in lower Larikai lava STV_LS_102, and as a microphenocryst in Roseau lavas STV_LS_154. Ilmenite has previously been reported in one of the Fedele et al. (2021) micro-xenoliths and is compositionally similar to the ilmenites identified in this study. In the Robertson (2002) xenoliths a different rhombohedral oxide, termed titanohematite, is identified and contains much lower titanium (~ 10 wt. % TiO_2), and higher iron (67 – 74 wt. % FeO^T), particularly ferric iron. There is a negative correlation between TiO_2 contents and Mg# in both cubic and rhombohedral oxides, due to the coupled substitution $Fe^{2+} + Ti^{4+} = 2Fe^{3+}$. The presence of multiple oxides is common in island arcs (Arculus and Wills, 1980; Barnes and Roeder, 2001)

3.4 Discussion

3.4.1 Thermobarometry

A number of geothermobarometers have been applied to the La Soufrière lava and dyke samples presented here to obtain magma pressure and temperature estimates. Results are reported in Table 3.2. These include: clinopyroxene-orthopyroxene (± 40ºC; Putirka, 2008), clinopyroxene-only (Higgins et al., 2022; Ágreda-López et al., 2024), and bulk chemistry (MagMaTaB; Weber and Blundy, 2024). Olivine-spinel thermometry (O'Neill and Wall, 1987) and olivine-orthopyroxene-spinel oxybarometry (Ballhaus et al., 1991) could not be used due to the presence of magnetite rather than chrome-spinel in all samples (≤ 8 wt. % Al_2O_3).

Table 3.2. Temperature, pressure and fO_2 estimates for La Soufrière lavas and dykes

Sample #	Unit	cpx-opx (P.2008)	MagMaTaB (W&B 2024)				cpx-only (H.2022)				cpx-only (Á-L.2024)				ILMAT (L.2013)			
		T (ºC)	T (ºC)	sd	P (GPa)	sd	T (ºC)	sd	P (GPa)	sd	T (ºC)	sd	P (GPa)	sd	T (ºC)	sd	fO_2	sd
STV_LS_3	CL-1	963	1057	46	0.47	0.28	1002	24	0.20	0.07	1041	21	0.08	0.04				
STV_LS_4a	CL-1		1056	48	0.43	0.28												
STV_LS_4b	CL-1	960	1054	48	0.39	0.26	1015	31	0.20	0.02	1065	34	0.07	0.06				
STV_LS_8	CL-2	969	1057	46	0.44	0.29	1019	28	0.20	0.00	1063	16	0.03	0.01				
STV_LS_10	CL-2	951	1056	46	0.44	0.29	1009	33	0.21	0.05	1047	19	0.04	0.05				
STV_LS_17	CL-5	955	1049	36	0.46	0.30	1012	28	0.20	0.01	1069	18	0.02	0.02				
STV_LS_16	CL-5	951	1049	35	0.47	0.30	1004	28	0.20	0.03	1064	25	0.03	0.03				
STV_LS_11	CL-4	944	1065	47	0.49	0.28	1005	32	0.24	0.08	1045	15	0.08	0.08				
STV_LS_48	CL-16	971	1061	47	0.60	0.27	1013	30	0.21	0.04	1058	15	0.06	0.07				
STV_LS_47	CL-15	910	1036	42	0.35	0.20	992	38	0.22	0.09	1053	27	0.07	0.06				
STV_LS_46	CL-14	982	1034	41	0.34	0.20	999	41	0.21	0.08	1068	23	0.04	0.05				
STV_LS_45	CL-13	945	1066	43	0.61	0.28	986	41	0.21	0.07	1056	29	0.05	0.06				
STV_LS_6	CL-7	935	1079	40	0.74	0.25	996	30	0.19	0.03	1062	21	0.04	0.03				
STV_LS_15	CL-12	922	1036	43	0.36	0.26	989	40	0.22	0.10	1049	21	0.06	0.08				
STV_LS_7	**CL-9**						1015	30	0.21	0.08	1056	22	0.08	0.06	880	21	-0.13	0.15
STV_LS_13	**CL-9**	1002	1217	72	0.89	0.29	1141	55	0.62	0.33	1066	34	0.11	0.09	888	59	0.04	0.17
STV_LS_14	**CL-11**	997					1115	56	0.37	0.25	1069	39	0.10	0.09	877		-0.47	
STV_LS_106	LL dyke 1	954	1044	42	0.33	0.24	1003	42	0.22	0.11	1055	23	0.04	0.07				
STV_LS_107	LL dyke	951	1046	42	0.35	0.25	1000	40	0.25	0.10	1057	24	0.06	0.10				

STV_LS_132	UL dyke	941	1044	39	0.46	0.29	1008	36	0.20	0.05	1058	16	0.03	0.04		
STV_LS_133	UL dyke	932	1054	40	0.49	0.28	1004	39	0.20	0.07	1048	15	0.03	0.02		
STV_LS_134	UL dyke	934	1047	40	0.43	0.29	1005	45	0.20	0.06	1051	22	0.02	0.03		
STV_LS_103	LL lava	962	1084	47	0.43	0.27	1014	32	0.22	0.07	1059	19	0.07	0.09		
STV_LS_167	Roseau lava	988	1077	46	0.71	0.25	1001	40	0.23	0.10	1039	26	0.09	0.08		
STV_LS_5a	CL-10	918	1050	43	0.39	0.27	1012	35	0.24	0.06	1042	15	0.06	0.07		
STV_LS_5b	CL-10		1047	40	0.36	0.25										
STV_LS_154	Roseau lava	956	1052	43	0.37	0.27	1033	44	0.31	0.15	1060	45	0.11	0.12	924	0.22
STV_LS_160	Roseau lava	945	1050	42	0.36	0.26	1032	40	0.27	0.11	1064	37	0.10	0.11		
STV_LS_100	LL lava	947	1084	47	0.43	0.27	1017	30	0.26	0.09	1054	29	0.11	0.10		
STV_LS_102	LL lava	946	1084	46	0.42	0.27	1003	36	0.23	0.06	1048	23	0.06	0.09	887	0.34
STV_LS_104	LL lava	963	1087	46	0.43	0.27	1003	34	0.23	0.10	1042	20	0.09	0.08		
STV_LS_130	UL lava	940	1082	48	0.42	0.27	1000	32	0.27	0.10	1035	19	0.15	0.21		
STV_LS_131	UL lava	939	1079	48	0.42	0.27	1004	38	0.23	0.08	1044	21	0.07	0.06		

Bold indicated mafic crater lavas
P.2008 uncertainty of ± 40ºC
Abbreviations include P.2008 – Putirka, 2008; W&B.2024 – Weber and Blundy, 2024; H.2022 – Higgins et al., 2022; A-L.2024 – Ágreda-López et al., 2024; L.2003 – Lepage, 2003.

Clinopyroxene-orthopyroxene

Clinopyroxene-orthopyroxene (cpx-opx) pairs are present in all lavas except mafic crater lava sample STV_LS_7 which is lacking orthopyroxene (Table 3.1). Using the Putirka (2008) thermometer, estimates of magmatic temperatures where clinopyroxene and orthopyroxene are in equilibrium range from 910-1002 ºC (± 40 ºC), with no correlation to age. The highest temperatures are found in the mafic crater lavas and Roseau lava STV_LS_167 (Table 3.2).

Clinopyroxene-only

Average clinopyroxene-only (cpx-only) crystallisation pressures and temperatures calculated using the Higgins et al. (2022) thermobarometer range from 0.19 to 0.31 GPa (± ≤ 0.15 GPa), and 986 to 1033 ºC (± ≤ 45 ºC), excluding the mafic crater lavas which give a wider range of pressures and temperatures of 0.21 – 0.62 GPa and 1015 – 1141ºC, with much higher uncertainty (± ≤ 0.33 GPa and ± ≤ 56 ºC; Table 3.2). Average cpx-only pressure estimates cluster at ~ 0.2 GPa, thought to represent a minimum crystallisation estimate for the upper crust (Plank et al., 2013; Higgins et al., 2022). Individual clinopyroxenes instead give pressure estimates down to ~ 0.6 GPa (Figure 3.10) for the Roseau and Larikai lavas, though are still heavily skewed to 0.2 GPa, suggesting early crystallisation of some crystals at 0.6 GPa but that most clinopyroxene crystallisation occurs at shallower depths (Putirka, 2008). Individual results are shown in Figure 3.10 to display the range of pressures and temperatures over which clinopyroxene crystallises. Cpx-only temperatures are consistently ~ 50ºC higher than cpx-opx temperatures for samples where both estimates are possible.

The Ágreda-López (2024) cpx-only thermobarometer gives average pressures of ≤ 0.1 GPa for all samples, with uncertainties often overlapping with zero. Some individual clinopyroxene crystals give pressures of ≤ 0.4 GPa, though are far outweighed by much

lower pressure values. Average temperatures range from 1035 – 1069 ºC (± ≤ 45 ºC), higher than cpx-opx estimates by ~ 100 ºC (Table 3.2). Weiser et al. (2023) explored the limits of cpx-only and cpx-liquid barometers and found that those without a H_2O-term tend to underestimate pressure and temperature, thus the values reported in Table 3.2 are only a minimum P-T estimate. Additionally, clinopyroxene is not necessarily a near-liquidus phase in the La Soufrière magmas (explored in chapter 4), meaning cpx-only thermobarometry may not provide the source, but crystallisation P-T conditions of these magmas. Instead, we look at bulk magma chemistry to estimate source conditions.

MagMaTaB

MagMaTaB is a model derived from experimental data that uses machine learning to estimate source pressure and temperature from the bulk composition of a magma and its associated phase assemblage (Weber and Blundy, 2024). MagMaTaB estimates for the La Soufrière lava and dyke samples range from 0.33 – 0.74 GPa and 1034 – 1087 ºC, with uncertainties of ± ≤ 0.3 GPa and ± ≤ 48 ºC. Results for only one of the mafic crater lava samples are reported due to filtering for high standard deviation. This mafic crater lava gives a higher P-T estimate of 0.89 ± 0.3 GPa and 1217 ± 72 ºC (Table 3.2). Roseau lava STV_LS_167 and crater lava STV_LS_6 give the next highest pressure and temperature estimates of ~ 0.7 GPa and 1070 ºC, though are within error of all other lava and dyke samples. Applying the MagMaTaB thermobarometer to two high-magnesium basalts considered as possible parent melts to the La Soufrière basaltic andesite magmas (STV301 and RSV49; Heath et al., 1998a; Robertson 2002), finds P-T estimates closer to the mafic crater lava at 0.84 GPa and 1220ºC (STV301) and 0.92 GPa and 1245ºC (RSV49; Figure 3.10), with uncertainties of ± 0.4 GPa and ± 90ºC. The experimentally derived sources of these magmas are deeper and slightly cooler at 1.3 – 1.6 GPa and ~ 1180ºC for wet melts (4.5 wt. % H_2O; Pichavant et al., 2002a; Melekhova

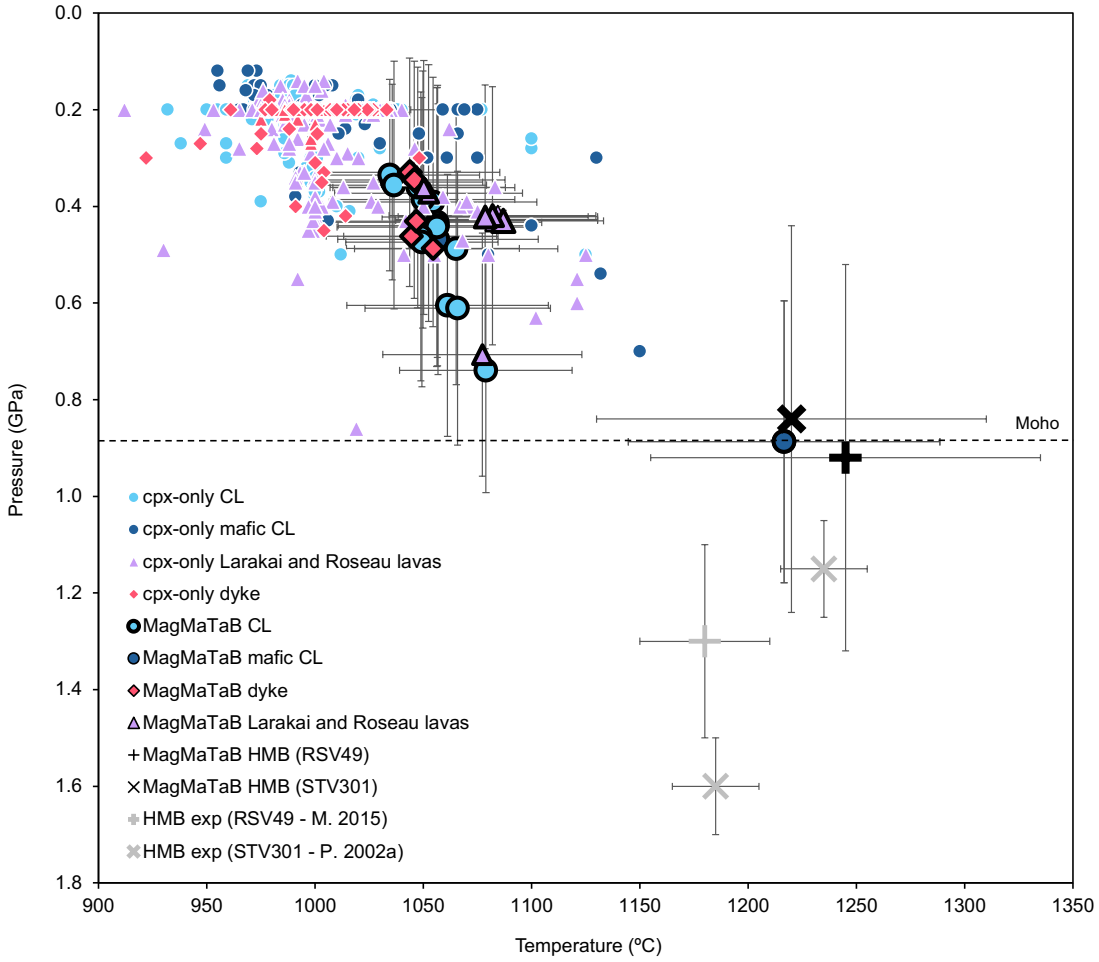


Figure 3.10: Pressure and temperature estimates of lavas and dykes using whole-rock thermobarometry (MagMaTaB; Weber and Blundy, 2024) and clinopyroxene-only thermobarometry (Higgins et al., 2022). Whole-rock thermobarometry estimates of source pressures and temperatures for high-magnesium basalts (HMB) are also shown (compositions STV301 from Heath et al., 1998a and RSV49 from Robertson, 2002), along with experimentally derived source P-T conditions (Pichavant et al., 2002a; Melekhova et al., 2015). Moho is shown at 29 km depth from Schlaphorst et al. (2018), calculated to be ~ 0.87 GPa from crustal densities identified by Melekhova et al. (2019)

et al., 2015), and 1.1 GPa and 1235ºC for melts with 1.5 wt. % H_2O (Pichavant et al., 2002a), providing a more accurate estimate with considerably lower uncertainty.

3.4.2 Oxybarometry

Co-existing magnetite and ilmenite pairs provide temperature and fO_2 estimates for erupted magmas (Buddington and Lindsley, 1964; Lepage, 2003). The ilmenites identified in the mafic crater lavas are present only as exsolution lamellae, thus

calculated temperature and fO_2 values are not representative of magmatic conditions and instead provide the T-fO_2 conditions experienced during exsolution, as Fe-Ti oxides are known to rapidly re-equilibrate (Venezky and Rutherford, 1999; Hou et al., 2021). Temperature estimates are low at 877 – 888 ºC ± 59 ºC and give fO_2 estimates, relative to the Ni-NiO buffer (NNO), of NNO-0.47 to NNO+0.04 (± 0.17; Table 3.2). Oxygen fugacities close to the NNO buffer for the basaltic mafic crater lavas agree with previous estimates for St. Vincent primitive basaltic magmas (Heath et al., 1998a; Melekhova et al., 2015). Ilmenite is identified as a microphenocryst inclusion within a clinopyroxene xenocryst in lower Larikai lava STV_LS_102, and as a microphenocryst in a glomerocryst cluster in Roseau lava STV_LS_154, giving fO_2 estimates of NNO+0.34 and NNO+0.22 respectively. Basaltic andesite magmas have previously been estimated at NNO+2.3 to +4.3 (Melekhova et al., 2015), however the xenocryst inclusion could represent deeper more reducing conditions. The presence of ilmenite only as an exsolution phase or microphenocryst precludes it's use as a reliable oxybarometer here.

3.4.3 Complex crystal cargo of La Soufrière magmas

High-An plagioclase

Two populations of plagioclase core compositions are identified (Figure 3.4a). All lavas and dykes contain high An plagioclase cores (≥ An_{85}) and just over half of the samples contain a lower An core population (An_{55} to An_{75}), similar to the composition of plagioclase rims. High anorthite plagioclase (≥ An_{85}) is typical in Lesser Antilles arc magmas (Arculus and Wills, 1980) and found to form at very wet conditions (e.g. ≥ 6 wt. % H_2O; Panjasawatwong et al., 1995; Pichavant et al., 2002b). The calcium content of plagioclase is strongly dependent on water concentrations (Sisson and Grove, 1993a), such that at high H_2O contents more Ca partitions into plagioclase forming higher An plagioclase. Anorthite content is also dependent on temperature (Cashman and Blundy, 2013), with lower An plagioclase forming at lower temperatures. However, the change in

An content from temperature decrease alone (considered to be small as magmas are assumed to ascend almost adiabatically (Wilson and Head, 1981; McKenzie, 1985; Couch et al., 2003)) is minor compared to the decrease in An content brought on by degassing during decompression. Figure 3.4a illustrates that calculated An values of plagioclase in equilibrium with bulk magma compositions (i.e. whole rock composition of the host magma) with 6 – 10 wt. % H_2O (dark grey) are in very good agreement with natural high-An core compositions (light blue). This supports early plagioclase crystallisation, when the melt water content is high and the bulk rock is close to fully molten. The second population of plagioclase cores with lower An contents are instead in equilibrium with bulk magma compositions with ~ 2 wt. % H_2O (Baker and Eggler, 1987; Sisson and Grove, 1993a), recording a second stint of crystallisation after degassing and perhaps upon water saturation driven crystallisation (Cashman and Blundy, 2000; Hammer and Rutherford, 2002; Annen et al., 2006; Waters et al., 2015). Rim compositions of high and low An cores extend down to ~ An_{50} to An_{60}, in agreement with growth from magmas experiencing H_2O loss (Frey and Lange, 2011).

Some of the low-An cores exhibit reverse zoning, a consequence of decompression (Nelson and Montana, 1992) or an increase in temperature by mafic recharge and magma mixing (Streck, 2008). Bennett et al. (2019) use plagioclase TiO_2 contents in cores and rims to distinguish between reverse zoning caused by decompression or magma mixing. The consistent TiO_2 contents in reversely zoned plagioclases reported in this study (Table S3.1; appendix) adhere to decompression driven reverse zoning, along with their resorbed nature. Sieve texturing is abundant in crystal cores and/or rims (Figure 3.2) in all plagioclase populations, thus is interpreted to signify rapid decompression (Nelson and Montana, 1992; Cashman and Blundy, 2013) rather than magma mixing (Tsuchiyama, 1985; Humphreys et al., 2006b) as all crystal types exhibit similar textures. Resorbed plagioclase cores are observed in all lava and dyke samples,

usually in crystals ≥ 500 μm. Some of these crystals also display patchy cores due to resorption during decompression (Vance, 1969).

Relict crystals from parent magma

Olivine compositions are mostly in agreement with Kd estimates from bulk magma compositions (Figure 3.4d). However, there are a small population of phenocrysts that have very high Fo contents (≥ Fo_{85}), more Mg-rich than Kd estimates (except for the mafic crater lavas which have a Kd range of Fo_{83} to Fo_{89}), and higher than xenolith (≤ Fo_{80}) and micro-xenolith (≤ Fo_{85}; Figure 3.8) olivine compositions. High-Fo olivines phenocrysts (higher than xenolith compositions) have previously been observed on St. Vincent (Heath et al., 1998a; Pichavant and Macdonald, 2007), Bequia (Camejo-Harry et al., 2018) and Grenada (Parkinson et al., 2003; Stamper et al., 2014a) and are considered to be relict from more primitive parent melts (Thirlwall and Graham, 1984). High-Fo olivines with ≤ 0.1 wt. % CaO have also been suggested as crystals from mantle xenoliths (Pichavant and Macdonald, 2007), however more recent studies suggest forsterite contents ≥ Fo_{90} as well as ≤ 0.07 wt. % CaO are required for a mantle source (De Hoog et al., 2010; Johnson, 2014). The possibility that these high-Fo crystals are derived from parent magmas is therefore explored further. Using the high-magnesium basalts identified by Melekhova et al. (2015) as parent magmas to the erupted basaltic andesites on St. Vincent, olivine compositions calculated to be in equilibrium with these parent melts range from Fo_{88} to Fo_{92}. These values agree with the anomalously high-Fo olivines identified in the samples studied here (Figure 3.4d), suggesting they are likely antecrysts left over from deeper parent melts. High-Fo olivines all display significant breakdown and resorption textures supporting disequilibria in more evolved melt compositions (e.g. Figure 3.2f).

A small number of lavas, different to those with high-Fo olivine, contain a second Mg-rich clinopyroxene core population (≥ $Mg\#_{82}$). These Mg-rich cores are at the upper end

or above Mg# estimates from Kd equilibrium calculations (Figure 3.4b). Xenolith clinopyroxenes extend up to $Mg\#_{80}$ and only the recrystallised micro-xenoliths reach compositions of $Mg\#_{88}$, thus are not the source of the Mg-rich cores due to distinct textural differences. Clinopyroxene compositions calculated to be in equilibrium with the high-magnesium basaltic parent melt (as described above) range from $Mg\#_{88}$ to $Mg\#_{94}$, too high for the Mg-rich cores observed in the La Soufrière basaltic andesite magmas. The Mg-rich core population could have instead formed from other genetically related melts in the St. Vincent magmatic system such as low-magnesium basalts, also derived from the high-magnesium basalt parent melt (e.g. STV315; Pichavant and Macdonald, 2007; Melekhova et al., 2015). Low-magnesium basalts are calculated to be in equilibrium with clinopyroxenes with compositions between $Mg\#_{83}$ and $Mg\#_{90}$., overlapping with observed values. The high Mg# clinopyroxene cores in the samples studied here are all large euhedral crystals up to ~ 2 mm in size, often cracked and containing inclusions, but do not display significant breakdown textures suggesting they did not experience considerable disequilibrium.

Two high Mg# orthopyroxenes are identified, one in the mafic crater lava ($Mg\#_{84}$) and the other in the ~ 25 ka old crater lava ($Mg\#_{77}$; Figure 3.4c), both of which also contain relict olivine. These high Mg# compositions are in agreement with estimated Kd equilibrium values however are anomalous to the general orthopyroxene population and display extensive dissolution and resorption textures. In hydrous magmas, orthopyroxene usually joins the crystallising assemblage late as it is unstable at high water contents (Gaetani et al., 1994; Pichavant et al., 2002b; Grove et al., 2003). Lower Mg# values than Kd estimates are therefore typical as crystallisation tends to occur after olivine and clinopyroxene have depleted the melt in MgO, making the high Mg# orthopyroxenes anomalous. Orthopyroxene compositions calculated to be in equilibrium with the high-magnesium basaltic parent melt have higher Mg#'s compared to in the basaltic andesites ($Mg\#_{88}$ to $Mg\#_{93}$), though late-stage crystallisation after olivine and clinopyroxene could

result in lower Mg# orthopyroxene. Xenoliths only contain orthopyroxene with compositions up to $Mg\#_{72}$, and micro-xenoliths up to $Mg\#_{73}$. Some meta-igneous xenoliths on Petit St. Vincent have previously been found to contain $Mg\#_{84}$ orthopyroxene (Melekhova et al., 2022), suggesting a deep arc material source.

Some of the high-An plagioclase crystals previously interpreted as forming at hydrous conditions (see above) have An values above estimated equilibrium values (e.g. ≥ An_{93}; Figure 3.4a) and exhibit extensive resorption and dissolution textures. These crystals may therefore also be antecrystic. The high-magnesium basaltic parent melt is calculated to be in equilibrium with plagioclase compositions of An_{93} to An_{96} at high melt water contents, thus could have formed the very high-An plagioclases observed. Distinguishing between relict plagioclases from the parent melt and disaggregated xenolith material, which are also anorthite rich (An_{90} to An_{96}; Figure 3.5) is difficult and would require further work such as trace element or isotopic analysis (e.g. Davidson et al., 2007b; Shane et al., 2019).

Breakdown textures

Olivine has a narrow stability field in low-magnesium basaltic andesite melts such as those frequently erupted at La Soufrière (Pichavant et al., 2002b; Mercer and Johnson, 2008). This is reflected in the ubiquity of olivine disequilibria textures and the observation that olivine only comprises a small fraction of the phenocryst population when present. All olivines have fine to coarse reaction rims, indicative of changes in P-T-X conditions after crystallisation (Coombs and Gardner, 2004; Andújar et al., 2017). Olivine reaction rim thickness has previously been found to be a function of melt water contents, with higher water contents facilitating olivine dissolution and increasing rim growth (Coombs and Gardner, 2004). At decreasing pressures olivine reacts with the melt to form orthopyroxene (Grove and Baker, 1984), the dominant reaction rim phase. Coarse recrystallised rims often also contain Fe-Ti oxides, clinopyroxene and plagioclase (e.g.

Figure 3.2e), as found previously (Reagan et al., 1987). Some olivines are also rimmed with iddingsite (e.g. Figure 3.2f), a product of low temperature oxidising reactions, usually in the presence of fluids (Edwards, 1938; Evans et al., 2017; Camejo-Harry et al., 2024a). The occurrence of iddingsitised olivine in xenoliths at St. Vincent (Brown, 2022) and neighbouring islands (Stamper et al., 2014a; Camejo-Harry et al., 2018; Melekhova et al., 2019), suggests this process may occur within the crust and not just upon eruption at the Earth's surface. These abundant reaction textures support an early crystallisation of olivine followed by instability during ascent through the crust.

A small number of clinopyroxene crystals (~ 2 – 4 mm in length) in the lava and dyke samples display significant breakdown textures including resorption, sieve texturing, and rimming with plagioclase, Fe-Ti oxides and orthopyroxene (e.g. Figure 3.2h). Such clinopyroxenes are identified in the lower Larikai lavas STV_LS_100 and 103, lower Larikai dyke STV_LS_107 and upper Larikai dyke STV_LS_132. Compositionally these clinopyroxenes are similar to the main phenocryst population ($Mg\#_{70}$ to $Mg\#_{81}$) but texturally indicate considerable disequilibrium in the host melt composition and point towards an antecrystic origin (Streck, 2008). The previously identified high Mg# clinopyroxenes (discussed above) are also considered antecrystic and relict from the deeper St. Vincent magmatic system, but are not resorbed, suggesting erupted magmas contain at least two different clinopyroxene antecryst populations.

Orthopyroxene phenocryst cores with clinopyroxene rims as seen in Figure 3.2d are identified in five crater lava samples (STV_LS_8, 10, 11, 46 and 47) and have previously been noted in La Soufrière magmas (Heath et al., 1998a). Clinopyroxene either entirely surrounds the original orthopyroxene crystal or is present on two sides of the orthopyroxene crystal parallel to the c-axis, sometimes referred to as epitaxic growth (Tarney, 1969; Nicholls and Stout, 1997). Previous studies suggest such textures reflect changes in P-T-H_2O conditions resulting in the dissolution of orthopyroxene and

subsequent nucleation of clinopyroxene (Pan et al., 2022; Johnston and Draper, 1992), or early orthopyroxene crystallisation (at high pressures and dry conditions) followed by shallower clinopyroxene crystallisation (Tarney, 1969). In the crater lavas discussed here, orthopyroxene cores appear resorbed with clinopyroxene mantling the entire interior crystal, and Fe-Ti oxides, plagioclase and olivine sometimes appearing on the rim. Interestingly, not all orthopyroxene crystals in these crater lava samples display such overgrowth rims suggesting the existence of two orthopyroxene populations, though Mg# values are the same in both. Further work is required to understand the origin of the numerous orthopyroxene, clinopyroxene, olivine and plagioclase populations.

Glomerocrysts

Glomerocrysts are crystal clusters that either form in a process known as synneusis, whereby crystals 'drift' together and nucleate on each other (Vance, 1969); or represent fragments of the crystalline mush entrained in melts (Hogan, 1993; Camejo-Harry et al., 2018; Zellmer, 2021). Evidence for the synneusis of plagioclase crystals is observed in all lava and dyke samples by the joining of crystals along euhedral crystal faces, joining of resorbed crystals, overgrowths around multiple cores of crystals and inclusions of smaller plagioclase crystals within larger crystals and continued growth around them (e.g. Figure 3.2a; Vance, 1969; Hogan, 1993). Such textures support early crystallisation in a melt-rich magma. The larger monomineralic glomerocrysts and polymineralic glomerocrysts observed in the samples studied here display mainly interlocking or adjoined crystals that protrude into the groundmass (Figure 3.3a, b), interpreted as nucleation and growth from the host magma rather than entrained fragments of disaggregated mush (Seaman, 2000; Bennett et al., 2019). The lack of spiney and radiating glomerocrysts in La Soufrière magmas further suggests glomerocrysts did not form during rapid disequilibrium crystallisation at shallow magmatic conditions (Bennett et al., 2019; McCarthy et al., 2020). Glomerocryst compositions agree with those of

phenocrysts supporting growth from the melt. Some glomerocrysts contain high Fo olivine and high Mg# clinopyroxene and orthopyroxene, indicating that antecrysts may have provided points of nucleation for newly growing crystals.

3.4.4 Micro-xenolith assemblages as a proxy for arc crust compositions

Micro-xenoliths identified in recent magmas erupted from La Soufrière are mostly gabbroic in composition and contain plag ± cpx ± opx ± ol ± ox (Table 3.1; Fedele et al., 2021). Unlike previously identified xenoliths at St. Vincent (Lewis, 1973; Rowley, 1978; Robertson, 2002; Tollan et al., 2012), these micro-xenoliths contain almost no amphibole, little olivine, and considerably more orthopyroxene. The new micro-xenoliths could represent a different region of the arc crust not previously sampled or could suggest that the crust is changing in composition over time. Both of these hypotheses are explored below.

Xenoliths erupted from neighbouring islands to St. Vincent display different mineral assemblages and compositions (Stamper et al., 2014a; Camejo-Harry et al., 2018; Melekhova et al., 2019), reflecting the lateral variation in the composition of the arc crust, over distances less than 20 km south of La Soufrière in some cases (e.g. Bequia; Camejo-Harry, 2018). Xenolith assemblages are therefore assumed to vary over such distances vertically, often exemplified by the range of xenolith compositions erupted at a single volcanic centre (e.g. Tollan et al., 2012). Micro-xenolith compositions identified in this study extend to higher Mg# clinopyroxene and higher Fo olivine than previously erupted xenoliths (Figure 3.6 and 3.8). Oxide compositions in micro-xenoliths are also in better agreement with mineral compositions observed in the lava and dyke samples, with higher Fe^{3+} and Fe^{2+}#'s (Figure 3.9), than previous xenoliths. These different compositions could reflect entrainment from different locations within the crust, at different P-T-X-H_2O conditions. Micro-xenoliths have also been observed in other arc

settings, including the Chilean Andes, and are interpreted to represent recycled cumulates from the deep plutonic roots, due to large high-Fo olivines with healed micro-fractures (Dungan and Davidson, 2004). These Chilean micro-xenoliths contain olivine, plagioclase and clinopyroxene; amphibole is absent from the assemblage even though amphibole-rich cumulates are known to dominate in the subsurface beneath the Tatara-San Pedro complex (Costa et al., 2002), as in St. Vincent. The lack of amphibole in micro-xenoliths suggests formation at conditions where amphibole is not stable, for example at low pressure and water content or at high temperatures (Eggler, 1972; Krawczynski et al., 2012; Mandler and Grove, 2016).

The arc crust is likely a dynamic environment (Sparks et al., 2019), where variations in temperature and percolating melts and volatiles can result in melting and recrystallisation (Bachman and Bergantz, 2006; Cooper, 2019, Liao, 2023). Such activity is often evidenced by the textures and compositions observed in xenoliths, such as clinopyroxene breaking down to amphibole or olivine to orthopyroxene (Erdmann et al., 2014b; Cooper et al., 2016; Brown, 2022). Tollan et al. (2012) attributed the presence or absence of amphibole in St. Vincent xenoliths to changes in water contents in the source region. Additionally, oxidation state controls mineral stability (e.g. Feig et al., 2010), with previous studies identifying a decrease in the oxidation state of the young arc crust in the southern Lesser Antilles (~ 2 Ma) compared to the old arc (~ 30 – 68 Ma; Rojas-Agramonte et al., 2017). However, the young age of St. Vincent (≤ 2.74 Ma) places all magmatism during the more oxidised period.

Three of the new micro-xenoliths identified here display recrystallisation textures suggesting they have experienced changes in P-T-H_2O conditions and are instead meta-igneous. Meta-igneous xenoliths have previously been interpreted as fragments of the deeper arc crust that have experienced significant reworking (Melekhova et al., 2022;

Camejo-Harry et al., 2024a). Such textures within micro-xenoliths further attest to the wide range of crystal cargo entrained in magmas and erupted at La Soufrière.

3.4.5 Crystallisation history of La Soufrière basaltic andesite magmas

The basaltic andesite magmas erupted at La Soufrière were previously estimated to be generated in the lower crust (0.7 – 1 GPa, 1050ºC) by differentiation of hydrous primitive high-magnesium basalts (Melekhova et al., 2015). Whole-rock thermobarometry results for the basaltic andesites studied here overlap with previous source pressure and temperature estimates and find natural basaltic andesite magmas to have originated between 0.4 – 0.7 GPa and ~ 1050 – 1075ºC (Figure 3.10). The mafic crater lavas have higher estimated source pressures and temperatures of ~ 0.9 GPa and ~ 1220ºC, closer to the high-magnesium basalts, supporting its more primitive composition. As discussed in the previous chapter, the generated basaltic andesite magmas have trace element concentrations that indicate chemical differentiation from a parent magma. Further evidence for derivation from a parent magma includes the presence of relict minerals in erupted magmas. High-Fo olivine cores that are too Mg-rich to be in equilibrium with basaltic andesite melts or from xenoliths, are instead proposed to have formed from high-magnesium basaltic parent melts and remained present in differentiated magmas. High Mg# clinopyroxene cores are found to be in equilibrium with low-magnesium basaltic magma compositions also derived from the high-magnesium basaltic parent magmas (Melekhova et al., 2015). The small fraction of these relict cores within erupted magmas are not considered significant enough to alter the whole-rock composition of the original melt.

The identification of two discrete plagioclase phenocryst core compositions (Figure 3.4a) suggests magmas may have experienced two main episodes of crystallisation. Plagioclase is often found on or close to the liquidus in basaltic andesite magmas, along

with Fe-Ti oxides (Pichavant et al., 2002b; Pertermann and Lundstrom, 2006; Mercer and Johnson, 2008; Rader and Larsen, 2015), resulting in the crystallisation of high An plagioclase early on when melt water content is still high. Olivine and clinopyroxene stability are relatively unaffected by melt water content, thus join the crystallising assemblage when they become saturated. High-Fo olivine inclusions within high-An plagioclase crystals in the mafic crater lava and crater lava STV_LS_45 suggest early olivine crystallisation. Olivine in other samples is often inclusion free or contains small oxide minerals, in accordance with oxides saturating on the liquidus. Early olivine crystallisation is also evidenced by its breakdown to form orthopyroxene at lower pressures (Grove and Baker, 1984). Plagioclase is often found as an inclusion phase within clinopyroxene and orthopyroxene minerals suggesting later crystallisation of pyroxenes.

A second stage of plagioclase crystallisation, inferred from a population of low An cores, likely occurred at lower water contents after degassing at shallower pressures, and possibly upon interaction with the water saturated liquidus (Annen et al., 2006; Applegarth et al., 2013; Waters et al., 2015). Orthopyroxene is only stable at low water contents, therefore joining the crystallising assemblage late (Gaetani et al., 1994), reflected in its low Mg#'s (Figure 3.4c). All minerals display signs of decompression and resorption, though these are more significant in plagioclase and olivine crystals pointing towards their earlier crystallisation. Clinopyroxene-only thermobarometry suggests magmas mostly begin crystallising clinopyroxene at pressures of ~ 0.4 – 0.5 GPa, but that the majority of crystallisation occurs at ~ 0.2 GPa, where such magmas would be water saturated if they contain ≥ 5 wt. % H_2O at 1050ºC (Ghiorso and Gualda, 2015).

In general, the lavas and dyke samples studied here have broadly similar mineral compositions and textures. Interestingly, relict olivines are only found in the older lavas from Larikai and Roseau valley, as well as the mafic and old crater lava units. This could

be a sampling bias due to the heterogeneity within each thin section or could indicate that older and deeper lavas contain more material remnant from parental magmas. Crater lava unit STV_LS_5a dated at ~ 25 ka is distinguishable from the much younger crater lavas by the presence of high Fo olivine, higher Mg# clinopyroxene and orthopyroxene, and an abundance of minerals displaying breakdown textures (Figure 3.2). These observations support the idea that this lava could represent a different period of La Soufriere's eruptive history (as suggested in chapter 2). However, no textural data exist for the previously sampled pre-Somma lavas for comparison. The dykes presented in this study tend to display a more restricted compositional range than the lavas and have abundant low An plagioclase core compositions, reflecting a more rapid ascent and shallow crystallisation.

3.5 Conclusions

La Soufrière has continuously erupted basaltic andesite magmas throughout its lifetime, with little variation in composition. The erupted basaltic andesite magmas explored here contain phenocrysts, antecrysts, xenocrysts and glomerocrysts of broadly the same composition and displaying similar textural features. Plagioclase is the dominant crystal phase, followed by clinopyroxene, orthopyroxene, Fe-Ti oxides and olivine. Core mineral compositions are generally in equilibrium with the bulk magma, suggesting that it was initially a liquid at the point of separation from its source. An exception is orthopyroxene that is often Mg-poor compared to calculated equilibrium compositions, interpreted as a result of late-stage crystallisation of orthopyroxene. Two populations of plagioclase core compositions are identified (≥ An_{85} and An_{55} to An_{75}) and suggest two stages of crystallisation at high (6 – 10 wt. %) and low (~ 2 wt. %) water contents, the latter ascribed to degassing driven crystallisation.

The crystal cargoes in erupted basaltic andesite magmas reflect their ascent path from source to surface. Relict minerals are identified in a number of magmas and attributed to crystallisation from parent high-magnesium basalts or genetically related low-magnesium basalts, supporting polybaric fractionation from a parent magma. Erupted basaltic andesite magmas also contain micro-xenoliths with opx-rich and amph-poor mineral assemblages different to previous xenoliths. These are interpreted to represent regions of the arc crust beneath St. Vincent not previously sampled. Some micro-xenoliths display recrystallisation textures suggesting sampling of the deeper reworked arc crust (Melekhova et al., 2022; Camejo-Harry et al., 2024a). The low volume of antecrystic material identified in samples is not considered significant enough to impact overall bulk magma compositions.

Whole-rock thermobarometry estimates indicate that the basaltic andesite magmas erupted at La Soufrière are sourced from pressures of ~ 0.4 – 0.7 GPa at temperatures of ~ 1040 – 1090ºC. The mafic crater lavas are sourced from slightly higher pressures and temperatures of ~ 0.9 GPa and 1220ºC. Parental high-magnesium basaltic magmas appear to have been sourced from the sub-arc mantle, based on experimental data (Pichavant et al., 2002a; Melekhova et al., 2015). The large uncertainty associated with whole-rock barometry estimates reinforces the need for a more precise geobarometer applicable to magmas not saturated in olivine, chrome-spinel or hornblende, for which well-calibrated models already exist. Clinopyroxene thermobarometry gives overall much shallower pressure estimates, interpreted as crystallisation conditions rather than where magmas are generated. The basaltic andesite magmas erupted at La Soufrière are therefore found as liquids in the lower crust via differentiation from a high-magnesium, mantle-derived basaltic parent magma and experience similar crystallisation histories during their ascent through the crust.

Chapter 4

Experimentally-determined lower-crustal origin of calc-alkaline basaltic andesite magmas from La Soufrière volcano, St. Vincent, Lesser Antilles.

4.1 Introduction

Identifying the origin and evolution of erupted magmas helps constrain locations of melt accumulation in the crust or mantle prior to eruption, improves our understanding of the crustal structure beneath volcanoes, and aids the interpretation of crustal processes at such volcanoes. Arc volcanoes can erupt a wide range of magma compositions, from basalts to andesites to rhyolites, of both calc-alkaline and tholeiitic descent. Yet individual volcanic centres often erupt a more restricted compositional range of magmas, despite lifetimes on the order of hundreds of thousands to millions of years (Grove and Donnelley-Nelson, 1986; Schmidt and Grunder 2011; Brophy, 1991; Dufek and Bachmann, 2010; Melekhova et al., 2013). Volcanic centres that produce magmas of very similar composition throughout their entire lifetime include: Arenal, Costa Rica (Streck et al., 2005; Parat et al., 2014); Calbuco, Chile (Mixon et al., 2021); Klyuchevskoy, Kamchatka (Melekhova and Blundy, 2024), North Sister and Mt. Rainier, Cascades (Mercer and Johnson, 2008; Schmidt and Grunder, 2011; Sisson et al., 2014) and La Soufrière, St. Vincent (Heath et al., 1998a). Magma chemistry has been proposed to reflect the mineralogy of the crystal-rich crustal mush from which these melts are

sourced (Blundy 2022). To test this hypothesis, I use La Soufrière volcano, St. Vincent, as an example of a volcano erupting magmas of very similar basaltic andesite composition throughout its history, straddling the calc-alkaline-tholeiitic trendline, and as a location where the crustal structure is well-studied from erupted xenoliths (Lewis, 1973; Tollan et al., 2012; Fedele et al., 2021) and seismology (Schlaphorst et al., 2018; Melekhova et al., 2019; Camejo-Harry et al., 2024b). By performing high-pressure, high-temperature experiments at crustal conditions and comparing results to natural xenolith assemblages and compositions, this study explores whether the erupted basaltic andesite magmas at La Soufrière, St. Vincent are true liquids, and thus determine their origin and genesis, or if these magmas instead represent chemically modified liquids that experienced fractionation, mixing or assimilation after segregating from their source. The inverse experimental approach used to find liquidus multiple saturation for crustal igneous rocks offer a novel magma source thermobarometer and hygrometer.

4.1.1 Multiple saturation

Primary magmas thought to represent true liquids that form by the partial melting of mantle source rocks (e.g. peridotite; Kushiro, 1973; Tatsumi et al., 1983; Wyllie, 1984) without subsequent chemical evolution, are rare in volcanic arcs. Instead, most arc magmas show evidence for chemical differentiation within the crust through processes such as fractional crystallisation, crustal assimilation, magma mixing and reactive flow of melt through crystal-rich mushes (Green, 1971; McBirney, 1980; Grove et al., 2002; Lissenberg et al., 2018; Clemens and Stevens, 2012; Jackson et al., 2018; Stock et al., 2020). Consequently, an erupted magma is the time-integrated product of such processes operating within its crustal source region. Once a parcel of melt detaches from its source and ascends rapidly to the surface, however, the scope for further chemical modification, beyond simple degassing of volatile species, is limited. Hence there is a relationship between the chemistry of an erupted magma and the conditions in its source

region prior to segregation. In the case of tracing melts back to their source, this can be achieved by identifying whereabouts in P-T-fO_2-H_2O space the melt last equilibrated with its source rock, by performing inverse multiple saturation experiments (Asimow and Longhi, 2004; Blatter et al., 2017; Becerra-Torres et al., 2020; Melekhova and Blundy, 2024). The same concept can be applied to melts erupted from within the crust, provided that they represent true liquids, meaning they have not experienced magma mixing, assimilation or stalling; and the crustal composition is known (Wyllie, 1984; Blundy 2022).

Some volcanoes bring to the surface abundant fragments of the underlying crust as xenoliths, providing insight into the crustal composition. The Lesser Antilles volcanic arc is known for its plentiful occurrence of crustal xenoliths (e.g. Lewis, 1973; Arculus and Wills, 1980), which can be used to reconstruct crustal structure and composition (e.g. Cooper et al., 2016, 2020; Melekhova et al., 2019, 2022; Camejo-Harry et al., 2024b). Typical xenolith assemblages erupted from St. Vincent include olivine- and hornblende-gabbros, clinopyroxenites, and troctolites (Tollan et al., 2012), providing the source rock mineralogy that erupted melts (if true liquids) last equilibrated with. Multiple saturation experiments on these erupted compositions, and comparison to xenolith assemblages can be used to determine the source conditions, and hence depth, of such melts.

The concept of multiple saturation stems from the Gibbs phase rule (Equation 4.1), where the degree of freedom (F), or variance, in a system, is a function of the number of chemical components (c), phases (p) and fixed parameters (e.g. pressure, temperature, water contents).

$$F = c - p + 2 \qquad \text{(Equation 4.1)}$$

In a system of *n*-components and 2 fixed terms, *n+2* phases results in invariance (no degrees of freedom). For *n+1* phases, the system is univariant (one degree of freedom), and for *n* phases the system is divariant (two degrees of freedom; Zen, 1966).

In a system with relatively low thermodynamic variance, the conditions at which a melt last equilibrated with the mush prior to eruption can be reduced to an invariant point (or univariant line) on the liquidus of the melt in P-T- fO_2-H_2O space. The number of major oxide components in a natural magmatic system is typically eleven (SiO_2-MgO-Al_2O_3-TiO_2-FeO-Fe_2O_3-CaO-K_2O-Na_2O-H_2O-CO_2). However, natural magmas do not occupy this entire compositional space, such that the *effective* number of components can be reduced to five or six by principal components analysis (Weber and Blundy, 2024). Projecting natural magmatic compositions into a reduced component space is a well-known principle in igneous petrology (e.g. O'Hara, 1968; Walker et al., 1979; Grove et al., 1982). In a six-component, volatile-saturated system, comprising of melt plus fluid plus five mineral phases (e.g. plag + cpx + amph + mt + ilm + melt + fluid), the thermodynamic variance is one. Given independent constraints on FeO/Fe_2O_3 (from oxygen fugacity) the system becomes invariant. Thus, saturation of five mineral phases at the liquidus of a magma defines the P-T point of last equilibration within an H_2O-CO_2 fluid-saturated mush source region consisting of those minerals. This is sometimes referred to as the multiple saturation point (MSP), although the term MSP is more commonly used to define a low variance region rather than a singular point.

4.1.2 Calc-alkaline and tholeiitic evolutionary trends

Magmas are regularly classified by their major element chemistry (e.g. total alkali versus silica). Those with high alkali contents (Na_2O + K_2O) are termed alkalic (Iddings, 1892; Miyashiro 1978), whilst those with lower alkali contents are sub-alkalic, and further divided into calc-alkaline (Fe-depleted) and tholeiitic (Fe-enriched). Miyashiro (1974) originally distinguished between the two trends by comparing the ratio of total iron to magnesium contents (FeO*/MgO) with silica contents (SiO_2 wt. %); calc-alkaline magmas becoming more silica enriched as they evolve, whereas tholeiitic magmas see little change in silica contents but increase in FeO*/MgO. The origin of the calc-alkaline

and tholeiitic divide is still widely debated. Fe-depletion or enrichment is thought to be a consequence of tectonic setting (Gill, 1981; Kay et al., 1982; Kelley and Cottrell, 2012; Chin et al., 2018; Muth and Wallace, 2021; Chen et al., 2023); magma source composition, fractional crystallisation and magma mixing (Grove and Baker 1984; Grove and Kinzler, 1986; Matthews et al., 1994; Kawamoto, 1996; Grove et al., 2012); water content and oxygen fugacity (Osborn 1959; Sisson and Grove, 1993a; Pichavant et al., 2002b; Berndt et al., 2005; Feig et al., 2006; Zimmer et al., 2010; Nandedkar et al., 2014; Waters et al., 2021). Typically, mid-ocean ridge basalts are more primitive, have low water contents, are more reducing and produce tholeiitic magmas; whereas subduction zone magmas tend to be more evolved, experience crustal contamination and mixing, contain high water contents, are more oxidised and produce primarily calc-alkaline magmas, though some also produce tholeiitic magmas (Wood et al., 1990; Carmichael, 1991; Parkinson and Arculus, 1999; Kelley and Cottrell, 2009, 2012; Zimmer et al., 2010; Evans and Tomkins, 2011, 2021; Brounce et al., 2014; Richards, 2015).

La Soufrière, St. Vincent is just one example of an arc volcano that produces both calc-alkaline and tholeiitic magmas (Heath et al., 1998a; Pichavant et al., 2002b; Pichavant and Macdonald 2007), with others including those in Japan (Miyashiro, 1974; Fujinawa, 1988, 1990; Hunter and Blake 1995), the Aleutians (Kay et al., 1982; Zimmer et al., 2010), and the Cascades (Baker et al., 1994; Blatter et al., 2013). The co-existence of both differentiation trends at such volcanoes has been attributed to heterogeneous source water contents and oxidation states (Baker et al., 1994), variable sediment input (Parkinson and Arculus, 1999; Richards et al., 2015), arc maturity (Miyashiro, 1974; Chen et al., 2023) and intracrustal processes (Hunter and Blake, 1995; Kelley and Cottrell, 2012). All of these processes contribute to the Fe-depletion or Fe-enrichment of a magma, ultimately controlling calc-alkaline versus tholeiitic differentiation. Here, in addition to searching for liquidus multiple saturation, I also explore the role of oxidation

state as a control on the calc-alkaline and tholeiitic evolutionary trends observed in the La Soufrière basaltic andesite magmas.

4.1.3 Previous basaltic andesite experiments

Basaltic andesite magmas are common eruption products for volcanoes worldwide, notably in volcanic arcs. Experimental studies on the phase relations of basaltic andesites have previously explored temperatures in the range 900 – 1350ºC, 0.1 MPa to 2 GPa, water contents up to 10 wt. % H_2O and oxygen fugacities between NNO-1 and NNO+4 (e.g. Gaetani et al., 1994; Pichavant et al., 2002b, 2018; Moore and Carmichael, 1998; Pertermann and Lundstrom, 2006; Mercer and Johnson, 2008; Almeev et al., 2013; Rader and Larsen, 2013; Andújar et al., 2015, 2017; Erdmann et al., 2016; Melekhova et al., 2017; Melekhova and Blundy, 2024). Plagioclase, clinopyroxene and magnetite are ubiquitous liquidus phases, with the presence of olivine, orthopyroxene and amphibole dependent on starting composition and experimental conditions. Basaltic andesites with high magnesium contents (≥ 5 wt. % MgO) tend to crystallise olivine at or close to the liquidus (e.g. Moore and Carmichael, 1998; Weber et al., 2012; Almeev et al., 2013; Melekhova and Blundy, 2024); whereas starting compositions with < 5 wt. % MgO find olivine either to be a sub-liquidus phase (Pichavant et al., 2002b; Andújar et al., 2017; Melekhova et al., 2017) or absent from the crystallising assemblage (Pertermann and Lundstrom, 2006; Rader and Larsen, 2013). Oxidation state, water contents and pressure also appear to play a role in the stability of olivine (Feig et al., 2006, 2010; Friese et al., 2009; Andújar et al., 2017). Orthopyroxene tends to crystallise below the liquidus, reflecting its generally low abundance in basaltic andesite magmas. Amphibole is commonly found as a sub-liquidus phase, dependent on water content and temperature (e.g. Foden and Green 1992; Juriček and Keppler, 2023; Melekhova and Blundy 2024).

Previous multiple saturation experiments on basaltic andesite magmas found such melts to have last equilibrated with a narrow range of source assemblages. For example, at Klyuchevskoy, Kamchatka, erupted basaltic andesite magmas are multiply saturated with a lherzolite assemblage (ol + cpx + opx + sp) at 1220 – 1240ºC, 0.6 – 1 GPa, with 3 wt. % H_2O (Melekhova and Blundy 2024); basaltic andesites at Mt Pelée, Martinique, are multiply saturated with an amphibole-olivine gabbro assemblage (plag + cpx + mt + amph + ol) just below the liquidus (74% melt) at 0.4 GPa, 1000ºC and with 6.8 wt. % H_2O (Pichavant et al., 2002b); and, although not multiply-saturated experimentally, basaltic andesites of North Sister volcano, Cascades, are inferred to have last equilibrated with an augite-gabbro (plag + cpx ± mt ± ol ± amph) at 1.2 GPa, 1175ºC, with 3 wt. % H_2O (Mercer and Johnson, 2008). Basaltic andesites thus may form at varying depths within the crust. Experimental studies exploring the phase relations of basaltic andesite melts with similar compositions to La Soufrière basaltic andesites are presented in Table 4.1 and discussed throughout this chapter.

4.1.4 St. Vincent magmas

Previous experimental studies identified the source of primitive high-magnesium basalts erupted from St. Vincent to be in the mantle, at 1.0 – 1.6 GPa, 1160 – 1240ºC, with 1.5 – 4.5 wt. % H_2O and at oxygen fugacities between NNO+1 to NNO+2.3 (RSV49, Melekhova et al., 2015; STV301, Pichavant et al., 2002a; Pichavant and Macdonald, 2007). Basaltic andesites, formed by differentiation of these primitive magmas, are the most frequently erupted magma composition at St. Vincent (Tomblin, 1975; Cole et al., 2019; Fedele et al., 2021).

Geophysical studies highlight the variation in crustal structure beneath the Lesser Antilles arc, and the distribution of faulting and fractures along the arc (Schlaphorst et al., 2018, 2021; Bie et al., 2020; Cooper et al., 2020; Braszus et al., 2021). Beneath St.

Vincent, the Moho lies at approximately 29 km depth (Schlaphorst et al., 2018), with crustal densities estimated between 2.88 to 3.93 g/cm^3 (Melekhova et al., 2019). Heightened seismic activity during the 2020-2021 eruption at St. Vincent (Joseph et al., 2022; Camejo-Harry et al., 2024b; Contreras-Arratia et al., 2024), found earthquake epicentres to extend down to the lower crust (17 ± 2.5 km depth), with the majority of earthquakes clustering at depths of ≤ 5 km. Modelled pre- and syn- eruptive Mogi source depths, from GPS and InSAR deformation data, are estimated at 18 ± 1.9 km and 6 ± 0.5 km respectively (Camejo-Harry et al., 2024b).

4.1.5 Petrology

The basaltic andesite magma produced during both the effusive and explosive stages of the 2020-2021 eruption at La Soufrière, St. Vincent contain phenocrysts of plagioclase (26 vol%), orthopyroxene (8 vol. %), clinopyroxene (6 vol. %) and Fe-Ti oxides (5 vol. %), with rare olivine (0.6 – 2 vol. %; Weber et al., 2024). This phenocryst assemblage is typical for historical St. Vincent juvenile eruption products (Graham and Thirlwall, 1981; Heath et al., 1998a; Robertson, 2002; Cole et al., 2019; Fedele et al., 2021). Plagioclase phenocrysts (An_{48} to An_{96}) are prevalent, appearing euhedral and normally zoned. Clinopyroxene phenocrysts are euhedral with zoning to lower Mg contents at the rim (e.g. $Mg\#_{73}$ core to $Mg\#_{66}$ rim) and contain 0.6 – 5.8 wt. % Al_2O_3. Fe-Ti oxides are often present as inclusions within other minerals. Different Fe-Ti oxide populations have previously been identified (Robertson, 2002; Melekhova et al., 2015) including both cubic oxides (magnetite-spinel) and rhombohedral oxides (ilmenite-hematite), a common feature of island arc magmas (Barnes and Roeder, 2001). Fe-Ti oxides in explosive eruption products appear homogenous, whilst those in effusive material display exsolution textures (Morrison-Evans et al., 2024), due to different cooling histories. Orthopyroxene varies in abundance in juvenile material and is often considered a late crystallising phase, hence is found to only be in equilibrium with clinopyroxene rims

(Graham and Thirlwall, 1981; Weber et al., 2024). Olivine appears as sub-anhedral grains, often as remnant cores (e.g. Fo_{82} core and Fo_{62} rim), or with symplectitic reaction rims (Joseph et al., 2022; Morrison-Evans et al., 2024; Camejo-Harry et al., 2025). The majority of these olivines are antecrystic or xenocrystic as they are not in equilibrium with the melt and show strong disequilibria textures (Weber et al., 2024; Camejo-Harry et al., 2025). The low volume fraction of antecrystic or xenocrystic olivine is considered small enough to not impact the bulk composition of the liquid. In the more magnesian basaltic (pre-Somma) lavas, olivine is more abundant (up to 30 vol%; Heath, 1997; Robertson 2002), forming euhedral to subhedral grains with some zoning and a high forsterite content (≥ Fo_{87}). The higher volume of olivine reflects the higher magnesium contents of these magmas and suggests that earlier volcanism on St. Vincent tapped a more primitive, olivine-bearing source.

Eruption temperature estimates for the 2020-2021 eruption range from ~ 960 – 1020ºC using plagioclase-liquid; clinopyroxene-liquid, and two-pyroxene thermometry (Putirka 2005, 2008; Weber et al., 2024). Previous oxybarometry estimates for basaltic magmas on St. Vincent find oxidation states to be a few log units above the nickel-bunsenite reference buffer determined using the Ballhaus et al. (1991) olivine-orthopyroxene-spinel oxybarometer (NNO to NNO+1; Heath et al., 1998a; Pichavant et al., 2002a, Pichavant and Macdonald, 2007) and using the mineral-melt vanadium oxybarometer (NNO+1.8; Erdmann et al., 2024). Previous basaltic andesite estimates are slightly more oxidised at NNO+2.3 to NNO+4.3 (Melekhova et al., 2015). In the previous chapter magnetite-ilmenite pairs are used to calculate oxygen fugacity, however ilmenite is only present as an exsolution phase or microphenocryst inclusion, thus the results are not considered representative of true magmatic T- fO_2 conditions. The experimental fO_2 used here is instead based on previous estimates (~ NNO+2; Melekhova et al., 2015).

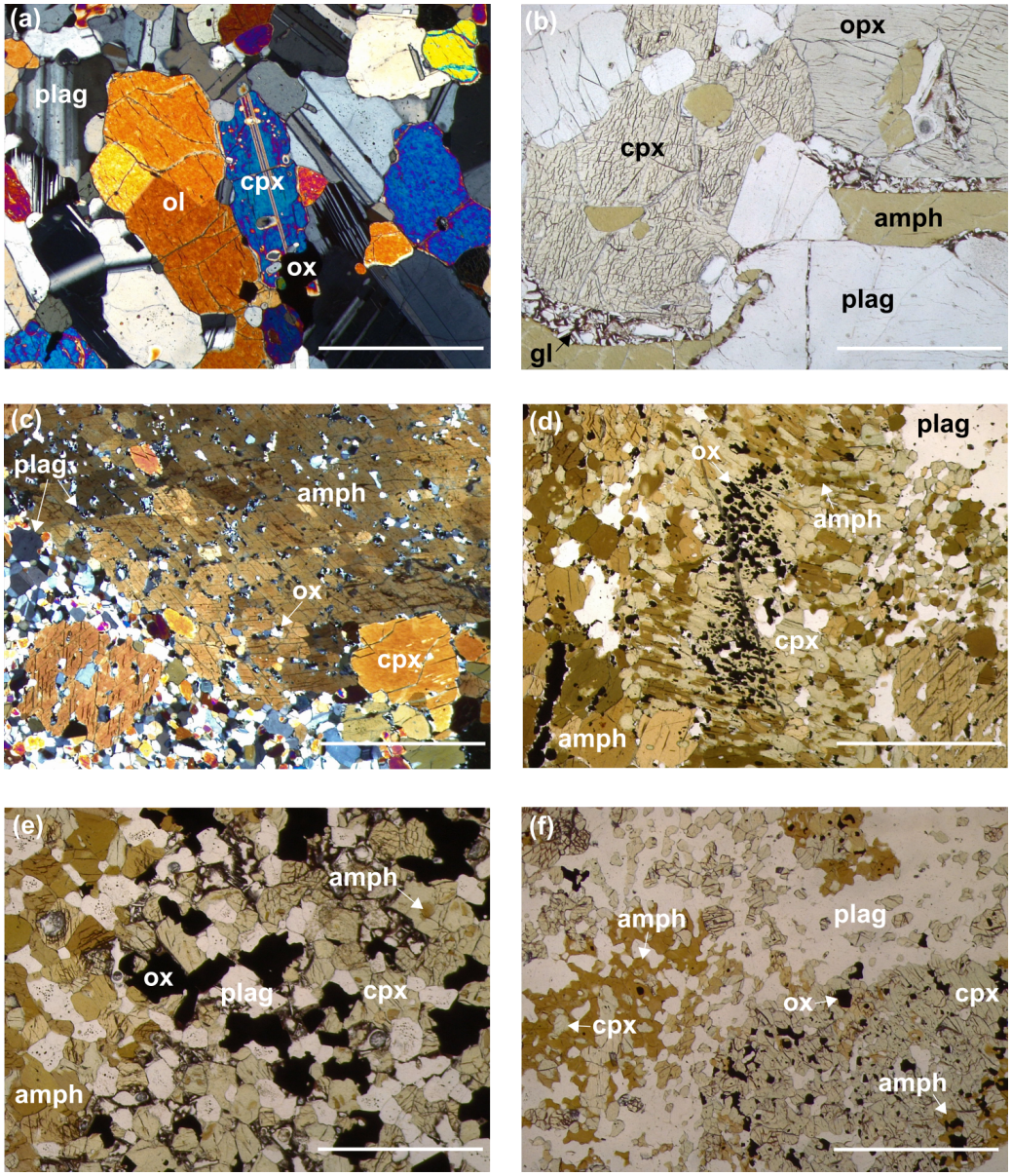


Figure 4.1: Photomicrographs of xenoliths from St Vincent. **(a)** Olivine-gabbro with adcumulate texture. (STV_LS_31; XPL). **(b)** Hornblende-gabbro with mesocumulate texture due to the presence of interstitial glass. Hornblende is only present as an inclusion or interstitial phase (STV_LS_12; PPL). **(c)** Hornblende-gabbro with heteradcumulate texture. Hornblende oikocryst containing chadacrysts of plagioclase, clinopyroxene and an oxide phase. Matrix comprised of granoblastic plagioclase, clinopyroxene and oxides (STV_LS_29; XPL). **(d)** Hornblende-gabbro with granoblastic texture. Clinopyroxene and oxide core with amphibole present towards the rim. Hornblende oikocrysts also present. (STV_LS_29; XPL). **(e)** Banded hornblende-gabbro with mesocumulate texture. Layer 1 is comprised of plagioclase, clinopyroxene and oxides, and layer 2 contains predominantly plagioclase and hornblende, both with some interstitial glass. (STV_LS_32; PPL). **(f)** Hornblende-gabbro with granoblastic adcumulate texture. Clinopyroxene displays clear dissolution textures. Unstable clinopyroxene oikocryst reacting to form plagioclase and amphibole in the bottom right. Amphibole oikocryst growing in the middle-left. (STV_LS_36; PPL). Scale bar is 1 mm. Abbreviations include ol - olivine, plag - plagioclase, cpx - clinopyroxene, opx - orthopyroxene, amph - amphibole, ox - Fe-Ti oxide, gl - glass.

4.1.6 Xenoliths

Xenoliths are common in the Lesser Antilles arc (Arculus and Wills, 1980) and have previously been used to constrain the underlying crustal structure (Tollan et al., 2012; Schlaphorst et al., 2018; Melekhova et al., 2019). Olivine and amphibole-gabbros, containing plagioclase, clinopyroxene, magnetite, olivine and/or amphibole, are the most common xenolith lithologies at St. Vincent (Figure 4.1; Melekhova et al., 2019). Orthopyroxene is rare in St. Vincent xenoliths, although more recent studies have identified a greater presence of orthopyroxene in micro-xenoliths entrained in both scoria (Fedele et al., 2021) and lava samples (discussed in Chapter 3).

Plagioclase is ubiquitous in St. Vincent xenoliths; its highly calcic composition ($\geq An_{85}$) is characteristic of the Lesser Antilles (e.g. Lewis, 1973; Tollan et al., 2012; Camejo-Harry et al., 2018; Cooper et al., 2016). Plagioclase appears euhedral, with little zoning, and often displays equilibrium triple junction grain boundaries (Figure 4.1a). Clinopyroxene has high magnesium contents ($\geq Mg\#_{70}$), and often contains inclusions of other mineral phases (Figure 4.1b). When amphibole is present, co-existing clinopyroxene tends to display dissolution and recrystallisation textures (Figure 4.1d-f; and Brown, 2022), suggesting a reaction relationship. Magnetite is often found closely associated with another mineral phase (e.g. clinopyroxene; Figure 4.1f) and sometimes forms in clusters or bands (Figure 4.1e).

Olivine and amphibole abundances vary in St. Vincent xenoliths, resulting in the formation of both olivine/amphibole-free and olivine/amphibole-bearing varieties (Tollan et al., 2012; Melekhova et al., 2019). Although olivine is rare as a phenocryst phase at La Soufrière, it is a common xenolith phase, occurring as subhedral cumulate grains or as inclusions, with Fo_{71} to Fo_{79} (Tollan et al., 2012; Fedele et al., 2021), and little variation within each sample. Amphiboles are predominantly hornblende and typically appear as

a poikilitic or interstitial phase, or on the rim of clinopyroxene (Figure 4.1c-f; Brown, 2022). As in many volcanic arcs, amphibole is only found in xenoliths at St. Vincent and does not appear in lavas. Cryptic fractionation, whereby amphibole is consumed during differentiation, is often used to explain the abundance of amphibole in cumulates, yet absence as a phenocryst phase in lavas (Davidson et al, 2007a; Smith, 2014). Peritectic reactions involving amphibole and a combination of clinopyroxene, olivine or orthopyroxene, have previously been explored through detailed petrological analyses of cumulates and exhumed arc rocks (Ban et al., 2005; Dessimoz et al., 2012; Erdmann et al., 2010, 2012; Klaver et al., 2017; Wang et al., 2019; Brown, 2022); and phase equilibria experiments (Holloway and Burnham, 1972; Cawthorn and O'Hara, 1976; Foden and Green, 1992; Médard et al., 2006; Blatter et al., 2017). Amphibole stability is primarily dependent on temperature, water content, pressure and to some extent oxygen fugacity (Eggler, 1972; Gilbert et al., 1982; Allen and Boettcher, 1983; Krawczynski et al., 2012; Mandler and Grove, 2016, Juriček and Keppler, 2023). The dominance of amphibole in the crust is thought to be key in understanding the magmatic differentiation processes and, ultimately, the composition of the continental crust (Dessimoz et al., 2012; Smith, 2014; Klaver et al., 2017).

Trace element studies on xenoliths from St. Vincent and Martinique (Cooper et al., 2016; Brown, 2022) found elevated REE and incompatible trace element levels in interstitial amphibole compared to poikilitic and reaction rim amphibole. REE patterns in amphibole are often similar to those in clinopyroxene but elevated, suggesting that interstitial amphibole grew after an influx of new melt, but poikilitic and reaction rim amphibole grew by a peritectic reaction between clinopyroxene and residual melt (Brown, 2022; Melekhova et al., 2022). Similar trace element signatures have been reported for other cumulate amphiboles (e.g. Nisyros, Greece; Klaver et al., 2017).

A recent collection of much smaller xenoliths (micro-xenoliths) found entrained within scoriacious material from St. Vincent (≤ 1 – 2 cm; Fedele et al., 2021), contain predominantly gabbroic assemblages. Plagioclase, clinopyroxene and magnetite are common, with olivine and orthopyroxene also present. Unlike the previously described xenoliths, little to no amphibole is found in these micro-xenoliths. Xenoliths provide insight into the composition of the underlying crystal mush, with different mineral assemblages forming at different P-T-fO_2-H_2O conditions. The presence of orthopyroxene in these micro-xenoliths, and lack of amphibole, suggests they could be sampling a different part of the crust where orthopyroxene is stable relative to amphibole.

Xenoliths can also be used to provide estimates of the oxidation state of the mantle and crust and have been used to establish the more oxidising nature of subduction zones compared to mid-ocean ridges (Wood et al., 1990; Parkinson and Arculus, 1999; Chin et al., 2018). Peridotite xenoliths from Grenada find the mantle source beneath the Lesser Antilles arc to extend up to FMQ +3 (~ NNO+4; Parkinson et al., 2003).

4.1.7 Melt inclusions

Melt inclusions capture the composition of quenched liquids within the crust, therefore the most primitive melt inclusions represent possible true liquids before, for example, any fractionation. Melt inclusions can form at any stage in the magmatic cycle, from the source region to the surface. They may also occur in xenocrysts. The only requirement is that the host mineral was crystallising at that stage. Phenocryst-hosted melt inclusions (MI) from St. Vincent capture liquids from basalts to rhyolites (Figure 2.3). The more evolved melts contain elevated potassium and sodium contents (0.7 – 1.8 wt. % K_2O; 4 – 6 wt. % Na_2O; Figure 2.4d,e), although MI's with sodium contents ≤ 2 wt. % Na_2O possibly show sodium loss to a fluid phase (e.g. Blundy et al., 2008). The composition of a basaltic population of melt inclusions from Bouvier et al. (2008) lie close to those of

erupted magmas, albeit with slightly lower SiO_2 (42 – 48 wt. % SiO_2; Figure 2.4a) and higher CaO (≥ 12 wt. % CaO; Figure 2.4b). Such high calcium contents are thought to be due to interactions with Ca-rich lithologies (e.g. amphibole-bearing; Bouvier et al., 2008). Many of the less evolved melt inclusions match erupted magma compositions, suggesting that erupted magmas could represent true liquids (Heath et al., 1998a).

Volatile concentrations in St. Vincent melt inclusions range from 0.9 to 5.3 wt. % H_2O and ≤ 3230 ppm CO_2, with the more evolved melts containing the lowest water contents (e.g. 0.9 wt. % H_2O at 75 wt. % SiO_2 versus 5.3 wt. % H_2O at 65 wt. % SiO_2; Bouvier et al., 2008, Cooper et al., 2020; Balcone-Boissard et al., 2023; Metcalfe et al., 2023) indicative of degassing, probably due to decompression accompanying crystallisation.

4.2 Methods

4.2.1 Starting materials

The starting material used in this study is a synthetic equivalent of the basaltic andesite magma from the 2020-2021 La Soufrière effusive eruption, collected from the exterior of the growing lava dome on January 11th 2021 (SV2021; Table 4.1). Both hydrous and dry starting compositions were synthesised using a mixture of oxides (MgO, SiO_2, Al_2O_3, TiO_2, MnO, Fe_2O_3) carbonates (Na_2CO_3, $CaCO_3$, K_2CO_3), calcium phosphate ($Ca_3(PO_4)_2$), aluminium hydroxide ($Al(OH)_3$) and fayalite (Fe_2SiO_4). Oxides (except Fe_2O_3), carbonates and phosphates were dehydrated, ground together under ethanol, and decarbonated before iron species and aluminium hydroxide were added. Hydrous and dry starting compositions are reported in Table 4.1. Aluminium hydroxide provided a source of structurally bound water, up to 3 wt. % H_2O, for hydrous starting compositions, allowing water contents to remain consistent from run to run. For higher water contents (≥ 4 wt. % H_2O), deionised H_2O was pipetted into the capsule with a micro-syringe.

Table 4.1. Experimental starting compositions

	St. Vincent 2020-2021	sd	SV2021_dry	sd	SV2021_a 2.5 wt. % H_2O	sd	SV2021_b 3 wt. % H_2O	sd	St Kitts KS_BR1	Martinique 031-22b	Costa Rica AR	Cascades CNM	Ecuador TUNG-PS-51B	St. Vincent RSV49
SiO_2	55.70	0.12	54.76	0.41	54.94	0.16	54.62	0.19	54.96	53.42	54.35	53.39	58.51	47.59
TiO_2	1.03	0.01	1.01	0.05	1.05	0.03	1.06	0.02	0.96	0.79	0.60	1.14	0.89	0.75
Al_2O_3	18.12	0.09	18.80	0.09	18.08	0.12	17.87	0.14	18.46	19.15	18.82	19.83	16.74	14.53
FeO	8.49	0.12	8.02	0.32	8.23	0.09	8.38	0.14	8.68	8.92	8.51	7.62	6.84	8.99
MnO	0.21	0.00	0.23	0.02	0.21	0.04	0.19	0.04	0.25	0.17		0.09	0.15	0.16
MgO	3.80	0.08	3.90	0.04	4.13	0.10	4.22	0.08	3.96	4.27	5.11	5.39	4.18	14.61
CaO	8.53	0.07	8.98	0.13	8.83	0.08	8.98	0.10	8.60	9.68	9.01	8.47	7.20	10.77
Na_2O	3.39	0.04	3.49	0.09	3.73	0.11	3.90	0.11	3.56	2.81	3.00	3.53	3.53	2.29
K_2O	0.59	0.01	0.63	0.03	0.66	0.04	0.64	0.03	0.49	0.68	0.60	0.54	1.76	0.24
P_2O_5	0.14	0.00	0.19	0.02	0.14	0.05	0.16	0.03	0.08	0.11			0.21	0.08

All analyses normalised to 100% anhydrous

St. Vincent 2020-2021 dome analysed by X-ray fluorescence (Weber et al., 2024)

SV2021_dry starting material fused at 1300ºC for 30 minutes at 1 atm. Analysed by electron microprobe (epma) at the University of Bristol, average of 3 analyses.

SV2021_a and SV2021_b wet starting materials are glass averages from runs BA_StV_21 and 23, respectively, see appendix.

KS_BR1 from Melekhova et al., 2017

031-22b from Pichavant et al., 2002b

AR from Petermann and Lundstrom, 2006

CNM from Mercer and Johnson, 2008

TUNG-PS-51B from Andujar et al., 2017

RSV49 from Melekhova et al., 2015.

The oxygen fugacity of erupted basaltic andesite magmas are estimated to be at least NNO+2 (see section 4.1.5; Melekhova et al., 2015). Hematite (ferric iron) and fayalite (ferrous iron) were added to the starting material in the correct ferric to ferrous (Fe^{3+}/Fe^{2+}) ratio to achieve an oxidation state close to NNO+2, calculated for a melt at 900ºC using the Kress and Carmichael (1991) model. The starting material was stored in the oven at 150ºC to limit water absorption from the atmosphere. Dehydration of aluminium hydroxide in the form of gibbsite begins at ~ 150ºC (Mercury et al., 2006), until complete dehydration at ~ 300ºC (Du et al., 2009), thus the hydrous starting material contains slightly lower H_2O than calculated gravimetrically.

4.2.2 One atmosphere experimental setup

The dry synthetic powder (SV2021) was mixed with PVA glue as a binder and loaded onto thin (0.25 mm) platinum (Pt) wire loops. Pt-loops were pre-saturated with iron by running an initial experiment at 1300ºC and NNO; the wire was then recovered and re-used for subsequent experiments. In total fifteen successful experiments were performed (Table S4.1), with two runs that constrain the dry liquidus reported in Table 4.2. Experiments were run in a vertical box furnace and air quenched. Oxygen fugacity was set using a CO_2-CO gas mix (Deines et al., 1976) and calibrated using an yttria-doped zirconia probe and the Nernst equation (Boulliung et al., 2020). Temperature was set with a Eurotherm temperature controller and calibrated to the melting point of gold using a type-B thermocouple at the furnace hotspot. Charges were lowered into the hot zone of the furnace and run for the desired duration. Experiments run at temperatures ≤ 1000ºC were initially held at 1300ºC (above the liquidus) for 30 minutes to glass the synthetic powder and reduce the amount of unreacted starting material; the temperature was then lowered to the desired set point. Temperature cycling was employed to increase crystal growth over nucleation (Mills and Glazner, 2013) in lower temperature runs. For

runs with low melt fractions, only the phase assemblage is reported as glass pools were too small to analyse (Table S4.1).

4.2.3 Piston cylinder experimental setup

The majority of experiments (BA_StV_1 to BA_StV_75; Table 4.2) were performed in $Au_{80}Pd_{20}$ capsules, and the double capsule technique (Figure 4.2a) employed to maintain the run oxygen fugacity at or close to NNO+2, by minimising hydrogen diffusion through the capsule walls (Kagi, 2005). Fe-loss to the capsule wall is not considered a problem at wet, oxidising conditions (Kawamoto and Hirose, 1994), as explored in this study. Analyses of Fe content in the capsule walls confirms this and are discussed in section 4.3.4. The inner capsule (2 mm OD, $Au_{80}Pd_{20}$) was filled with starting material (± added water), welded shut and pressed into a cylinder. The capsule was weighed, submerged in acetone, and re-weighed to check that the capsule was completely sealed (Ulmer et al., 2018). The outer capsule (4 mm OD, $Au_{80}Pd_{20}$) was then filled with the same ratio of starting material to water as the inner capsule. The inner capsule was placed vertically in the centre of the outer capsule, welded shut, pressed into a cylinder, and the acetone check repeated. All welded capsules were stored in the oven prior to experiments.

A sub-series of controlled fO_2, water-saturated experiments were performed using Co-CoO, Ni-NiO and Re-ReO_2 solid metal buffers. Au capsules were used for experiments < 1000ºC, and $Au_{80}Pd_{20}$ capsules for experiments ≥ 1000ºC (Table 4.3). Inner Au or $Au_{80}Pd_{20}$ capsules (2mm OD) were filled with the dry starting material (SV2021) and ~ 14 wt. % initial H_2O to ensure water saturation. For runs at Co-CoO and Re-ReO_2, the metal and metal oxide powders were mixed in molar ratio and added (with water) to the outer capsule (4mm OD), along with the inner capsule containing the starting material. For runs at Ni-NiO, the Ni and NiO powders were mixed in a 60:40 ratio, respectively, and added (with water) to an inner Pt capsule (2mm OD), following the setup of Marxer

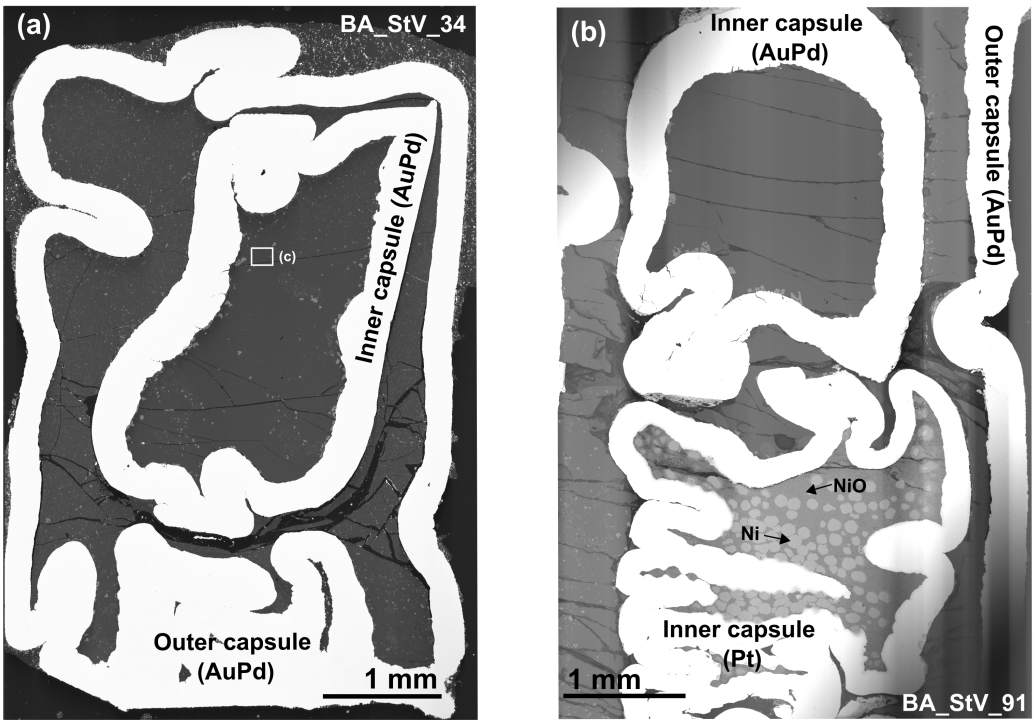


Figure 4.2: Backscattered electron images (BSE) of experimental setups. **(a)** Inner and outer $Au_{80}Pd_{20}$ capsules containing basaltic andesite starting material in double capsule setup after Kagi et al. (2005). **(b)** One inner $Au_{80}Pd_{20}$ capsule containing the basaltic andesite starting material and the second inner Pt capsule containing Ni-NiO buffer material. Both inner capsules are inside an outer $Au_{80}Pd_{20}$ capsule filled with the basaltic andesite starting material as a filler media after Marxer et al. (2022).

et al. (2022) and Matjuschkin et al. (2015). The higher proportion of Ni metal powder allows for some alloying of the Ni metal with the Pt capsule. The inner capsules containing the starting material and Ni-NiO buffer were placed in an outer capsule (Au or $Au_{80}Pd_{20}$, 4mm OD), filled with additional starting material as the spacer media (Figure 4.2b; Marxer et al., 2022), and the same water content as the inner capsule. Capsules were prepared and checked for holes as described above.

Experiments were performed at pressures of 0.2 – 0.9 GPa and temperatures of 980-1180ºC, using end-loaded piston cylinder apparatus at the University of Oxford. A ¾" setup (19.1 mm) was used for experiments at 0.2 – 0.35 GPa, and a ½" setup (12.7 mm) for experiments at 0.5-0.9 GPa. The ¾" set-up was calibrated using the NaCl-melting curve and water solubility in albite (Masotta et al., 2012). A pressure correction of –3 %

(McDade et al., 2002) was applied to all ½" experiments. Temperatures were controlled using type-C thermocouples (W_{95}-Re_5 – W_{74}-Re_{26}) for the ½" setup and type-B thermocouples (Pt_{70}-Rh_{30} – Pt_{94}-Rh_6) for the ¾" setup and in the controlled-fO_2 experiments, to reduce the chances of oxidation of the thermocouple. Temperatures are expected to lie within ± 10ºC of the pre-set temperature at the centre of the assembly (Holtz, 2001) and are reported as the thermocouple temperature reading.

For the ¾" setup, crushable MgO and pressed Pyrex were used as pressure media around the capsule within the graphite furnace. Capsules were positioned vertically in the hot zone of the furnace to minimise the thermal gradient. For the ½" setup, crushable MgO only was used as the pressure medium. Alumina spacers between the top of the capsule and upper MgO prevented piercing of the capsule by the thermocouple. Pyrex cylinders and NaCl sleeves were placed around the graphite furnaces for all experiments (Condamine et al., 2022). Steel plugs were used for ½" experiments and brass plugs for ¾" experiments, to create a softer assemblage that better grips the thermocouple tubing and reduces the chances of thermocouple oxidation and failure.

Assemblies were pressurised to half the target psi or 400 psi, whichever higher, for a minimum of 2 hours. The 'hot piston-in' technique was used for all experimental runs. Experiments were quenched isobarically at the end of the run. A series of cooling experiments were performed by reducing the output power (OP) over the course of the run duration to explore sub-liquidus reactions. Partial oxidation of the thermocouple and its subsequent failure in these runs required temperatures to be calculated from the corresponding operating power (OP; Table S4.5) and, where possible, mineral thermometry.

4.2.4 Analytical methods

Experimental run products were mounted in epoxy, polished and analysed using the Cameca SX-5 FE electron microprobe at the University of Oxford. Experimental glasses were analysed with a defocused beam (5 – 20 μm spot size depending on the size of glass pools) at an accelerating potential of 15 kV and a beam current of 4 nA. Silicate minerals and oxides were analysed with a focused beam (1 – 2 μm) at 15 kV and 10 nA. Na and K were analysed first, with lower counting times (20s rather than 30s) to reduce alkali loss. All secondary standards are reported in the appendix (Table S4.2).

In all double-capsule experiments (Table 4.3), Fe, Au and Pd were analysed in the inner capsule wall, adjacent to the silicate melt of the inner capsule, to determine fO_2 (see section 4.3.4; Barr and Grove, 2010). Iron was measured on two spectrometers, to increase counting times, due to the low abundance of Fe in the $Au_{80}Pd_{20}$ capsule walls (e.g. 0.04 wt. % Fe; Table S4.3). Capsules were measured with an accelerating potential of 15 kV, a beam current of 100 nA and a 1 μm spot size. Profiles were setup in both the horizontal and vertical capsule walls, with measurements starting 15 – 20 μm from the capsule wall and silicate melt interface, and ending in the glass in the inner capsule. The composition of the capsule wall was measured at ~ 1 – 2 μm intervals. Secondary fluorescence from Fe in the glass occurred only in measurements close to the silicate melt-capsule wall interface, thus only measurements ≥ 10 μm from the interface are used for calculating fO_2.

Glasses from 28 experimental run products were analysed for H_2O and CO_2 using Secondary Ion Mass Spectrometry (SIMS) at the NERC ion microprobe facility, University of Edinburgh. Volatiles were measured using the Cameca IMS-7f GEO instrument with a primary beam of $^{16}O^-$ ions, at 5 nA, 18 kV, and a spot size of 10 μm (as described in Wieser et al., 2022). Basalt (0 – 7 wt. % H_2O) and andesite (7.6 wt. % H_2O)

standards were used for H_2O and CO_2 calibrations. A non-linear H_2O calibration was applied (Table S4.6). Although CO_2 was not added to the starting materials, carbon diffusion into the capsule is inevitable during piston cylinder experiments (Stamper et al., 2014b; Brooker et al., 1998) hence the presence of analysed CO_2 in all run product glasses.

Phase proportions for each run were calculated by weighted least-squares regression (Albarede and Provost, 1977). Assessment of the goodness of fit is reported as the sum of square of residuals. Ferric iron in the melt was calculated using the Kress and Carmichael (1991) model at the experimental conditions. Volatiles by difference (vbd) were estimated using the revised total that includes ferric and ferrous iron. Vbd estimates are compared to SIMS measurements in the following section. Ferric iron contents in Fe-Ti oxides and amphibole were determined using charge balance and stoichiometry and are reported in the appendix (Table S4.4).

4.3 Experimental results

Two one-atmosphere experiments and forty-six piston-cylinder equilibrium experiments are presented in Table 4.2; five controlled fO_2 experiments in Table 4.3; and seven cooling experiments in Table 4.4. Melt and mineral chemistry data are reported in the appendix (Table S4.4). Experimental run conditions, phase assemblages and water contents calculated 'by difference' ($H_2O_{diff.}$), and from SIMS (H_2O_{SIMS} and CO_2), are reported in Tables 4.2 to 4.4. Water calculated using the 'by difference' method and measured by SIMS are in very good agreement (e.g. ≤ 1 wt. % H_2O average absolute difference). Oxygen fugacity is calculated using the Barr and Grove (2010) oxybarometer in all runs in AuPd capsules. Fe-Ti oxide pairs in experimental runs where both phases are present were also used to estimate fO_2 (Lepage et al., 2003).

Table 4.2. Experimental run table organised by water contents and increasing pressure

Run #	P	T	$H_2O_{initial}$	t	Phase assemblages	$\sum R^2$	H_2O (wt. %)	sd	H_2O (wt. %)	sd	CO_2 (ppm)	sd	aH_2O	ΔNNO (ILMAT)		ΔNNO (B&G 2010)				*An*	*Fe-loss*	*Na-loss*
	(GPa)	(°C)	(wt. %)	(hrs)			diff.		SIMS		SIMS			Avg	sd	Max	Min	Avg	sd		(%)	(%)
Dry																						
SV23	0.0001	1225	0	1	gl (94), plag (6), ox (tr)	0.32	0													72	*4.0*	*-2.2*
SV24	0.0001	1245	0	1	gl (100), ox (tr)	0.05	0														*0.0*	*0.5*
~ 1-2 wt. % H_2O																						
BA_StV_56	0.3	1020	6.0	24	gl (58), plag (29), cpx (9), sp (4)	0.05	0.77	0.55					0.1			1.7	1.4	1.6	0.1	*55*	*0.4*	*-4.5*
BA_StV_48	0.35	1080	4.5	24	gl (91), plag (9), mt (tr)	0.10	1.89	0.35	1.32	0.01	244	33	0.2			1.0	0.9	1.0	0.1	*73*	*1.0*	*-4.4*
BA_StV_52	0.35	1050	4.5	20	gl (60), plag (34), cpx (3), mt (3)	0.39	1.69	0.53					0.2			1.5	1.1	1.3	0.1	*62*	*0.7*	*0.2*
BA_StV_71	0.35	970	10.6	21	gl (42), plag (43), cpx (10), mt (4), ilm (1)	0.77	1.65	0.55					0.2			0.4	-0.2	0.1	0.2	*51*	*0.8*	*7.8*
~ 2-3 wt. % H_2O																						
BA_StV_59	0.2	1020	6.2	24	gl (81), plag (17), mt (2)	0.22	2.41	0.70	2.32	0.16	424	74	0.4			1.2	0.7	0.9	0.2	*68*	*0.4*	*-3.0*
BA_StV_21[a]	0.35	1150	2.5	6	gl, v	0.46	2.70	0.56	2.54	0.02	1599	18	0.5			0.9	0.7	0.8	0.1		*-3.6*	*8.5*
BA_StV_26[b]	0.35	1100	3	6	gl (99), mt (tr), v	0.33	3.62	0.39	2.89	0.02	1634	3	0.5			2.2	1.4	1.8	0.3		*0.0*	*4.2*
BA_StV_24[a]	0.35	1140	2.5	11	gl (98), mt (2)†, v	0.31	3.27	0.39	2.94	0.02	1744	14	0.4			1.3	1.2	1.2	0.1		*-0.2*	*7.1*
BA_StV_5[a]	0.6	1150	2.5	21	gl (75), plag (20), cpx (4), mt (1), v	0.35	2.01	0.34					0.2			1.4	1.3	1.3	0.1	*60 (70)*	*0.4*	*2.8*
BA_StV_3[a]	0.6	1100	2.5	14	gl (89), plag (11), mt (tr), v	0.22	3.30	0.44	2.59	0.10	2822	29	0.4			1.4	1.0	1.3	0.1	*66*	*0.3*	*4.1*
BA_StV_1[a]	0.6	1050	2.5	24	gl (44), plag (34), cpx (12), sp (7), mt (3), ilm (tr), v	0.03	2.80	0.56					0.4	2.28	0.11	1.3	0.5	0.9	0.4	*52*	*0.0*	*-4.8*
BA_StV_23[b]	0.6	1130	3	13.5	gl, v	0.89	3.57	0.38	2.89	0.04	2979	41	0.4			2.5	1.9	2.2	0.3		*-2.8*	*14.8*
BA_StV_74	0.6	1040	7.5	17	gl (72), plag (18), cpx (5), mt (3), ilm (2), v	0.49	2.83	0.42					0.3			2.4	1.4	1.8	0.3	*71*	*0.7*	*-14.3*
BA_StV_6[a]	0.8	1170	2.5	18	gl (90), plag (10), v	0.19	1.82	0.47	2.03	0.09	3115	119	0.2			1.7	1.5	1.6	0.1	*63*	*-1.6*	*3.1*
BA_StV_18[b]	0.8	1180	3	6	gl, v	0.46	2.72	0.42	2.37	0.10	4598	136	0.2			2.5	2.1	2.2	0.2		*0.8*	*7.4*

BA_StV_20[b]	0.8	1165	3	6	gl (99), plag (1), v	0.51	2.85	0.46	2.40	0.05	4269	69	0.2			2.0	1.7	1.8	0.1	*64*	*-4.4*	*9.3*
BA_StV_25[b]	0.8	1140	3	12	gl (96), plag (4), v	0.86	3.29	0.40	2.46	0.03	4316	27	0.3			1.8	1.3	1.5	0.2	*62*	*-5.0*	*18.1*
BA_StV_22[b]	0.8	1150	3	15.5	gl, v	0.64	3.80	0.40	2.96	0.08	3246	55	0.3			1.8	1.5	1.7	0.1		*-4.6*	*5.8*
~ 3-4 wt. % H_2O																						
BA_StV_66	0.2	990	10.8	22	gl (51), plag (35), cpx (8), mt (5), ilm (1)	0.82	3.00	0.80					0.5	2.58	0.04	0.9	0.1	0.5	0.3	*64*	*0.9*	*-11.2*
BA_StV_43	0.35	1090	4.5	23	gl	0.73	4.15	0.58	3.95	0.02	823	10	0.5			1.2	0.8	1.0	0.1		*1.0*	*-4.8*
BA_StV_30	0.35	1030	5.3	6	gl (91), plag (8)†, mt (1)†	0.28	3.50	0.50	3.21	0.01	839	29	0.4			-0.5	-0.8	-0.7	0.1		*0.5*	*-5.6*
BA_StV_46	0.6	1035	14.8	24	gl (41), plag (49), cpx (6), ilm (4), mt (tr), v	0.25	3.10	0.31					0.3			1.6	1.1	1.4	0.2	*61*	*0.2*	*-6.1*
BA_StV_4[a]	0.8	1120	2.5	23.5	gl (75), plag (20), cpx (2), opx (2), mt (1), v	0.02	2.95	0.32					0.3			1.6	1.2	1.4	0.1	*57*	*0.1*	*-1.0*
~ 4-5 wt. % H_2O																						
BA_StV_35	0.35	1010	6.0	6	gl (95), plag (5), mt (tr)	0.33	5.04	0.55	4.34	0.54	815	37	0.6			-1.3	-1.5	-1.4	0.0	*65 (74)*	*0.0*	*-2.2*
BA_StV_42	0.35	1005	6.2	23	gl (73), plag (18), cpx (4), ilm (3), mt (2), v	0.07	4.57	0.35					0.6	2.78	0.07	-1.5	-1.6	-1.5	0.0	*65 (78)*	*0.1*	*-7.1*
BA_StV_75	0.35	980	12.3	25	gl (61), plag (27), cpx (5), opx (5), mt (2), v	0.21	4.95	0.74					0.6			2.6	1.1	1.8	0.5	*74*	*0.2*	*-12.3*
BA_StV_64	0.6	1080	7.5	7	gl (64), plag (26), cpx (6), ilm (3), mt (1)	0.46	3.95	0.48					0.4	2.59	0.10	1.9	1.4	1.7	0.2	*62*	*0.7*	*-5.1*
BA_StV_32	0.6	1045	6.0	7	gl (69), plag (19), cpx (7), mt (3), ilm (2) v	0.14	4.64	0.14					0.5			2.7	1.5	2.1	0.4	*69*	*0.4*	*-6.8*
BA_StV_14[b]	0.8	1100	3	19	gl (63), plag (22), cpx (10), mt (3), opx (2), v	0.03	4.75	0.44					0.4			1.3	0.9	1.1	0.1	*61*	*0.0*	*4.1*
BA_StV_67	0.8	1040	13.4	22	gl (86), plag (7), cpx (4), mt (3), ilm (tr)	0.13	5.06	0.40	4.97	0.04	574	9	0.4	2.73	0.02	2.8	1.2	1.6	0.5	*70*	*0.4*	*-5.3*
~ 5-6 wt. % H_2O																						
BA_StV_31	0.35	1020	6.0	7	gl (99), mt (tr), v	0.63	4.76	0.39	5.12	0.09	1006	16	0.6			0.7	0.3	0.5	0.1		*1.0*	*0.9*
BA_StV_33	0.35	1000	12.8	7	gl (87), plag (9), cpx (2), mt (2), v	0.09	4.81	0.50	5.37	0.40	830	79	0.6			0.8	0.3	0.5	0.1	*62 (74)*	*0.3*	*-5.3*
BA_StV_68	0.35	1050	15.1	15	gl (96), ilm (4), v	0.73	6.01	0.49	5.92	0.07	526	46	0.7			1.3	0.9	1.1	0.2		*-0.1*	*-4.4*
BA_StV_28	0.6	1030	5.7	6	gl (65), plag (21), cpx (9), mt (5), ilm (tr), v	0.05	5.13	0.40					0.5	2.58	0.07	2.4	1.4	1.8	0.3	*68*	*0.2*	*-4.2*
BA_StV_13[b]	**0.6**	**1050**	**3**	**17**	**gl (41), plag (37), cpx (12), opx (3), ilm (4), mt (3), v**	**0.06**	**4.72**	**0.42**					**0.5**	**2.59**	**0.04**	**0.9**	**0.4**	**0.6**	**0.2**	***60***	***0.0***	***-6.9***
BA_StV_2[a]	**0.8**	**1050**	**2.5**	**21**	**gl (29), plag (46), cpx (12), opx (8), ilm (3), mt (2), v**	**0.07**	**5.08**	**0.54**					**0.5**	**1.68**	**0.01**	**0.4**	**-0.1**	**0.2**	**0.1**	***53***	***0.0***	***6.0***

BA_StV_45	0.8	1075	6.2	24	gl (68), plag (20), cpx (9), mt (3)	0.13	5.37	0.45					0.4			1.8	1.3	1.5	0.2	*69*	*0.4*	*-4.8*
~ 6-7 wt. % H_2O																						
BA_StV_29	0.6	1000	11.1	13	gl (59), plag (22), cpx (12), ilm (3), mt (4), v	0.54	6.28	0.49					0.6	3.86	0.16	2.0	0.1	0.8	0.6	*72 (81)*	*0.8*	*-12.9*
BA_StV_49	0.6	1050	7.0	24	gl (87), cpx (5), plag (3), ilm (3), mt (2), v	0.14	7.18	0.46	6.92	0.04	1133	19	0.7			2.7	1.5	2.0	0.4	*74*	*0.2*	*-10.1*
≥ 7 wt. % H_2O																						
BA_StV_36	0.35	1000	9.8	6	gl (96), plag (4)†, mt (tr), v	0.50	7.48	0.27	7.29	0.11	58	22	0.9			0.5	-0.3	0.0	0.2		*0.0*	*-13.9*
BA_StV_65	0.6	1080	7.7	6	gl (99), mt (1)	0.32	7.34	0.41	7.47	0.01	544	46	0.7			2.8	2.4	2.6	0.1		*0.0*	*-8.2*
BA_StV_72	0.6	1040	14.9	22.5	gl (96), ilm (4), v	0.79	6.37	0.33	7.85	0.08	1127	17	0.6			1.7	0.9	1.3	0.3		*0.0*	*-25.0*
BA_StV_69	0.6	980	13.9	24	gl (76), plag (13)†, cpx (4), mt (6), ilm (1), v	0.59	8.21	0.51	8.35	0.15	1705	39	0.8	3.08	0.02	0.8	0.1	0.4	0.3		*0.8*	*-13.8*
BA_StV_34	**0.6**	**1020**	**14.3**	**7**	**gl (85), cpx (6), ilm (5), plag (3), amph (1), mt (tr), v**	**0.22**	**8.17**	**0.47**	**8.67**	**0.07**	**1241**	**24**	**0.7**	**3.52**	**0.16**	**2.2**	**0.3**	**1.2**	**0.5**	***86***	***-0.1***	***-13.0***
BA_StV_73	0.6	1050	15.3	21.5	gl (98), ilm (2), v	1.00	7.58	0.18	8.81	0.11	1855	318	0.7			1.9	1.7	1.8	0.1		*0.0*	*-23.6*
BA_StV_61	0.9	1030	14.6	25	gl (88), cpx (8), ilm (4), mt (tr), v	0.11	7.33	0.49	7.86	0.05	2235	23	0.5	3.24	0.08	1.2	0.3	0.8	0.3		*-0.1*	*-7.3*

$H_2O_{initial}$ - water added at the start

t – run duration

H_2O_{diff} - calculated as volatile by difference from epma analyses. Fe3+:Fe2+ ratio at NNO+2

SIMS - analyses from Secondary Ion Mass Spectrometer (SIMS) using non-linear calibration. For details see analytical methods section.

aH_2O - calculated using Burnham 1975 using H_2O_{diff}

ΔNNO (ILMAT) - calculated for runs with two oxides present (Lepage, 2003) using Andersen and Lindsley (1985) geothermobarometer. Difference relative to NNO buffer.

ΔNNO (B&G 2010) - minimum fO_2 estimate calculated from Fe content in AuPd capsules using Barr and Grove (2010) algorithm (pressure corrected). Difference relative to NNO buffer.

Anorthite content (An) calculated as mol fraction (Ca / (Ca + Na)) in plagioclase minerals after Putirka (2005); two values indicate rim (core)

Fe and Na loss calculated as a relative % of original starting material composition

a, b - water added structurally as $Al(OH)_3$, as in Table 4.1

† mt in BA_StV_24 from BA_StV_26; plag in BA_StV_30 from BA_StV_42; plag in BA_StV_36 from BA_StV_35; plag in BA_StV_69 from BA_StV_49

Abbreviations include gl - glass ; plag - plagioclase ; cpx - clinopyroxene ; opx - orthopyroxene ; amph - amphibole ; mt - magnetite ; ilm - ilmenite ; sp - spinel ; v - vapour ; tr - trace

Bold indicates multiply saturated runs

4.3.1 One-atmosphere experiments

Experiments SV23 and SV24 (Table 4.2) constrain the dry liquidus temperature at one atmosphere to lie between 1225 and 1245ºC at NNO. Plagioclase and spinel are the liquidus phases at 1225ºC, with traces of spinel found at 1245ºC. Small crystal sizes (≤ 5 – 10 μm) made analyses difficult. The oxide phase is identified as a pleonaste spinel on the basis of its high aluminium, iron and magnesium contents. Two successful plagioclase analyses in run SV23 find the anorthite contents to be An_{72} (Table S4.4). Experiments performed at NNO+2 and NNO-2 also crystallise plagioclase and spinel on the liquidus, followed by clinopyroxene and an Fe-Ti oxide phase (instead of spinel) at lower temperatures. Anorthite content decreases systematically with temperature and does not appear to vary with fO_2.

4.3.2 Approach to equilibrium in piston-cylinder experiments

Experimental run durations were based on those shown previously to achieve equilibrium in basaltic andesite systems, e.g. ≥ 6 hours for dry, high temperature runs (≤ 1240ºC; Bartels et al., 1991). Since all experiments performed in this study are hydrous, 6 hours was considered sufficient for high temperature (≥ 1000°C) experiments. Experiments performed at temperature below 1000ºC were run for ≥ 22 hrs due to slower reaction kinetics. Longer run durations increase the likelihood of H_2 loss by diffusion and FeO loss to the capsule, neither of which appear to have significantly affected the runs reported here (Table 4.2).

To support attainment of equilibrium, a set of criteria was established for the experimental run products: (1) glass compositions should be homogenous across the capsule; (2) mineral compositions should be near-homogenous with little to no zoning and vary systematically with temperature, pressure and water contents; (3) crystalline phases

should be euhedral to subhedral (e.g. Figure 4.3); (4) mass balance against the starting material, including H_2O, should be achievable within reasonable limits ($\sum R^2 < 1$). In total, forty-six equilibrium experiments and four controlled fO_2 experiments meet these criteria and are deemed successful. Experimental run product BA_StV_80, at the Co-CoO buffer, has a slightly higher $\sum R^2$ value of 1.67 due to elevated Fe-loss to the capsule at more reducing conditions.

4.3.3 Volatiles

Water 'by difference' estimates ($H_2O_{diff.}$), made using melt compositions that include calculated ferric and ferrous iron, are in very good agreement (± 0.1-1.0 wt. %) with H_2O_{SIMS} data, similar to previous findings (Humphreys et al., 2006a). The 'by difference' method often overestimates water contents due to the presence of other volatiles such as CO_2, sulfur, chlorine, and fluorine; however, the starting material used in this study was prepared synthetically, thus limiting the presence of such volatiles. CO_2 (up to 5000 ppm; Table 4.2) was present in all glasses analysed by SIMS, and concentrations generally increase with increasing pressure. These high CO_2 contents are likely to have been sourced from either the graphite furnace (by diffusion) or from carbonate starting materials (e.g. $CaCO_3$) that did not fully decarbonate. Experiments performed at the highest pressures (0.8 GPa) and temperatures (≥ 1150ºC) explored in this study display the highest CO_2 contents. Graphite furnaces are known to become increasingly damaged over long run durations at high pressures and temperatures (Brooker et al., 1998; Matjuschkin et al., 2015), allowing the carbon to become increasingly mobile and diffuse through the noble metal capsule suggesting this could be the carbon source in experiments presented here.

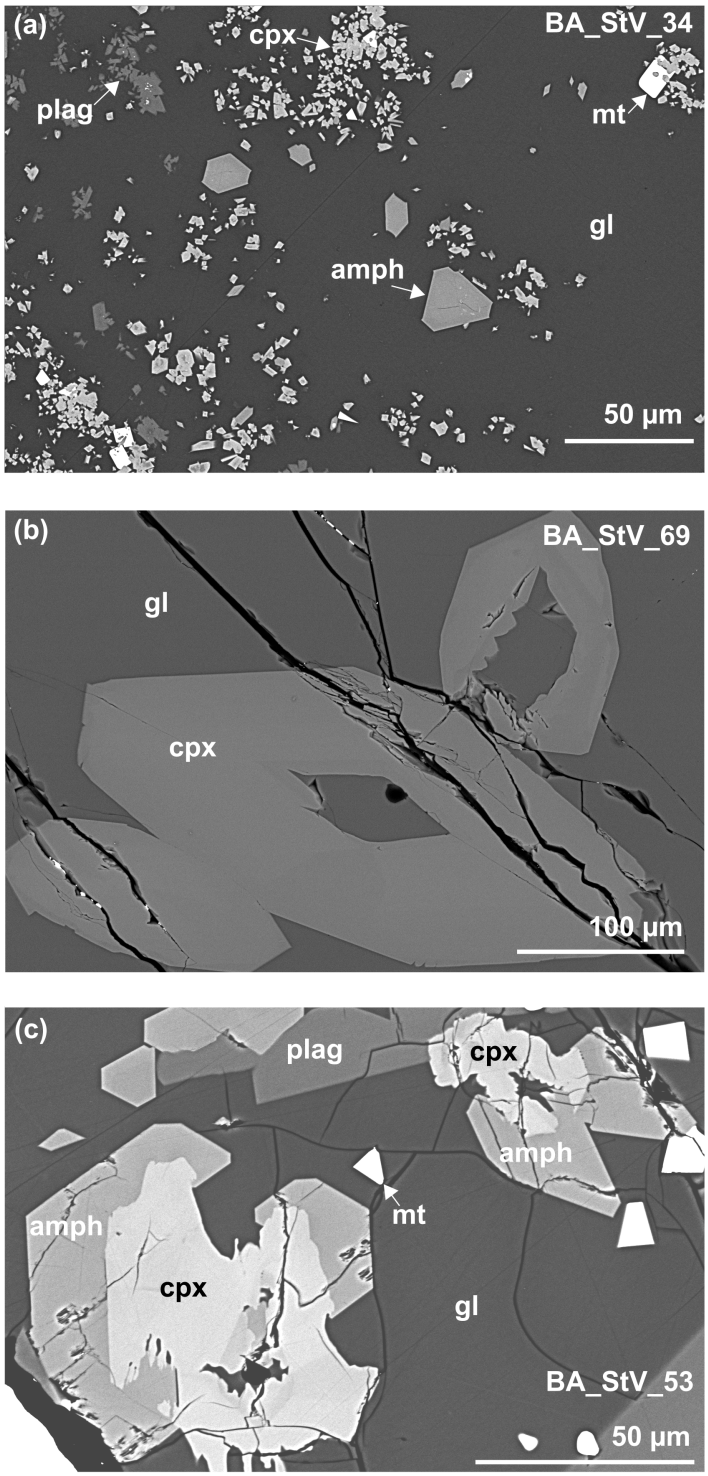


Figure 4.3: BSE images of experimental run products. **(a)** Multiply saturated experimental run BA_StV_34 containing five mineral phases and a high melt fraction (F=85). **(b)** Large euhedral clinopyroxene with melt inclusion at the centre in experimental run BA_StV_69. Sector zoning is visible. **(c)** Clinopyroxene core with amphibole rim in cooling experimental run BA_StV_53. Abbreviations as in Figure 4.1 as well as mt - magnetite.

4.3.4 Oxidation state

Experiments were designed to run close to NNO+2 by setting the Fe^{2+}/Fe^{3+} ratio in the synthetic starting material and using the double capsule technique (Kagi et al., 2005). For water-undersaturated experiments, this approach offers some advantages over the use of solid-state buffers in the presence of H_2O because of the dependence of fO_2 on fH_2 (e.g. Sisson et al., 2005). To check the oxidation state of experimental runs using the double capsule technique and AuPd capsules, the amount of Fe-exchange into the capsule can be measured, as it is a function of oxygen fugacity, melt composition and temperature (Barr and Grove, 2010). By measuring the Au, Pd and Fe content of the capsule wall adjacent to the Fe-bearing melt, an estimate of oxygen fugacity for an experimental run can be obtained. Au, Pd and Fe were analysed for the forty-six experimental run products reported in Table 4.2 (analytical procedure described above). Calculated average fO_2 values range from NNO -1.5 to NNO +2.6 (absolute data are reported in the appendix; Table S4.3).

Previous studies using the Barr and Grove (2010) model (Jakobsson, 2012; Jakobsson et al., 2014; Stamper et al., 2014b; Neave et al., 2019; Marxer et al., 2022), compare fO_2 values to those calculated using different models (e.g. O'Neill and Wall, 1987; Ballhaus et al., 1991; Burnham, 1979; Lepage, 2003; XANES) and tend to find that the Barr and Grove (2010) algorithm underestimates fO_2 by 1-3 log units at more oxidising conditions (≥ NNO). The Barr and Grove (2010) model is calibrated for oxygen fugacities between NNO-2.5 and NNO+0.3, and temperatures ≥ 1175ºC for $Au_{80}Pd_{20}$ capsules. At more oxidising conditions there is a greater proportion of ferric to ferrous iron, such that less ferrous iron is available to alloy with the AuPd capsule. The low Fe content in the AuPd capsules at more oxidising conditions is often at or below the detection limit of the electron microprobe (< 131 ppm in this case), thus providing only a minimum fO_2 estimate. The fO_2 values reported in Table 4.2 should therefore be viewed as minima.

For experiments with two Fe-Ti-oxide minerals present, pairs of co-existing oxides were chosen to calculate run T-fO_2 conditions using ILMAT (Lepage, 2003). Calculated oxygen fugacities, expressed relative to NNO, lie within ±1.7 log units (Table 4.2) of the starting material (NNO+2), however corresponding calculated temperatures were consistently 100-200ºC lower than run temperatures. Comparison of calculated ILMAT fO_2 to one of the controlled fO_2 experiments, fixed at NNO (BA_StV_91), finds ILMAT to overestimate fO_2 by ~ 3 log units. ILMAT does not account for Mg^{2+}, Al^{3+} or Mn^{2+} oxide substitutions; the oxides reported in this study contain significant magnesium and aluminium (≤ 7 wt. % MgO and ≤ 8 wt. % Al_2O_3; see below), thus calculated fO_2 from ILMAT cannot be considered reliable estimates and are not used to indicate experimental run fO_2.

4.3.5 Controlled fO_2 experiments

A small subset of controlled fO_2 experiments were performed to explore the change in mineralogy at different fO_2's and determine the role of oxygen fugacity in calc-alkaline versus tholeiitic differentiation. Metal-metal oxide buffers fix the oxidation state of an experimental run by controlling the fH_2, as long as the buffer remains water-saturated (Euguster, 1957; Ganguly and Newton, 1968). The controlled fO_2 experiments reported here (Table 4.3) contain both the metal and metal oxide phase in the outer capsule, or buffer capsule, at the end of each experimental run, confirming that the oxygen fugacity of the run remained fixed at the set buffer (Jakobsson, 2012).

One controlled fO_2 experiment (BA_StV_89) used a particularly long capsule (~ 11 mm) due to the addition of a separate buffer capsule, resulting in a higher temperature at the centre of the capsule than the thermocouple reading, and consequently a higher melt fraction. The centre of the starting material inner capsule is calculated to be 6 mm from the thermocouple, with a thermal gradient of ~ 10ºC / mm (Schilling and Wunder, 2004),

Table 4.3. Experimental run table for controlled fO_2 experiments

Run #	Capsule material	P (GPa)	T (°C)	$H_2O_{initial}$ (wt. %)	Duration (hrs)	Phase assemblages	$\sum R^2$	H_2O (wt. %) diff.	sd	aH_2O	*Fe-loss (%)*	*Na-loss (%)*
Co-CoO												
BA_StV_80	Au	0.6	980	14	24	gl (78), amph (22), quench, v	1.67	10.39	0.66	1.0	*-8.3*	*-24.1*
Ni-NiO												
BA_StV_83	Au-Pt	0.6	980	14	18	gl (74), amph (25), mt (1), v	0.73	9.95	0.35	0.9	*0.1*	*-20.2*
BA_StV_89	AuPd-Pt	0.6	1080*	14	16	gl (99), mt (1)	0.50	4.34	0.40	0.4	*-0.4*	*-1.2*
BA_StV_91	AuPd-Pt	0.7	1045	13	16	gl (97), cpx (1), mt (1), ilm (1), quench, v	0.69	8.82	0.44	0.9	*0.2*	*-22.7*
Re-ReO₂												
BA_StV_82	Au	0.6	980	14	15	gl (90), amph (2), cpx (4), mt (4), v	0.09	9.92	0.49	0.9	*0.1*	*-3.2*

Abbreviations and calculations as in Table 4.2

* Temperature of thermocouple 1020ºC. Long capsule resulted in 6 mm to centre of capsule. 10ºC increase per 1mm gives actual temperature of 1080ºC (Schilling and Wunder 1999)

the run temperature is therefore recalculated to be 60ºC higher than the set temperature (1080ºC; Table 4.3).

4.3.6 Cooling experiments

Seven cooling experiments were performed to explore peritectic mineral-melt reactions occurring below the liquidus in the melt source region. Experiments were first held at near-liquidus temperatures to provide reactant minerals and then cooled slowly to lower temperatures, as monitored by OP (Table S4.5). These runs have low melt fractions (F = 19 to 65), with minerals appearing sub-anhedral and showing considerable zoning and reaction rims (Figure 4.3c).

To estimate the final equilibration temperature of these runs (and to cross-check the OP method), mineral thermometry using the two-pyroxene (Putirka 2008) and plagioclase-hornblende (Holland and Blundy, 1994) thermometers was carried out. For the amphibole-plagioclase thermobarometer, results from Thermometer B (edenite-richterite) were used due to the absence of quartz in experimental run products. For all but two runs (BA_StV_57 and 53) agreement between amphibole-plagioclase thermometry and estimated temperature from OP are within 2 s.d. (± 64ºC) of the Thermometer B calibration uncertainty (Holland and Blundy, 1994). Two-pyroxene thermometry was used to determine the temperature in the only amphibole-free cooling experiment (BA_STV_44). Again, the calculated temperature is within 2 s.d. (± 40ºC) of the OP estimate (Table 4.4). These cooling experiments provide useful insight into sub-liquidus phase relations, in particular the stability of amphibole.

Table 4.4. Experimental run table of slow cooling experiments.

Run #	P (GPa)	$T_{initial}$ (ºC)	T_{final} (ºC)	T_{calc} (ºC)	$H_2O_{initial}$ (wt. %)	Duration (hrs)	Phase assemblages	$\sum R^2$	H_2O (wt. %) diff.	sd	aH_2O	*An*	*Fe-loss*	*Na-loss*
BA_StV_37	0.35	1000	750	705	6.0	29	gl (40), plag (24), amph (21), cpx (11), mt (4), v	0.38	8.75	0.91	1.0	*44 (72)*	*-0.2*	*-16.2*
BA_StV_40[a]	0.35	1090	800	814	2.5	24	gl (24), plag (37), amph (26), cpx (11), mt (2), v	0.08	7.90	0.88	1.0	*46*	*0.2*	*-1.2*
BA_StV_57	0.35	980	880	953	19.0	37	gl (29), plag (41), amph (15), cpx (7), mt (5), ol (3), v	0.72	8.45	0.47	1.0	*63*	*-0.4*	*-23.3*
BA_StV_60	0.35	990	820	877	7.0	25	gl (28), plag (41), amph (19), cpx (6), mt (6), opx (tr), v	0.82	7.54	0.52	1.0	*59 (73)*	*-0.1*	*-24.6*
BA_StV_53	0.5	1075	980	852	4.5	24	gl (45), plag (30), amph (14), cpx (5), ilm (6), v	0.27	7.95	0.52	0.9	*68*	*-0.7*	*-9.9*
BA_StV_39[a]	0.6	1110	960	960	2.5	24	gl (32), plag (41), cpx (13), amph (4), opx (4), mt (6), v	0.09	6.44	0.42	0.6	*59*	*-0.1*	*-7.9*
BA_StV_44	0.6	1110	1030	992	4.5	25	gl (65), plag (19), cpx (11), mt (3), opx (2)	0.07	5.77	0.46	0.6	*61*	*0.0*	*-7.0*

Abbreviations and calculations as in Table 4.2

T_{calc} average calculated temperature from plagioclase-hornblende thermometry (Holland and Blundy 1994) on select mineral pairs in all runs except BA_StV_44 where two pyroxene thermometry (Putirka 2008) was used instead.

T_{final} calculated from final OP reading, see appendix

a- water added structurally as $Al(OH)_3$, as in Table 4.1

4.3.7 Phase proportions

Mass balance calculations were performed on melt and mineral compositions in run products against the relevant starting material; the sum of residuals squared are reported in Tables 4.2-4.4 ($\sum R^2$) and are generally low. Experiments with the highest sums of residuals ($\sum R^2 > 0.7$) also experienced considerable Na-loss into the vapour phase (see below), which is not accounted for in the mass balance calculation. In four equilibrium experiments (BA_StV_24, 30, 36 and 69) plagioclase and/or an Fe-Ti oxide phase could not be identified, so compositions of minerals in experiments at similar conditions were used in mass balance calculations to determine phase proportions (Table 4.2 and 4.3). For example, plagioclase could not be found in run BA_StV_69, likely due to its low abundance. Plagioclase is required to complete the mass balance for this experimental run, so the composition of the plagioclase used in the mass balance (An_{79}) was selected following the An contours in Figure 4.4.

Na-loss is reported as relative percent; the highest observed Na-loss is 25 rel. % (Table 4.2). Runs with significant Na loss correspond to runs that contain vesicles, as indicated by a 'v' in their phase assemblage (Table 4.2). The vapour phase in experimental run products is likely predominantly carbon dioxide, inferred from the high levels of CO_2 measured in the melt (from the graphite furnaces and/or incomplete decarbonation, see section 4.3.3), and the low solubility of CO_2 compared to H_2O in the melt (e.g. Lowenstern, 2001). Sodium is known to readily partition into the vapour phase (Frank et al., 2003) and has been shown to decrease in natural, H_2O-rich melt inclusions at high SiO_2 due to sequestration into the exsolving fluid (Blundy et al., 2008). No significant (< 5 rel. %) FeO-loss was observed in experimental runs, except BA_StV_80 (8 rel. % loss) likely due to the more reducing run conditions. Quench crystals (≤ 2 – 5 μm) were identified in two of the controlled fO_2 experimental run products (Table 4.3).

4.3.8 Phase relationships

Plagioclase, clinopyroxene and Fe-Ti oxides are ubiquitous near-liquidus phases at all investigated conditions. Orthopyroxene stability increases with pressure and amphibole is found at pressures ≤ 0.6 GPa and temperatures ≤ 1020ºC. Isobaric phase diagrams at 0.35, 0.6 and 0.8 GPa are illustrated in T-H_2O space in Figures 4.4 and 4.5 with contours of plagioclase composition superimposed. Anorthite contours represent lines of average plagioclase composition derived from electron microprobe analyses (epma) of equilibrium experiments (Table 4.2). As expected, anorthite content increases with water content and temperature (Cashman and Blundy, 2013; Melekhova et al., 2017). Water saturation curves were determined using MagmaSat (Ghiorso and Gualda, 2015) for all P-T-H_2O conditions. Controlled fO_2 experiments at the same P-T-H_2O conditions illustrate the difference in mineral assemblage from reducing (NNO-2) to oxidising (NNO+2) conditions (Figure 4.5).

0.35 GPa

Magnetite is the liquidus phase at 0.35 GPa, closely followed by plagioclase and clinopyroxene (Figure 4.4a), similar to previous basaltic andesite experiments (Rader and Larson, 2013). Anorthite contents are low (≤ An_{74}). Ilmenite forms below 1005ºC and ≤ 4.6 wt. % H_2O. Orthopyroxene is present in one equilibrium experimental run product at 980ºC and 4.9 wt. % H_2O and inferred to stabilise down temperature. Amphibole is abundant in all cooling experiments at 0.35 GPa, appearing at 950ºC close to water saturation (8.5 wt. % H_2O), and remaining stable down to at least 700ºC, at high water contents and high water activity (≥ 7.5 wt. % H_2O; aH_2O = 1; Table 4.4). Olivine is only present in one cooling experiment (BA_StV_57) at 950ºC, 8.5 wt. % H_2O and with a melt fraction of F=29, suggesting that olivine is not a stable liquidus phase.

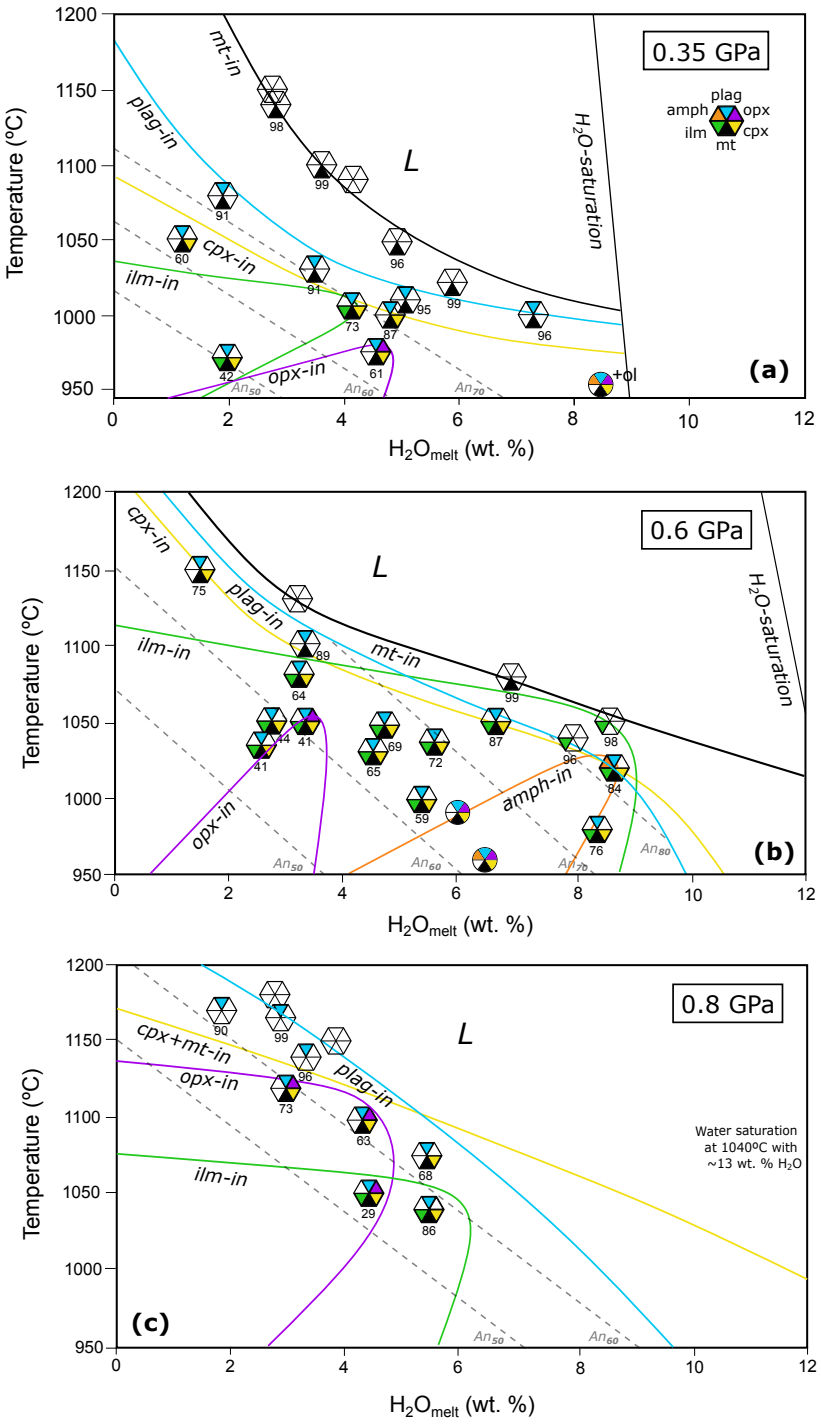


Figure 4.4: Isobaric temperature-H_2O_{melt} plots showing phase relations at **(a)** 0.35 GPa, **(b)** 0.6 GPa, and **(c)** 0.8 GPa, for the SV2021 basaltic andesite at ~ NNO+2. Hexagons show phase assemblages in equilibrium experimental run products, with melt fraction written below. Circles represent cooling experimental run products. Coloured solid lines illustrate the stability of mineral phases. Dashed grey lines show Anorthite (An) contours for plagioclase. H_2O saturation curves were calculated using MagmaSat. Abbreviations as in Figure 4.1, as well as ilm - ilmenite, and *L* - liquid.

0.6 GPa

At 0.6 GPa magnetite and ilmenite are on the liquidus, followed by plagioclase and clinopyroxene (Figure 4.4b). Liquidus temperatures at high water contents (≥ 6 wt. % H_2O) are close to the upper estimate of the eruption temperature (~ 1020ºC; Weber et al., 2024). Anorthite contours extend to An_{80} at water contents ≥ 8 wt. % H_2O. The stability fields of orthopyroxene and amphibole are narrow. Orthopyroxene is stable at ≤ 4 wt. % H_2O and temperatures below 1050ºC; whilst amphibole is stable at ≥ 6 wt. % H_2O and up to 1020ºC. Experimental run product BA_StV_34 is multiply-saturated close to the liquidus (F = 85) at 1020ºC and 8.2 wt. % H_2O with five mineral phases, corresponding to an amphibole-gabbro assemblage (plag + cpx + mt + ilm + amph). Although this multiple saturation point (MSP) lies 20 – 30ºC below the liquidus, the melt composition in this run product is similar to the initial basaltic andesite starting material, with the exception of FeO and TiO_2 contents (discussed below; Figure 4.6). Crystallisation of an oxide phase close to the liquidus is a product of the oxidising nature of these runs (NNO+2), as previously reported (Sisson and Grove, 1993a; Thy and Lofgren, 1994; Berndt et al., 2005; Sisson et al., 2005; Freise et al., 2009; Feig et al., 2010; Waters et al., 2020). A second Ti-rich oxide phase, termed ilmenite, is present at ≤ 9 wt. % H_2O. Plagioclase and clinopyroxene also become unstable at high water contents.

A second experimental run is multiply-saturated with five mineral phases at 0.6 GPa: sub-liquidus run BA_StV_13 (F = 41), in equilibrium with a gabbroic assemblage (plag + cpx + opx + mt + ilm) at 1050ºC and 5.4 wt. % H_2O. The melt composition in this run is very evolved, sitting along the differentiation trend and more similar to some of the dacitic melt inclusions from St. Vincent (~ 68 wt. % SiO_2). Thus, this run is not a basaltic andesite liquidus MSP.

The controlled fO_2 experiments performed at 0.6 GPa are presented in Figure 4.5, with different hexagon outline colours representing the different oxidation states. These experiments highlight the change in stability of different mineral phases across three different oxidation states at identical P-T-H_2O conditions (0.6 GPa, 980ºC and ~ 10 wt. % H_2O; Table 4.3). At Re-ReO_2 (~ NNO+2; BA_StV_82), the most oxidising conditions explored here, amphibole, clinopyroxene and magnetite are all present close to the liquidus (F=90). At Ni-NiO (BA_StV_83; F = 74), amphibole is the dominant mineral phase, with a small fraction of magnetite; and at Co-CoO (~ NNO-2; BA_StV_80; F= 78), only amphibole is present. Amphibole is known to increase in stability, and abundance, at more oxidising conditions, higher water contents and lower temperatures (Rutherford and Devine, 1988; Krawczynski et al., 2012), linked to the destabilisation of plagioclase (Sisson et al., 2005), as shown here.

0.8 GPa

Plagioclase is the liquidus phase at 0.8 GPa, followed by clinopyroxene, magnetite and orthopyroxene (Figure 4.4c). Liquidus temperatures at all water contents are ≥ 100ºC higher than the estimated eruption temperature (Weber et al., 2024). Orthopyroxene is stable over a wider range of water contents (≤ 6 wt. % H_2O) and up to temperatures of 1100ºC. Ilmenite is less abundant and only appears below 1040ºC (≥ 80ºC below the liquidus). Anorthite contents at this pressure extend only to An_{70}. Another sub-liquidus multiple saturation point (BA_StV_2) is found at 0.8 GPa, 1050ºC and with 5.0 wt. % H_2O, in equilibrium with a gabbroic assemblage. Again, the melt fraction is too low (F=29) and glass composition too evolved for this to be a basaltic andesite MSP.

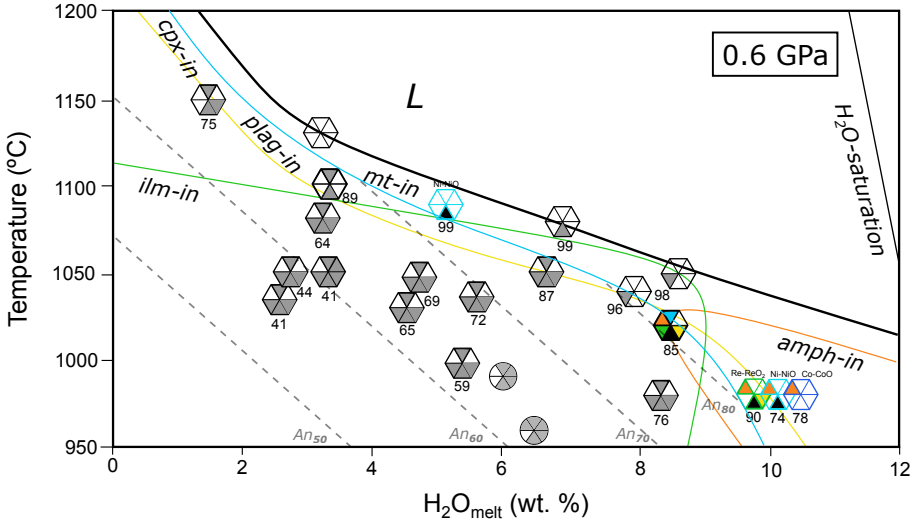


Figure 4.5: Isobaric temperature-H_2O_{melt} plot at 0.6 GPa. Equilibrium experiments as in Figure 4.4b are now shown in grey, except multiply saturated run BA_StV_34. Controlled fO_2 experiments are shown in colour. Outline colours illustrate different oxidation states: green is Re-ReO_2, pale blue is Ni-NiO and dark blue is Co-CoO. Note the change in the amphibole stability field.

4.3.9 Phase compositions

In this section, experimental phase compositions are discussed and compared to those in the natural lavas, scoria and plutonic xenoliths from St. Vincent using data from Rowley (1978), Heath (1998a), Robertson (2002), Tollan et al. (2012), Fedele et al. (2021) and Weber et al. (2024) and the GEOROC database.

Glass

Experimental glass compositions are plotted against MgO in Figure 4.6. Pale grey symbols represent natural lavas and melt inclusions. Dark grey and coloured filled symbols represent near liquidus experiments (F ≥ 85) and plot, as expected, close to the starting material (SV2021) for all major oxides. The melt composition in experiments with melt fractions ≤ 85 (white filled symbols) mostly follow the liquid line of descent of the La Soufrière lavas. Symbol shape and outline colour depict experimental run product

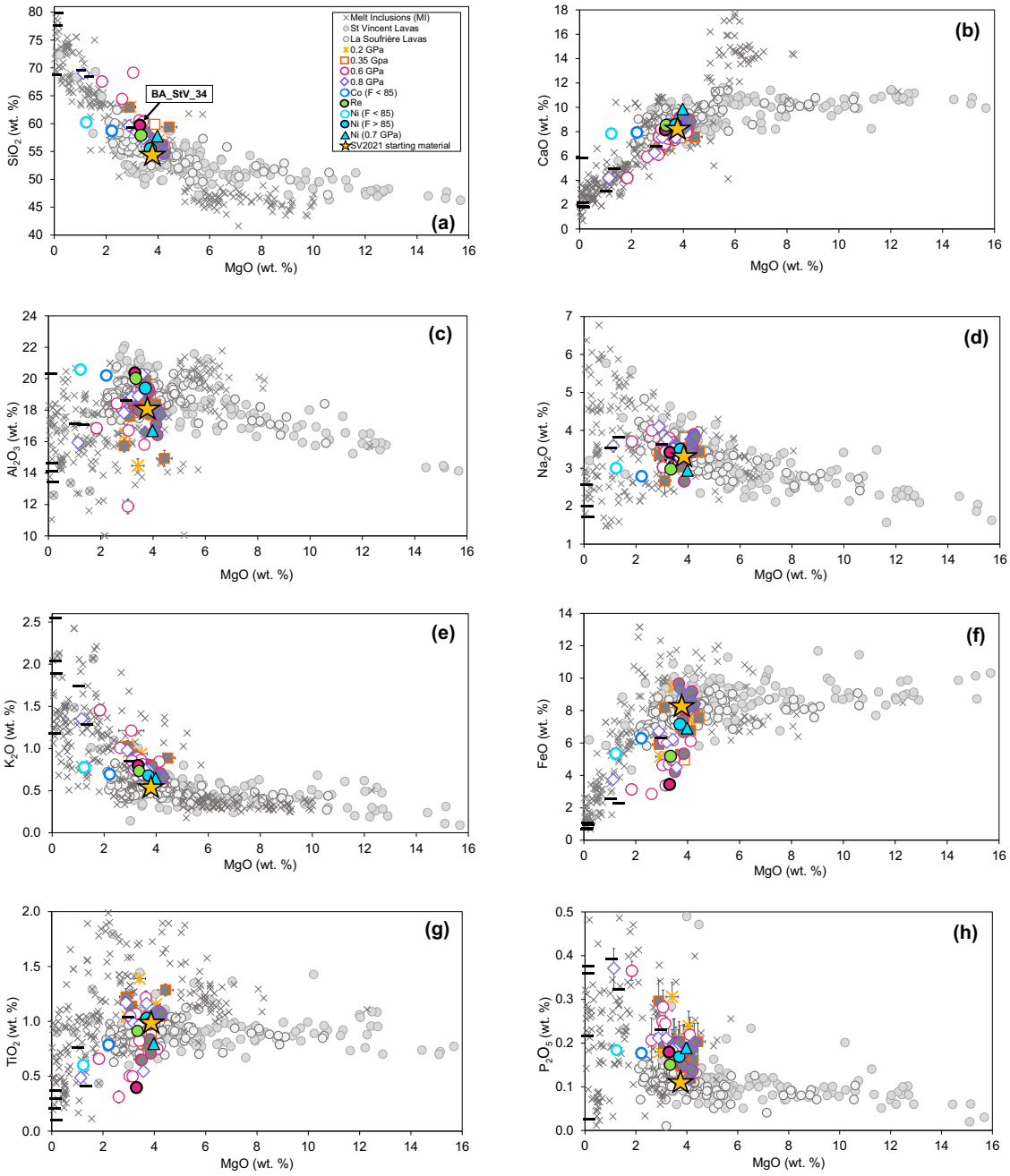


Figure 4.6: Composition of experimental melts plotted as major oxides versus MgO. Different colours and symbol types denote pressure and oxygen fugacity, including yellow cross symbols for experimental run products at 0.2 GPa, orange squares for 0.35 GPa, pink circles for 0.6 GPa and purple diamonds for 0.8 GPa. Symbols are grey filled for melt fractions F ≥ 85 and white filled for F < 85. Multiply saturated experiment (BA_StV_34) is labelled and filled pink. Dashes represent cooling experiments. Controlled fO_2 experiments are shown as circles (0.6 GPa) and triangles (0.7 GPa) in green (Re-ReO_2), pale blue (Ni-NiO), and dark blue (Co-CoO). Again fill colour depicts melt fraction. Experimental melts are plotted as an average with standard deviation. The yellow star is the SV2021 basaltic andesite starting material. St. Vincent lavas (pale grey circles), La Soufrière lavas (cream circles) and melt inclusion (crosses) data are from GEOROC, Rowley (1978), Heath (1998a), and Robertson (2002).

pressure and oxygen fugacity. Near-liquidus, five-phase multiply saturated run BA_StV_34 is labelled (pink filled symbol). Na_2O contents remain unchanged (< 1 wt. % decrease) in all experiments, reflecting the formation of Ca-rich plagioclase, and the absence of an Na-rich mineral phase. Two near-liquidus experiments at 0.6 GPa and one at 0.8 GPa show slightly lower Na_2O contents than the starting material (Figure 4.6d) indicative of Na loss, plausibly into a vapour phase (Table 4.2). In controlled fO_2 runs BA_StV_80 and 83 (blue outlined circles), crystallisation of 22 – 25 % amphibole accounts for the depletion in melt Na_2O and MgO contents.

Several near-liquidus runs show lower FeO and TiO_2 contents than the starting material (Figure 4.6f,g) due to the crystallisation of Fe-Ti oxides rather than Fe-loss to the capsule. Experimental run BA_StV_80 at Co-CoO (NNO-2) is the only run at 0.6 GPa that is oxide-free but has ~ 8 wt. % relative Fe-loss due to the more reducing nature of the run. Fractionation of ilmenite and/or magnetite appears to be driving Fe and Ti depletion in the melt for all other runs. Figure 4.7 illustrates the evolutionary path of a melt fractionating average experimental ilmenite and magnetite compositions. Interestingly, magnetite and ilmenite are on the liquidus in controlled fO_2 run BA_StV_91 at 0.7 GPa and NNO, highlighting that even at the more reduced conditions of NNO, Fe-Ti oxide crystallisation is capable of driving melt FeO and TiO_2 contents down. TiO_2 contents shows two populations for lower melt fraction runs; those with higher TiO_2 in the melt are runs without an ilmenite phase present.

Elevated Al_2O_3 contents reflect the absence, or low proportion, of plagioclase. Multiply saturated run BA_StV_34 (pink filled symbol; Figure 4.6c) has high Al_2O_3 contents likely due to the crystallisation of only 3 % plagioclase. P_2O_5 contents in experimental glasses are slightly higher than the starting material (Figure 4.6h), consistent with the absence of apatite in all experimental run products. Cooling-experiment glasses (F ≤ 65; dashes in Figure 4.6) are more evolved than the low melt fraction equilibrium experiments,

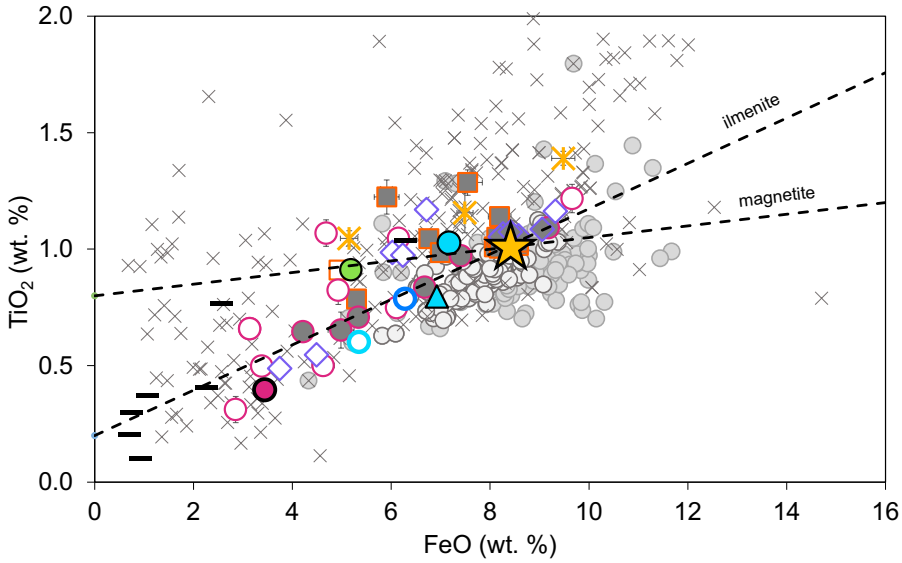


Figure 4.7: FeO versus TiO_2 (wt. %) for experimental melts and natural samples. Symbols and colours as in Figure 4.6. Ilmenite and magnetite control lines from experimental oxide compositions shown as dashed lines through the starting composition.

containing ≥ 68 wt. % SiO_2 and ≥ 1.2 K_2O contents. Such melt compositions overlap with dacitic melt inclusions.

Plagioclase

Plagioclase is the liquidus phase at 0.8 GPa and forms close to the liquidus alongside Fe-Ti oxides at 0.35 and 0.6 GPa (Figure 4.4). Plagioclase laths are euhedral and range from 1 – 50 μm in size. Anorthite content decreases down-temperature away from the liquidus and towards lower melt H_2O conditions (Figure 4.4), as observed previously (Sisson and Grove, 1993b; Melekhova et al., 2017). The T-H_2O slope of the An isopleths is independent of pressure, at approximately 30ºC per 1 wt. % H_2O. Isopleth spacing changes little with pressure. An contents increase by 10 mol % for an increase of ~2 wt. % melt H_2O or ~70ºC. This is a significantly lower temperature dependence than observed for more evolved, water-saturated dacitic melts, where the corresponding ΔT for 10 mol % change in An is only 27ºC (Cashman and Blundy, 2013), but is very similar to what has been shown by Melekhova et al (2017) for a similar basaltic andesite composition.

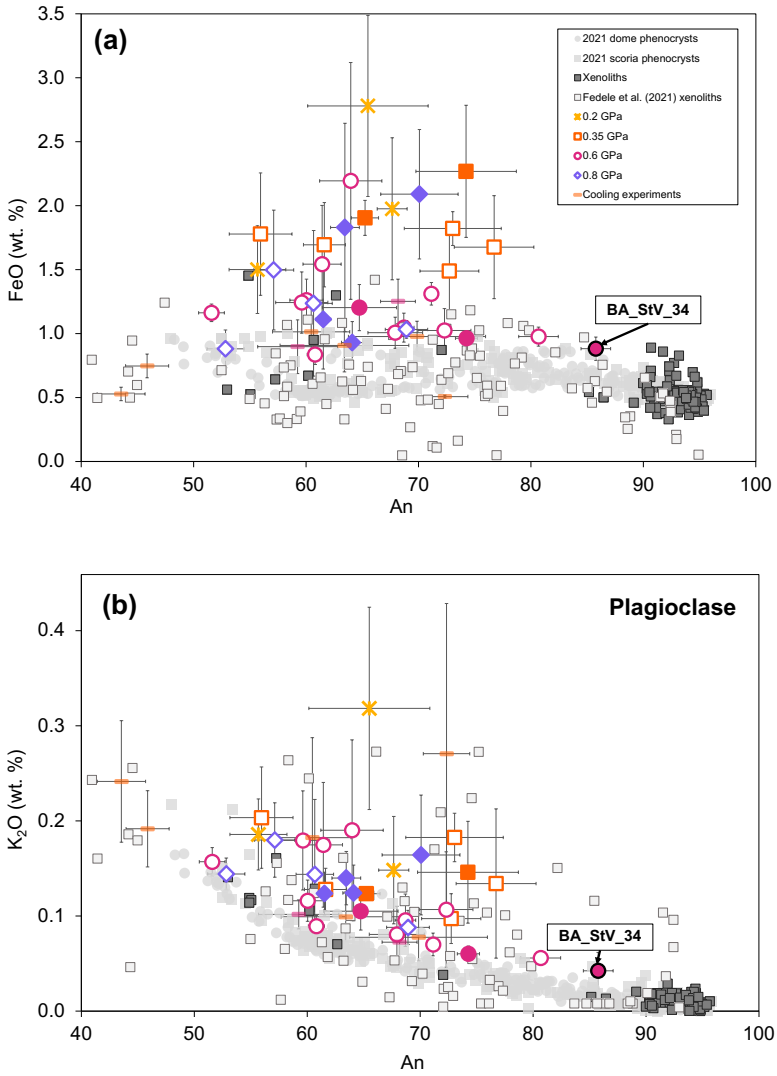


Figure 4.8: Composition of experimental plagioclases plotted as anorthite content (An) versus **(a)** FeO and **(b)** K_2O (wt. %). Anorthite content calculated as mol fraction Ca / (Ca + Na). Symbols as in Figure 4.6, with filled coloured symbols depicting melt fractions ≥ 85. Orange and pink dashes distinguish between cooling experiments performed at 0.35 and 0.6 GPa respectively. Grey circles and triangles are natural phenocryst compositions from the 2020-2021 eruption (Weber et al., 2024). Dark grey squares are xenoliths from Robertson (2002), Tollan et al. (2012) and Table S3.2 (appendix); pale grey squares are micro-xenoliths from Fedele et al. (2021).

One experiment (BA_StV_34) produced high-Ca plagioclase (An_{86} at 0.6 GPa, 8.2 wt. % H_2O and 1020ºC). Notably, this is the only run in this series to crystallise amphibole near to the liquidus (F=85). The lowest anorthite plagioclases (An_{52}) were produced in experimental runs with low melt fractions (F ≤ 44) and low water contents (≤ 3 wt. % H_2O). Experimental plagioclase anorthite contents overlap with those of natural xenoliths (An_{40} to An_{95}; Figure 4.8). Plagioclase typically contains ~ 1 wt. % FeO at QFM, with

higher FeO contents found at more oxidising conditions and vice versa (Aigner-Torres et al., 2007; Wilke and Behrens, 1999). St. Vincent xenolith plagioclases contain up to ~ 1.5 wt. % FeO (Figure 4.8a), in good agreement with the majority of experimental crystals (0.5 – 1.5 wt. % FeO). The high (> 1.5 wt. %) FeO contents of some experimental plagioclases reported in this study reflects coeval crystallisation with Fe-Ti oxides. Nucleation of plagioclase on initial oxide minerals, or very small (<1 μm) Fe-Ti oxide inclusions within plagioclase, confirmed by the presence of high titanium contents (≤ 0.6 wt. % TiO_2) in plagioclases with high FeO. Thus, the high FeO and TiO_2 contents likely reflect fluorescence of these elements from adjacent or included Fe-Ti oxide grains during electron microprobe analysis rather than enhanced partitioning at the experimental conditions.

Potassium contents in experimental plagioclase increase with decreasing anorthite contents extending up to 0.3 wt. % K_2O (Figure 4.8b). This behaviour is in good agreement with the lava and xenolith phenocrysts. The micro-xenoliths from La Soufrière (Fedele et al., 2021) show a considerable spread in An and K_2O content.

Clinopyroxene

Experimental clinopyroxenes have compositions in the range $Wo_{40\text{-}48}En_{34\text{-}44}Fs_{11\text{-}22}$ and $Mg\#_{60}$ to $Mg\#_{80}$ (Mg# calculated using FeO_T). Clinopyroxene crystals are euhedral, ≤ 20 μm, and generally form in clusters (Figure 4.3a), except for experimental runs BA_StV_49, 61, 69, 91 that contain much larger crystals (200 – 1000 μm; Figure 4.3b). Clinopyroxenes in cooling experiments are ≤ 300 μm. Mg#'s are higher in experiments at lower pressures (Figure 4.9a), with temperature having little influence. Clinopyroxenes in the experimental run buffered at Re-ReO_2 and 0.6 GPa (BA_StV_83) have the highest magnesium numbers (≥ $Mg\#_{79}$), at relatively low Al_2O_3 contents (~4 wt. % Al_2O_3) and are in good agreement with the highest magnesium xenolith clinopyroxenes (> $Mg\#_{78}$) in

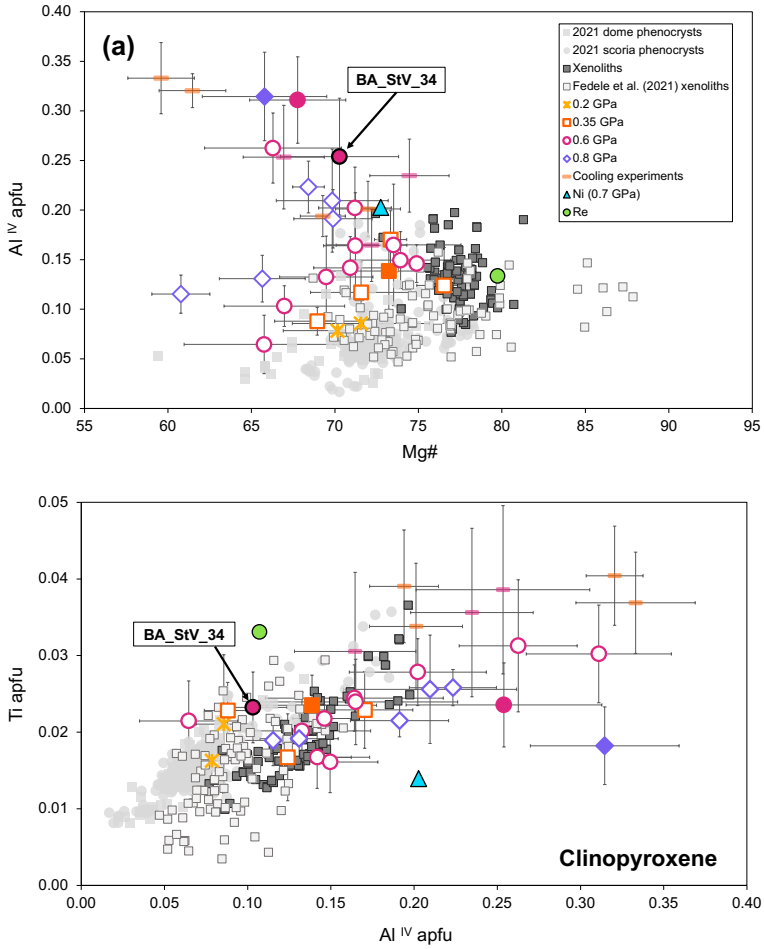


Figure 4.9: Composition of experimental clinopyroxenes plotted as **(a)** Al_2O_3 (wt. %) versus Mg# and **(b)** TiO_2 (wt. %) versus Al (IV) atoms per formula unit (apfu). Symbols as in Figure 4.6 and 4.8.

olivine-gabbros and wehrlites. Cooling experiments produce clinopyroxenes with generally lower Mg#'s and higher aluminium contents.

Al_2O_3 contents increase with pressure (2 – 10 wt. %; Figure 4.9a), as found in previous experimental studies (Wood and Henderson, 1978; Villiger et al., 2004, 2007; Laukert et al., 2014). Aluminium contents extend to 12 wt. % Al_2O_3, higher than La Soufrière natural lava and xenolith samples (< 6 wt. % Al_2O_3) and the typical range of volcanic arc clinopyroxenes (≤ 9 wt. % Al_2O_3; Nisbet and Pearce, 1977). Experimental clinopyroxenes with ≥ 7 wt. % Al_2O_3 are often associated with very wet melts (≥ 7 wt% H_2O), suggesting water may play a role in the observed elevated aluminium contents. Na_2O contents (0.4 – 0.8 wt. %) also increase with pressure in experimental crystals, as previously found

(e.g. Blundy et al., 1995; Feig et al., 2006). Experimental clinopyroxenes with ≥ $Mg\#_{70}$ and ≤ 6 wt. % Al_2O_3 overlap with the La Soufrière 2020-2021 phenocrysts and some xenoliths (Figure 4.9a).

Tetrahedral aluminium (Al^{IV}) contents in experimental clinopyroxenes range from 0.06 – 0.31 apfu (calculated on a 6 O basis) and are in good agreement with previous experimental studies (e.g. Pichavant et al., 2002b, Melekhova et al., 2017). Titanium contents in experimental clinopyroxenes (0.5 – 1 wt. % TiO_2) overlap with values for natural phenocrysts (0.3 – 1.3 wt. % TiO_2) and xenoliths (0.1 – 1.3 wt. % TiO_2) and show a strong positive correlation with Al^{IV} (Figure 4.9b) due to the coupled substitution: $(Mg,Fe)^{2+} + 2\ Si^{4+} = Ti^{4+} + 2\ Al^{3+}$ (Yagi and Omura, 1967; Baginski et al., 2009). TiO_2 contents are highest in clinopyroxenes from cooling experiments (1.1 – 1.4 wt. % TiO_2).

Orthopyroxene

Experimental orthopyroxenes are euhedral, tabular, and consistently larger than co-existing clinopyroxene (20 – 100 μm). Compositions are in the range $Wo_{3\text{-}5}En_{66\text{-}81}Fs_{15\text{-}31}$ and $Mg\#_{68}$ to $Mg\#_{85}$. Orthopyroxene is present at all pressures but lies closest to the liquidus and has the largest stability field at higher pressures and temperatures (0.8 GPa and ≥ 1020ºC), and lower water contents (≤ 6 wt. % H_2O; Figure 4.4). Magnesium numbers in experimental orthopyroxenes at 0.8 GPa ($Mg\#_{68}$ to $Mg\#_{72}$) are in good agreement with phenocrysts from lavas and xenoliths ($Mg\#_{65}$ to $Mg\#_{75}$; Figure 4.10). In cooling experiments, orthopyroxene has a generally higher magnesium number ($Mg\#_{72\text{-}74}$). Orthopyroxene in sub-liquidus multiply-saturated run BA_StV_13 is significantly more magnesian ($Mg\#_{84}$) than orthopyroxenes from any of the natural samples (Figure 4.10). Aluminium contents in all experimental orthopyroxenes are notably higher (4 – 6 wt. % Al_2O_3) than the natural samples (≤ 2 wt. % Al_2O_3). Previous studies also note the high aluminium contents of experimental orthopyroxenes (e.g. 6 – 10 wt. % Al_2O_3; Pichavant et al., 2002a; Melekhova et al., 2015). Both experiments and natural samples contain

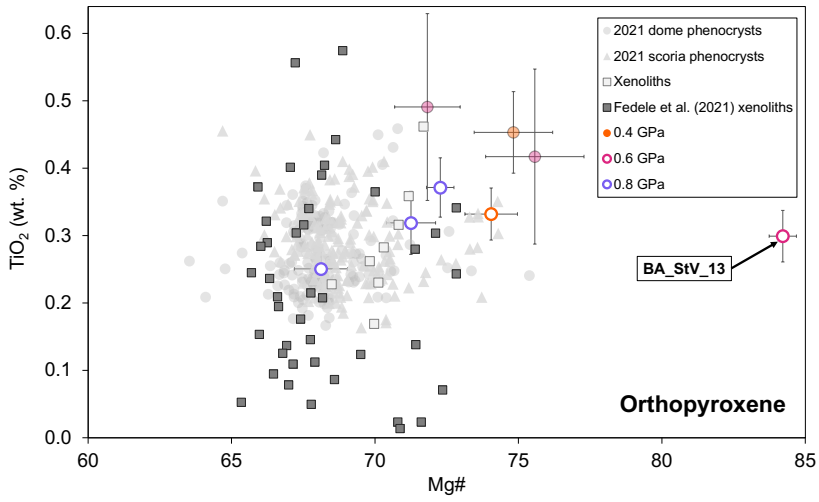


Figure 4.10: Composition of experimental orthopyroxenes plotted as TiO_2 (wt. %) versus Mg#. Symbols as in Figure 4.8.

very little sodium (≤ 0.1 wt. % Na_2O), titanium (≤ 0.5 wt.% TiO_2) and calcium (≤ 2.2 wt. % CaO; Table S4.4) suggestive of low pressures and temperatures of crystallisation. Two-pyroxene thermometry of experimental run products containing both orthopyroxene and clinopyroxene yields calculated temperatures to be 40 – 100ºC below the run temperatures, with the biggest temperature difference at 0.8 GPa (Table S4.7; Putirka, 2008).

Iron-titanium oxides

Iron-titanium oxides are ubiquitous in run products at all conditions studied (Figure 4.4). Liquidus oxides at 0.35 and 0.6 GPa are titanomagnetites of the magnetite-ulvöspinel solid solution series (mt, Table 4.2) with different proportions of titanium (1 – 8 wt. % TiO_2; 0.01 – 0.23 Ti apfu), magnesium (4 – 7 wt. % MgO) and aluminium (7 – 8 wt. % Al_2O_3). Titanomagnetites range from < 1 µm to 10's µm, with size often correlating to run duration. Oxides were identified in runs BA_StV_3 and BA_StV_48 but were too small to analyse (≤ 1 µm). Experimental oxides are sub- to euhedral, with some containing inclusions of other mineral phases and some showing skeletal textures. At a given pressure, with increasing temperature, liquidus titanomagnetites become more

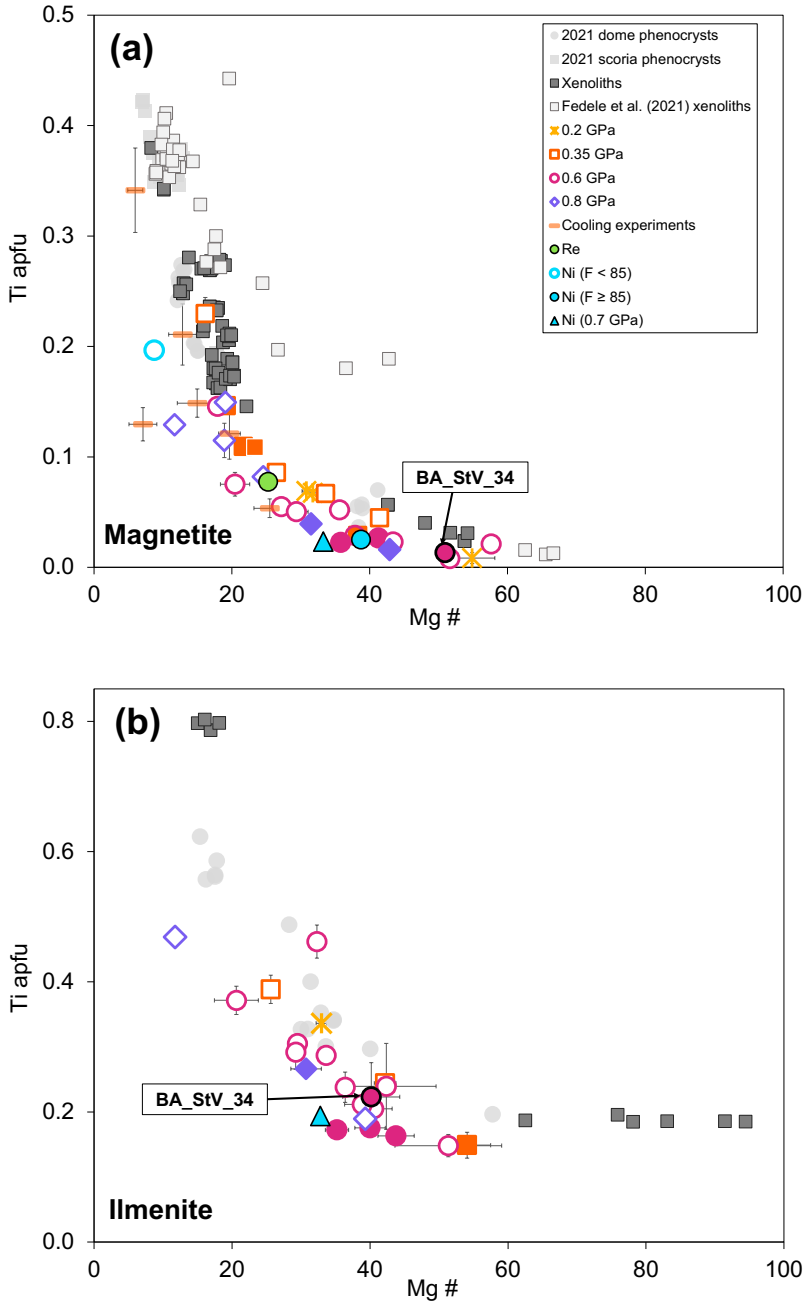


Figure 4.11: Composition of experimental **(a)** magnetites and **(b)** ilmenites plotted as Ti atoms per formula unit (apfu) versus Mg #. Symbols as in Figure 4.6 and 4.8.

magnesian and less titanian. Experimental titanomagnetites containing 4 – 8 wt. % TiO_2 (0.1 – 0.2 Ti apfu) are in good agreement with the Ti-rich population of titanomagnetites in xenoliths from St. Vincent (Tollan et al., 2012; Table S3.2) and phenocrysts from the effusive stage of the 2021 eruption (Weber et al., 2024; Figure 4.11a). A second population of Ti-poor (≤ 1.5 wt. % TiO_2; ≤ 0.05 Ti apfu) and Mg-rich ($Mg\#_{50}$ to $Mg\#_{70}$; calculated using Fe^{2+}) xenolith titanomagnetites exist and are referred to as 'spinels' in

the literature (Heath et al., 1998a; Tollan et al., 2012; Fedele et al., 2021). These Mg-rich titanomagnetites primarily form in experimental runs that co-crystallise ilmenite. The range of TiO_2 in experimental titanomagnetites matches the bimodality previously reported for natural oxides from St. Vincent (Melekhova et al., 2015). Experimental titanomagnetites complete the trendline between the two distinct xenolith titanomagnetite populations (Figure 4.11a), with near-liquidus runs forming oxides with compositions closer to those in xenoliths. The Ti-poor oxides in multiply saturated run BA_StV_34 are Mg-rich and plot close to the St. Vincent xenoliths (e.g. gabbros, hornblendites, dunites).

A second Fe-Ti oxide phase forms down temperature at all experimental pressures explored (Figure 4.4), with higher titanium (15 – 20 wt. % TiO_2) and ferric iron contents (≥ 59 wt. % Fe_2O_3); and lower magnesium and aluminium (< 2 wt. % MgO, < 2 wt. % Al_2O_3). Charge balance and stoichiometry were used to determine that these are rhombohedral oxides of the ilmenite-hematite solid solution series, hereafter referred to as ilmenite (ilm, Table 4.2). As for titanomagnetites, two discrete xenolith populations exist, a Ti-rich (0.8 Ti apfu) mineral phase, referred to as ilmenite in norite xenoliths (Fedele et al., 2021); and an Mg-rich mineral phase with low ferrous iron contents, referred to as titanohematite in the literature and found in olivine-gabbro xenoliths (Figure 4.11b; Robertson, 2002). Most experimental ilmenites sit closest to the Mg-rich xenolith variety, but with generally lower magnesium contents.

Reports of multiple oxide phases in lavas and xenoliths from the Lesser Antilles are common (e.g. Arculus and Wills, 1980; Melekhova et al., 2015, 2017) and are considered to be a feature of island arc volcanism globally (Lewis, 1970; Barnes and Roeder, 2001; Nandedkar et al., 2014). Barnes and Roeder (2001) find a prominent ‘spinel gap’ in oceanic arc settings, with two discrete compositional populations identified in terms of Ti, Fe, Mg and Al contents. The experiments presented in this study appear to complete the compositional gap between end-member oxide phases.

Amphibole

Calcic amphibole is found in one equilibrium experiment (BA_StV_34), and in three of the controlled fO_2 experiments (Table 4.3). In run BA_StV_34, amphibole appears as a near-liquidus phase (F = 85) at 0.6 GPa, 1020ºC and with 8.2 wt. % H_2O_{melt} (Figure 4.4b). Crystals are euhedral, unzoned and ≤ 30 μm in size (Figure 4.3a). In controlled fO_2 experiment BA_StV_82, at Re-ReO_2, amphibole is again a near-liquidus phase (F=90), crystals are euhedral, unzoned and ≤ 50 μm. At Co-CoO and NNO, amphibole is the liquidus phase but with 22 – 25 % crystallisation at 980ºC. Crystals are euhedral, 100 – 500 μm in size and some zoning is observed (Mg-rich cores of $Mg\#_{75}$ at CoCoO and $Mg\#_{90}$ at NNO). All experimental amphiboles are similar in composition, with high aluminium (13 – 15 wt. % Al_2O_3), titanium (1.5 – 2.6 wt. % TiO_2) and magnesium contents ($Mg\#_{60}$ to $Mg\#_{75}$; calculated as FeO_T). The Fe^{3+}/Fe^{2+} content, as determined by stoichiometry, is ~ 3, similar to xenoliths. Amphibole compositions lie close to the pargasite and kaersutite end members (Leake, 1978), similar to amphiboles in basaltic andesites previously studied (Sisson and Grove, 1993b; Moore and Carmichael 1998; Pichavant et al., 2002b; Freise et al., 2009; Ridolfi and Renzulli, 2012).

Experimental amphiboles are compositionally in good agreement with xenoliths from St. Vincent (Lewis, 1973; Tollan et al., 2012), with near-identical calcium, sodium and potassium contents; and very similar iron, magnesium, titanium and aluminium contents (Figure 4.12). The Ti-Tschermaks substitution ($M^{2+} + Ti^{4+} = 2^{VI}Al^{3+}$, where M is a divalent cation on the M-site; Zenk and Schulz, 2004) is likely responsible for accommodating Ti. Other substitutions, such as edenitic and oxy-kaersutitic substitutions (Saxena and Ekström, 1970; Popp and Bryndzia, 1992; Leake, 1978) also allow for complex amphibole compositions to exist. Hornblende-plagioclase thermometry estimates for BA_StV_34 gives temperatures of 960 ± 40ºC (Holland and Blundy, 1994), only slightly lower than the thermocouple reading of the run temperature (1020 ± 10ºC).

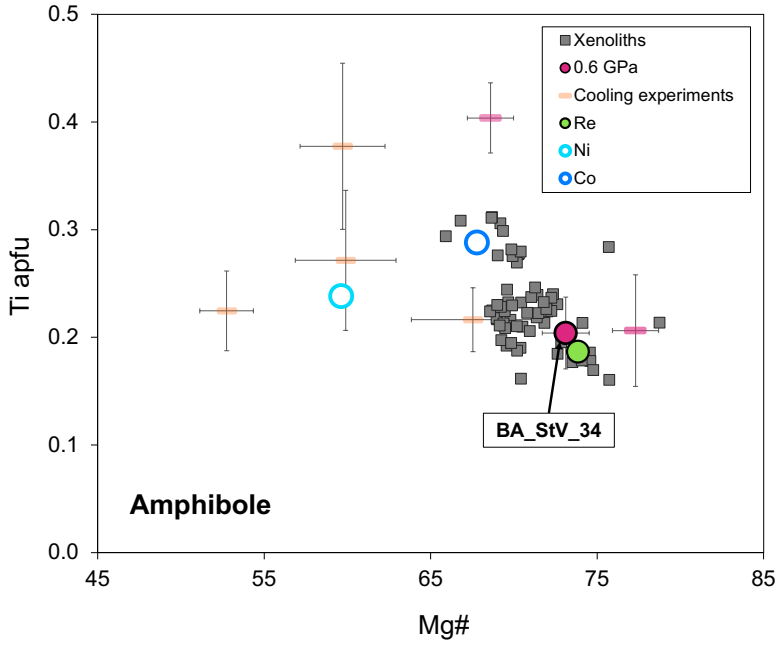


Figure 4.12: Composition of experimental amphiboles plotted as Ti atoms per formula unit (apfu) versus Mg #. Note the lack of amphibole phenocrysts and Fedele et al. (2021) xenoliths. Symbols as in Figure 4.6 and 4.8.

Amphibole is present in all but one of the cooling experiments (Table 4.4), forming at temperatures between 700 – 960ºC and with ≥ 6.5 wt. % H_2O_{melt}. The amphibole in these experiments is peritectic (e.g. Foden and Green, 1992; Wang et al., 2019), occurring on the rims of clinopyroxene crystals (Figure 4.3c). Compositionally, the amphiboles in cooling experiments are also hornblende, however they have lower magnesium contents (≤ $Mg\#_{68}$) than xenolith amphiboles, with the exception of run BA_StV_53 (Figure 4.11). Such compositions likely reflect the availability of certain elements in clinopyroxene and the melt during cooling to lower temperatures. Amphiboles in St. Vincent xenoliths often occur as interstitial or poikilitic grains, or as reaction rims on olivine or clinopyroxene (Figure 4.1; Tollan et al., 2012; Brown, 2022), again indicative of a down-temperature, peritectic reaction.

Olivine

Olivine (Fo_{70}) occurs as small (≤ 10 µm) subhedral crystals in a single cooling experiment (BA_StV_57; Table 4.4). Olivines in xenoliths have slightly higher forsterite contents (Fo_{71} to Fo_{85}; Tollan et al., 2012; Fedele et al., 2021), whereas phenocrystic olivines from the 2021 La Soufrière eruption span a wider range of compositions (Fo_{61} to Fo_{82}; Weber et al., 2024). The absence of olivine as a near-liquidus phase in the experimental results presented here is not unusual for basaltic andesites with relatively low magnesium contents (≤ 4 wt. % MgO; Pertermann and Lundstrom, 2006; Mercer and Johnson 2008; Rader and Larsen, 2013). Olivine stability has been shown to be dependent on water contents, oxygen fugacity and pressure (Feig et al., 2006, 2010; Friese et al., 2009), as well as starting composition (see discussion below).

4.4 Discussion

4.4.1 Near- and sub-liquidus multiple saturation points

Results from the equilibrium experiments presented in this study find the basaltic andesite melt erupted from La Soufrière (SV2021) to be multiply saturated on its liquidus with an amphibole-gabbro assemblage (plag + cpx + amph + mt + ilm; BA_StV_34) at 0.6 GPa, 1020ºC, with 8.2 wt. % H_2O_{melt} at ~ NNO+2 (Figure 4.4b). Saturation of five mineral phases, plus a melt and vapour phase, in a six component system (from PCA; Weber and Blundy, 2024), corresponds to an invariant point on the liquidus at which the melt last equilibrated with the surrounding mush in P-T-H_2O-fO_2 space. The multiple saturation temperature lies close to the eruption temperature for the 2020-2021 eruption (Weber et al., 2024); fO_2 also lies close to estimates for basaltic andesites from St. Vincent (Heath et al., 1998a; Melekhova et al., 2015).

The experimental glass composition in equilibrium with the amphibole-gabbro multiple saturation assemblage in run BA_StV_34 matches closely the composition of the magmas erupted at the surface (Figure 4.6), albeit a little less rich in FeO and TiO_2 due to Fe-Ti oxide crystallisation. True liquidus multiple saturation ideally requires melt fractions ≥ 90% (Asimow and Longhi, 2004; Melekhova and Blundy, 2024). The slightly lower melt fraction of BA_StV_34 is likely a consequence of the peritectic nature of the reaction between clinopyroxene and amphibole, which leads to rapid changes in melt fraction over a narrow temperature interval. A feature of peritectic (and eutectic) reactions is that they occur at near isothermal conditions until one of the reacting phases is entirely consumed (Pelton, 2001). For example, in the peritectic reaction liquid + $solid_1$ = $solid_2$, the liquid will continue to react with $solid_1$, until either phase runs out. In this case, clinopyroxene is $solid_1$ and amphibole is $solid_2$, thus consumption of the melt and clinopyroxene to form amphibole results in melt fraction reduction at a near-constant temperature. Multiple saturation in BA_StV_34 occurs just 20 – 30 °C below the liquidus, therefore this run is considered to have a sufficiently high melt fraction and lies close enough to the liquidus, to be a true liquidus multiple saturation point. Experimental mineral compositions from this run are in good agreement with xenolith compositions (Figures 4.8 - 4.12), with high anorthite plagioclase (An_{85}), magnesium-rich clinopyroxene (≥ $Mg\#_{70}$), and pargasitic to kaersutitic calcic-amphibole present.

Two sub-liquidus multiply saturated runs are identified, one at 0.6 GPa, 1050ºC, with 4.7 wt. % H_2O and F = 41 (BA_StV_13); and the other at 0.8 GPa, 1050ºC, with 5.1 wt. % H_2O and F = 29 (BA_StV_2). Both are in equilibrium with gabbroic assemblages (plag + cpx + opx + mt + ilm), with melt compositions that no longer match the basaltic andesite liquid erupted at the surface, but are instead similar to some of the dacitic melt inclusions (Figure 4.6). Plagioclase (An_{60}), clinopyroxene ($Mg\#_{75}$) and Fe-Ti oxide minerals overlap with certain phenocryst and xenolith compositions, however the extremely magnesium-rich orthopyroxene ($Mg\#_{84}$) in BA_StV_13 is not in agreement with any natural minerals

from St. Vincent (Figure 4.10). Such magnesium-rich orthopyroxenes are however found in meta-igneous xenoliths on the nearby island of Petit St. Vincent ($Mg\#_{79}$ to $Mg\#_{84}$; Melekhova et al., 2022), illustrating that such compositions occur elsewhere in the arc.

Mineral compositions in runs at ≤ 0.35 and 0.8 GPa mostly do not match those in the crustal xenoliths from St. Vincent. For example, experimental plagioclases at 0.35 and 0.8 GPa have low anorthite contents (≤ An_{70}) unlike the characteristically calcic plagioclase of the Lesser Antilles (An_{85} to An_{95}); and magnesium contents in 0.8 GPa experimental clinopyroxenes are generally low (≤ $Mg\#_{70}$). This observation supports a source pressure of the erupted magmas closer to 0.6 GPa than at higher or lower pressures.

The presence of both amphibole and orthopyroxene in cooling experiment BA_StV_39 below the liquidus (F = 32), at 0.6 GPa, 960ºC and 6.5 wt. % H_2O, suggests at different P-T-fO_2-H_2O conditions saturation with amphibole and orthopyroxene, plus plagioclase, clinopyroxene and Fe-Ti oxides could be possible, but the exact conditions depend on the amphibole-orthopyroxene peritectic (Blatter et al., 2017).

4.4.2 Near-liquidus assemblages as a proxy for crustal composition

A liquidus surface phase diagram projected onto P-T space for runs with 85 to 95 wt. % melt is shown in Figure 4.13. The melt fraction range excludes monomineralic runs (> 95 wt. % melt) and those with evolved melt compositions no longer representative of the basaltic andesite starting composition (< 85 wt. % melt). H_2O_{melt} content is contoured. The water saturated liquidus is calculated using MagmaSat (a fluid saturation model; Ghiorso and Gualda, 2015). Dry and 1 - 10 wt % H_2O liquidi are constrained experimentally, guided by both MagmaSat and MAGEMin (a thermodynamic energy minimising model; Riel et al., 2022) estimates. Liquidus mineral stability fields are labelled and their topology derived from near-liquidus mineral assemblages in the

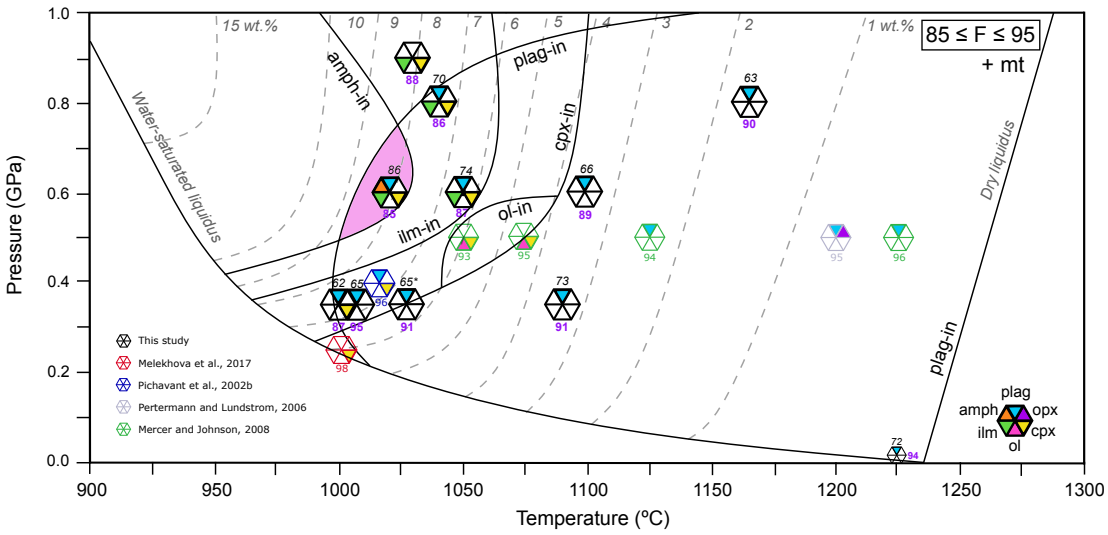


Figure 4.13: Near-liquidus surface diagram (85 ≤ F ≤ 95) in P-T-H_2O space for basaltic andesite melts. Dashed lines represent wet liquidi as wt. % H_2O in the melt; solid black lines show the dry and water-saturated liquidi and mineral stability fields. Filled hexagons show equilibrium experimental phase assemblages. Black outlines hexagons depict experiments performed in this study, with magnetite present everywhere. Numbers below hexagons indicate melt fraction, and numbers above are the plagioclase anorthite contents. Other hexagon outline colours represent previous near-liquidus phase assemblages for basaltic andesite melts with melt fractions up to F = 98: red (Melekhova et al., 2017), blue (Pichavant et al., 2002b), grey (Pertermann and Lundstrom, 2006), green (Mercer and Johnson, 2008). Pink shading highlights region of near-liquidus five-phase multiple saturation. Abbreviations as in Figure 4.1.

experiments reported here. Amphibole is not found on the liquidus at 0.35 GPa and is only stable at water contents ≥ 8 wt. % H_2O, thus the amphibole-in boundary curves to higher water contents at lower pressures. Previous studies that performed equilibrium experiments using basaltic andesite starting compositions similar to SV2021 (Table 4.1) are used to interpolate near-liquidus phase relations outside the P-T range explored in this study. The orthopyroxene stability field is not drawn due to its presence in only one near-liquidus experiment (Pertermann and Lundstrom, 2006). Mineral stability fields are generally in good agreement with predictions from MAGEMin (Riel et al., 2022), though the model fails to identify two separate oxide phases and olivine at near-liquidus conditions.

The liquidus phase assemblages shown in Figure 4.13 represent possible mineral assemblages in the crust, at different P-T-H_2O conditions, in equilibrium with a basaltic

andesite melt. These liquidus phase assemblages agree with natural xenolith assemblages found on St. Vincent (e.g. gabbros, clinopyroxenites, troctolites; Tollan et al., 2012; Fedele et al., 2021), thus can act as a proxy for crustal source region compositions. Gabbroic assemblages (plag + cpx + mt) appear to dominate, with amphibole present at higher water contents (≥ 8 wt. % H_2O), and orthopyroxene present at lower water contents and higher pressures. Plagioclase is present at all conditions except ≥ 0.8 GPa and ≥ 9 wt. % H_2O where clinopyroxene becomes the silicate liquidus phase. Olivine is absent from the liquidus assemblage for the basaltic andesite investigated here, however is observed in experiments performed by Mercer and Johnson (2008), that have a slightly higher magnesium contents in their basaltic andesite starting material (5.4 wt. % MgO; Table 4.1).

Five-phase multiple saturation close to the liquidus at 0.6 GPa (BA_StV_34) suggests that erupted basaltic andesites from La Soufrière likely last equilibrated with an amphibole-gabbro in the lower crust at ~ 1020ºC with ~ 8 wt. % H_2O (pink shaded region; Figure 4.13). The absence of any five-phase MSP's close to the liquidus at all other pressures explored, constrains upper and lower bounds on the estimated source pressure to be 0.6 ± 0.1 GPa. High water content in the source region is required for amphibole stability and is found at other calc-alkaline volcanoes (e.g. Mt Shasta, Cascades; Grove et al., 2003). High water content is also consistent with the relatively low eruption temperature of St. Vincent basaltic andesites (Weber et al., 2024). Melt inclusion data contain 0.9 – 5.3 wt. % H_2O (Bouvier et al., 2008) suggesting melt inclusions do not form in the source region, but during ascent after degassing.

Figure 4.14a shows the liquidus phase assemblages of Figure 4.13 as their respective xenolith assemblages in the crust at different PT conditions. Dashed lines indicate mid-crustal discontinuities (MCD) and Moho depths from Melekhova et al. (2019). The near liquidus five-phase multiple saturation point identified in this study (BA_StV_34; orange

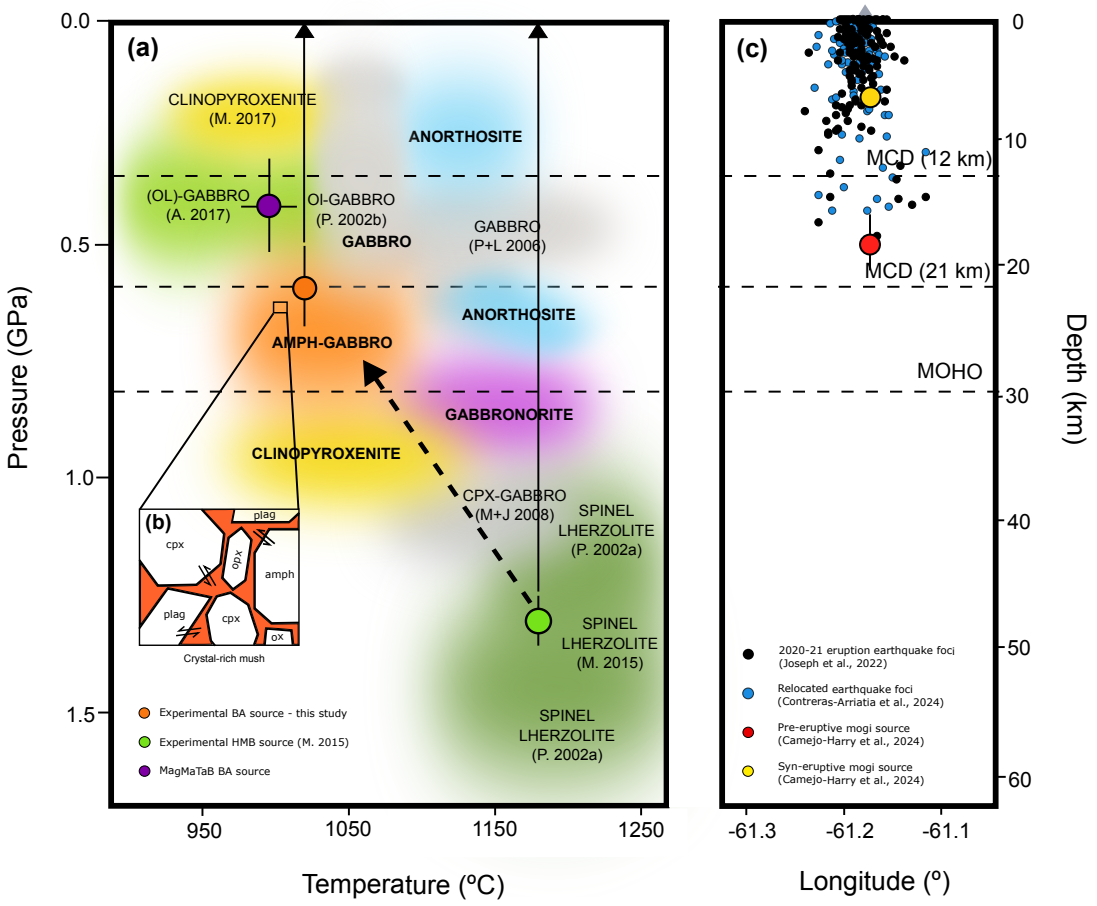


Figure 4.14: Crustal structure beneath La Soufrière, St. Vincent determined using experiments, petrology and geophysics. Dashed lines show estimated mid-crustal discontinuities (MCD) at 12 and 21 km and the Moho at 29 km depth (Melekhova et al., 2019). **(a)** Near-liquidus crustal assemblages shown as corresponding xenolith compositions in pressure and temperature space. Orange circle represents experimental source depth of 2021 La Soufrière basaltic andesite melt (0.6 ± 0.1 GPa, 1020 ± 10ºC). Green circle represents experimental source depth of high-magnesium basalts (HMB) from St. Vincent in equilibrium with a spinel lherzolite assemblage (1.3 ± 0.05 GPa, 1180 ± 10ºC; Melekhova et al., 2015). Purple circle denotes estimated source depth of 2021 La Soufrière basaltic andesite melt using MagMaTaB thermobarometer (0.4 ± 0.13 GPa, 996 ± 21ºC; Weber and Blundy., 2024). Bold xenolith names depict near liquidus phase assemblages determined from experimental runs reported in this study. Other near liquidus assemblages are from experiments with similar basaltic andesite starting materials: M. 2015,2017 – Melekhova et al., 2015,2017; P. 2002a,b – Pichavant et al., 2002a,b; A. 2017 – Andújar et al., 2017; P+L 2006 – Pertermann and Lundstrom, 2006; M+J 2008 – Mercer and Johnson, 2008. **(b)** Schematic of multiple saturation in the source region with an amphibole-gabbro assemblage. Melt is continuously re-equilibrating with the surrounding mineral phases. **(c)** Black circles show earthquake foci from the 2020-21 eruption (Joseph et al., 2022), blue circles depict relocated earthquakes epicentres (Contreras-Arratia et al. 2024). Red and yellow circles show the modelled pre- and syn- eruptive mogi source depths at 18 ± 1.9 km and 6 ± 0.05 km, respectively (Camejo-Harry et al., 2024b).

filled circle) finds the La Soufrière 2020-2021 erupted basaltic andesite melt to have last equilibrated with an amphibole-gabbro assemblage in the lower crust. Previous basaltic

andesite multiple saturation experiments, with similar compositions to the La Soufrière erupted melt (Table 4.1), are also shown as their source mineralogy. For example, Pichavant et al. (2002b) find the basaltic andesite melts erupted at Mt Pelée to be sourced from 0.4 GPa at ≤ 1050ºC and with 5 – 6 wt. % H_2O, in equilibrium with an olivine-gabbro assemblage (ol + cpx + mt), with plagioclase and amphibole present down temperature. Mercer and Johnson (2008) find the basaltic andesites erupted at North Sister volcano (Cascades) to have last equilibrated with a clinopyroxene-gabbro assemblage (cpx + plag) at 1.2 GPa, 1175ºC and with 3.5 wt. % H_2O. Although Arenal basaltic andesites are found not to represent true liquids, and instead reflect a complex crystallisation history (Pertermann and Lundstrom, 2006; Parat et al., 2014), experimental results find plagioclase and orthopyroxene on the liquidus at 0.5 GPa, 1150ºC and with 2 wt. % H_2O. Melekhova et al. (2017) explore the phase relations of basaltic andesites from St. Kitts at 0.24 GPa and find clinopyroxene and magnetite on the liquidus at 1000ºC and 9.8 wt. % H_2O.

Multiple saturation experiments exploring the origin of primitive high-magnesium basalts erupted from the older, more southern, volcanic centres on St. Vincent and the early pre-Somma lavas at La Soufrière (see Chapter 2), found these melts to come from 1.3 GPa, 1180ºC, with 4 – 5 wt% H_2O (green filled circle; Melekhova et al., 2015) and 1.6 – 1.2 GPa, 1230 – 1180ºC with 1.5 and 4.5 wt. % H_2O, respectively (Pichavant et al., 2002a). Magmatism on St. Vincent has migrated north over the last 2 – 3 Ma (Briden, 1979), with the melt composition becoming more evolved over time. In the past, primitive basaltic melts were frequently erupted from the southern volcanic centres (Robertson, 2002), however over the last few hundred-thousand years the currently active volcanic centre (La Soufrière) has produced predominantly basaltic andesite melts (Rowley, 1978; Heath et al., 1998a).

4.4.3 Lower crustal source depth of basaltic andesite magmas at La Soufrière, St. Vincent

Based on Figures 4.13 and 4.14, and the discussion above, source conditions for the La Soufrière erupted basaltic andesites are constrained to lie in the range 0.6 ± 0.1 GPa and ~ 1000 – 1020ºC. These pressures can be converted to depth estimates using crustal density. The crustal structure beneath St. Vincent is known from seismic receiver functions and analysed erupted crustal xenoliths (~ 2.88 to 3.93 g/cm^3; Schlaphorst et al., 2018; Melekhova et al., 2019). Crustal density increases exponentially with depth as described by Tomiya et al. (2010). The following expression is used to describe the crustal density beneath La Soufrière:

$$\rho(z) = \rho_1 + \alpha z - (\rho_1 - \rho_0) \exp\left(-\frac{z}{d}\right) \qquad \text{(Equation 4.2)}$$

where z is depth, ρ is density and $\rho 1, \rho 0, \alpha$ and d are all fitting parameters. This equation can then be integrated to give pressure as a function of depth:

$$P = g \int_0^z \rho(z) \; dz \qquad \text{(Equation 4.3)}$$

where P is pressure and g is gravitational acceleration. A source pressure of 0.6 GPa corresponds to a depth of ~ 21 km and 0.4 GPa to ~ 14 km. With the source pressure constrained to ± 0.1 GPa, the source depth for the basaltic andesite magmas of La Soufrière equates to ± 3.5 km below surface. The close correspondence of the source temperature (~ 1000 – 1020ºC) and the eruption temperatures from mineral thermometry (Weber et al., 2024), suggest that the melt ascended adiabatically from its source to surface, with crystallisation occurring upon decompression. The phenocrysts formed reflect the changing pressure conditions and melt composition during ascent, effectively tracking the near-isothermal phase relations of a fixed basaltic andesite composition to

lower pressures. The presence of zoning in phenocrysts reflects the rapidity of the decompression crystallisation process. Although experiments indicate that amphibole is present in the source, it is notably absent as a phenocryst phase (Davidson et al., 2007a).

The calculated source depth (21 ± 3.5 km) is consistent with several geophysical observations. During the 2020-2021 La Soufrière eruption, three seismic swarms were detected, with the majority of earthquakes located ≤ 5 km depth (Figure 4.14b; Joseph et al., 2022; Contreras-Arratia et al., 2024). Contreras-Arratia et al. (2024) used a non-linear location model (NonLinLoc; Lomax et al., 2000) to relocate the La Soufrière 2021 volcano tectonic (VT) earthquakes to provide more accurate locations. The new earthquake data extend to 15 ± 2.5 km depth (blue circles; Figure 4.14b), with previous depths reaching 17 ± 2.5 km (Joseph et al., 2022). The deepest earthquakes likely indicate locations of magma generation or degassing (Melnik et al., 2020); hotter temperatures and more ductile regimes reduce the number of earthquakes at such locations. Camejo-Harry et al. (2024b) used INSAR to characterise the deformation signal around La Soufrière and determined a Mogi pre-eruptive (point) source depth for the 2021 eruption of 18 ± 1.9 km (red circle; Figure 4.14b).

Melt inclusions can also be used to provide pressure estimates, provided that dissolved volatile contents are unmodified by post-entrapment processes and that melts were volatile-saturated at the time of entrapment. Balcone-Boissard et al. (2023) report melt inclusion data for 28 melt inclusions from the 1902 and AD1477 basaltic andesite eruptions of La Soufrière, St. Vincent. H_2O contents range from 0.8 to 4.0 wt%; CO_2 from 31 to 3227 ppm. The calculated saturation pressures range from 0.012 to 0.645 GPa. The highest pressure (from a single AD1477 melt inclusion) matches our estimated source depth, although the calculated fluid XH_2O (0.05) is significantly lower than that of our multiple saturation experiment (aH_2O = 0.7; Table 4.2). This reflects the fact that melt

inclusions can form at any depth between the source and the surface and do not necessarily provide constraints on the source depth itself.

Whole-rock thermobarometry estimates for the source of the 2020-2021 basaltic andesite melt, saturated with plagioclase, clinopyroxene, Fe-Ti oxides and amphibole, suggest the melt originated at 0.41 ± 0.13 GPa (~ 14 ± 4 km) and 996 ± 21ºC (purple filled circle; Figure 4.14a), calculated using MagMaTaB (Weber and Blundy, 2024). These estimates are within error of the source depth derived from the multiple saturation experiments presented here. Additionally, values overlap with whole-rock thermobarometry P-T estimates for older basaltic andesite magmas erupted at La Soufrière presented in chapter 3.

4.4.4 Calc-alkaline and tholeiitic magmas of St. Vincent

St. Vincent produces magmas that are both Fe-enriched (tholeiitic) and Fe-depleted (calc-alkaline), and are shown to straddle the calc-alkaline and tholeiitic boundary line (Figure 4.15) as defined by Miyashiro (1974). Oxidation state is one of the primary factors thought to control whether magmas become calc-alkaline or tholeiitic, often related to the stability field of Fe-Ti oxides (Osborn, 1959; Pichavant et al., 2002b; Berndt et al., 2005; Feig et al., 2006; Zimmer et al., 2010; Waters et al., 2020). Previous experimental studies that use primitive high-magnesium basaltic magmas erupted from St. Vincent (black star; Pichavant and Macdonald, 2007; Melekhova et al., 2015), or basaltic andesites similar to the La Soufrière 2020-2021 erupted magma (purple star; Pichavant et al., 2002b; Melekhova et al., 2017), as starting material, and constrain and report experimental fO_2, are shown in Figure 4.15a. The data clearly illustrate that experiments performed at ≥ NNO+1.5 (green symbols) evolve along the calc-alkaline trend, and experiments at ≤ NNO+1.5 (blue symbols) follow the tholeiitic trend. Pichavant et al. (2002b) contoured the change from calk-alkaline to tholeiitic differentiation for oxidation

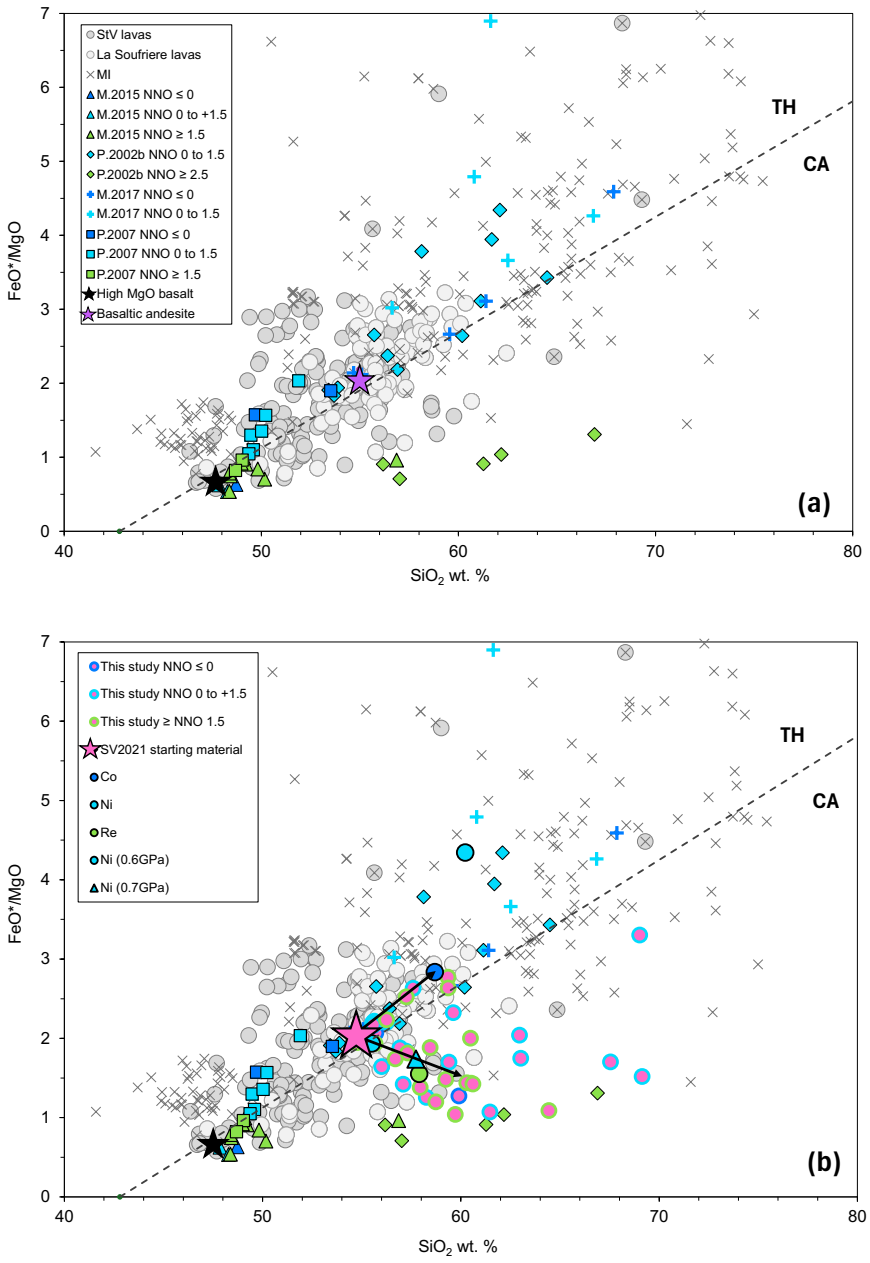


Figure 4.15: FeO*/MgO versus SiO_2 (wt. %) after Miyashiro (1974), where FeO is total iron. The dashed line depicts the calc-alkaline (CA) and tholeiitic (TH) boundary, defined as SiO_2 (wt. %) = 6.4 * (FeO*/MgO) + 42.8. Pale grey and white circles show St. Vincent and La Soufrière lavas straddling the boundary line, and melt inclusion data as crosses. **(a)** Previous experiments that use a basaltic andesite starting material similar to SV2021 (purple star; P. 2002 - diamonds, M. 2017 - crosses) or the St. Vincent high-magnesium basalt (black star; P. 2007 - squares, M. 2015 - triangles), and report experimental fO_2 are plotted here. Oxidation state is divided by colour into clusters of NNO ≤ 0 (dark blue), NNO 0 to +1.5 (pale blue) and NNO ≥ 1.5 (green). **(b)** The same as Figure 4.15a, with experimental data from this study also plotted. All forty-six equilibrium experiments are shown as pink circles with outline colours illustrating fO_2 estimates from Fe content in AuPd capsules (Barr and Grove, 2010). Maximum fO_2 values are used (Table 4.2), though are likely an underestimate (see text). Controlled fO_2 experiments are shown as dark blue (Co-CoO ≈ NNO-2), pale blue (NNO) and green (Re-ReO_2 ≈ NNO+2) symbols. The pink star represents the SV2021 starting material composition and covers the purple star in (a).

state, with the calc-alkaline field at ≥ NNO+1.2 and the tholeiitic field ≤ NNO+1.2. This variation in oxidation state across the calc-alkaline and tholeiitic boundary has also been illustrated by Sisson et al. (2005), Freise et al. (2009) and Marxer et al. (2022).

The equilibrium experiments performed in this study that use a starting material set at NNO+2 are shown in Figure 4.15b (pink filled circles). Outline colours depict the estimated oxygen fugacity from Fe content in AuPd capsules (maximum estimate in Table 4.2; Barr and Grove, 2010). All experiments sit either on the calc-alkaline-tholeiitic boundary line or in the calc-alkaline field, a consequence of early iron depletion likely from Fe-Ti oxide saturation. Crystallisation of one or two Fe-Ti oxide phases close to the liquidus at oxidising conditions depletes the silicate melt in FeO and TiO_2 contents, simultaneously enriching silica (Thy and Lofgren, 1994). Only in more reducing, or drier, environments (e.g. ≤ NNO) does the lack of, or delay in, Fe-Ti oxide crystallisation allow the melt FeO*/MgO content to remain high with little change in silica. Experimental data agree with the natural lava samples and trend towards the dacitic melt inclusions in the calc-alkaline field. Only one experiment from this study is shown with an fO_2 of NNO ≤ 0 (dark blue outline; BA_StV_42), with a minimum calculated fO_2 of NNO-1.5 using the Barr and Grove (2010) model. From its low FeO contents and location in Figure 4.15b, it is likely more oxidised than shown.

The controlled fO_2 experiments performed in this study (NNO-2 to NNO+2), also show a calc-alkaline and tholeiitic divide dependant on fO_2. The Co-CoO experiment (dark blue circle) sits in the tholeiitic field, and the Re-ReO_2 experiment (green circle) sits firmly in the calc-alkaline field. Interestingly, experiments performed at NNO (pale blue symbols) follow both calc-alkaline and tholeiitic differentiation trends, with high water contents. One reason for this divide could be the temperature dependence of magnetite saturation (Baker and Eggler, 1983), found to be ~ 950ºC at ≤ NNO+1 and 995 at ≥ NNO+1.3 for basaltic andesites of a similar composition (Pichavant et al., 2002b). The NNO

experiment from this study that sits in the tholeiitic field (pale blue circle; BA_StV_83) was performed at 980ºC and fractionates 25 % amphibole with only 1 % magnetite, whereas the NNO experiment in the calc-alkaline field (pale blue triangle; BA_StV_91) was performed at 1045ºC and fractionates 1 % magnetite, 1 % ilmenite and 1 % clinopyroxene.

The results presented in Figure 4.15b suggest that the presence of both calc-alkaline and tholeiitic magmas beneath St. Vincent are a function of oxidation state, and ultimately Fe-Ti oxide crystallisation. Experiments at ~ NNO+2 and with variable water contents replicate the calc-alkaline evolutionary trend. Controlled fO_2 experiments, using metal-metal oxide buffers, find that only at more reducing conditions (≤ NNO) do magmas follow the tholeiitic trendline, in agreement with previous experimental studies. The change in fO_2 across the calc-alkaline and tholeiitic divide is on the order of 2-3 log units (this study, Pichavant et al., 2002b), an fO_2 range often observed within arc settings (Brounce et al., 2014; Evans and Tomkins, 2021). Oxygen fugacity estimates for the basaltic andesite magmas of La Soufrière, St. Vincent range from NNO+2 to NNO+4.3; Heath et al., 1998a; Melekhova et al., 2015), too oxidising for tholeiitic differentiation, thus other factors such as water contents, sediment input and intracrustal processes must also play a role in producing tholeiitic basaltic andesite magmas.

4.4.5 Olivine stability in low-magnesium basaltic andesite melts

The absence of olivine in the equilibrium experiments presented in this study, suggests olivine stability in basaltic andesite melts is very sensitive to P-T-H_2O-fO_2 conditions and the chemical composition of the magma. Olivine has previously been found to be absent or a sub-liquidus phase for basaltic andesite melts with ≤ 4 wt% MgO (Pichavant et al., 2002b; Pertermann and Lundstrom, 2006; Rader and Larsen, 2013; Andújar et al., 2017; Melekhova et al., 2017). For example, sub-liquidus olivine is found in only one

experimental run product in the phase equilibria experiments presented by Pichavant et al. (2002b; run HAB7) at 0.4 GPa, 1000ºC, NNO+0.4, with 6.8 wt. % H_2O and a melt fraction of F = 74. Equilibrium experiments performed by Mercer and Johnson (2008) at 0.5 GPa, 1050 – 1075ºC and 5 wt. % H_2O, use a basaltic andesite starting material with 5.4 wt. % MgO and find trace levels of olivine on the liquidus (≤ 0.5 vol. %; Figure 4.13).

Feig et al. (2006, 2010) and Freise et al. (2009) explore the effect of water content and oxygen fugacity on olivine stability in basaltic liquids and find that at more oxidising (and consequentially wetter) conditions, olivine stability reduces. Andújar et al. (2017) find olivine to be present and stable at pressures of 0.1 – 0.2 GPa at ≥ NNO+1, with stability decreasing at higher pressures of 0.4 GPa for a high-magnesium andesite. These experiments, although not basaltic andesite, highlight the narrow stability region of olivine as a liquidus phase in the lower crust.

Olivine is rare in the phenocryst assemblage at La Soufrière (0.6 – 2 vol. %; Weber et al., 2024), with phenocrysts from the dome-forming stage of the eruption displaying extensive symplectite reaction rims, and olivines from the explosive stage having high Fo cores (Fo_{72} to Fo_{82}) and low Fo rims (Fo_{62} to Fo_{66}). Disequilibria textures and low Fo rims suggest olivine is an antecrystic or xenocrystic phase, supported by diffusion modelling and detailed petrographic analysis (Weber et al., 2024; Camejo-Harry et al., 2025). Estimates from diffusion modelling find that olivine crystals were entrained days to years prior to the 2020-2021 eruption, with some olivines entrained up to ten years before the 2020-2021 eruption. The extremely low abundance of olivine in the phenocryst assemblage is still considered small enough to not chemically modify the melt composition during this time.

Xenoliths erupted from St. Vincent often contain fresh, magnesium-rich, unaltered olivine crystals (e.g. ≥ Fo_{71}, Lewis, 1973; Rowley, 1978; Tollan et al., 2012). Thermobarometry

estimates suggest these ol-bearing xenoliths come from ≤ 0.5 GPa, with ol-rich troctolites likely sourced from even shallower depths (0.1 – 0.2 GPa; Melekhova et al., 2019). Further work is required to explore the stability of olivine at lower pressures, representative of shallow crustal conditions. If olivine is a stable low-pressure phase, this may explain the freshness of olivine crystals in xenoliths erupted from St. Vincent and entrained in melts prior to eruption. The incorporation of olivine crystals into the melt several years before an eruption, must have instead occurred closer to the source region, during melt accumulation (Camejo-Harry et al., 2025), suggesting a second, deeper, olivine stability field.

4.4.6 Amphibole-clinopyroxene peritectic

The formation of amphibole on the rim of clinopyroxene in the cooling experiments presented in this study provides textural evidence for the down-temperature peritectic reaction cpx + liq = amph + liq (Foden and Green, 1992; Erdmann et al., 2012; Nandedkar et al., 2014; Wang et al., 2019), in a closed system. Embayed experimental clinopyroxenes support mineral instability and breakdown (Figure 4.3c). Furthermore, the melt compositions in the amphibole-bearing cooling experiments are extremely silica rich (≥ 68 wt. % SiO_2), as expected for incongruent peritectic melting from clinopyroxene breakdown (≥ 64 wt. % SiO_2; Foden and Green, 1992; Kawamoto, 1996) and the production of silica-poor amphibole. The abundance of amphibole in cooling experiments, and crustal xenoliths, supports amphibole stability in the lower crust at temperatures of ≤ 950 – 1020ºC.

Amphibole is found in one equilibrium experiment (BA_StV_34), just below the liquidus (F = 85). The rapid decrease in melt fraction over such a small temperature window (15 % melt over 20 – 30ºC; Figure 4.4b) is characteristic of peritectic reactions (Foden and Green, 1992; Ulmer et al., 2018). Near-liquidus multiple saturation with coexisting

peritectic mineral phases is often difficult to achieve due to mineral metastability close to the peritectic (Asimow and Longhi, 2004). Forced saturation has previously been used to try and navigate this problem (Blatter et al., 2017), however this still requires conditions close enough to the peritectic not to completely consume the added mineral phase.

Previous studies find that interstitial and poikilitic amphibole in xenoliths are the product of the peritectic reaction between clinopyroxene and infiltrating melts rich in REE and incompatible trace elements (Cooper et al., 2016; Brown, 2022). Multiple saturation experiments on dacitic liquids also find the amphibole-orthopyroxene peritectic close to the liquidus (Blatter et al., 2017). Peritectic reactions appear to play a crucial role in controlling near liquidus, polymineralic assemblages in the crust.

4.5 Conclusions

The experimental results presented here find the frequently erupted basaltic andesite magmas of La Soufrière volcano, St. Vincent to be true liquids sourced from the lower crust. Near-liquidus multiple saturation is achieved at 0.6 ± 0.1 GPa, 1020 ± 10ºC, with ~ 8 wt. % H_2O and at ~ NNO+2. Erupted basaltic andesite melts are found to have last equilibrated with an amphibole-gabbro assemblage in the crust, one of the most common xenolith types at St. Vincent. Mineral compositions at the point of multiple saturation are in good agreement with the natural xenoliths, including high anorthite plagioclase (An_{85}), characteristic of the Lesser Antilles, the presence of two Fe-Ti oxides, magnesium-rich clinopyroxene (≥ $Mg\#_{70}$), and pargasitic to kaersutitic calcic-amphibole. Olivine is not stable in the investigated source region. Estimated source pressures of ~ 0.6 ± 0.1 GPa equate to depths of ~ 21 ± 3.5 km, agreeing with geophysical estimates for the pre-eruptive source of the 2020-2021 eruption (18 ± 1.9 km; Camejo-Harry et al., 2024b) and in close proximity to the deepest recorded earthquakes (15 ± 2.5 km; Contreras-Arratia

et al., 2024) but significantly deeper than the highest pressures recorded by melt inclusions.

Multiple saturation is found 20 – 30ºC below the liquidus, at 1020ºC, and is at the upper end of the calculated eruption temperature range for the 2020-2021 eruption (960 – 1020ºC; Weber et al., 2024) supporting near-adiabatic magma ascent. High water contents in the source melt (~ 8 wt. % H_2O) is required for the formation of calcic-rich plagioclase and the stability of amphibole close to the liquidus at low magmatic temperatures (e.g. ≤ 1020ºC; Sisson and Grove, 1993a; Krawczynski et al., 2012). Experimental results highlight the importance of the clinopyroxene-amphibole peritectic reaction in the source region, at near-liquidus conditions. Such peritectic reactions are capable of reducing the melt fraction by consuming the liquid phase at near-isothermal conditions. Crystallisation of Fe-Ti oxides close to the liquidus is found to be ubiquitous at oxidising conditions (~ NNO+2), rapidly depleting the melt in FeO and TiO_2 contents, and encouraging calc-alkaline differentiation. Only at more reducing conditions (≤ NNO) do wet basaltic andesite magmas studied here follow the tholeiitic differentiation trend. These experimental results suggest that oxidation state, and Fe-Ti oxide crystallisation, play a significant role in the formation of calc-alkaline versus tholeiitic magmas, with a difference of only 2 – 3 log fO_2 units needed to change evolutionary trajectory.

Chapter 5

Experimental insight into basaltic andesite lava dome oxidation textures at La Soufrière, St. Vincent.

The findings of the following chapter have been published in "Morrison-Evans, B., Melekhova, E., Blundy, J., 2024. Experimental insight into basaltic andesite lava dome oxidation textures at La Soufrière, St Vincent. SP 539, 121–152. https://doi.org/10.1144/SP539-2022-298". Author contributions are detailed in the paper.

5.1 Introduction

Lava domes are the product of viscous magma extrusion at Earth's surface and can range in composition from basaltic to rhyolitic. Most dome-forming volcanoes experience explosive behaviour alongside effusive dome growth (Newhall and Melson, 1983), from violent vent-clearing eruptions to pyroclastic density currents (PDC's) induced by dome or column collapse (Calder et al., 2015). Depressurisation, degassing and crystallisation are often invoked to explain the effusive-explosive transition at volcanoes by increasing magma viscosity (Hammer et al., 1999; Edmonds and Herd, 2007; Cassidy et al., 2018; Bain et al., 2021). The mineralogy and textures observed in erupted volcanic products offer insight into these controls, for example recording the depth and conditions at which crystallisation occurs (Cashman and Blundy, 2000; Preece et al., 2013). Lava domes are often characterised by unusual alteration textures that are absent in associated explosive phases (Turner et al., 2008; Preece et al., 2016). Determining the origins of these

textures, increases our understanding of where magmas reside prior to the onset of explosive activity, whether in the shallow subsurface or at Earth's surface.

Basaltic andesite lava domes are identified as having the highest frequency of associated explosive activity (Ogburn et al., 2015). Some of the most active basaltic andesite domes include Merapi, Java, Indonesia (Hammer et al., 1999; Voight et al., 2000; Costa et al., 2013; Preece et al., 2013, 2016; Kelfoun et al., 2021), Sinabung, Sumatra, Indonesia (Carr, 2016; Nakada et al., 2019), South Soufrière Hills, Montserrat (Harford et al., 2002; Cassidy et al., 2014), La Soufrière, St Vincent (Heath et al., 1998a; Fedele et al., 2021), Redoubt, Alaska, US (Miller, 1994) and Shiveluch, Kamchatka, Russia (Dirksen et al., 2006; Zharinov and Demyanchuk, 2013; Gorbach et al., 2020). The recent extrusion of a basaltic andesite lava dome, followed by a series of explosive eruptions at La Soufrière, St Vincent, provides a unique opportunity to explore the petrological transition between the effusive and explosive stages of the eruption.

La Soufrière volcano, St. Vincent has throughout its lifetime produced both effusive lava domes and explosive pyroclastic flow deposits (see Chapter 2). Petrological analysis of the 2020-2021 La Soufrière lava dome reveals ubiquitous oxidation textures. Comparison of the natural dome rock to the subsequent explosive scoria phases highlights the lack of any oxidation features in the latter, indicating that oxidation processes affected only the dome-forming magma, either during pre-eruptive storage or upon emplacement. This study uses experimental petrology to explore the conditions and timescales of the formation of distinctive alteration textures in the 2020-2021 basaltic andesite lava dome at La Soufrière volcano, and ultimately increases our understanding of where magmas reside prior to the onset of explosive activity, whether in the shallow subsurface or at Earth's surface, with implications for interpretations of geophysical signals.

5.1.1 Lava dome petrology

Detailed petrological analyses of lava domes provide essential information on dome crystallinity (Swanson et al., 1987; Fink et al., 1990), rate of extrusion (Walker et al., 1973; Huppert et al., 1982; Fink and Griffiths, 1998), magma temperature and oxidation state (Pallister et al., 2008; Ridolfi et al., 2010; Costa et al., 2013; Laeger et al., 2013; Grocke et al., 2016), and porosity and permeability (Colombier et al., 2017; Heap et al., 2019; Darmawan et al., 2022). Petrological studies documenting the alteration and mineral breakdown textures often observed in lava domes allude to high-temperature sub-solidus oxidation during dome growth at the Earth's surface due to, for example, interaction with the atmosphere or groundwater (Von Gruenewaldt et al., 1985; Saito et al., 2004a; Turner et al., 2008). Lava domes are characteristically microlite-rich (Preece et al., 2013; Murch and Cole, 2019) and exhibit the breakdown of some minerals, such as amphibole (Genareau and Clarke, 2010; Ludlam et al., 2018; Gorbach et al., 2020), Fe-Ti oxides (Saito et al., 2004a, b, 2007) and olivine (Weber et al., 2024). There is a paucity of published literature regarding the simultaneous breakdown of co-existing mineral phases, as seen in natural dome rocks, over a range of physico-chemical conditions. In such cases, breakdown or alteration reactions of different phases may operate in tandem. Subsequent explosive phases of similar magma during the same eruptions often appear unaltered and are instead highly vesicular and more glassy (Hammer et al., 1999). In such cases the textural differences between effusive and explosive phases can be used to distinguish the eruptive style and provide insight into changing magma ascent, storage and eruption conditions.

Experimental studies complement petrological findings by providing constraints on the mechanisms and timescales over which dome-rock mineralogy and textures form. Heating and oxidation experiments using natural samples elucidate dome-forming processes, finding that sustained high temperatures play a significant role in facilitating

sub-solidus oxidation at Earth's surface (Vincent, 1957; Buddington and Lindsley, 1964; Haggerty and Baker, 1967; Haggerty, 1976a; D'Oriano et al., 2013, 2014; Knafelc et al., 2019). Synthetic experiments supplement those using natural starting materials by further constraining the stability fields of specific minerals, in pressure, temperature, and oxygen fugacity (P-T-fO_2) space (Turnock and Eugster, 1962; Speidel, 1967; Woermann et al., 1969; Freer and Hauptman, 1978; Sack, 1982; Harrison and Putnis, 1998). Comparison of experimentally produced exsolution textures and compositions, to those in natural samples, are used in this study to identify the magmatic conditions and timescales at which oxidation occurred, and hence infer the likely mechanism responsible.

Oxidation mechanisms

Extruded magmas undergo oxidation at or near the Earth's surface by three main end-member processes: hydrothermal alteration (Ball et al., 2013, 2015; Heap et al., 2019; Darmawan et al., 2022); interaction with air (Saito et al., 2004a; Burkhard, 2005a); or deuteric alteration (Hekinian, 1982; Burgisser and Scaillet, 2007). Of these mechanisms, the first two are considered exogenous, and the third exogenous in terms of the source of the oxidising agent. The processes are not mutually exclusive and may operate in tandem or sequentially. There may be spatial heterogeneity in the extent to which different processes operate, for example with greater oxidation at the sample surface and greater deuteric alteration in the interior.

Hydrothermal alteration involves interactions between magmas and high temperature fluids (< 500ºC; Darmawan et al., 2022) that may be meteoric, seawater, groundwater or surficial (e.g. crater lake) in origin (Ball et al., 2013). Oxidation of primary magmatic minerals to form hydrothermal alteration textures and deposit secondary hydrous minerals such as clays (Ball et al., 2015) typically occurs on timescales of months to years (Heap et al., 2019).

Lava emplaced at the Earth's surface inevitably interacts with the atmosphere and consequently can become oxidised. High temperatures are required for such oxidation reactions to be kinetically feasible on eruption timescales (Burkhard, 2001, 2005a). Examples of maintained heat sources at the Earth's surface include lava lakes, growing lava domes, or the extrusion of successive lava lobes (Saito et al., 2004a; Burkhard, 2005a, b). The ability of air to penetrate into extruding magma, via pore spaces or growing microfractures, controls the pervasiveness of the oxidation observed (Colombier et al., 2017). Thus, oxidation is more likely to affect the exposed exterior surface of domes rather than their interiors.

Deuteric alteration involves the auto-oxidation (or reduction) of a magma by volatile species (e.g. H_2O or SO_2) produced by the magma itself, either during degassing or crystallisation (Sato and Wright, 1966; Mathez, 1984; Holloway, 2004; Burgisser and Scaillet, 2007). The composition and mass of exsolved water and sulfur in an ascending magma, determines the extent of oxidation or reduction, of up to ± 2 log fO_2 units (Anderson and Wright, 1972; Hekinian, 1982; Carmichael and Ghiorso, 1986; Burgisser and Scaillet, 2007). The fact that both oxidation and reduction can occur reflects the different speciation and solubility of, for example, H_2, H_2S and SO_2, in fluids and melts. The influence of CO_2 is considered to be negligible (Burgisser and Scaillet, 2007). Deuteric alteration tends to effect pore spaces, volcanic glass and interstices between crystals, often recorded by zoning and exsolution around the rims of iron-titanium oxide minerals (Duchesne, 1972), and can occur either at the Earth's surface or during sub-surface storage and cooling, for example in volcanic conduits. Previous studies find the extent of oxidation within an extruding magma to be related to the ability of water to dissociate, and hydrogen to escape from a magma, subsequently increasing the oxidation state (Sato and Wright, 1966; Mathez, 1984; Burkhard, 2005a). Gas streaming, whereby fluids released from deeper parts of the same magmatic system interact with hot, extruded magma, may also be considered a variant of deuteric alteration.

Iron-Titanium oxides

Fe-Ti oxides are typically one of the first minerals to crystallise at the liquidus of basaltic andesite magmas, hence they may become unstable in the presence of melt at low temperatures and can readily oxidise at Earth's surface (Haggerty and Baker, 1967; Woermann et al., 1969; Goode, 1974; Nitsan, 1974; Haggerty, 1976a,b). The structure and composition of Fe-Ti oxides varies widely, with the most common oxide groups being the cubic spinels (AB_2O_4) and rhombohedral ilmenites (ABO_3), each forming a variety of solid solutions. The ulvöspinel (Fe_2TiO_4) - magnetite (Fe_3O_4) solid solution (usp-mnt) is particularly common in volcanic rocks, along with the spinel ($MgAl_2O_4$) - hercynite ($FeAl_2O_4$) and pleonaste ($(MgFe)Al_2O_4$) - magnesioferrite ($MgFe_2O_4$) solid solutions. In more evolved magmas it is the ilmenite ($FeTiO_3$) - hematite (Fe_2O_3) solid solution (ilm-hmt) that becomes predominant (Haggerty, 1976a, b). Geikielite ($MgTiO_3$) and qandilite (Mg_2TiO_4) are the magnesian end-members of ulvöspinel and ilmenite, respectively, found almost exclusively as minor components in spinels from Mg-rich magmas (Pascal et al., 2011). The terms 'titanomagnetite' and 'titanohematite' are commonly used, and are used hereafter, to refer to intermediate oxides within the usp-mnt and ilm-hmt solid solutions, respectively (Buddington and Lindsley, 1964).

Co-existing titanomagnetite and titanohematite pairs are frequently used as thermo-oxybarometers to estimate the temperature and oxidation state (expressed as fO_2) of a magma prior to eruption (Buddington and Lindsley, 1964; Frost and Lindsley, 1991; Lepage, 2003). Fe-Ti oxides re-equilibrate relatively quickly (<100 hrs; Freer and Hauptman, 1978; Gardner et al., 1995; Venezky and Rutherford, 1999; Hou et al., 2021) to changes in P-T-fO_2, and thus record the most recent magmatic conditions experienced, including slow, sub-solidus cooling in some cases (Hammond and Taylor, 1982). During re-equilibration, Fe-Ti oxides may undergo exsolution, with different exsolving phases and textures dependant on the initial grain composition and new P-T-

fO_2 conditions (Nickel, 1958). One of the challenges in interpreting oxide exsolution features is the many solid-solutions and potential exsolution mechanisms involved (Arguin et al., 2018).

Petrological analyses of naturally exsolved Fe-Ti oxides commonly find the oxidation-exsolution of ilmenite from magnetite, with ulvöspinel exsolving initially and subsequently oxidising to ilmenite (Verhoogan, 1962; Buddington and Lindsley, 1964; Grommé et al., 1969; Duchesne, 1972; Arguin et al., 2018; Hu et al., 2015). Pleonaste and magnesioferrite are also found to exsolve from magnetite (Haggerty, 1976a; Sack, 1982; Von Gruenewaldt et al., 1985). Oxidation-exsolution textures progress, with increasing oxidation, from fine cloth-like lamellae, to coarser and more irregular 'sandwich-type' lamellae, to uniform trellis lamellae and granules, and finally to vermicular exsolution and external recrystallisation (Buddington and Lindsley, 1964; Haggerty, 1976a). The formation of exsolution lamellae along grain boundaries and fractures supports oxidation-exsolution by the external environment, such as air (Haggerty, 1976a, 1991). Complete recrystallisation and reprecipitation of exsolving phases to form grains with triple junctions can occur when conditions are highly oxidising, or in high stress environments where re-equilibration timescales are protracted (Von Gruenewaldt et al., 1985; Duchesne, 1972; Pang et al., 2007).

Heating and oxidation experiments using naturally exsolved Fe-Ti oxides have previously explored the re-homogenisation of exsolution features (Vincent et al., 1957; Nickel, 1958; Price, 1980), the diffusivity of cations between phases and their associated activation energies (Creer et al., 1970; Petersen, 1970; Freer and Hauptman, 1978; Price and Putnis, 1979; Freer and O'Reilly, 1980; Price, 1981), the influence of Mg, Al, Cr, Mn, Zn substitutions (Sack, 1982; Von Gruenewaldt et al., 1985; Lattard, 1995) and solid solution solvus temperatures (Vincent et al., 1957; Turnock and Eugster, 1962; Woermann et al., 1969; Muan et al., 1972; Harrison and Putnis, 1998; Frost, 1991; Tan et al., 2016). The

exsolution of titanohematite and pleonaste from titanomagnetite is found to be above 600ºC and 900ºC, respectively (Tan et al., 2016); the exsolution of hercynite from magnetite above 860ºC at the FMQ buffer and 2 kbar (Turnock and Eugster, 1962); and the exsolution of magnesioferrite from magnetite above 823ºC (Harrison and Putnis, 1998). There are few studies, however, that investigate the exsolution of numerous co-existing oxide phases from complex solid solutions in natural rocks.

Olivine

Olivine is generally confined to lava domes with more primitive/high-magnesium basaltic andesite compositions (e.g. Merapi, Costa et al., 2013; Arenal, Reagan et al., 1987; Kelud, Utami et al., 2021; St. Vincent, Weber et al., 2024). Olivine is unstable in the presence of melt at low temperatures (< 1180ºC at 1 atm; Nicholls and Ringwood, 1974), thus may break down during ascent, eruption and cooling at Earth's surface (Nitsan, 1974; Goode, 1974; Champness, 1970; Moore et al., 2022). Olivine symplectites (vermicular exsolution textures) form by either discontinuous or continuous breakdown, producing intergrowths of either orthopyroxene and magnetite (discontinuous), or high-forsterite (Fo) olivine and hematite (continuous) (Johnston and Stout, 1984; Del Moro et al., 2013). Analyses of natural olivine symplectites found the composition of exsolved phases to depend on the forsterite content of the initial olivine crystals (Moseley, 1984; Ejima et al., 2013, 2017), and whether exsolution occurred by atmospheric oxidation (Haggerty, 1976a; Gualtieri et al., 2003; Knafelc et al., 2019) or by magma mixing (Ueki et al., 2020). High degrees of oxidation can produce rims of Fe-oxides along grain boundaries, of variable thickness, known as oxide diffusion rims. Such rims reflect the efficient diffusion and subsequent oxidation of iron from the host olivine crystal. They are often composed of hematite in association with Fe-depleted adjacent olivine (Haggerty and Baker, 1967). Previous experimental studies also highlight the temperature dependence of the extent of olivine exsolution (Knafelc et al., 2019; Moore et al., 2022).

Pyroxene

Orthopyroxene and clinopyroxene are common in basaltic andesite magmas and are part of the stable mineral assemblage in La Soufrière lavas. The composition of two co-existing pyroxene phases can be used to determine crystallisation temperatures by two-pyroxene thermometry (Wells, 1977; Lindsley and Anderson, 1983; Putirka, 2008). Slow cooling may result in pyroxenes undergoing sub-solvus exsolution, skewing thermometry estimates; but instead providing new, reset values for equilibration temperatures (Kuno, 1966; Longhi and Bertka, 1996). Orthopyroxene and clinopyroxene are stable over different P-T ranges, often determined experimentally (Kuno, 1966; Canil, 1994) and as described in Chapter 4 (Figure 4.4). Pyroxenes can also form as reaction products from the oxidation and breakdown of olivine (Johnston and Stout, 1984; Barton and Van Gaans, 1988; Barton et al., 1991), garnet (Ringwood and Lovering, 1970), and clinopyroxene (Boland and Otten, 1985).

5.2 Methods and materials

5.2.1 Experimental Methods

The starting material selected for this experimental study is the basaltic andesite scoria from the 2020-2021 eruption at La Soufrière, St. Vincent. The scoria (LS21-38a) is from the U3 phase (see Cole et al., 2024 for further details) of the explosive sequence and was collected hot in April 2021. The bulk chemical composition of the dome and scoria from this eruption are very similar (Table 5.1) and both contain the same phenocryst assemblage (plag + cpx + opx + tmt ± ol), although microlite assemblages and compositions differ (Table S5.1; Frey et al., 2024; Weber et al., 2024). The scoria provides a sample of the 2020-2021 magma that quenched rapidly, thus remaining fresh and unmodified by surface processes. By subjecting this magma to different

Table 5.1. Whole rock compositions of dome and U3 scoria

	Dome		Scoria		
	average*	**sd**	**LS21-38a***	**average U3 scoria***	**sd**
SiO_2	54.68	0.23	53.92	53.75	0.49
TiO_2	1.01	0.02	0.97	0.95	0.03
Al_2O_3	17.79	0.1	18.38	18.52	0.37
FeO^T	8.33	0.13	8.31	8.25	0.23
MnO	0.21	0	0.2	0.19	0.01
MgO	3.73	0.08	3.84	4.19	0.34
CaO	8.38	0.08	8.81	8.93	0.12
Na_2O	3.33	0.05	3.19	3.27	0.07
K_2O	0.58	0.01	0.56	0.54	0.02
P_2O_5	0.13	0	0.13	0.13	0.01
Total	98.17		98.31	98.72	
n	8			9	

* Analysed using XRF by Weber et al. 2024

n is number of analyses

experimental conditions, I aim to explore whether the dome- and scoria- forming magmas could plausibly be derived from similar batches of basaltic andesite magma that experienced distinctive surface and near surface conditions, giving rise to the observed textural differences.

The LS21-38a scoria was lightly crushed in an agate mortar, allowing phenocrysts to be preserved and only the interstitial groundmass to become powdered and disaggregated. This technique enables new microlites to grow in the groundmass, if run for sufficient time, and facilitates reactions between phenocrysts and the interstitial reactive melt during experimental runs (Cassidy et al., 2019). The crushed scoria was mixed with PVA glue as a binder and loaded onto thin platinum wire loops. The Pt wire was later analysed to ensure that no Fe-loss had occurred. In total, eight one-atmosphere experiments are reported, carried out in a vertical furnace and air-quenched, each at a different fO_2 and temperature (Table 5.2). Oxygen fugacity was set using a CO_2-CO gas mix (Deines et al., 1976) and calibrated before each experiment using an yttria-doped zirconia probe and the Nernst equation (Boulliung et al., 2020). Experiments run in air did not require

fO_2 calibration. The temperature was set with a Eurotherm temperature controller and calibrated to the melting point of gold using a type-B thermocouple at the furnace hotspot. Charges were lowered into the hot zone of the furnace and run for the duration of a week, to facilitate chemical exchange (Freer and Hauptman, 1978; Cottrell et al., 1999) on a comparable timescale to that experienced by the natural dome at the surface.

Subduction zone magmas, such as those from St. Vincent, have oxidation states in their sources between NNO-2 and NNO+2 (Carmichael, 1991; Cashman, 1992; Heath et al., 1998a), where NNO denotes the nickel-bunsenite reference curve at the P-T of interest, typically becoming more oxidised upon eruption as they crystallise and degas (Mathez, 1984; Burgisser and Scaillet, 2007). Basaltic andesite eruption temperatures are typically in the range of 1000 to 1200ºC, depending on initial volatile content and ascent trajectory through P-T space (Gaetani et al., 1994; Moore and Carmichael, 1998). Estimates of the eruption temperature of the 2020-2021 St. Vincent basaltic andesites, are in the range ~ 960 – 1020ºC (Weber et al., 2024) and estimated fO_2 for similar historic magmas are in the range of NNO to NNO+2 (Heath et al., 1998a), with some estimates of up to NNO+4.3 (Melekhova et al., 2015). The one atmosphere basaltic andesite solidus under anhydrous (fully degassed) conditions is at or slightly below 900ºC (Schiavi et al, 2009). Therefore, experimental conditions chosen here include two temperature series of 900 and 1020ºC; oxygen fugacities of NNO-2, NNO, NNO+2 and air; and run durations of a week, each to allow for comparison with the natural dome that extruded at the surface less than twenty days prior to sampling.

5.2.2 Analytical Methods

Experimental run products were mounted in epoxy, polished, and analysed on a Cameca SX-5 FE electron microprobe at the Department of Earth Sciences, University of Oxford. Phenocrysts and microlites were analysed with a focused beam, at an accelerating

potential of 15 keV and beam current of 20 nA (10 nA for microlites). Secondary standards include SJI olivine, labradorite and glass (T1, GOR128 and KL2G; Table S4.2). Total iron was determined as Fe^{2+} (FeO^T). For iron oxides containing Fe in more than one valence state, FeO^T was recalculated to Fe^{2+} and Fe^{3+} on the basis of stoichiometry and checked by charge balance. Oxides were normalised to 32 oxygens, those with 21 cations forming part of the rhombohedral oxide group and those with 24 cations the cubic oxide group. High resolution back scattered electron (BSE) images were acquired using the Zeiss Merlin (field emission gun - FEG) and Zeiss Evo (tungsten filament) scanning electron microscopes (SEMs) at the Department of Materials, University of Oxford. Analytical conditions were 20 keV accelerating potential and 5 nA beam current. Thin sections of the dome (SV3) and scoria (LS21-38a) rock samples were also imaged on the SEM using the same analytical conditions. Chemical analyses of the natural dome and scoria samples were carried out by Frey et al. (2024) and Weber et al. (2024). Representative analyses of whole-rock are presented in Table 5.1 and mineral compositions in Table S5.1.

5.3 2020-2021 La Soufrière lava dome and scoria petrology

Both the effusive dome and explosive scoria phases of the 2020-2021 eruption have a basaltic andesite bulk composition, with 45 – 50 vol. % phenocrysts in a microlite-rich or vesicular groundmass respectively. Phenocrysts (volume percentages and compositions from Weber et al., 2024), in order of abundance, are plagioclase (An_{60} to An_{86} ; ~ 26 vol. %), orthopyroxene ($Mg\#_{67}$ to $Mg\#_{70}$; ~ 8 vol. %), clinopyroxene ($Mg\#_{71}$ to $Mg\#_{73}$; ~ 6 vol. %), titanomagnetite (Ti pfu 0 – 0.6; ≤ $Mg\#_{46}$; ~ 5 vol. %) and olivine, which is notably rarer in the dome than the scoria (Fo_{74} to Fo_{82} and 0.5 vol.% in dome; Fo_{65} to Fo_{75} and ~ 2 vol. % in scoria). Although phenocryst phase assemblages and bulk compositions in the dome and scoria are almost identical, the phenocrysts in the dome are texturally distinct to those in the erupted scoria. Dome textures are suggestive of breakdown

reactions of mineral phases originally co-existing with melt in the dome-forming magma (Figure 5.1, and shown in Joseph et al., 2022). The lack of such textures in the scoria highlights the difference in eruptive conditions (*sensu lato*) between the two stages of the eruption. Microlite assemblages in the dome (plag + opx + ox) and scoria (plag + opx + cpx ± ol ± ox) units are also different (Frey et al., 2024).

5.3.1 Textural differences

Microlites.

The scoria groundmass is vesicular and glassy, with swallow-tail and acicular microlites (1 – 30 μm; Cashman, 1992) of dominantly plagioclase and pyroxene (Figure 5.1a). The groundmass of the dome is instead more crystalline with microlites appearing slightly larger than those in the scoria (Figure 5.1b) and composed of laths of plagioclase and pyroxenes rimmed with oxide nanolites (defined as microcrystals < 1 μm in size; Mujin et al., 2017). Oxide microlites and nanolites are notably more abundant in the dome.

Pyroxene phenocrysts.

Orthopyroxene and clinopyroxene phenocrysts in the scoria and dome are subhedral, fractured, and contain inclusions of oxides and melt (Figure 5.1c, d). In the dome, orthopyroxene phenocrysts are rimmed with iron oxide nanolites (Figure 5.1d), similar to those seen around the pyroxene microlites. There are no obvious alteration textures seen in clinopyroxene.

Iron-titanium oxide phenocrysts.

Titanomagnetites in the scoria are homogenous with no evidence of exsolution (Figure 5.1e). Fe-Ti oxides in the dome, on the other hand, are significantly altered, displaying a range of exsolution textures. Four different styles of exsolution are observed (Figure 5.1f)

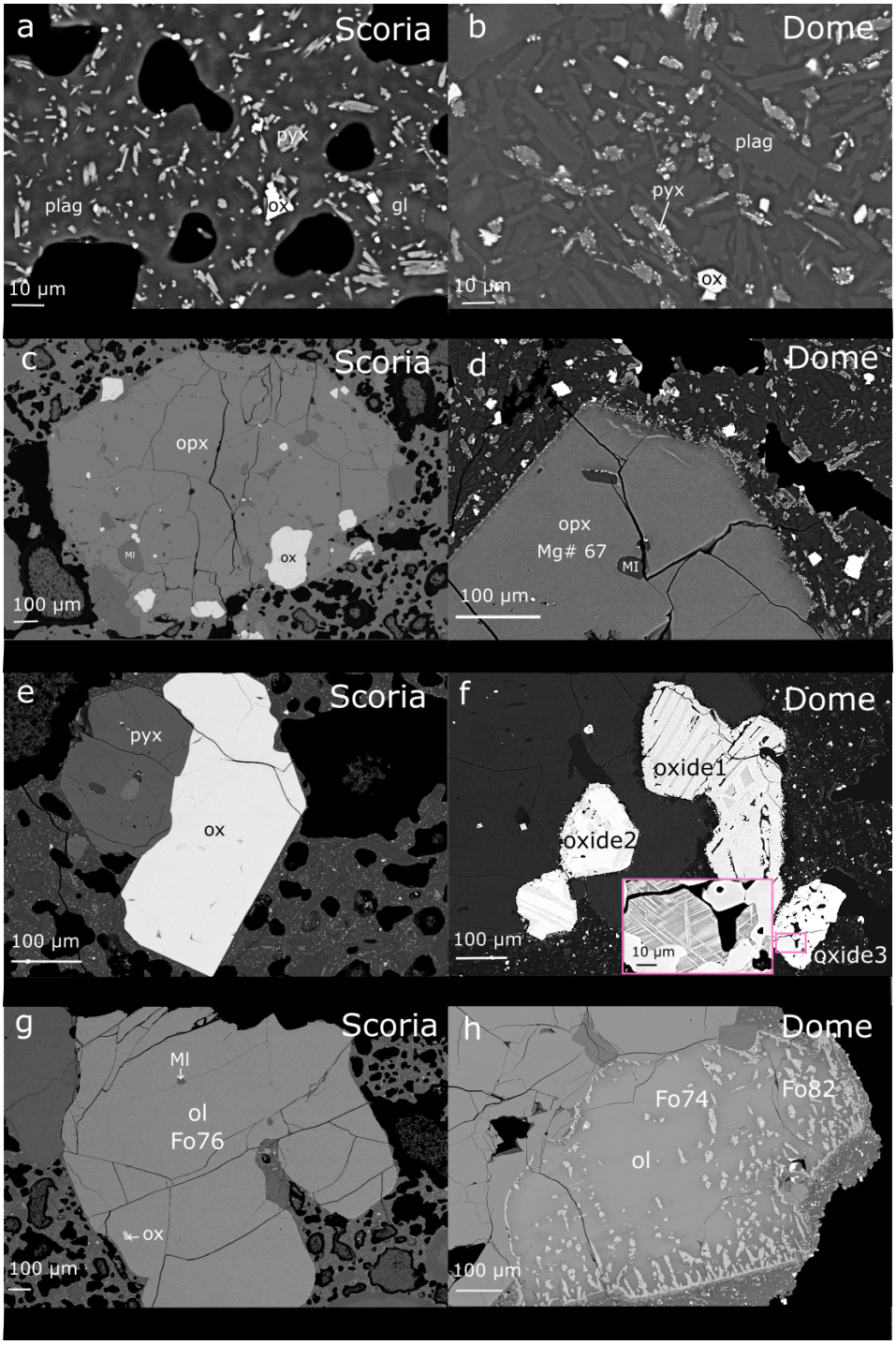


Figure 5.1: Backscattered electron (BSE) images of the textural differences between the erupted dome and scoria material. (**a**) Glassy and vesicular scoria groundmass with skeletal microlites. (**b**) Microlite-rich dome groundmass containing oxide-rimmed pyroxene microlites. (**c**) Homogenous orthopyroxene phenocryst in scoria. (**d**) Orthopyroxene phenocryst in dome rimmed with oxides along grain boundaries (**e**) Homogenous oxide phenocryst in scoria. (**f**) Oxide phenocrysts in dome exhibiting different types of exsolution lamellae (oxide 1-3). Oxide 1 displays uniform trellis lamellae; oxide 2 displays irregular 'sandwich-type' lamellae, and oxide 3 contains cloth exsolution lamellae and recrystallised grains – see inset. (**g**) Homogenous olivine phenocryst in scoria. (**h**) Olivine phenocryst in dome exsolving Fe-oxide symplectites. Abbreviations: gl, glass; pyx, pyroxene; opx, orthopyroxene; plag, plagioclase; ox, oxide; ol, olivine; MI, melt inclusion.

and are described following Buddington and Lindsley (1964) and Haggerty's (1976a) classification schemes: cloth-like, sandwich-type, trellis lamellae, and recrystallisation granules. These oxide exsolution textures are described as oxides 1 – 4 in the subsequent discussion. Oxide 1 illustrates well-developed coarse trellis lamellae along two planes, forming exsolution cells in the centre of the grain. Oxide 2 displays 'sandwich-type' lamellae, with irregular exsolution bands. Oxide 3, previously connected to oxide 1, as evidenced by their irregular adjacent grain boundaries, is dominated by recrystallised external granules of a white (high-Z) phase in the BSE image and contains pockets of a dark grey (low-Z) phase displaying fine cloth-like exsolution lamellae along three different planes (Figure 5.1f inset). Cloth-like exsolution textures are usually associated with sub-solvus exsolution (≤ 600ºC; Arguin et al., 2018) and could represent further exsolution during cooling. Oxide 4 (not shown) is similar to oxide 2 in that it forms irregular 'sandwich type' lamellae, but instead predominantly along grain boundaries and fractures.

Olivine phenocrysts.

As noted above, olivine is significantly more abundant in the scoria than in the dome. Olivine phenocrysts in the scoria form subhedral, homogenous, unzoned crystals, with fractures and sometimes containing oxide or melt inclusions (Figure 5.1g). A detailed study on the different types of olivine crystals identified in the scoria, include findings of zoned antecrysts and xenocrysts (Camejo-Harry et al., 2025) However I consider only the phenocrystic olivines here, grown from the melt. Olivines in the dome are rarer, and those identified are heavily altered, with symplectitic exsolution occurring predominantly along grain boundaries and fractures (Figure 5.1h). Symplectites extend inwards towards the centre of the crystal and appear to grow as fibrous lobes, previously described as 'budding' (Haggerty and Baker, 1967).

5.3.2 Compositional differences

Microlites.

Plagioclase microlites in the scoria have a slightly higher anorthite content than those in the dome, for example An_{79-56} (scoria) and An_{75-51} (dome) in terms of core-rim values (Table S5.2, Frey et al., 2024). Conversely, pyroxene microlites appear to be compositionally similar in both the dome and scoria (opx $Mg\#_{67}$ and $Mg\#_{69}$; cpx $Mg\#_{76}$ and $Mg\#_{78}$). Oxide microlites are more abundant in the dome and are ulvöspinel-rich (higher Ti and Fe^{2+}) compared to the few oxide microlites in the scoria (5.4 vol. % vs 0.2 – 0.9 vol. %; Frey et al., 2024); with both containing minor concentrations of MgO (≤ 6 wt. %) and Al_2O_3 (≤ 6 wt. %). Olivine microlites in the scoria range from Fo_{68} to Fo_{74}; no olivine microlites were identified in the dome.

Pyroxene phenocrysts.

Both the orthopyroxene ($Mg\#_{67}$ to $Mg\#_{70}$) and clinopyroxene ($Mg\#_{71}$ to $Mg\#_{73}$) phenocrysts in the dome and scoria are compositionally very similar, with little titanium and aluminium present (< 0.4 wt. % TiO_2 and < 1.5 wt. % Al_2O_3 in orthopyroxene and < 0.7 wt. % TiO_2 and < 2.3 wt. % Al_2O_3 in clinopyroxene; Table S5.2). There is no sign of zoning or compositional variation from crystal cores to rims.

Iron-titanium oxide phenocrysts.

Two distinct oxide compositions are found in the scoria, one ulvöspinel-rich (higher Ti and Fe^{2+}) and one magnetite-rich (higher Fe^{3+}, Mg, and Al; Table S5.2). Different Fe-Ti oxide compositions are typical in island arc magmas and can reflect different crystallisation pressures, magma mixing or crustal assimilation during ascent (Barnes and Roeder, 2001). In the dome, four compositionally distinct host and exsolved oxide

phases are found, following the four different exsolution textures previously described (see above). Oxide 1 is an ulvöspinel-rich titanomagnetite host, exsolving an Mg-Fe-Al spinel. Oxide 2 and oxide 4 are titanomagnetites exsolving titanohematite, with variable Mg, Fe, Al and Ti contents. Oxide 3 appears to be predominantly recrystallised hematite, with pockets of a dark grey (in BSE) Mg-Fe-Al spinel (pleonaste-magnesioferrite), which further exsolves a magnetite-rich phase as cloth-like lamellae (Figure 5.1f inset). Oxide 3 contains no titanium except along the grain boundary previously in contact with oxide 1, suggesting diffusion of titanium between adjacent grains prior to separation.

Olivine phenocrysts.

Olivine phenocrysts in the scoria have forsterite contents of Fo_{65} to Fo_{75} separated into two distinct groups by their different manganese contents. Olivines with ~ Fo_{65} contain ~ 0.6 wt. % MnO, whereas those with ~ Fo_{75} contain ~ 0.4 wt. % MnO (Table S5.2). Mn-Mg exchange within olivine is recognised to be a function of temperature, pressure and fO_2 (Evans et al., 2006; Blundy et al., 2020) and variations in these parameters could account for the variable MnO contents. Forsterite values agree with those reported by Camejo-Harry et al. (2025) for phenocrystic olivine in the scoria (Fo_{63} to Fo_{73}). Olivine crystals in the dome range from Fo_{74} in the centre of the crystal, to Fo_{82} adjacent to symplectite exsolution at the crystal edge. The composition of the exsolved Fe-oxide phase could not be analysed directly due to the very fine grainsize of the symplectites (< 1 μm). The high Fo content (Fo_{82}) and lack of orthopyroxene does, however, suggest the continuous breakdown of olivine, as described above, with hematite as the product Fe-oxide phase (Haggerty and Baker, 1967; Champness, 1970; Johnston and Stout, 1984). Equation 5.1 is a balanced reaction that describes the oxidation-exsolution of olivine to form hematite symplectites in the St. Vincent dome; where the primary olivine (Fo_{74}; in the centre of the crystal, Figure 5.1f) oxidises to form an Mg-enriched olivine (Fo_{82}), hematite and melt (SiO_2):

$$8.5\ Mg_{1.5}Fe^{2+}_{0.5}SiO_4 + 0.5\ O_2 = 7.5\ Mg_{1.7}Fe^{2+}_{0.3}SiO_4 + Fe_2O_3 + SiO_2$$

(Equation 5.1)

5.4 Experimental Results

Experimental run conditions and phase assemblages for eight runs are reported in Table 5.2 and phase compositions in Table S5.2. Microlites were analysed where sufficiently large (≥ 2 μm). Plagioclase, orthopyroxene, and clinopyroxene phenocrysts were analysed in all runs, with olivine and Fe-Ti oxides identified in all runs except SV28 and SV29. Figure 5.2 illustrates the experimentally-derived stability limits in T-fO_2 space of orthopyroxene phenocrysts; newly exsolved and co-existing Fe-Ti oxide phases and their textures; and the development of olivine symplectites. Plagioclase and clinopyroxene phenocrysts remain stable at all experimental conditions and are texturally and compositionally consistent within both the dome and the scoria. Orthopyroxene phenocrysts are stable at 900ºC, but progressively breakdown with increasing fO_2 at 1020ºC (dashed line; Figure 5.2). Host Fe-Ti oxides exsolve one or two new oxide phases at certain T-fO_2 conditions, with three co-existing oxides present at NNO+2 in both temperature series, and above NNO+2 at 900ºC (Figure 5.2). Exsolution textures also vary with temperature and fO_2. Olivine symplectites form at and above NNO. A detailed description of the textural and compositional differences in each experiment, and comparison with the dome and scoria, are presented below.

5.4.1 Textural variations

Microlites.

Microlites of plagioclase are present in all experimental runs and appear as elongate laths, with larger crystals sometimes exhibiting normal zoning (Figure 5.3). The smaller microlites (≤ 10 μm) most likely grew during experimental runs, as seen in previous

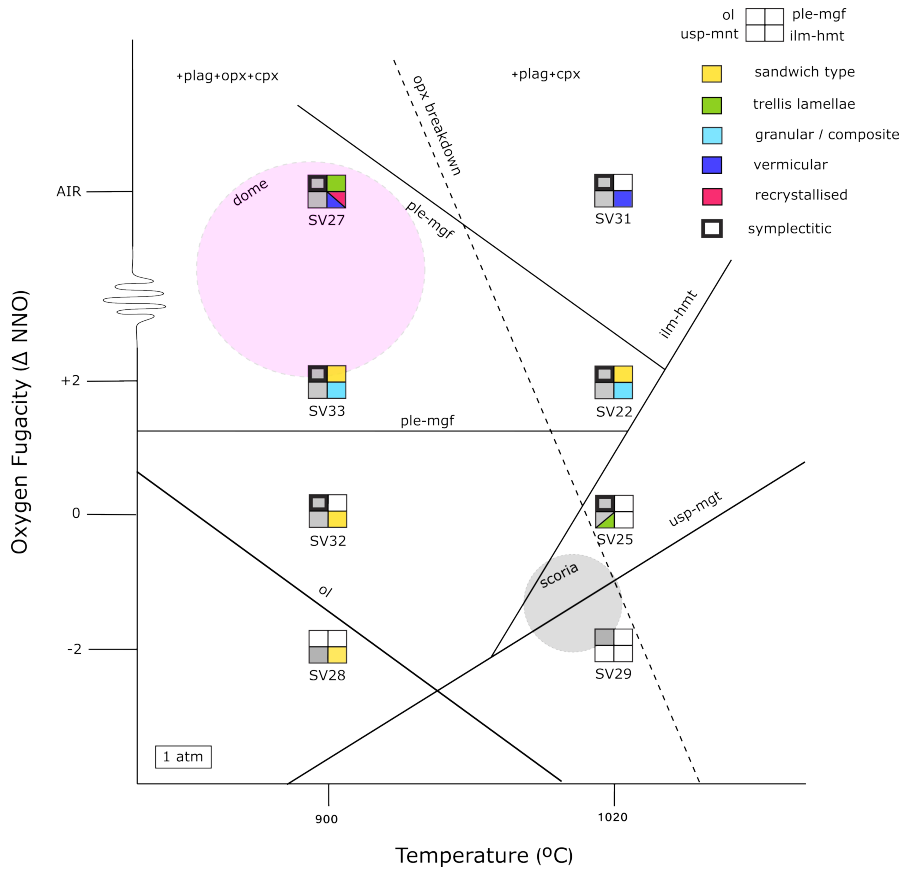


Figure 5.2: Experimental phase diagram illustrating stability of iron-titanium oxide exsolution phases and textures, olivine symplectites and orthopyroxene in T-fO_2 space at one atmosphere. Grey shading illustrates phases present, with different colours representing the type of exsolution observed. Exsolution descriptions after Haggerty (1976a). Dashed line depicts breakdown of orthopyroxene. Pink and grey shaded areas represent proposed T-fO_2 conditions for the dome forming rocks and scoria upon eruption. Abbreviations as in Figure 5.1 as well as usp, ulvöspinel; mnt, magnetite; ilm, ilmenite; hmt, hematite; ple, pleonaste; mgf, magnesioferrite.

reheating experiments (D'Oriano et al., 2013; Deardorff and Cashman, 2017) whilst larger microlites (10 – 30 μm), exhibit new rim overgrowths and are likely remnant from the crushed scoria starting material. Pyroxene microlites are also present in all experimental runs and are acicular to subhedral in form. A small proportion of pyroxene microlites display minor alteration at NNO and 900ºC (Figure 5.3c), however ubiquitous breakdown of pyroxene microlites only begins at NNO+2 in both temperature series. The breakdown process involves pyroxene microlites becoming rimmed with oxide nanolites (Figure 5.3e-h), as seen in the dome. Larger microlites in the high temperature (1020°C) series also show signs of more significant breakdown to form oxide nanolites across the

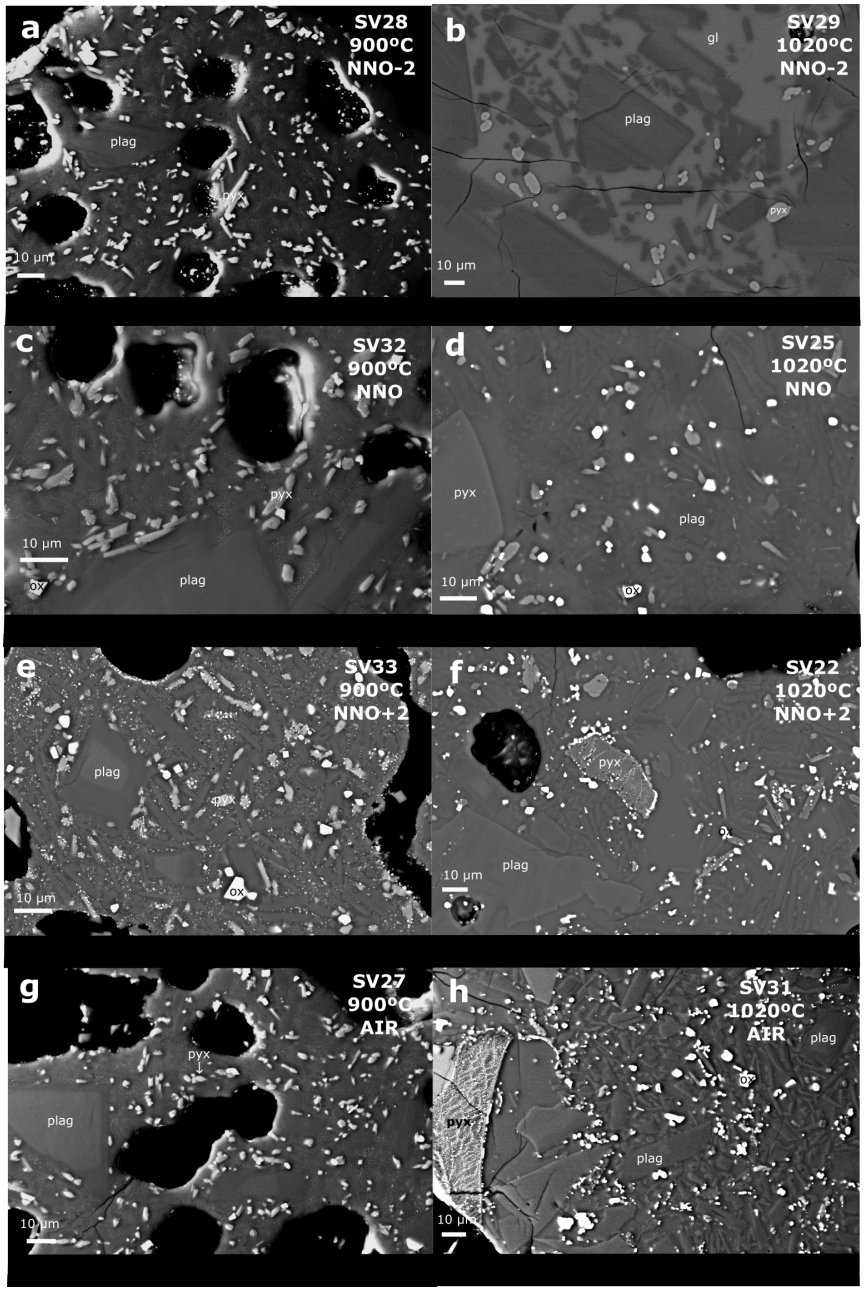


Figure 5.3: BSE images of the microlite-rich groundmass in experimental run products. Pyroxene microlites are stable below NNO (**a-d**) but begin to form oxides along their rims at oxygen fugacities ≥ NNO+2; co-eval with an increase in the abundance of oxide microlites (**e-h**). No oxide microlites are present in SV29 (**b**). Abbreviations as in Figure 5.1.

entire crystal face (Figure 5.3f, h; labelled pyx). Similar pyroxene breakdown textures have been observed in oxidised juvenile ash particles (Matsumoto and Geshi, 2021) and reheated crystals (D'Oriano et al., 2013, 2014). Oxide microlites and nanolites become more abundant in the groundmass coeval with the formation of pyroxene breakdown textures. Olivine microlites were identified in two experimental run products: SV29, at

1020ºC and NNO-2, appearing homogenous and subhedral; and SV22, at 1020ºC and NNO+2, appearing unstable with fine symplectite textures present.

Pyroxene phenocrysts.

Orthopyroxene phenocrysts crystallised at NNO-2 are homogenous, with those at 900ºC appearing stable, whilst those at 1020ºC showing signs of resorption (Figure 5.4a, b). At and above NNO, and in the low temperature (900°C) series, oxide nanolites form along grain boundaries and within fractures of orthopyroxene phenocrysts (Figure 5.4c, e, g), similar to those seen in the dome. The breakdown of orthopyroxene phenocrysts is much more prominent in the higher temperature series, at and above NNO. Oxide nanolites form across the crystal face, becoming more extensive and abundant with an increase in fO_2 (Figure 5.4d, f, h), and are no longer restricted to crystal edges or along fractures. Such textures define the stability limit of orthopyroxene, with respect to temperature and oxygen fugacity, and delineate where orthopyroxene becomes a metastable phase at one atmosphere (Figure 5.2). Clinopyroxene phenocrysts appear euhedral and stable in all runs, with no sign of any overgrowth or resorption.

Iron-titanium oxide phenocrysts.

At the most reduced (NNO-2) experimental conditions, Fe-Ti oxides are absent at 1020ºC; and at 900ºC they are identified only as microlites, with some crystals displaying regions of weak exsolution. In experiments at NNO, irregular ‘sandwich-type’ exsolution is observed at 900ºC (Figure 5.5a), and weak trellis exsolution lamellae form along two planes at 1020ºC (Figure 5.5b). At NNO+2, two different phases exsolve along the edge of Fe-Ti crystals in both temperature series, each with a slightly different form. The first exsolution phase forms small irregular granules at the crystal edge that appear darkest (low-Z) in BSE images. The second exsolution phase, more dominant at 1020ºC, forms subtle ‘sandwich-type’ lamellae along the grain boundary, appearing as a lighter grey

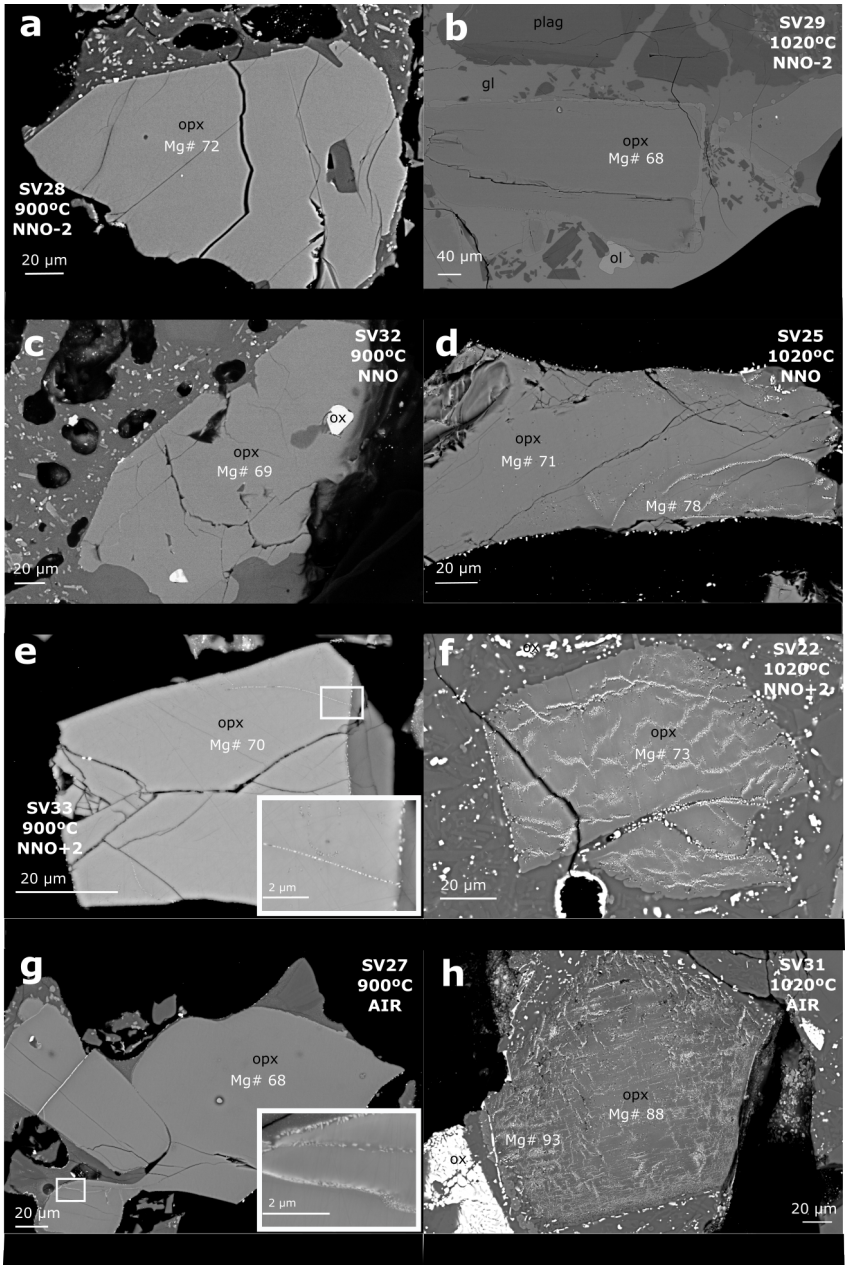


Figure 5.4: BSE images of the breakdown textures observed in orthopyroxene phenocrysts in experimental run products. Orthopyroxene phenocrysts are homogenous at the most reduced experimental conditions (**a,b)** and at NNO at 900ºC **(c**). At ≥ NNO+2 and 900ºC, orthopyroxenes begin to be rimmed with oxides (**e,g**). At ≥ NNO and 1020ºC, orthopyroxenes undergo significant alteration, breaking down to form oxide nanolites across the entire crystal face (**d,f,h**). Mg# in moles calculated as Mg / (Mg + Fe), assuming all Fe as Fe^{2+}. Abbreviations as in Figure 5.1.

(high-Z) in BSE images (Figure 5.5 c, d). The exsolution of phases along grain boundaries and fractures supports oxidation-exsolution by an external oxidising agent (Haggerty, 1976a, 1991). Dome oxide 2 and oxide 4 exhibit well-developed sandwich-type lamellae, suggesting conditions in the dome were likely above NNO+2 as sandwich-

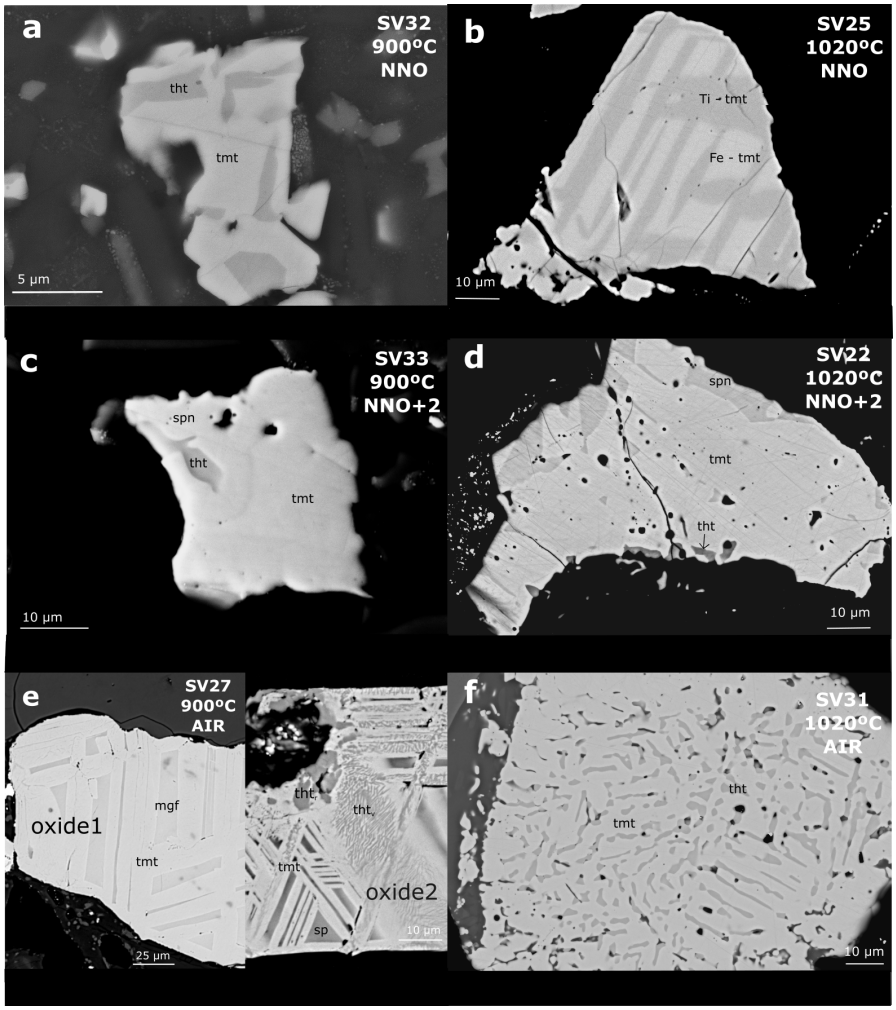


Figure 5.5: BSE images of exsolved oxide microlites and phenocrysts in experimental run products. (**a**) Host titanomagnetite microlite (tmt) exsolving irregular blebs of titanohematite (tht). (**b**) Iron-rich titanomagnetite host exsolving trellis lamellae of titanium enriched titanomagnetite. (**c**) Titanomagnetite host exsolving titanohematite (tht, dark grey) as composite grains at the edge of the crystal and Mg-Fe-Al spinel (spn) in the centre of the phenocryst (white dashed line). (**d**) Co-eval exsolution of titanohematite (dark grey) as composite blebs and Mg-Fe-Al spinel (lighter grey) as irregular sandwich-type lamellae, both on the edge of the crystal. (**e**) Oxide 1 is a titanomagnetite host with well-developed coarse trellis lamellae of magnesioferrite (mgf). Oxide 2 is a titanomagnetite host with coarse trellis lamellae Mg-Fe-Al spinel along three planes and patches of vermicular titanohematite exsolution (tht_v) and some recrystallised grains of titanohematite (tht_r). (**f**) Titanomagnetite host with ubiquitous vermicular exsolution of titanohematite (darker grey).

type lamellae become better developed with increasing fO_2 (Buddington and Lindsley, 1964).

Experiments run in air produced significantly altered Fe-Ti oxides. In experiment SV27 at 900ºC two Fe-Ti oxide crystals were identified, each with different exsolution textures

and compositions. The first oxide (SV27 oxide 1; Figure 5.5e) displays coarse well-developed trellis lamellae along two planes, similar to dome oxide 1. The second oxide (SV27 oxide 2; Figure 5.5e) exsolves two phases, one as coarse trellis lamellae along three planes, and the other as weak vermicular exsolution and as recrystallised granules. Recrystallisation is also observed in dome oxide 3. At 1020ºC Fe-Ti oxides undergo extreme vermicular exsolution, with grains appearing anhedral and unstable (Figure 5.5f). Only the exsolution textures observed in the air experiment at 900ºC appear similar to those in the dome. Figure 5.2 summarises the range of Fe-Ti oxide exsolution textures observed in all experimental run products and highlights the change from 'sandwich-type' exsolution to granular and trellis lamellae, to vermicular and finally recrystallisation textures with increasing fO_2.

Olivine phenocrysts.

At NNO-2, olivine is not present in the low temperature series. New subhedral microlites were observed in the high temperature series (Figure 5.4b), but no phenocrysts. Olivine phenocrysts are present in all experiments above NNO and display symplectite exsolution textures, as shown in Figure 5.6. At NNO and 900°C, linear symplectite bands traverse the crystal, with very fine exsolution stemming from the centre of bands. A small oxide diffusion rim is also present along the top edge of the olivine crystal (Figure 5.6a). At NNO and 1020ºC, the symplectitic olivine is hosted in an orthopyroxene grain, with exsolution extending inwards from the grain boundary (Figure 5.6b). Increasing fO_2 results in more prominent exsolution and oxide diffusion rims. At NNO+2 and 900ºC, coarse symplectitic bands form, with well-developed fibrous exsolution lobes (termed 'budding' after Haggerty and Baker, 1967) growing from the centre of bands (Figure 5.6c). At NNO+2 and 1020ºC, symplectite exsolution occurs in the form of clusters, with occasional thin exsolution bands or rods stretching between them (Figure 5.6d). Olivines exposed to air at 900ºC illustrate well-developed fibrous symplectite lobes along the

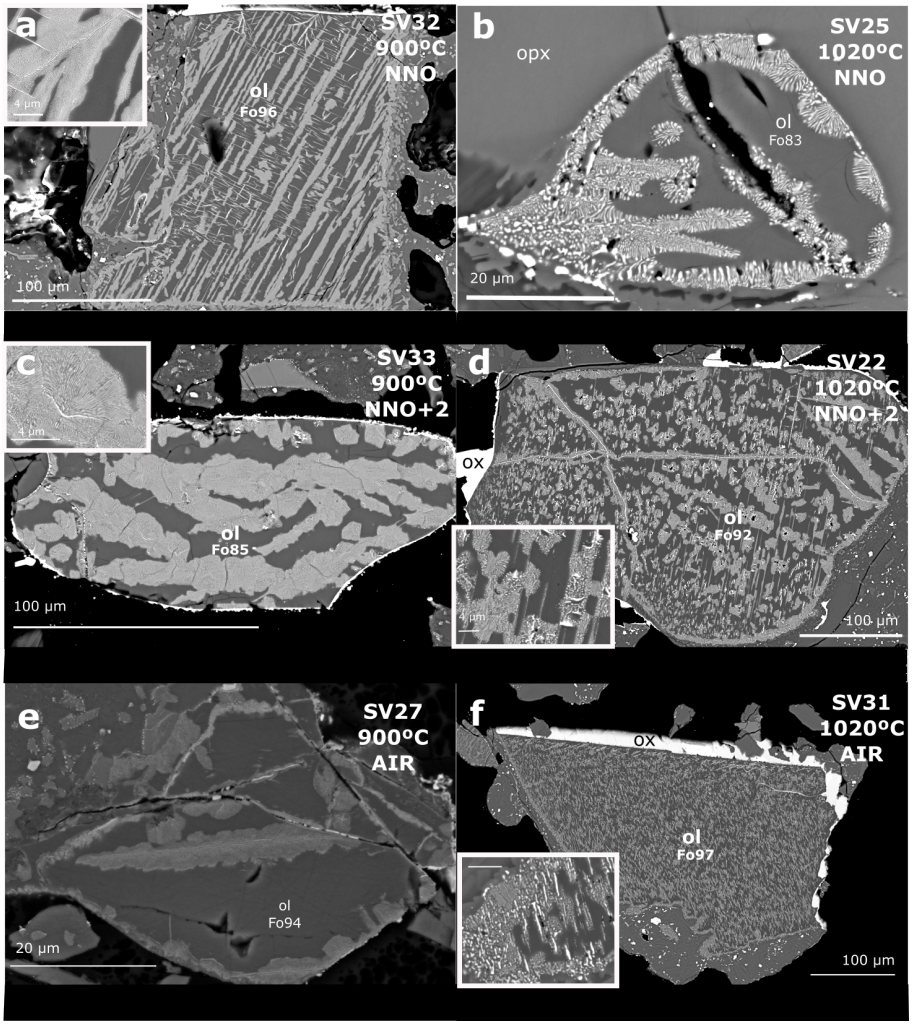


Figure 5.6: BSE images of symplectite exsolution in olivine phenocrysts from experiments. (**a**) Linear bands of fine symplectite exsolution across the crystal face. (**b**) Symplectite 'blebs' exsolving along the rim of an olivine intergrowth within an orthopyroxene grain. (**c**) Coarse symplectite exsolution bands, with Fe-oxides exsolving as well-developed fibrous budding lobes, (see inset). (**d**) Clusters of symplectite exsolution, connected by thin rods of exsolved Fe-oxide. (**e**) Well-developed fibrous and budding symplectite lobes following the edge of the crystal and along a single band in the centre. (**f**) Ubiquitous symplectite exsolution, with clusters of symplectite 'blebs'. Some olivine crystals also show an irregular oxide diffusion rim (white) around the edge of the crystal. Forsterite of olivine host (Fo) calculated in moles as Mg / (Mg + Fe + Mn) crystal. Abbreviations as in Figure 5.1.

edge of the crystal and stemming from a single central band (Figure 5.6e). In air and at 1020ºC, symplectite exsolution is ubiquitous across the entire crystal and forms clusters of elongated symplectites connected by thin rods (Figure 5.6f), similar to olivines observed in high temperature oxidised scoria (Ejima et al., 2017) and lunar samples (Bell et al., 1975).

5.4.2 Compositional variations

Microlites.

Experimental unzoned plagioclase microlites have anorthite contents ranging from An_{44} to An_{53}, whilst limited analyses of zoned plagioclase microlites have core values of An_{75} to An_{82} and a singular rim value of An_{56} (Table S5.1). Figure 5.7 illustrates the variation in An contents of unzoned and zoned plagioclase microlites in experimental runs and in the natural dome and scoria samples. Experimental plagioclase An contents are lower than the U3 scoria starting material in all runs, supporting growth of new (lower An) microlites and rims during experimental runs. Although only few analyses of pyroxene microlites were obtained, those grown at more reduced experimental conditions have lower Mg numbers ($Mg\#_{59}$ to $Mg\#_{64}$ opx; $Mg\#_{67}$ cpx) compared to those in more oxidising conditions with higher Mg numbers ($Mg\#_{61}$ to $Mg\#_{86}$ opx; $Mg\#_{75}$ to $Mg\#_{83}$ cpx; Table 5.2), consistent with the changing proportions of Fe^{2+} and Fe^{3+} in the system. Pyroxene microlite Mg# values in the dome and scoria are more similar to experimental runs at more oxidising conditions, suggesting crystallisation at or above NNO+2 (Figure 5.7). Additionally, pyroxene microlites rimmed with Fe-oxides become depleted in Fe^{2+} thus enriched in Mg^{2+}, giving them higher Mg# values.

Pyroxene phenocrysts.

The composition of orthopyroxene phenocrysts varies depending on the amount of alteration experienced and volume of breakdown Fe-oxides formed. In the low temperature series, Mg numbers of host orthopyroxene phenocrysts show little variation, from $Mg\#_{68}$ to $Mg\#_{70}$. In the higher temperature series, orthopyroxene crystals experience more significant breakdown, forming an abundance of Fe-oxide nanolites Formation of Fe-oxides depletes the host orthopyroxene in Fe^{2+}, thus increasing its Mg

Table 5.2. Experimental run conditions and products

Run #	Temperature	fO_2	Duration	Phases present	Plag			Opx		Cpx	
	(ºC)		(hours)		phenocryst core An	phenocryst rim An	microlite An	phenocryst Mg#	microlite Mg#	phenocryst Mg#	microlite Mg#
SV31	1020	AIR	161	gl, plag, opx, cpx, ol, tmt, tht	89 (6)	62 (2)	51 (7)	88 - 93†	na	72 (1)	83 (2)
SV27	900	AIR	161	gl, plag, opx, cpx, ol, tmt, tht, spn	83 (7)	65 (4)	46 (5)	68 (1)	61 (4)	71 (5)	na
SV22	1020	NNO+2	165	gl, plag, opx, cpx, ol, tmt, tht, spn	92 (1)	66 (8)	51	73	86	75 (1)	75 (1)
SV33	900	NNO+2	166	gl, plag, opx, cpx, ol, tmt, tht, spn	82 (2)	64 (2)	44 (5)	70 (1)	65 (3)	72 (2)	na
SV25	1020	NNO	168	gl, plag, opx, cpx, ol, tmt	84	51	45 (0.2)	71 (2) - 78†	na	76	76
SV32	900	NNO	161	gl, plag, opx, cpx, ol, tmt, tht	93	59 (2)	48	69 (3)	59 (3)	72 (3)	70 (0.02)
SV29	1020	NNO-2	144	gl, plag, opx, cpx, ol	88 (6)	66 (8)	82 (0.01) - 53 (2)*	68	64 (2)	71 (1)	na
SV28	900	NNO-2	161	gl, plag, opx, cpx, tmt, tht	74 (12)	60 (2)	80 - 50 (6)*	na	59 (4)	72 (1)	67

Phases present: gl - glass, plag - plagioclase, opx - orthopyroxene, cpx - clinopyroxene, ol - olivine, tmt - titanomagnetite, tht - titanohematite, spn - Mg-Fe-Al spinel

na - not analysed; bd - below detection; pfu - per formula unit

Units in parentheses are standard deviations of average phase compositions ; exsolution textural terms after Haggerty 1976a

Anorthite content (An) calculated as mol. % Ca / (Ca + Na); Forsterite content (Fo) as mol. % Mg / (Mg + Fe + Mn); Mg# as cation fraction (Mg^{2+} / (Mg^{2+} + Fe^{2+})); Fe^{3+} # as cation fraction (Fe^{3+} / (Fe^{3+} + Al^{3+}))

* Average core and rim values of zoned plagioclase microlites

† Analyses of unaltered core (low Mg#) and altered rim (high Mg#)

Ti pfu std < 0.01

Table 5.2 continued

Run #	Ol	Tmt host			Tht exsolved			spn			Fe-Ti oxide exsolution textures
	phenocryst Fo	Mg#	Fe^{3+}#	Ti pfu	Mg#	Fe^{3+}#	Ti pfu	Mg#	Fe^{3+}#	Ti pfu	
SV31	97 (1)	16 (6)	95 (3)	0.3	13 (1)	91 (6)	0.7	-	-	-	Vermicular
SV27	94 (1)	7 (2)	92 (1)	0.2	12 (2)	80 (10)	0.7	54 (4)	69 (4)	bd	Coarse regular trellis lamellae (spn), vermicular and recrystallised (tht)
SV22	92 (0.3)	12 (0.2)	92 (0.3)	0.4	15 (0.3)	83 (2)	0.7	39 (2)	85 (0.3)	bd	Sandwich type (spn) and granules at edge (tht)
SV33	85 (3)	9 (2)	91 (2)	0.5	15 (0.6)	73 (5)	0.8	22 (1)	85 (1)	0.1	Sandwich type (spn) and granules at edge (tht)
SV25	83 (0.01)	27 (1)	93 (0.01)	0.2	-	-	-	12 (0.1)	95 (0.2)	0.6	Sandwich type
SV32	96 (0.1)	6 (1)	93 (1)	0.4	7 (5)	84 (1)	0.73	-	-	-	Sandwich type
SV29	55 (0.1)	-	-	-	-	-	-	-	-	-	
SV28	-	6	86	0.4	7	96	0.6	-	-	-	

number. Mg numbers increase from core to rim and with increasing fO_2, for example $Mg\#_{71}$ to $Mg\#_{78}$ at the NNO buffer and $Mg\#_{88}$ to $Mg\#_{93}$ in air. This supports a decrease in orthopyroxene stability with increasing oxidation state at 1020ºC (Figure 5.2). Clinopyroxene phenocrysts remain stable, with Mg numbers ranging from $Mg\#_{71}$ to $Mg\#_{76}$ (Table 5.2). This may reflect the greater ability of clinopyroxene to incorporate Fe^{3+} relative to orthopyroxene.

Only one successful analysis of an oxide nanolite within an orthopyroxene crystal is reported (SV25; Table S5.2). Its composition is magnesioferrite with considerable Fe^{3+}, thus supporting oxidation-exsolution. Equation 5.2 is a balanced reaction that describes the oxidation of an original magmatic orthopyroxene ($Mg\#_{71}$) to form an Mg-enriched orthopyroxene rim ($Mg\#_{78}$) and magnesioferrite. SiO_2, Fe^{3+} and O^{2-} are required to balance the reaction, and are assumed to be present in the melt. The initial low-Mg orthopyroxene composition was obtained from the centre of the phenocryst (Figure 5.4d). Negligible change is observed in other cation species such as Ca and Mn.

$$12\ Mg_{1.3}Fe^{2+}_{0.7}Si_2O_6 + 0.7\ O_2 = 10\ Mg_{1.5}Fe^{2+}_{0.5}Si_2O_6 + 1.2Mg_{0.5}Fe^{2+}_{0.5}\ Fe^{3+}{}_2O_4 + 4\ SiO_2 + 0.4\ Fe^{3+} + 0.6\ O^{2-} \quad \text{(Equation 5.2)}$$

Iron-titanium oxide phenocrysts.

Experimentally exsolved oxides contain variable amounts of Fe and Ti, and minor amounts of Mg, Al and Mn. In Figure 5.8 Fe-Ti oxides are plotted in terms of their quadrivalent, trivalent and divalent cations ($(Ti^{4+}) - (Al^{3+}+Fe^{3+}) - (Mg^{2+}+Fe^{2+}+Mn^{2+})$) on a ternary diagram, along with oxides from the natural dome and scoria. Oxide formulae were recalculated as cations per 12 oxygens. All host oxides (solid symbols) form part of the titanomagnetite spinel solid solution series, plotting along the ulvöspinel-magnetite join. Two main exsolution phases are identified: the first is a Ti-rich titanohematite

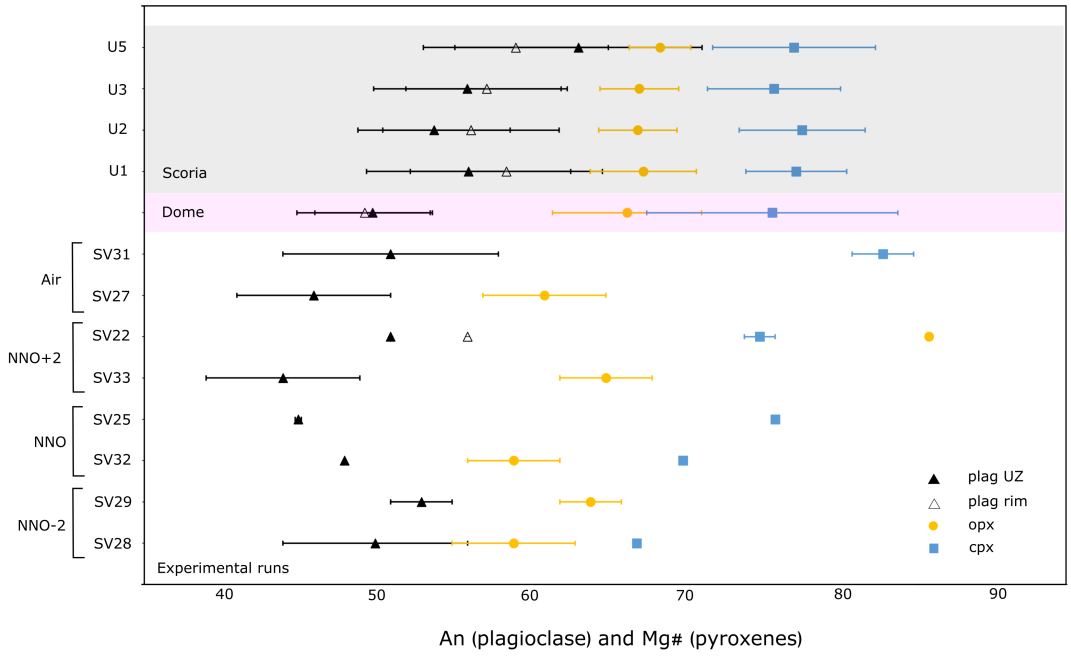


Figure 5.7: Plagioclase and pyroxene microlite compositions in experimental run products, the natural dome, and scoria samples. Anorthite (An) content of unzoned plagioclase microlites plotted as solid black triangles, with new rim growth of zoned plagioclase microlites plotted as open black triangles. Mg# of orthopyroxene and clinopyroxene microlites plotted as yellow circles and blue squares, respectively. Error bars to one standard deviation. An content calculated as mol% Ca / (Ca+Na). Mg# calculated as cation fraction Mg^{2+} / (Mg^{2+}+Fe^{2+}).

rhombohedral oxide that plots along the ilmenite-hematite solid solution (open symbols); the second is a Ti-poor Mg-Fe-Al cubic spinel (pleonaste-magnesioferrite), that plots towards the base of the quadrilateral (open symbols). Exsolved titanohematites contain ~ 33 – 43 wt. % TiO_2 (Table S5.2) and exsolve as small granules or as vermicular exsolution lamellae in all experimental runs, except SV29 and SV25. The Mg-Fe-Al spinel phase is rich in Mg^{2+} (5 – 11 wt. % MgO), Fe^{3+} (47 – 60 wt. % Fe_2O_3, calculated by stoichiometry) and Al^{3+} (6 – 15 wt. % Al_2O_3), but is depleted in Ti^{4+} (< 3 wt. % TiO_2), consistent with magnesioferrite-pleonaste stoichiometry ($MgFe_2O_4$-$Mg_xFe_{1-x}Al_2O_4$). The Mg-Fe-Al spinel exsolution phase, hereafter referred to as 'magnesioferrite-rich spinel', is found in both temperature series at NNO+2, but only at 900ºC in the presence of air. The lack of magnesioferrite-rich spinel in the most oxidising experimental environment (in air at 1020ºC), suggests a preference for titanohematite exsolution under these

conditions. Experimental runs exsolving both titanohematite and magnesioferrite-rich spinel form assemblages where three compositionally distinct oxides co-exist, shown as triangles in Figure 5.8. Host titanomagnetites are Al-poor (< 6 wt. % Al_2O_3), driving the exsolving magnesioferrite-rich spinel to incorporate a high proportion of Fe^{3+}.

Oxides in experimental runs at 900ºC, at NNO+2 and in air (SV22, SV27) are compositionally the most similar to the natural 2020-2021 St. Vincent dome rock regarding both host and exsolved magnesioferrite-rich spinel phases (Figure 5.8). Exsolved titanohematite compositions in the experimental runs are more variable and depleted in Fe^{3+} compared to the dome (Figure 5.8), likely due to the coeval exsolution of a magnesioferrite-rich spinel phase sequestering Fe^{3+}. Although the oxides analysed in the dome were not found to simultaneously exsolve titanohematite and magnesioferrite-rich spinel, all three of these oxide phases co-exist in the same rock sample (Figure 5.1f), a three-oxide assemblage represented with a dashed triangle in Figure 5.8. All experimentally defined three-oxide assemblage triangles enclose one of the original scoria oxide compositions, supporting exsolution from an initially homogenous Fe-Ti oxide crystal, formed under conditions that were hotter and more reduced (grey shading; Figure 5.2) than the experiments in which exsolution occurred. At one atmosphere pressure, the production and subsequent co-existence of three distinct oxide phases is confined to temperatures below 1020ºC and above NNO (Figure 5.2). Only experiment SV27, at 900ºC and in the presence of air, replicates both the textures and the compositions observed in the natural dome rock, forming well-developed trellis lamellae and recrystallisation textures (Figure 5.5e). Thus, the T-fO_2 conditions of dome growth are inferred to lie close to those of experiment SV27 (pink shading; Figure 5.2).

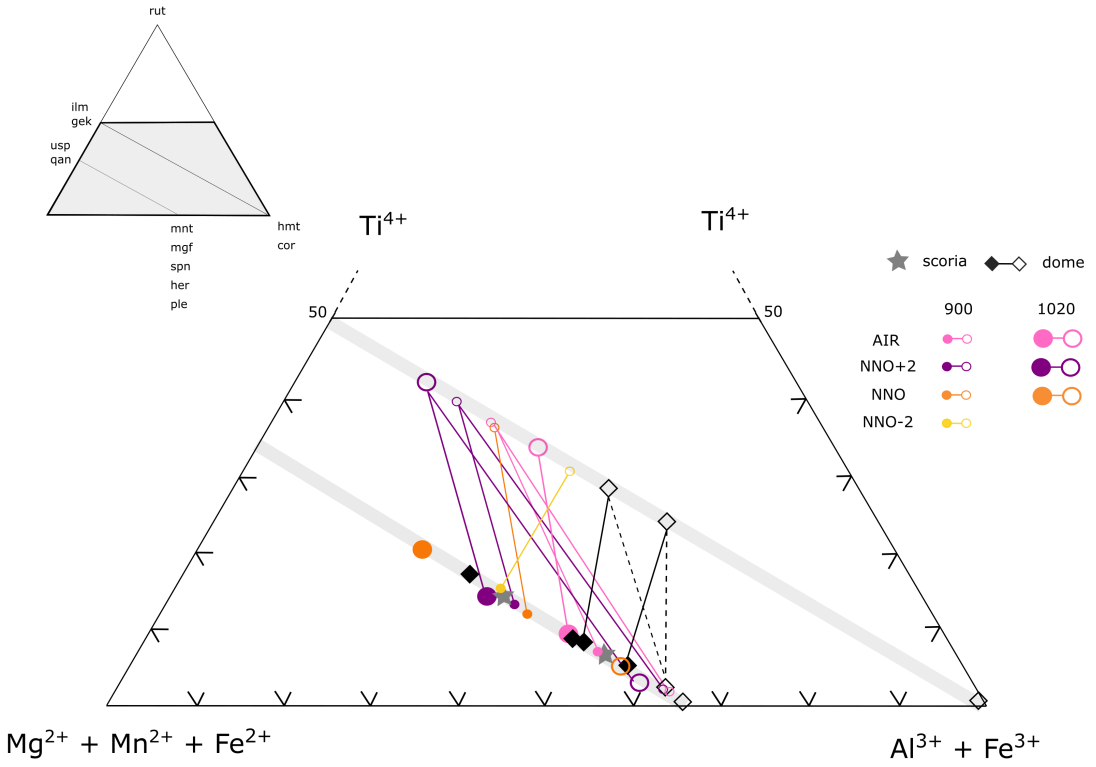


Figure 5.8: Fe-Ti oxide compositions in experimental run products and natural dome and U3 scoria samples, plotted in ternary space depending on their number of quadri-, tri- and di- valent cations: (Ti^{4+}) - (Al^{3+}+Fe^{3+}) - (Mg^{2+}+Fe^{2+}+Mn^{2+}) per 12 oxygens normalised to a percentage. Host crystals are plotted as solid symbols and exsolved phases as open symbols. Low temperature experiments are shown as small circles, high temperature experiments as larger circles, with different colours for different oxygen fugacities; the natural dome rock shown as black diamonds and scoria as grey stars. Rhombohedral oxides (8 cations per 12 oxygens) plot along the ilmenite-hematite solid solution; cubic oxides (9 cations per 12 oxygens) plot along the ulvöspinel-magnetite solid solution. Host and exsolved oxides are connected by tie lines, with phases on the ulvöspinel-magnetite solid solution line assumed to be connected. Host oxides exsolving two different phases form three-oxide assemblage triangles, only present in the experiments at ≥NNO+2 (pink and purple circles) and in the natural dome (black diamonds). Dashed lines connect oxides present in the same sample, but do not represent host and exsolved phases. Abbreviations as in Figure 5.2 as well as: gek, geikielite; qan, qandilite; cor, corundum; spn, spinel; her, hercynite; rut, rutile.

Olivine phenocrysts.

Olivine crystals in experimental runs can be divided compositionally into two distinct groups, as seen in the natural starting material: the first with 0.6 wt. % MnO and the second with 0.4 wt. % MnO. All olivine crystals in experimental runs at and above the NNO buffer display symplectite exsolution and have high host crystal Fo contents, ranging from Fo_{83} to Fo_{97} (Table 5.2). Host olivine crystals are enriched in Mg compared

to the original composition of olivines in the scoria starting material (Fo_{65} to Fo_{75}), due to the formation of Fe-oxide symplectites. The variation in Fo values in experiments reflects the degree of exsolution incurred and the proximity of analyses to the Fe-oxide symplectites within the crystal, indicative of a diffusive control on the reaction whereby temperature, fO_2 and time all play a role. Olivines subject to higher temperatures and fO_2 display more extensive symplectite exsolution, thus generating higher Fo contents in the host crystal (Figure 5.6). Symplectitic olivines analysed in the dome have lower Fo contents than those in experimental runs, (Fo_{74} to Fo_{82}, Figure 5.1h), suggesting more limited diffusion and exsolution, either over a shorter timescale or at lower temperatures. The low Fo contents (Fo_{55}) of the olivine microlite analysed in experiment SV29, at 1020ºC and NNO-2, is considerably Mg-poor compared to olivine microlites in the scoria (Fo_{71}, Table S5.1; Frey et al., 2024), thus supporting new growth during experimental runs.

The compositions of the exsolving Fe-oxide symplectites could not be analysed directly due to their small grainsize (≤ 1 μm), but the co-existence of high-Fo olivine and absence of orthopyroxene implies the formation of hematite, as described and reported in previous experimental studies (Haggerty and Baker, 1967; Champness, 1970; Gualtieri et al., 2003; Del Moro et al., 2013; Knafelc et al., 2019). Analysis of the oxide diffusion rims observed in SV33, SV22 and SV31 finds both magnesioferrite and hematite to be present, on the basis of stoichiometry. Well-developed diffusion rims effectively sequester Fe^{3+} and Mg, and suggest high degrees of oxidation, with their thickness and complexity reflecting the duration of oxidation (Haggerty and Baker, 1967; Venezky and Rutherford, 1999). Their absence in the 2020-2021 St. Vincent dome may reflect again different oxidation timescales between experimental runs and the natural dome.

Using the composition of the 0.4 wt. % MnO unaltered olivine (Fo_{75}) in the scoria as that of the original mineral prior to oxidation, equation 5.3 is a balanced reaction that

describes the oxidation-exsolution reaction in experiment SV27, forming Fo_{94} olivine (with 0.4 wt. % MnO), hematite and melt (SiO_2).

$$9.5\ Mg_{1.5}Fe^{2+}_{0.5}SiO_4 + O_2 = 7.5\ Mg_{1.9}Fe^{2+}_{0.1}SiO_4 + 2\ Fe_2O_3 + 2\ SiO_2$$

(Equation 5.3)

5.5 Discussion

5.5.1 Mechanisms of oxidation

Results presented in this study show that the alteration textures observed in the St. Vincent 2020-2021 lava dome are the products of high-temperature oxidation of basaltic andesite magma. As described in section 5.1.1, three main processes are capable of oxidising a magma at or near the Earth's surface: deuteric oxidation, hydrothermal alteration or interaction with air.

Deuteric oxidation of magmas can result from degassing or crystallisation. The magnitude of the fO_2 increase depends on the amount of H_2O exsolved and the amount of oxidisable Fe^{2+} in the magma. For example, take an Fe-poor rhyolite (1 wt. % FeO^T) with 5.5 wt. % H_2O; oxidation induced by degassing is of the order +2 log fO_2 units (Burgisser and Scaillet, 2007) corresponding to conversion of ~ 0.3 wt. % FeO to Fe_2O_3. For Fe-rich basaltic andesite magmas (~ 8 wt. % FeO^T; Table 5.1) with ~ 4 – 6 wt. % H_2O (Weber et al., 2024) the effect will be considerably less, on the order +0.3 log fO_2 units to oxidise the same amount of FeO. Sulfur degassing tends to counteract the effect of H_2O degassing depending on the initial redox state and sulphur content (Carmichael and Ghiorso, 1986; Burgisser and Scaillet, 2007). Sulfur contents of La Soufrière, St. Vincent melt inclusions, from the 1979 eruption, are in the range 320 – 560 ppm (Devine and Sigurdsson, 1983). Data for the 2021 scoria are even lower (40 – 270 ppm; Weber et al, 2024). Degassing this amount of sulfur would largely counterbalance any oxidative effect

of H_2O degassing (Burgisser and Scaillet, 2007). Thus, deuteric oxidation during dome magma degassing is not capable of delivering the high fO_2 required to generate the observed oxidation textures. Oxidation by streaming a much larger mass of SO_2-rich gas from deeper in the magmatic system through the dome magma cannot be ruled out, though low SO_2 degassing fluxes prior to and during dome extrusion (Esse et al., 2024) would tend to argue against this.

Hydrothermal fluids can also oxidise a magma via the reduction of externally-derived H_2O. The composition of the fluid determines the extent of fO_2 change, as hydrothermal fluids may contain other redox species, such as sulfur (Binder and Keppler, 2011; Ueda et al., 2021). Temperature estimates for hydrothermal alteration range from 50 – 500ºC (Ball et al., 2013, 2015; Darmawan et al., 2022), requiring over 60 years for Fe-Ti oxides to fully re-equilibrate and achieve diffusion on length-scales of more than 20 μm (Venezky and Rutherford, 1999). Prior to the 2020-2021 eruption at La Soufrière, the last volcanic activity occurred in 1979, meaning any remnant magmas from this eruption have had only 40 years to re-equilibrate (Graham and Thirlwall, 1981; Huppert et al., 1982). Hydrothermal alteration typically results in the precipitation of hydrous minerals such as chlorite and clay within three years, at shallow depths (Humphris, 1976; Ball et al., 2013; Heap et al., 2019), as well as the breakdown of clinopyroxene, plagioclase and orthopyroxene (Austrecheim and Robins, 1981; Boland and Otten, 1985; Del Moro et al., 2013). The absence of such key features in the St. Vincent dome samples suggests that hydrothermal fluids are unlikely responsible for generating the oxidation textures observed either in the conduit prior to eruption or on the crater floor.

Magmas oxidise readily at Earth's surface, however the extent of oxidation and textures formed are temperature dependant (Buddington and Lindsley, 1964; Haggerty and Baker, 1967; Burkhard, 2001; Del Moro et al., 2013; Gualtieri et al., 2013). For magmas to undergo extensive oxidation by air, temperatures must remain high for reactions to be

kinetically feasible (> 600ºC, Burkhard, 2001, 2005a; Del Moro et al., 2013; D'Oriano et al., 2013). The experimental results presented in this study illustrate that the dome-forming magma likely interacted with Earth's atmosphere at high temperatures to produce the well-developed trellis exsolution textures in Fe-Ti oxides that are seen in the dome (Figure 5.1f, Figure 5.5e). Other alteration textures include the development of olivine symplectites and rimming of pyroxene microlites and phenocrysts with oxides, occurring at and above NNO; with the exsolution of magnesioferrite-rich spinel from titanomagnetite requiring conditions ≥ NNO+2. The La Soufrière dome-forming magma therefore must have experienced oxidative conditions between NNO+2 and air to form both the textures and compositions of co-existing oxidised mineral phases. Further evidence for interaction with air includes the formation of olivine symplectites along grain boundaries (Del Moro et al., 2013; Haggerty, 1976a; Gualtieri et al., 2003; Knafelc et al., 2019) and the nucleation of oxide nanolites on the rims of pyroxene crystals (D'Oriano et al., 2013, 2014; Matsumoto and Geshi, 2021). Studies exploring the porosity and permeability of lava domes corroborate the possibility of heterogenous airflow to dome interiors via pore spaces or microfractures (Colombier et al., 2017; Darmawan et al., 2022). The difficulty of sampling the dome in 2021 makes it hard to assess the original location of the sample studied, with respect to the original dome surface or internal cracks.

5.5.2 Temperature of oxidation

The temperature range explored in this study (900 – 1020ºC) reflects magmatic temperature estimates from two-pyroxene thermometry for the La Soufrière 2020-2021 eruption (Weber et al., 2024). The temperature of the dome exterior at the time of extrusion was measured at ~ 590 ± 12ºC from thermal imaging (Stinton, 2024), providing a minimum temperature constraint for alteration at the Earth's surface. Reheating experiments in air illustrate the need for elevated temperatures to facilitate subsolidus

oxidation, which would otherwise be kinetically inhibited (Blondes et al., 2012; D'Oriano et al., 2013, 2014; Venezky and Rutherford, 1999). In past experiments oxide nanolites are initially formed at temperatures of 750ºC but only become dominant in the groundmass and rim pyroxene and plagioclase microlites, as seen in the St. Vincent 2020-2021 dome, at temperatures nearer 1000ºC (D'Oriano et al., 2013).

Experimental runs at 900ºC most closely replicate the symplectitic olivine textures in the natural dome, with exsolution restricted to grain boundaries and well-defined bands traversing the crystal. Experiments at 1020ºC instead display extensive exsolution throughout the crystal, illustrating the role of temperature in controlling the type and extent of symplectite exsolution produced. Olivine symplectites generally develop during sub-solidus oxidation (< 980 – 1060ºC; Barton et al., 1991). At lower temperatures (600 – 700ºC), the intermediate phase laihunite ($Fe^{2+}Fe^{3+}{}_2(SiO_4)_2$) forms during oxidation (Khisina et al., 1995, 1998), whereas at higher temperatures Fo-rich olivine initially breaks down to form orthopyroxene and magnesioferrite as metastable phases. With continued heating (≥ 820ºC), high-Fo olivine and hematite are produced (Haggerty and Baker, 1967). The lack of breakdown laihunite and orthopyroxene in the St. Vincent 2020-2021 dome, suggests temperatures were above 820ºC when oxidation occurred.

Fe-Ti oxides form a variety of solid solutions, each unmixing to form two (or rarely more) separate oxide phases during sub-solidus exsolution at a unique consulate temperature (Haggerty, 1976a). Previous experimental studies identify the magnetite-hematite consulate temperature to be between 527 – 600ºC (Kawai et al., 1954; Vincent, 1957; Lilovet et al., 2012); the magnetite-hercynite and magnetite-pleonaste consulate temperatures to be ~ 860ºC and ~ 900ºC, respectively (Turnock and Euguster, 1962; Tan et al., 2016), and the ulvöspinel-hercynite and qandilite-spinel consulate temperatures to be ~ 1300ºC and ~ 1370ºC, respectively (Muan et al., 1972; Ghiorso and Sack, 1991; Lindsley, 1991). The temperatures at which magnesioferrite-rich spinel and

titanohematite exsolve from titanomagnetite, as seen in this study, have not previously been established. Our results experimentally constrain the exsolution of such phases to temperatures above 900ºC in the presence of air and above 1020ºC at NNO+2 (Figure 5.2). The exsolved phases are rich in Fe^{3+}, indicative of significant oxidation (Haggerty, 1976a). Sub-solvus exsolution often occurs during slow cooling when Fe-Ti oxides re-equilibrate (Hammond and Taylor, 1982), however super-solvus oxidation-exsolution is possible in extremely oxidising conditions whereby newly-formed (more oxidised) components are excluded from the original host crystal lattice (Arguin et al., 2018; Von Gruenewaldt et al., 1985). Collectively the oxidation textures observed in the St. Vincent 2020-2021 dome define the minimum and maximum temperatures of oxidation to be ≥ 750ºC from the abundance of oxide rimmed microlites in the groundmass; ≥ 820ºC from the exsolution of hematite symplectites from olivine; and ≤ 900ºC from the presence of oxide rimmed orthopyroxene phenocrysts seen in this study.

5.5.3 Timescale of oxidation

The experiments presented in this study suggest that the oxidation textures observed in the St. Vincent 2020-2021 dome most likely formed within a week at temperatures close to 900ºC, at the Earth's surface. Fe-Ti oxides re-equilibrate very quickly with re-equilibration timescales dependant on the temperature, ranging from 50 hours at 1000ºC to 60 years at 600ºC (Hammond and Taylor, 1982; Venezky and Rutherford, 1999; Gardner et al., 1995; Hou et al., 2021). Previous experimental studies using more fayalite-rich olivine also found that rapid heating in air between 820 – 1000ºC results in the continuous breakdown of original olivine to hematite and high-Fo olivine, whereas slower heating forms orthopyroxene and magnesioferrite (Champness, 1970). This observation supports rapid high-temperature oxidation of the St. Vincent 2020-2021 dome. The lack of oxide diffusion rims around symplectitic olivines (usually formed during prolonged oxidation periods) further suggests that oxidation at La Soufrière could have

occurred on timescales of less than a week, the duration of experimental runs (Haggerty and Baker, 1967). However, longer oxidation timescales at slightly lower temperatures (down to ~ 820ºC, as suggested above) cannot be ruled out, but these are unlikely to have exceeded the twenty days between extrusion and sampling.

5.6 Conclusion

Petrological monitoring of the La Soufrière 2020-2021 lava dome, combined with the results from heating and oxidation experiments presented in this study, show that the textures of the dome rock are best explained by oxidation in the presence of air at temperatures ≤ 900ºC on timescales of weeks. Oxide nanolites are found to nucleate on the rims of pyroxene microlites and orthopyroxene phenocrysts in all experiments above the NNO buffer. Orthopyroxene phenocrysts become unstable above NNO at 1020ºC and one atmosphere. The composition of exsolved Fe-Ti oxides and olivines in the natural dome rock match those in experimental runs at 900ºC at NNO+2 and in air, suggesting an intermediate or fluctuating oxidation state. However, certain exsolution textures, such as Fe-Ti oxide trellis lamellae and recrystallisation, are only replicated experimentally in the presence of air at 900ºC (Figure 5.5e). In higher temperature runs (1020ºC), Fe-Ti oxides and olivines are considerably more altered than those observed in the dome, implying an upper temperature limit of dome oxidation at ~ 900ºC (Figure 5.2).

The experiments presented in this study demonstrate that oxidation-exsolution reactions can occur relatively quickly (≤ 168 hrs), particularly in the presence of air and at sustained high temperatures. The textures observed in the La Soufrière 2020-2021 lava dome are therefore inferred to have developed at the Earth's surface during dome emplacement, rather than during long-term magma sub-surface storage prior to eruption. Use of the U3 scoria as starting material and its ability to reproduce dome phenocryst textures

experimentally suggests that, plausibly, both dome and scoria could be sourced from the same basaltic andesite magma batch. This possibility is supported by near identical bulk rock and phenocryst assemblages, but with distinct post-eruptive cooling histories. On the basis of these experimental results, the characteristic alteration textures of the 2020-2021 La Soufrière dome are considered to be post- or syn-emplacement oxidation features, however, the limited number of samples from the active dome preclude any assessment of whether the observed textures are ubiquitous or confined to the surface of the dome at the sampling site.

Chapter 6

Conclusions

In this chapter I synthesise the results of the research presented in this thesis, including geochemical and petrological analyses of frequently erupted basaltic andesite magmas at La Soufrière volcano, St. Vincent, experimental determination of their origin in the lower crust and conditions of alteration at the surface.

6.1 Homogeneity of the basaltic andesite magmas at La Soufrière volcano, St. Vincent

New major and trace element data presented in chapter 2 for a series of lavas and dykes from La Soufrière volcano not previously sampled support compositional homogeneity within the system. Results find the majority of magmas to be basaltic andesite with ~ 4 wt. % MgO and in agreement with magma compositions erupted today. A single mafic crater lava unit (~ 8 wt. % MgO) is identified and is comparable in composition to rare mafic tephra and early low-magnesium basalt pre-Somma lavas. New $^{40}Ar/^{39}Ar$ dates help to constrain the period of time over which basaltic andesite magmas are continuously emplaced and find the crater lavas, occupying the walls of the current La Soufrière crater to be very young, giving either negative ages or ages with large uncertainty close to zero (7.9 ± 7.7 ka to 5.7 ± 4.4 ka). Interestingly, the lowermost crater lava unit is considered unconformably older (25.2 ± 3.1 ka) and could represent part of the Somma crater wall that slumped into the current crater during collapse of the Somma edifice, possibly linked with the large explosive YTF eruption. Dating of lavas on the western flanks of La Soufrière finds magmatism to have continued until much more

recently than previously thought (4.4 ± 4.2 ka), followed by at least one observed dyking event.

In chapter 3 the mineralogical variation in lava and dyke samples collected from La Soufrière are explored. Mineral assemblages are dominated by plagioclase, followed by clinopyroxene, orthopyroxene, Fe-Ti oxides and olivine. Olivine is absent in the more andesitic lavas, and orthopyroxene absent from the more basaltic lavas, highlighting the compositional control on the olivine-orthopyroxene peritectic relationship in these magmas. Mineral compositions are generally in equilibrium with Kd values suggesting crystallisation from the bulk magma. Values above equilibrium estimates are determined to be antecrystic and values below equilibrium estimates, particularly in the case of orthopyroxene, are interpreted to represent late-stage crystallisation. All samples contain high-An plagioclase, typical of the Lesser Antilles (Arculus and Wills, 1980), that are zoned and display significant decompression textures. Glomerocrysts are abundant in all samples, with textures representing nucleation and growth from the melt and compositions in good agreement with the phenocryst population.

In general, the basaltic andesite magmas erupted at La Soufrière are geochemically and petrologically very similar, with no signs of magma mixing or crustal assimilation from trace element ratios and mineral textures. The dyke samples display a significantly more refined mineral compositional range, supporting a rapid ascent to the surface and narrower window of crystallisation. Small variations in magma and mineral compositions amongst the lava samples are unavoidable due to minor differences in melting and crystallisation at the source and during ascent (Annen et al., 2006). The mafic crater lava unit corroborates the existence of more primitive magmas beneath La Soufrière that are rarely erupted at the surface.

6.2 Evidence for differentiation from a high-magnesium basaltic parent magma

Elevated REE concentrations and trace element ratios find erupted basaltic andesite magmas to have undergone coherent differentiation from a parental magma in chapter 2. Plagioclase and amphibole fractionation are inferred from Eu/Eu* and Dy/Dy* ratios, respectively (Davidson et al., 2013). A weak Eu negative anomaly and positive Sr anomaly in magmas indicates plagioclase fractionation at hydrous and oxidising conditions (Drake and Weill, 1975; Duchesne and Demaiffe, 1978; Blundy and Wood, 1991). Amphibole fractionation also supports a hydrous source region due to its stability at high water contents (Krawczynski et al., 2012).

Petrological analyses of the La Soufrière lava and dyke samples in chapter 3 finds further evidence for differentiation from a parent magma by the presence relict mineral cores. High-Fo olivine cores are found to be in equilibrium with high-magnesium basaltic magmas, previously identified as parental magmas to erupted basaltic andesites on St. Vincent, and similar in composition to the pre-Somma high-magnesium basalts (Heath et al., 1998a; Pichavant et al., 2002a; Melekhova et al., 2015). High Mg# clinopyroxene cores are instead found to be in equilibrium with low-magnesium basaltic magmas (similar to the mafic crater lava), generated from the same parental high-magnesium basalts, but rarely erupted at La Soufrière. These results support the idea of polybaric fractional crystallisation beneath La Soufrière, with basaltic andesites most frequently erupted. Interestingly relict mineral cores are primarily found in the older lavas sampled from the western flanks of La Soufrière, and the mafic crater lava unit suggesting relict minerals in more recently erupted magmas have either completely reacted away or been assimilated into the magma. The relatively low abundance of relict minerals in erupted magmas is not considered significant enough to alter the whole-rock composition.

6.3 Origin of erupted basaltic andesite magmas

Near-liquidus multiple saturation experiments find basaltic andesite magmas erupted at La Soufrière St. Vincent to be sourced from the lower crust at approximately 0.6 ± 0.1 GPa and 1020 ± 10 ºC, at ~ NNO+2 and with melt water contents of ~ 8 wt. % H_2O. Erupted magmas last equilibrated with an amphibole-gabbro source assemblage, a common cumulate xenolith erupted at St. Vincent (Tollan et al., 2012). Amphibole is found to be a peritectic near-liquidus phase and stable at lower temperatures as part of the hydrous crystalline mush. Fe-Ti oxides saturate on or close to the liquidus at all experimental conditions ≥ NNO, supporting Fe-depletion and the formation of calc-alkaline magmas in oxidising environments. Experimentally derived source pressure estimates equate to depths of approximately ~ 21 ± 3.5 km and are in good agreement with geophysical estimates for the pre-eruptive source for the 2020-2021 eruption (~ 18 ± 1.9 km; Camejo-Harry et al., 2024b) and the deepest earthquake foci (~ 15 ± 2.5 km; Contreras-Arratia et al., 2024).

In chapter 3 whole-rock thermobarometry estimates for the source of erupted basaltic andesite magmas at La Soufrière ranged from ~ 1030 – 1090 ± 50ºC and 0.4 – 0.7 ± 0.3 GPa. The high-pressure and high-temperature experiments presented in chapter 4 constrain source estimates to 0.6 ± 0.1 GPa and 1020 ± 10 ºC. Here I have shown that multiple saturation experiments can be used as a source thermobarometer and hygrometer, when the source assemblage is known and if erupted magma compositions have not experienced chemical modification after segregating from their source rock assemblage.

6.4 Magma ascent and crystallisation

Basaltic andesite magmas erupted at La Soufrière are found to be sourced from hydrous and oxidising conditions in the lower crust (see above). Low magmatic eruption temperatures (~ 960 – 1050ºC; Weber et al., 2024) support high dissolved water contents in the melt, as do high-An plagioclase core compositions (≥ An_{85}) identified in all samples studied here. A second population of plagioclase core compositions are found to be in equilibrium with melts at much lower water contents and highlight a second stage of plagioclase crystallisation after significant degassing. Adiabatic ascent of magmas initially containing ~ 8 wt. % water in the melt at 0.6 GPa would intersect the water-saturated liquidus at ~ 0.2 GPa with 5 wt. % H_2O, as shown by the P-T phase diagram derived in chapter 4. Degassing and decompression often induce crystallisation and can trigger eruptions (Cashman and Blundy, 2000; Hammer and Rutherford, 2002). Earthquake foci and the syn-eruptive mogi source for the 2020-2021 eruption at La Soufrière were determined at depths of ~ 6 km (~ 0.15 – 0.2 GPa; Camejo-Harry et al., 2024b; Contreras-Arratia et al., 2024) supporting shallow crystallisation. Clinopyroxene thermobarometry results also cluster at ~ 0.2 GPa, with few deep estimates, suggesting clinopyroxene predominantly crystallised in the shallow crust.

Low Mg# values for orthopyroxene in natural samples indicate late-stage crystallisation, after early olivine and clinopyroxene crystallisation. Equilibrium experiments in chapter 4 find orthopyroxene stable at low water contents (≤ 6 wt. % H_2O) and only a near liquidus phase at high pressures (≥ 0.8 GPa), supporting delayed orthopyroxene crystallisation until after degassing. Olivine is not observed in equilibrium experiments and is found rimmed with orthopyroxene in all natural samples, reflecting its narrow stability field and peritectic reaction relationship with orthopyroxene. Reaction rims and breakdown textures also evidence antecrystic material in erupted basaltic andesite magmas, with different antecrystic populations identified for each mineral phase from compositional

and textural data. Antecrysts are inferred to be sourced from both the surrounding crystalline mush and parental (or genetically related) magmas. Micro-xenoliths are identified in a small number of the magmas studied here, with orthopyroxene-rich and amphibole-free assemblages interpreted to represent different regions of the arc crust not previously sampled (Lewis, 1973; Arculus and Wills, 1980; Tollan et al., 2012). Recrystallisation textures in micro-xenoliths also support sampling of the deeper reworked arc crust (Melekhova et al., 2022).

6.5 Lava dome oxidation textures

Effusive magmatism at La Soufrière volcano today often involves the extrusion of lava domes refined to the crater, alongside large explosive eruptions, as seen in the 2020-2021 eruption. Alteration textures observed in the 2020-2021 erupted dome-rock, but absent from the subsequent scoria, are reproduced in high-temperature experiments at oxidising conditions and atmospheric pressure. The formation of co-existing symplectitic olivine, oxide-rimmed pyroxenes and trellis exsolution lamellae in Fe-Ti oxides is found to require temperatures close to 900ºC, an oxidation state between NNO+2 and air and can generate observed oxidation-exsolution textures on relatively quick timescales (≤ 168 hrs). The formation of high-Fo olivine symplectites with hematite as the exsolved oxide phase require temperatures of at least ≥ 820ºC (Haggerty and Baker, 1967), providing a thermal minima for reactions. Results suggest that the alteration textures observed in the 2020-2021 dome-rock could have occurred during emplacement at the Earth's surface, whilst temperatures remained high, and air infiltrated the lava dome. These findings indicate that both phases of the eruption could be sourced from the same batch of magma that experienced different T-fO_2 conditions during ascent and eruption at the Earth's surface.

References

Ágreda-López, M., Parodi, V., Musu, A., Jorgenson, C., Carfì, A., Mastrogiovanni, F., Caricchi, L., Perugini, D., Petrelli, M., 2024. Enhancing machine learning thermobarometry for clinopyroxene-bearing magmas. Computers & Geosciences 193, 105707. https://doi.org/10.1016/j.cageo.2024.105707

Ague, J.J., 2017. Element mobility during regional metamorphism in crustal and subduction zone environments with a focus on the rare earth elements (REE). American Mineralogist 102, 1796–1821. https://doi.org/10.2138/am-2017-6130

Aigner-Torres, M., Blundy, J., Ulmer, P., Pettke, T., 2007. Laser Ablation ICPMS study of trace element partitioning between plagioclase and basaltic melts: an experimental approach. Contrib Mineral Petrol 153, 647–667. https://doi.org/10.1007/s00410-006-0168-2

Albarede, F., Provost, A., 1977. Petrological and geochemical mass-balance equations: an algorithm for least-square fitting and general error analysis. Computers & Geosciences 3, 309–326. https://doi.org/10.1016/0098-3004(77)90007-3

Alidibirov, M., Dingwell, D.B., 1996. Magma fragmentation by rapid decompression. Nature 380, 146–148. https://doi.org/10.1038/380146a0

Allen, J.C., Boettcher, A.L., 1983. The stability of amphibole in andesite and basalt at high pressures. American Mineralogist 68, 307–314.

Almeev, R.R., Ariskin, A.A., Kimura, J.-I., Barmina, G.S., 2013. The role of polybaric crystallization in genesis of andesitic magmas: Phase equilibria simulations of the Bezymianny volcanic subseries. Journal of Volcanology and Geothermal Research 263, 182–192. https://doi.org/10.1016/j.jvolgeores.2013.01.004

Anderson, A., Wright, T., 1972. Phenocrysts and glass inclusions and their bearing on oxidation and mixing of basaltic magmas, Kilauea volcano, Hawaii. American Mineralogist: Journal of Earth and Planetary Materials 57, 188–216.

Anderson, T., 1908. VII. Report on the eruptions of the Soufrière in St. Vincent in 1902, and on a visit to Montagne Pelée in Martinique. - Part II. The changes in the districts and the subsequent history of the volcanoes. Phil. Trans. R. Soc. Lond. A 208, 275–303. https://doi.org/10.1098/rsta.1908.0020

Andújar, J., Martel, C., Pichavant, M., Samaniego, P., Scaillet, B., Molina, I., 2017. Structure of the Plumbing System at Tungurahua Volcano, Ecuador: Insights from Phase Equilibrium Experiments on July–August 2006 Eruption Products. Journal of Petrology 58, 1249–1278. https://doi.org/10.1093/petrology/egx054

Andújar, J., Scaillet, B., Pichavant, M., Druitt, T.H., 2015. Differentiation Conditions of a Basaltic Magma from Santorini, and its Bearing on the Production of Andesite in Arc Settings. Journal of Petrology 56, 765–794. https://doi.org/10.1093/petrology/egv016

Annen, C., Blundy, J.D., Sparks, R.S.J., 2006. The Genesis of Intermediate and Silicic Magmas in Deep Crustal Hot Zones. Journal of Petrology 47, 505–539. https://doi.org/10.1093/petrology/egi084

Applegarth, L.J., Tuffen, H., James, M.R., Pinkerton, H., 2013. Degassing-driven crystallisation in basalts. Earth-Science Reviews 116, 1–16. https://doi.org/10.1016/j.earscirev.2012.10.007

Arculus, R.J., 1976. Geology and geochemistry of the alkali basalt—andesite association of Grenada, Lesser Antilles island arc. Geological Society of America Bulletin 87, 612. https://doi.org/10.1130/0016-7606(1976)87<612:GAGOTA>2.0.CO;2

Arculus, R.J., Wills, K.J.A., 1980. The Petrology of Plutonic Blocks and Inclusions from the Lesser Antilles Island Arc. Journal of Petrology 21, 743–799. https://doi.org/10.1093/petrology/21.4.743

Arguin, J.-P., Pagé, P., Barnes, S.-J., Girard, R., Duran, C., 2018. An Integrated Model for Ilmenite, Al-Spinel, and Corundum Exsolutions in Titanomagnetite from Oxide-Rich Layers of the Lac Doré Complex (Québec, Canada). Minerals 8, 476. https://doi.org/10.3390/min8110476

Asimow, P.D., Longhi, J., 2004. The Significance of Multiple Saturation Points in the Context of Polybaric Near-fractional Melting. Journal of Petrology 45, 2349–2367. https://doi.org/10.1093/petrology/egh043

Aspinall, W.P., Sigurdsson, H., Shepherd, J.B., 1973. Eruption of Soufrière Volcano on St. Vincent Island, 1971-1972: This study of the latest activity and review of historic eruptions suggests a two-stage volcanic cycle. Science 181, 117–124. https://doi.org/10.1126/science.181.4095.117

Atlas, Z.D., Germa, A., Boss, B., Meireles, O., Ward, A., Ryan, J.G., 2022. Variable element enrichment sources and contributions to volcanic rocks along the Lesser Antilles Island Arc. Front. Earth Sci. 10, 782179. https://doi.org/10.3389/feart.2022.782179

Austrheim, H., Robins, B., 1981. Reactions involving hydration of orthopyroxene in anorthosite-gabbro. Lithos 14, 275–281. https://doi.org/10.1016/0024-4937(81)90055-4

Bachmann, O., Bergantz, G.W., 2006. Gas percolation in upper-crustal silicic crystal mushes as a mechanism for upward heat advection and rejuvenation of near-solidus magma bodies. Journal of Volcanology and Geothermal Research 149, 85–102. https://doi.org/10.1016/j.jvolgeores.2005.06.002

Bagiński, B., Dzierżanowski, P., Macdonald, R., Upton, B.G.J., 2009. Complex relationships among coexisting pyroxenes: the Palaeogene Eskdalemuir dyke, Scotland. Mineral. mag. 73, 929–942. https://doi.org/10.1180/minmag.2009.073.6.929

Bain, A.A., Kendrick, J.E., Lamur, A., Lavallée, Y., Calder, E.S., Cortés, J.A., Cortés, G.P., Gómez Martinez, D., Torres, R.A., 2021. Micro-Textural Controls on Magma Rheology and Vulcanian Explosion Cyclicity. Front. Earth Sci. 8, 611320. https://doi.org/10.3389/feart.2020.611320

Baker, D.R., Eggler, D.H., 1987. Compositions of anhydrous and hydrous melts coexisting with plagioclase, augite, and olivine or low-Ca pyroxene from 1 atm to 8 kbar; application to the Aleutian volcanic center of Atka. American Mineralogist 72, 12–28.

Baker, D.R., Eggler, D.H., 1983. Fractionation paths of Atka (Aleutians) high-alumina basalts: Constraints from phase relations. Journal of Volcanology and Geothermal Research 18, 387–404. https://doi.org/10.1016/0377-0273(83)90017-3

Baker, M.B., Grove, T.L., Price, R., 1994. Primitive basalts and andesites from the Mt. Shasta region, N. California: products of varying melt fraction and water content. Contr. Mineral. and Petrol. 118, 111–129. https://doi.org/10.1007/BF01052863

Balcone-Boissard, H., Boudon, G., d'Augustin, T., Erdmann, S., Deloule, E., Vicente, J., 2023. Architecture of the Lesser Antilles Arc Illustrated by Melt Inclusions. Journal of Petrology 64, egad020. https://doi.org/10.1093/petrology/egad020
Ball, J.L., Calder, E.S., Hubbard, B.E., Bernstein, M.L., 2013. An assessment of hydrothermal alteration in the Santiaguito lava dome complex, Guatemala: implications for dome collapse hazards. Bull Volcanol 75, 676. https://doi.org/10.1007/s00445-012-0676-z
Ball, J.L., Stauffer, P.H., Calder, E.S., Valentine, G.A., 2015. The hydrothermal alteration of cooling lava domes. Bull Volcanol 77, 102. https://doi.org/10.1007/s00445-015-0986-z
Ballhaus, C., Berry, R.F., Green, D.H., 1991. High pressure experimental calibration of the olivine-orthopyroxene-spinel oxygen geobarometer: implications for the oxidation state of the upper mantle. Contributions to Mineralogy and Petrology 27–40.
Ban, M., Witt-Eickschen, G., Klein, M., Seck, H.A., 2005. The origin of glasses in hydrous mantle xenoliths from the West Eifel, Germany: incongruent break down of amphibole. Contrib Mineral Petrol 148, 511–523. https://doi.org/10.1007/s00410-004-0623-x
Barnes, S.J., Roeder, P.L., 2001. The Range of Spinel Compositions in Terrestrial Mafic and Ultramafic Rocks. Journal of Petrology 42, 2279–2302. https://doi.org/10.1093/petrology/42.12.2279
Barr, J.A., Grove, T.L., 2010. AuPdFe ternary solution model and applications to understanding the fO2 of hydrous, high-pressure experiments. Contrib Mineral Petrol 160, 631–643. https://doi.org/10.1007/s00410-010-0497-z
Bartels, K.S., Kinzler, R.J., Grove, T.L., 1991. High pressure phase relations of primitive high-alumina basalts from Medicine Lake volcano, northern California. Contr. Mineral. and Petrol. 108, 253–270. https://doi.org/10.1007/BF00285935
Barton, M., Sheets, J.M., Lee, W.E., van Gaans, C., 1991. Occurrence of low-Ca clinopyroxene and the role of deformation in the formation of pyroxene-Fe−Ti oxide symplectites. Contr. Mineral. and Petrol. 108, 181–195. https://doi.org/10.1007/BF00307337
Barton, M., Van Gaans, C., 1988. Formation of orthopyroxene-Fe-Ti oxide symplectites in Precambrian intrusives, Rogaland, southwestern Norway. American Mineralogist 73, 1046–1059.
Becerra-Torres, E., Melekhova, E., Blundy, J.D., Brooker, R.A., 2020. Experimental evidence for decompression melting of metasomatized mantle beneath Colima Graben, Mexico. Contrib Mineral Petrol 175, 101. https://doi.org/10.1007/s00410-020-01740-x
Bell, P.M., Mao, H.K., Roedder, E., Weiblen, P.W., 1975. The problem of the origin of symplectites in olivine-bearing lunar rocks. Lunar and Planetary Science Conference Proceedings 1, 231–248.
Bennett, E.N., Lissenberg, C.J., Cashman, K.V., 2019. The significance of plagioclase textures in mid-ocean ridge basalt (Gakkel Ridge, Arctic Ocean). Contrib Mineral Petrol 174, 49. https://doi.org/10.1007/s00410-019-1587-1
Berndt, J., Koepke, J., Holtz, F., 2005. An Experimental Investigation of the Influence of Water and Oxygen Fugacity on Differentiation of MORB at 200 MPa. Journal of Petrology 46, 135–167. https://doi.org/10.1093/petrology/egh066
Bezard, R., Turner, S., Davidson, J.P., Macpherson, C.G., Lindsay, J.M., 2015. Seeing through the Effects of Crustal Assimilation to Assess the Source Composition beneath the Southern Lesser Antilles Arc. Journal of Petrology 56, 815–844. https://doi.org/10.1093/petrology/egv018
Bie, L., Rietbrock, A., Hicks, S., Allen, R., Blundy, J., Clouard, V., Collier, J., Davidson, J., Garth, T., Goes, S., Harmon, N., Henstock, T., van Hunen, J., Kendall, M., Krüger, F., Lynch, L., Macpherson, C., Robertson, R., Rychert, K., Tait, S., Wilkinson, J., Wilson, M., 2020. Along-Arc Heterogeneity in Local Seismicity across the Lesser Antilles Subduction Zone from a Dense Ocean-Bottom Seismometer Network. Seismological Research Letters 91, 237–247. https://doi.org/10.1785/0220190147
Bindeman, I.N., Bailey, J.C., 1999. Trace elements in anorthite megacrysts from the Kurile Island Arc: a window to across-arc geochemical variations in magma compositions. Earth and Planetary Science Letters 169, 209–226. https://doi.org/10.1016/S0012-821X(99)00086-2
Binder, B., Keppler, H., 2011. The oxidation state of sulfur in magmatic fluids. Earth and Planetary Science Letters 301, 190–198. https://doi.org/10.1016/j.epsl.2010.10.042
Blatter, D.L., Sisson, T.W., Hankins, W.B., 2017. Voluminous arc dacites as amphibole reaction-boundary liquids. Contrib Mineral Petrol 172, 27. https://doi.org/10.1007/s00410-017-1340-6
Blatter, D.L., Sisson, T.W., Hankins, W.B., 2013. Crystallization of oxidized, moderately hydrous arc basalt at mid- to lower-crustal pressures: implications for andesite genesis. Contrib Mineral Petrol 166, 861–886. https://doi.org/10.1007/s00410-013-0920-3
Blondes, M.S., Brandon, M.T., Reiners, P.W., Page, F.Z., Kita, N.T., 2012. Generation of Forsteritic Olivine (Fo99·8) by Subsolidus Oxidation in Basaltic Flows. Journal of Petrology 53, 971–984. https://doi.org/10.1093/petrology/egs006
Blundy, J., 2022. Chemical Differentiation by Mineralogical Buffering in Crustal Hot Zones. Journal of Petrology 63, egac054. https://doi.org/10.1093/petrology/egac054
Blundy, J., Cashman, K., 2008. Petrologic Reconstruction of Magmatic System Variables and Processes. Reviews in Mineralogy and Geochemistry 69, 179–239. https://doi.org/10.2138/rmg.2008.69.6
Blundy, J., Cashman, K.V., Berlo, K., 2008. Chapter 33: Evolving Magma Storage Conditions Beneath Mount St. Helens Inferred from Chemical Variations in Melt Inclusions from the 1980–1986 and Current (2004–2006) Eruptions, in: A Volcano Rekindled: The Renewed Eruption of Mount St. Helens, 2004–2006, U.S. Geological Survey Professional Paper 1750.
Blundy, J., Melekhova, E., Ziberna, L., Humphreys, M.C.S., Cerantola, V., Brooker, R.A., McCammon, C.A., Pichavant, M., Ulmer, P., 2020. Effect of redox on Fe–Mg–Mn exchange between olivine and melt and an oxybarometer for basalts. Contrib Mineral Petrol 175, 103. https://doi.org/10.1007/s00410-020-01736-7
Blundy, J.D., Falloon, T.J., Wood, B.J., Dalton, J.A., 1995. Sodium partitioning between clinopyroxene and silicate melts. J. Geophys. Res. 100, 15501–15515. https://doi.org/10.1029/95JB00954
Blundy, J.D., Wood, B.J., 1991. Crystal-chemical controls on the partitioning of Sr and Ba between plagioclase feldspar, silicate melts, and hydrothermal solutions. Geochimica et Cosmochimica Acta 55, 193–209. https://doi.org/10.1016/0016-7037(91)90411-W
Boland, J.N., Otten, M.T., 1985. Symplectitic augite: evidence for discontinuous precipitation as an exsolution mechanism in Ca-rich clinopyroxene. J Metamorph Geol 3, 13–20. https://doi.org/10.1111/j.1525-1314.1985.tb00302.x

Boudon, G., Komorowski, J.-C., Villemant, B., Semet, M.P., 2008. A new scenario for the last magmatic eruption of La Soufrière of Guadeloupe (Lesser Antilles) in 1530 A.D. Evidence from stratigraphy radiocarbon dating and magmatic evolution of erupted products. Journal of Volcanology and Geothermal Research 178, 474–490. https://doi.org/10.1016/j.jvolgeores.2008.03.006
Boudon, G., Le Friant, A., Komorowski, J., Deplus, C., Semet, M.P., 2007. Volcano flank instability in the Lesser Antilles Arc: Diversity of scale, processes, and temporal recurrence. J. Geophys. Res. 112, 2006JB004674. https://doi.org/10.1029/2006JB004674
Boulliung, J., Füri, E., Dalou, C., Tissandier, L., Zimmermann, L., Marrocchi, Y., 2020. Oxygen fugacity and melt composition controls on nitrogen solubility in silicate melts. Geochimica et Cosmochimica Acta 284, 120–133. https://doi.org/10.1016/j.gca.2020.06.020
Bouvier, A.-S., Métrich, N., Deloule, E., 2008. Slab-Derived Fluids in the Magma Sources of St. Vincent (Lesser Antilles Arc): Volatile and Light Element Imprints. Journal of Petrology 49, 1427–1448. https://doi.org/10.1093/petrology/egn031
Bouysse, P., Westercamp, D., 1990. Subduction of Atlantic aseismic ridges and Late Cenozoic evolution of the Lesser Antilles island arc. Tectonophysics 175, 349–380. https://doi.org/10.1016/0040-1951(90)90180-G
Boynton, C.H., Westbrook, G.K., Bott, M.H.P., Long, R.E., 1979. A seismic refraction investigation of crustal structure beneath the Lesser Antilles island arc. Geophysical Journal International 58, 371–393. https://doi.org/10.1111/j.1365-246X.1979.tb01031.x
Braszus, B., Goes, S., Allen, R., Rietbrock, A., Collier, J., Harmon, N., Henstock, T., Hicks, S., Rychert, C.A., Maunder, B., Van Hunen, J., Bie, L., Blundy, J., Cooper, G., Davy, R., Kendall, J.M., Macpherson, C., Wilkinson, J., Wilson, M., 2021. Subduction history of the Caribbean from upper-mantle seismic imaging and plate reconstruction. Nat Commun 12, 4211. https://doi.org/10.1038/s41467-021-24413-0
Brenan, J.M., Shaw, H.F., Ryerson, F.J., Phinney, D.L., 1995. Mineral-aqueous fluid partitioning of trace elements at 900°C and 2.0 GPa: Constraints on the trace element chemistry of mantle and deep crustal fluids. Geochimica et Cosmochimica Acta 59, 3331–3350. https://doi.org/10.1016/0016-7037(95)00215-L
Briden, J.C., Rex, D.C., Faller, A.M., Tomblin, J.F., 1979. K-Ar geochronology and palaeomagnetism of volcanic rocks in the Lesser Antilles island arc. Phil. Trans. R. Soc. Lond. A 291, 485–528. https://doi.org/10.1098/rsta.1979.0040
Brooker, R., Holloway, J.R., Hervig, R., 1998. Reduction in piston-cylinder experiments; the detection of carbon infiltration into platinum capsules. American Mineralogist 83, 985–994. https://doi.org/10.2138/am-1998-9-1006
Brophy, J.G., 1991. Composition gaps, critical crystallinity, and fractional crystallization in orogenic (calc-alkaline) magmatic systems. Contr. Mineral. and Petrol. 109, 173–182. https://doi.org/10.1007/BF00306477
Brounce, M.N., Kelley, K.A., Cottrell, E., 2014. Variations in Fe3+/∑Fe of Mariana Arc Basalts and Mantle Wedge fO2. Journal of Petrology 55, 2513–2536. https://doi.org/10.1093/petrology/egu065
Brown, G.M., Holland, J.G., Sigurdsson, H., Tomblin, J.F., Arculus, R.J., 1977. Geochemistry of the Lesser Antilles volcanic island arc. Geochimica et Cosmochimica Acta 41, 785–801. https://doi.org/10.1016/0016-7037(77)90049-7
Brown, J., 2022. Magma Chemical Evolution in the Lesser Antilles Arc Crust: Insights from Plutonic Xenoliths (PhD Thesis). Durham University.
Brown, J.R., Cooper, G.F., Nowell, G.M., Macpherson, C.G., Neill, I., Prytulak, J., 2021. Isotopic Compositions of Plagioclase From Plutonic Xenoliths Reveal Crustal Assimilation Below Martinique, Lesser Antilles Arc. Front. Earth Sci. 9, 682583. https://doi.org/10.3389/feart.2021.682583
Brown, W.L., Macaudèire, J., 1986. Mechanical twinning of plagioclase in a deformed meta-anorthosite ? the production of M-twinning. Contrib Mineral Petrol 92, 44–56. https://doi.org/10.1007/BF00373962
Buddington, A.F., Lindsley, D.H., 1964. Iron-Titanium Oxide Minerals and Synthetic Equivalents. Journal of Petrology 5, 310–357. https://doi.org/10.1093/petrology/5.2.310
Burgisser, A., Scaillet, B., 2007. Redox evolution of a degassing magma rising to the surface. Nature 445, 194–197. https://doi.org/10.1038/nature05509
Burkhard, D.J.M., 2001. Crystallization and Oxidation of Kilauea Basalt Glass: Processes during Reheating Experiments. Journal of Petrology 42, 507–527. https://doi.org/10.1093/petrology/42.3.507
Burkhard, D.J.M., 2005a. Crystallization and oxidation during emplacement of lava lobes, in: Kinematics and Dynamics of Lava Flows. Geological Society of America. https://doi.org/10.1130/0-8137-2396-5.67
Burkhard, D.J.M., 2005b. Nucleation and growth rates of pyroxene, plagioclase, and Fe-Ti oxides in basalt under atmospheric conditions. ejm 17, 675–686. https://doi.org/10.1127/0935-1221/2005/0017-0675
Burnham, C.W., 1979. Chapter 16. THE IMPORTANCE OF VOLATILE CONSTITUENTS, in: Evolution of the Igneous Rocks. Princeton University Press, pp. 439–482. https://doi.org/10.1515/9781400868506-017
Calder, E.S., Lavallée, Y., Kendrick, J.E., Bernstein, M., 2015. Lava Dome Eruptions, in: The Encyclopedia of Volcanoes. Elsevier, pp. 343–362. https://doi.org/10.1016/B978-0-12-385938-9.00018-3
Camejo-Harry, M., Blundy, J., Mutch, E.J.F., Hudson, T., Kendall, J., Christopher, T., Contreras-Arratia, R., Latchman, J.L., Henry, L., 2025. Petrological Evidence for Magma Mobilization Years Before the 2020/2021 Eruption of La Soufrière Volcano, St. Vincent. Geochem Geophys Geosyst 26, e2024GC012093. https://doi.org/10.1029/2024GC012093
Camejo-Harry, M., Melekhova, E., Aufrère, S., McCarthy, A., Blundy, J., 2024a. Early arc crust formation preserved in the Grenadines archipelago, southern Lesser Antilles arc. R. Soc. Open Sci. 11, 231914. https://doi.org/10.1098/rsos.231914
Camejo-Harry, M., Melekhova, E., Blundy, J., Attridge, W., Robertson, R., Christopher, T., 2018. Magma evolution beneath Bequia, Lesser Antilles, deduced from petrology of lavas and plutonic xenoliths. Contrib Mineral Petrol 173, 77. https://doi.org/10.1007/s00410-018-1504-z
Camejo-Harry, M., Pascal, K., Euillades, P., Grandin, R., Hamling, I., Euillades, L., Contreras-Arratia, R., Ryan, G.A., Latchman, J.L., Lynch, L., Jo, M., 2024b. Monitoring volcano deformation at La Soufrière, St Vincent during the 2020–21 eruption with insights into its magma plumbing system architecture. SP 539, 41–62. https://doi.org/10.1144/SP539-2022-270
Canil, D., 1994. Stability of clinopyroxene at pressure-temperature conditions of the transition region. Physics of the Earth and Planetary Interiors 86, 25–34. https://doi.org/10.1016/0031-9201(94)05059-7
Carey, S.N., Sigurdsson, H., 1978. Deep-sea evidence for distribution of tephra from the mixed magma eruption of the Soufrière on St. Vincent, 1902: Ash turbidites and air fall. Geol 6, 271. https://doi.org/10.1130/0091-7613(1978)6<271:DEFDOT>2.0.CO;2

Carmichael, I.S.E., 1991. The redox states of basic and silicic magmas: a reflection of their source regions? Contr. Mineral. and Petrol. 106, 129–141. https://doi.org/10.1007/BF00306429
Carmichael, I.S.E., Ghiorso, M.S., 1986. Oxidation-reduction relations in basic magma: a case for homogeneous equilibria. Earth and Planetary Science Letters 78, 200–210. https://doi.org/10.1016/0012-821X(86)90061-0
Carpentier, M., Chauvel, C., Mattielli, N., 2008. Pb–Nd isotopic constraints on sedimentary input into the Lesser Antilles arc system. Earth and Planetary Science Letters 272, 199–211. https://doi.org/10.1016/j.epsl.2008.04.036
Carr, B., 2016. Transitions in Eruption Style at Silicic Volcanoes: From Stable Domes to Pyroclastic Flows and Explosive Plumes. Arizona State University.
Cashman, K., Blundy, J., 2013. Petrological cannibalism: the chemical and textural consequences of incremental magma body growth. Contrib Mineral Petrol 166, 703–729. https://doi.org/10.1007/s00410-013-0895-0
Cashman, K., Blundy, J., 2000. Degassing and crystallization of ascending andesite and dacite. Philosophical Transactions of the Royal Society of London. Series A: Mathematical, Physical and Engineering Sciences 358, 1487–1513. https://doi.org/10.1098/rsta.2000.0600
Cashman, K.V., 1992. Groundmass crystallization of Mount St. Helens dacite, 1980-1986: a tool for interpreting shallow magmatic processes. Contr. Mineral. and Petrol. 109, 431–449. https://doi.org/10.1007/BF00306547
Cassidy, M., Cole, Paul.D., Hicks, K.E., Varley, N.R., Peters, N., Lerner, A.H., 2015. Rapid and slow: Varying magma ascent rates as a mechanism for Vulcanian explosions. Earth and Planetary Science Letters 420, 73–84. https://doi.org/10.1016/j.epsl.2015.03.025
Cassidy, M., Ebmeier, S.K., Helo, C., Watt, S.F.L., Caudron, C., Odell, A., Spaans, K., Kristianto, P., Triastuty, H., Gunawan, H., Castro, J.M., 2019. Explosive Eruptions With Little Warning: Experimental Petrology and Volcano Monitoring Observations From the 2014 Eruption of Kelud, Indonesia. Geochem. Geophys. Geosyst. 20, 4218–4247. https://doi.org/10.1029/2018GC008161
Cassidy, M., Manga, M., Cashman, K., Bachmann, O., 2018. Controls on explosive-effusive volcanic eruption styles. Nat Commun 9, 2839. https://doi.org/10.1038/s41467-018-05293-3
Cassidy, M., Trofimovs, J., Watt, S.F.L., Palmer, M.R., Taylor, R.N., Gernon, T.M., Talling, P.J., Le Friant, A., 2014. Chapter 20 Multi-stage collapse events in the South Soufrière Hills, Montserrat as recorded in marine sediment cores, in: The Eruption of Soufrière Hills Volcano, Montserrat from 2000 to 2010, Geological Society, London, Memoirs. pp. 383–397. https://doi.org/10.1144/M39.20
Cawthorn, R.G., 1976. Some chemical controls on igneous amphibole compositions. Geochimica et Cosmochimica Acta 40, 1319–1328. https://doi.org/10.1016/0016-7037(76)90121-6
Cawthorn, R.G., O'Hara, M.J., 1976. Amphibole fractionation in calc-alkaline magma genesis. American Journal of Science 276, 309–329. https://doi.org/10.2475/ajs.276.3.309
Champness, P.E., 1970. Nucleation and growth of iron oxides in olivines, $(Mg,Fe)_2SiO_4$. Mineral. mag. 37, 790–800. https://doi.org/10.1180/minmag.1970.037.291.05
Chen, K., Tang, M., Hu, Z., Liu, Y., 2023. Generation of tholeiitic and calc-alkaline arc magmas and its implications for continental growth. Geochimica et Cosmochimica Acta 355, 173–183. https://doi.org/10.1016/j.gca.2023.07.002
Chin, E.J., Shimizu, K., Bybee, G.M., Erdman, M.E., 2018. On the development of the calc-alkaline and tholeiitic magma series: A deep crustal cumulate perspective. Earth and Planetary Science Letters 482, 277–287. https://doi.org/10.1016/j.epsl.2017.11.016
Churikova, T., Dorendorf, F., Wörner, G., 2001. Sources and Fluids in the Mantle Wedge below Kamchatka, Evidence from Across-arc Geochemical Variation. Journal of Petrology 42, 1567–1593. https://doi.org/10.1093/petrology/42.8.1567
Clemens, J.D., Stevens, G., 2012. What controls chemical variation in granitic magmas? Lithos 134–135, 317–329. https://doi.org/10.1016/j.lithos.2012.01.001
Cole, P.D., Barclay, J., Robertson, R.E.A., Mitchell, S., Davies, B.V., Constantinescu, R., Sparks, R.S.J., Aspinall, W., Stinton, A., 2024. Explosive sequence of La Soufrière, St Vincent, April 2021: insights into drivers and consequences via eruptive products. SP 539, 81–106. https://doi.org/10.1144/SP539-2022-292
Cole, P.D., Robertson, R.E.A., Fedele, L., Scarpati, C., 2019. Explosive activity of the last 1000 years at La Soufrière, St Vincent, Lesser Antilles. Journal of Volcanology and Geothermal Research 371, 86–100. https://doi.org/10.1016/j.jvolgeores.2019.01.002
Colombier, M., Wadsworth, F.B., Gurioli, L., Scheu, B., Kueppers, U., Di Muro, A., Dingwell, D.B., 2017. The evolution of pore connectivity in volcanic rocks. Earth and Planetary Science Letters 462, 99–109. https://doi.org/10.1016/j.epsl.2017.01.011
Condamine, P., Tournier, S., Charlier, B., Médard, E., Triantafyllou, A., Dalou, C., Tissandier, L., Lequin, D., Cartier, C., Füri, E., Burnard, P.G., Demouchy, S., Marrocchi, Y., 2022. Influence of intensive parameters and assemblies on friction evolution during piston-cylinder experiments. American Mineralogist 107, 1575–1581. https://doi.org/10.2138/am-2022-7958
Contreras-Arratia, R., Chouet, B., Caudron, C., Nath, N., Balchan, A., Madoo, F., Ramsingh-Reddock, H., 2024. Tracking seismicity in an underfunded institution: The case of La Soufrière St Vincent volcanic eruption 2020–2021. Journal of Volcanology and Geothermal Research 446, 107990. https://doi.org/10.1016/j.jvolgeores.2023.107990
Coombs, M.L., Gardner, J.E., 2004. Reaction rim growth on olivine in silicic melts: Implications for magma mixing. American Mineralogist 89, 748–758. https://doi.org/10.2138/am-2004-5-608
Cooper, G.F., Davidson, J.P., Blundy, J.D., 2016. Plutonic xenoliths from Martinique, Lesser Antilles: evidence for open system processes and reactive melt flow in island arc crust. Contrib Mineral Petrol 171, 87. https://doi.org/10.1007/s00410-016-1299-8
Cooper, G.F., Inglis, E.C., 2022. A Crustal Control on the Fe Isotope Systematics of Volcanic Arcs Revealed in Plutonic Xenoliths From the Lesser Antilles. Front. Earth Sci. 9, 795858. https://doi.org/10.3389/feart.2021.795858
Cooper, G.F., Macpherson, C.G., Blundy, J.D., Maunder, B., Allen, R.W., Goes, S., Collier, J.S., Bie, L., Harmon, N., Hicks, S.P., Iveson, A.A., Prytulak, J., Rietbrock, A., Rychert, C.A., Davidson, J.P., the VoiLA team, Cooper, G.F., Macpherson, C.G., Blundy, J.D., Maunder, B., Allen, R.W., Goes, S., Collier, J.S., Bie, L., Harmon, N., Hicks, S.P., Rietbrock, A., Rychert, C.A., Davidson, J.P., Davy, R.G., Henstock, T.J., Kendall, M.J., Schlaphorst, D., van Hunen, J., Wilkinson, J.J., Wilson, M., 2020. Variable water input controls evolution of the Lesser Antilles volcanic arc. Nature 582, 525–529. https://doi.org/10.1038/s41586-020-2407-5
Cooper, K.M., 2019. Time scales and temperatures of crystal storage in magma reservoirs: implications for magma reservoir dynamics. Phil. Trans. R. Soc. A. 377, 20180009. https://doi.org/10.1098/rsta.2018.0009

Costa, F., Andreastuti, S., Bouvet de Maisonneuve, C., Pallister, J.S., 2013. Petrological insights into the storage conditions, and magmatic processes that yielded the centennial 2010 Merapi explosive eruption. Journal of Volcanology and Geothermal Research 261, 209–235. https://doi.org/10.1016/j.jvolgeores.2012.12.025
Costa, F., Dungan, Singer, 2002. Hornblende- and Phlogopite-Bearing Gabbroic Xenoliths from Volcan San Pedro (36degreesS), Chilean Andes: Evidence for Melt and Fluid Migration and Reactions in Subduction-Related Plutons. Journal of Petrology 43, 219–241. https://doi.org/10.1093/petrology/43.2.219
Cottrell, E., Gardner, J.E., Rutherford, M.J., 1999. Petrologic and experimental evidence for the movement and heating of the pre-eruptive Minoan rhyodacite (Santorini, Greece). Contrib Mineral Petrol 135, 315–331. https://doi.org/10.1007/s004100050514
Couch, S., Sparks, R.S.J., Carroll, M.R., 2003. The Kinetics of Degassing-Induced Crystallization at Soufriere Hills Volcano, Montserrat. Journal of Petrology 44, 1477–1502. https://doi.org/10.1093/petrology/44.8.1477
Creer, K.M., Ibbetson, J., Drew, W., 1970. Activation Energy of Cation Migration in Titanomagnetites. Geophys J Int 19, 93–101. https://doi.org/10.1111/j.1365-246X.1970.tb06740.x
Czamanske, G.K., Wones, D.R., 1973. Oxidation During Magmatic Differentiation, Finnmarka Complex, Oslo Area, Norway: Part 2, The Mafic Silicates1. Journal of Petrology 14, 349–380. https://doi.org/10.1093/petrology/14.3.349
Darmawan, H., Troll, V.R., Walter, T.R., Deegan, F.M., Geiger, H., Heap, M.J., Seraphine, N., Harris, C., Humaida, H., Müller, D., 2022. Hidden mechanical weaknesses within lava domes provided by buried high-porosity hydrothermal alteration zones. Sci Rep 12, 3202. https://doi.org/10.1038/s41598-022-06765-9
Davidson, J., Turner, S., Handley, H., Macpherson, C., Dosseto, A., 2007a. Amphibole “sponge” in arc crust? Geol 35, 787. https://doi.org/10.1130/G23637A.1
Davidson, J., Turner, S., Plank, T., 2013. Dy/Dy*: Variations Arising from Mantle Sources and Petrogenetic Processes. Journal of Petrology 54, 525–537. https://doi.org/10.1093/petrology/egs076
Davidson, J.P., Morgan, D.J., Charlier, B.L.A., Harlou, R., Hora, J.M., 2007b. Microsampling and Isotopic Analysis of Igneous Rocks: Implications for the Study of Magmatic Systems. Annu. Rev. Earth Planet. Sci. 35, 273–311. https://doi.org/10.1146/annurev.earth.35.031306.140211
Davidson, J.P., Tepley, F.J., 1997. Recharge in Volcanic Systems: Evidence from Isotope Profiles of Phenocrysts. Science 275, 826–829. https://doi.org/10.1126/science.275.5301.826
De Hoog, J.C.M., Gall, L., Cornell, D.H., 2010. Trace-element geochemistry of mantle olivine and application to mantle petrogenesis and geothermobarometry. Chemical Geology 270, 196–215. https://doi.org/10.1016/j.chemgeo.2009.11.017
Deardorff, N., Cashman, K., 2017. Rapid crystallization during recycling of basaltic andesite tephra: timescales determined by reheating experiments. Sci Rep 7, 46364. https://doi.org/10.1038/srep46364
Deines, P., Nafziger, R.H., Ulmer, G.C., Woermann, E., 1976. Temperature-oxygen fugacity tables for selected gas mixtures in the system C-H-O at one atmosphere total pressure. MTB 7, 143–143. https://doi.org/10.1007/BF02652831
Del Moro, S., Renzulli, A., Landi, P., La Felice, S., Rosi, M., 2013. Unusual lapilli tuff ejecta erupted at Stromboli during the 15 March 2007 explosion shed light on the nature and thermal state of rocks forming the crater system of the volcano. Journal of Volcanology and Geothermal Research 254, 37–52. https://doi.org/10.1016/j.jvolgeores.2012.12.017
DePaolo, D.J., 1981. Trace element and isotopic effects of combined wallrock assimilation and fractional crystallization. Earth and Planetary Science Letters 53, 189–202. https://doi.org/10.1016/0012-821X(81)90153-9
Dessimoz, M., Müntener, O., Ulmer, P., 2012. A case for hornblende dominated fractionation of arc magmas: the Chelan Complex (Washington Cascades). Contrib Mineral Petrol 163, 567–589. https://doi.org/10.1007/s00410-011-0685-5
Devine, J.D., Sigurdsson, H., 1983. The liquid composition and crystallization history of the 1979 soufriere magma, St. Vincent, W.I. Journal of Volcanology and Geothermal Research 16, 1–31. https://doi.org/10.1016/0377-0273(83)90082-3
Devine, J.D., Sigurdsson, H., 1980. Garnet–fassaite calc-silicate nodule from La Soufrière, St. Vincent. American Mineralogist 65, 302–305.
Dirksen, O., Humphreys, M.C.S., Pletchov, P., Melnik, O., Demyanchuk, Y., Sparks, R.S.J., Mahony, S., 2006. The 2001–2004 dome-forming eruption of Shiveluch volcano, Kamchatka: Observation, petrological investigation and numerical modelling. Journal of Volcanology and Geothermal Research 155, 201–226. https://doi.org/10.1016/j.jvolgeores.2006.03.029
D’Mello, N.G., Zellmer, G.F., Kereszturi, G., Ubide, T., Procter, J.N., Stewart, R.B., 2023. Crystal entrainment from cool, low-silica rocks into hot, high-silica melts: diverse primary melt compositions at Taranaki volcano, New Zealand. JGS 180, jgs2022-036. https://doi.org/10.1144/jgs2022-036
D’Oriano, C., Bertagnini, A., Cioni, R., Pompilio, M., 2014. Identifying recycled ash in basaltic eruptions. Sci Rep 4, 5851. https://doi.org/10.1038/srep05851
D’Oriano, C., Pompilio, M., Bertagnini, A., Cioni, R., Pichavant, M., 2013. Effects of experimental reheating of natural basaltic ash at different temperatures and redox conditions. Contrib Mineral Petrol 165, 863–883. https://doi.org/10.1007/s00410-012-0839-0
Dostal, J., Dupuy, C., Carron, J.P., Le Guen De Kerneizon, M., Maury, R.C., 1983. Partition coefficients of trace elements: Application to volcanic rocks of St. Vincent, West Indies. Geochimica et Cosmochimica Acta 47, 525–533. https://doi.org/10.1016/0016-7037(83)90275-2
Drake, M.J., Weill, D.F., 1975. Partition of Sr, Ba, Ca, Y, Eu2+, Eu3+, and other REE between plagioclase feldspar and magmatic liquid: an experimental study. Geochimica et Cosmochimica Acta 39, 689–712. https://doi.org/10.1016/0016-7037(75)90011-3
Du, X., Su, X., Wang, Y., Li, J., 2009. Thermal decomposition of grinding activated bayerite. Materials Research Bulletin 44, 660–665. https://doi.org/10.1016/j.materresbull.2008.06.031
Duchesne, J.-C., 1972. Iron-Titanium Oxide Minerals in the Bjerkrem-Sogndal Massif, South-western Norway. Journal of Petrology 13, 57–81. https://doi.org/10.1093/petrology/13.1.57
Duchesne, J.-C., Demaiffe, D., 1978. Trace elements and anorthosite genesis. Earth and Planetary Science Letters 38, 249–272. https://doi.org/10.1016/0012-821X(78)90134-6

Dufek, J., Bachmann, O., 2010. Quantum magmatism: Magmatic compositional gaps generated by melt-crystal dynamics. Geology 38, 687–690. https://doi.org/10.1130/G30831.1
Dungan, M.A., Davidson, J., 2004. Partial assimilative recycling of the mafic plutonic roots of arc volcanoes: An example from the Chilean Andes. Geol 32, 773. https://doi.org/10.1130/G20735.1
Edmonds, M., Cashman, K.V., Holness, M., Jackson, M., 2019. Architecture and dynamics of magma reservoirs. Phil. Trans. R. Soc. A. 377, 20180298. https://doi.org/10.1098/rsta.2018.0298
Edmonds, M., Herd, R.A., 2007. A volcanic degassing event at the explosive-effusive transition. Geophys. Res. Lett. 34, L21310. https://doi.org/10.1029/2007GL031379
Edwards, A.B., 1938. The Formation of Iddingsite. American Mineralogist 23, 277–281.
Eggler, D.H., 1972. Amphibole stability in H2O-undersaturated calc-alkaline melts. Earth and Planetary Science Letters 15, 28–34. https://doi.org/10.1016/0012-821X(72)90025-8
Eichelberger, J.C., Izbekov, P.E., Browne, B.L., 2006. Bulk chemical trends at arc volcanoes are not liquid lines of descent. Lithos 87, 135–154. https://doi.org/10.1016/j.lithos.2005.05.006
Ejima, T., Akasaka, M., Nagao, T., Ohfuji, H., 2013. Oxidation states of Fe and precipitates within olivine from orthopyroxene-olivine-clinopyroxene andesite lava from Kasayama volcano, Hagi, Yamaguchi, Japan. Journal of Mineralogical and Petrological Sciences 108, 25–36. https://doi.org/10.2465/jmps.120621a
Ejima, T., Yoneda, M., Akasaka, M., Ohfuji, H., Kon, Y., Nagashima, M., Nakamuta, Y., 2017. Precipitates within olivine phenocrysts in oxidized andesitic scoria from Kasayama volcano, Hagi, Japan. Journal of Mineralogical and Petrological Sciences 112, 116–126. https://doi.org/10.2465/jmps.161219
Elliott, T., 2003. Tracers of the slab, in: Eiler, J. (Ed.), Geophysical Monograph Series. American Geophysical Union, Washington, D. C., pp. 23–45. https://doi.org/10.1029/138GM03
Elliott, T., Plank, T., Zindler, A., White, W., Bourdon, B., 1997. Element transport from slab to volcanic front at the Mariana arc. J. Geophys. Res. 102, 14991–15019. https://doi.org/10.1029/97JB00788
Erdmann, S., Martel, C., Pichavant, M., Bourdier, J.-L., Champallier, R., Komorowski, J.-C., Cholik, N., 2016. Constraints from Phase Equilibrium Experiments on Pre-eruptive Storage Conditions in Mixed Magma Systems: a Case Study on Crystal-rich Basaltic Andesites from Mount Merapi, Indonesia. J. Petrology 57, 535–560. https://doi.org/10.1093/petrology/egw019
Erdmann, S., Martel, C., Pichavant, M., Kushnir, A., 2014. Amphibole as an archivist of magmatic crystallization conditions: problems, potential, and implications for inferring magma storage prior to the paroxysmal 2010 eruption of Mount Merapi, Indonesia. Contrib Mineral Petrol 167, 1016. https://doi.org/10.1007/s00410-014-1016-4
Erdmann, S., Pichavant, M., Gaillard, F., 2024. Mineral-melt vanadium oxybarometry for primitive arc magmas: effect of hydrous melt composition on fO2 estimates. Contrib Mineral Petrol 179, 39. https://doi.org/10.1007/s00410-024-02113-4
Erdmann, S., Scaillet, B., Kellett, D.A., 2012. Textures of Peritectic Crystals as Guides to Reactive Minerals in Magmatic Systems: New Insights from Melting Experiments. Journal of Petrology 53, 2231–2258. https://doi.org/10.1093/petrology/egs048
Erdmann, S., Scaillet, B., Kellett, D.A., 2010. Xenocryst assimilation and formation of peritectic crystals during magma contamination: An experimental study. Journal of Volcanology and Geothermal Research 198, 355–367. https://doi.org/10.1016/j.jvolgeores.2010.10.002
Erdmann, S., Scaillet, B., Martel, C., Cadoux, A., 2014b. Characteristic Textures of Recrystallized, Peritectic, and Primary Magmatic Olivine in Experimental Samples and Natural Volcanic Rocks. Journal of Petrology 55, 2377–2402. https://doi.org/10.1093/petrology/egu060
Esse, B., Burton, M., Hayer, C., Contreras-Arratia, R., Christopher, T., Joseph, E.P., Varnam, M., Johnson, C., 2024. SO_2 emissions during the 2021 eruption of La Soufrière, St Vincent, revealed with back-trajectory analysis of TROPOMI imagery. SP 539, 231–244. https://doi.org/10.1144/SP539-2022-77
Eugster, H.P., 1957. Heterogeneous Reactions Involving Oxidation and Reduction at High Pressures and Temperatures. The Journal of Chemical Physics 26, 1760–1761. https://doi.org/10.1063/1.1743626
Evans, B.W., Kuehner, S.M., Joswiak, D.J., Cressey, G., 2017. Serpentine, Iron-rich Phyllosilicates and Fayalite Produced by Hydration and Mg Depletion of Peridotite, Duluth Complex, Minnesota, USA. Journal of Petrology 58, 495–512. https://doi.org/10.1093/petrology/egx024
Evans, B.W., Scaillet, B., Kuehner, S.M., 2006. Experimental determination of coexisting iron–titanium oxides in the systems FeTiAlO, FeTiAlMgO, FeTiAlMnO, and FeTiAlMgMnO at 800 and 900°C, 1–4 kbar, and relatively high oxygen fugacity. Contrib Mineral Petrol 152, 149–167. https://doi.org/10.1007/s00410-006-0098-z
Evans, K.A., Tomkins, A.G., 2021. Redox Variables and Mechanisms in Subduction Magmatism and Volcanism, in: Moretti, R., Neuville, D.R. (Eds.), Geophysical Monograph Series. Wiley, pp. 63–91. https://doi.org/10.1002/9781119473206.ch4
Evans, K.-A., Tomkins, A.-G., 2011. The relationship between subduction zone redox budget and arc magma fertility. Earth and Planetary Science Letters 308, 401–409. https://doi.org/10.1016/j.epsl.2011.06.009
Fedele, L., Cole, P.D., Scarpati, C., Robertson, R.E.A., 2021. Petrological insights on the last 1000 years of explosive activity at La Soufrière volcano, St. Vincent (Lesser Antilles). Lithos 392, 106150. https://doi.org/10.1016/j.lithos.2021.106150
Feig, S.T., Koepke, J., Snow, J.E., 2010. Effect of oxygen fugacity and water on phase equilibria of a hydrous tholeiitic basalt. Contrib Mineral Petrol 160, 551–568. https://doi.org/10.1007/s00410-010-0493-3
Feig, S.T., Koepke, J., Snow, J.E., 2006. Effect of water on tholeiitic basalt phase equilibria: an experimental study under oxidizing conditions. Contrib Mineral Petrol 152, 611–638. https://doi.org/10.1007/s00410-006-0123-2
Fink, J.H., Griffiths, R.W., 1998. Morphology, eruption rates, and rheology of lava domes: Insights from laboratory models. J. Geophys. Res. 103, 527–545. https://doi.org/10.1029/97JB02838
Fink, J.H., Malin, M.C., Anderson, S.W., 1990. Intrusive and extrusive growth of the Mount St Helens lava dome. Nature 348, 435–437. https://doi.org/10.1038/348435a0
Flett, J., 1908. VIII. Petrographical notes on the products of the eruptions of May, 1902, at the Soufrière in St. Vincent. Phil. Trans. R. Soc. Lond. A 208, 305–332. https://doi.org/10.1098/rsta.1908.0022
Foden, J.D., Green, D.H., 1992. Possible role of amphibole in the origin of andesite: some experimental and natural evidence. Contr. Mineral. and Petrol. 109, 479–493. https://doi.org/10.1007/BF00306551

Frank, M.R., Candela, P.A., Piccoli, P.M., 2003. Alkali exchange equilibria between a silicate melt and coexisting magmatic volatile phase: an experimental study at 800°C and 100 MPa. Geochimica et Cosmochimica Acta 67, 1415–1427. https://doi.org/10.1016/S0016-7037(02)01181-X
Freer, R., Hauptman, Z., 1978. An experimental study of magnetite-titanomagnetite interdiffusion. Physics of the Earth and Planetary Interiors 16, 223–231. https://doi.org/10.1016/0031-9201(78)90015-8
Freer, W., O'Reilly, R., 1980. The diffusion of Fe^{2+} ions in spinels with relevance to the process of maghemitization. Mineral. mag. 43, 889–899. https://doi.org/10.1180/minmag.1980.043.331.12
Freise, M., Holtz, F., Nowak, M., Scoates, J.S., Strauss, H., 2009. Differentiation and crystallization conditions of basalts from the Kerguelen large igneous province: an experimental study. Contrib Mineral Petrol 158, 505–527. https://doi.org/10.1007/s00410-009-0394-5
Frey, H.M., Lange, R.A., 2011. Phenocryst complexity in andesites and dacites from the Tequila volcanic field, Mexico: resolving the effects of degassing vs. magma mixing. Contrib Mineral Petrol 162, 415–445. https://doi.org/10.1007/s00410-010-0604-1
Frey, H.M., Manon, M.R., Barclay, J., Davies, B.V., Walters, S.A., Cole, P.D., Christopher, T.E., Joseph, E.P., 2024. Petrology of the explosive deposits from the April 2021 eruption of La Soufrière volcano, St Vincent: a time-series analysis of microlites. SP 539, 201–230. https://doi.org/10.1144/SP539-2022-291
Frost, B.R., 1991. Magnetic petrology; factors that control the occurrence of magnetite in crustal rocks. Reviews in Mineralogy and Geochemistry 25, 489–509.
Frost, B.R., Lindsley, D.H., 1991. Chapter 12.OCCURRENCE OF IRON-TITANIUM OXIDES IN IGNEOUS ROCKS, in: Lindsley, Donald H. (Ed.), Oxide Minerals. De Gruyter, pp. 433–468. https://doi.org/10.1515/9781501508684-015
Fujinawa, A., 1990. Tholeiitic and calc-alkaline magma series at Adatara volcano, Northeast Japan: 2. Mineralogy and phase relations. Lithos 24, 217–236. https://doi.org/10.1016/0024-4937(90)90033-W
Fujinawa, A., 1988. Tholeiitic and calc-alkaline magma series at Adatara volcano, northeast Japan: 1. Geochemical constraints on their origin. Lithos 22, 135–158. https://doi.org/10.1016/0024-4937(88)90022-9
Gaetani, G., Grove, T., Bryan, W., 1994. 32. EXPERIMENTAL PHASE RELATIONS OF BASALTIC ANDESITE FROM HOLE 839B UNDER HYDROUS AND ANHYDROUS CONDITIONS. Proceedings of the Ocean Drilling Program, 135 Scientific Results, Proceedings of the Ocean Drilling Program 135. https://doi.org/10.2973/odp.proc.sr.135.1994
Gaetani, G.A., Grove, T.L., 2003. Experimental constraints on melt generation in the mantle wedge, in: Eiler, J. (Ed.), Geophysical Monograph Series. American Geophysical Union, Washington, D. C., pp. 107–134. https://doi.org/10.1029/138GM07
Ganguly, J., Newton, R.C., 1968. Thermal Stability of Chloritoid at High Pressure and relatively High Oxygen Fugacity. Journal of Petrology 9, 444–466. https://doi.org/10.1093/petrology/9.3.444
Gardner, J.E., Carey, S., Rutherford, M.J., Sigurdsson, H., 1995. Petrologic diversity in Mount St. Helens dacites during the last 4,000 years: implications for magma mixing. Contr. Mineral. and Petrol. 119, 224–238. https://doi.org/10.1007/BF00307283
Genareau, K., Clarke, A.B., 2010. Heterogeneous clasts as windows into magma mingling at Soufrière Hills volcano: Small-scale magma mingling processes. Geophys. Res. Lett. 37, n/a-n/a. https://doi.org/10.1029/2009GL041968
Gerlach, D.C., Grove, T.L., 1982. Petrology of Medicine Lake Highland volcanics: Characterization of endmembers of magma mixing. Contr. Mineral. and Petrol. 80, 147–159. https://doi.org/10.1007/BF00374892
Germa, A., Quidelleur, X., Labanieh, S., Chauvel, C., Lahitte, P., 2011. The volcanic evolution of Martinique Island: Insights from K–Ar dating into the Lesser Antilles arc migration since the Oligocene. Journal of Volcanology and Geothermal Research 208, 122–135. https://doi.org/10.1016/j.jvolgeores.2011.09.007
Geschwind, C.-H., Rutherford, M.J., 1995. Crystallization of microlites during magma ascent: the fluid mechanics of 1980–1986 eruptions at Mount St Helens. Bull Volcanol 57, 356–370. https://doi.org/10.1007/BF00301293
Ghiorso, M.S., Gualda, G.A.R., 2015. An H2O–CO2 mixed fluid saturation model compatible with rhyolite-MELTS. Contrib Mineral Petrol 169, 53. https://doi.org/10.1007/s00410-015-1141-8
Ghiorso, M.S., Sack, O., 1991. Fe-Ti oxide geothermometry: thermodynamic formulation and the estimation of intensive variables in silicic magmas. Contr. Mineral. and Petrol. 108, 485–510. https://doi.org/10.1007/BF00303452
Gilbert, M.C., Helz, R.T., Popp, R.K., Spear, F.S., 1982. Chapter 2. EXPERIMENTAL STUDIES OF AMPHIBOLE STABILITY, in: Veblen, D.R., Ribbe, P.H. (Eds.), Amphiboles. De Gruyter, Berlin, Boston, pp. 229–354. https://doi.org/10.1515/9781501508196-006
Gill, J.B., 1981. Orogenic Andesites and Plate Tectonics, Minerals and Rocks. Springer Berlin Heidelberg, Berlin, Heidelberg. https://doi.org/10.1007/978-3-642-68012-0
Ginibre, C., Worner, G., Kronz, A., 2007. Crystal Zoning as an Archive for Magma Evolution. Elements 3, 261–266. https://doi.org/10.2113/gselements.3.4.261
Goode, A.D.T., 1974. Oxidation of natural olivines. Nature 248, 500–501. https://doi.org/10.1038/248500a0
Gorbach, N., Philosofova, T., Portnyagin, M., 2020. Amphibole record of the 1964 plinian and following dome-forming eruptions of Shiveluch volcano, Kamchatka. Journal of Volcanology and Geothermal Research 407, 107108. https://doi.org/10.1016/j.jvolgeores.2020.107108
Graham, A.M., Thirlwall, M.F., 1981. Petrology of the 1979 eruption of Soufriere volcano, St. Vincent, Lesser Antilles.
Green, D.H., 1971. Composition of basaltic magmas as indicators of conditions of origin: application to oceanic volcanism. Phil. Trans. R. Soc. Lond. A 268, 707–725. https://doi.org/10.1098/rsta.1971.0022
Grocke, S.B., Cottrell, E., de Silva, S., Kelley, K.A., 2016. The role of crustal and eruptive processes versus source variations in controlling the oxidation state of iron in Central Andean magmas. Earth and Planetary Science Letters 440, 92–104. https://doi.org/10.1016/j.epsl.2016.01.026
Grommé, C.S., Wright, T.L., Peck, D.L., 1969. Magnetic properties and oxidation of iron-titanium oxide minerals in Alae and Makaopuhi Lava Lakes, Hawaii. J. Geophys. Res. 74, 5277–5293. https://doi.org/10.1029/JB074i022p05277
Grove, T., Parman, S., Bowring, S., Price, R., Baker, M., 2002. The role of an H2O-rich fluid component in the generation of primitive basaltic andesites and andesites from the Mt. Shasta region, N California. Contrib Mineral Petrol 142, 375–396. https://doi.org/10.1007/s004100100299
Grove, T.L., Baker, M.B., 1984. Phase equilibrium controls on the tholeiitic versus calc-alkaline differentiation trends. J. Geophys. Res. 89, 3253–3274. https://doi.org/10.1029/JB089iB05p03253

Grove, T.L., Donnelly-Nolan, J.M., 1986. The evolution of young silicic lavas at Medicine Lake Volcano, California: Implications for the origin of compositional gaps in calc-alkaline series lavas. Contr. Mineral. and Petrol. 92, 281–302. https://doi.org/10.1007/BF00572157
Grove, T.L., Elkins-Tanton, L.T., Parman, S.W., Chatterjee, N., M□ntener, O., Gaetani, G.A., 2003. Fractional crystallization and mantle-melting controls on calc-alkaline differentiation trends. Contributions to Mineralogy and Petrology 145, 515–533. https://doi.org/10.1007/s00410-003-0448-z
Grove, T.L., Gerlach, D.C., Sando, T.W., 1982. Origin of calc-alkaline series lavas at Medicine Lake Volcano by fractionation, assimilation and mixing. Contr. Mineral. and Petrol. 80, 160–182. https://doi.org/10.1007/BF00374893
Grove, T.L., Kinzler, R.J., 1986. Petrogenesis of Andesites. Annual Review of Earth and Planetary Sciences 14, 417. https://doi.org/10.1146/annurev.ea.14.050186.002221
Grove, T.L., Till, C.B., Krawczynski, M.J., 2012. The Role of H_2 O in Subduction Zone Magmatism. Annu. Rev. Earth Planet. Sci. 40, 413–439. https://doi.org/10.1146/annurev-earth-042711-105310
Gualtieri, A.F., Gemmi, M., Dapiaggi, M., 2003. Phase transformations and reaction kinetics during the temperature-induced oxidation of natural olivine. American Mineralogist 88, 1560–1574. https://doi.org/10.2138/am-2003-1019
Haggerty, S.E., 1991a. Chapter 5.OXIDE TEXTURES - A MINI-ATLAS, in: Lindsley, D.H. (Ed.), Oxide Minerals. De Gruyter, pp. 129–220. https://doi.org/10.1515/9781501508684-008
Haggerty, S.E., 1991b. Chapter 10.OXIDE MINERALOGY OF THE UPPER MANTLE, in: Lindsley, D.H. (Ed.), Oxide Minerals. De Gruyter, pp. 355–416. https://doi.org/10.1515/9781501508684-013
Haggerty, S.E., 1976a. Chapter 4. OXIDATION of OPAQUE MINERAL OXIDES in BASALTS, in: Rumble, D. (Ed.), Oxide Minerals. De Gruyter, pp. 113–212. https://doi.org/10.1515/9781501508561-009
Haggerty, S.E., 1976b. Chapter 8. OPAQUE MINERAL OXIDES in TERRESTRIAL IGNEOUS ROCKS, in: Rumble, D. (Ed.), Oxide Minerals. De Gruyter, pp. 303–502. https://doi.org/10.1515/9781501508561-013
Haggerty, S.E., Baker, I., 1967. The alteration of olivine in basaltic and associated lavas: Part I: High temperature alteration. Contr. Mineral. and Petrol. 16, 233–257. https://doi.org/10.1007/BF00371094
Hammarstrom, J., Zen, E., 1986. Aluminum in hornblende:An empirical igneousgeobarometer. American Mineralogist 71, 1297–1313.
Hammer, J.E., Cashman, K.V., Hoblitt, R.P., Newman, S., 1999. Degassing and microlite crystallization during pre-climactic events of the 1991 eruption of Mt. Pinatubo, Philippines. Bulletin of Volcanology 60, 355–380. https://doi.org/10.1007/s004450050238
Hammer, J.E., Rutherford, M.J., 2002. An experimental study of the kinetics of decompression-induced crystallization in silicic melt. J. Geophys. Res. 107. https://doi.org/10.1029/2001JB000281
Hammond, P.A., Taylor, L.A., 1982. The ilmenite/titano-magnetite assemblage: kinetics of re-equilibration. Earth and Planetary Science Letters 61, 143–150. https://doi.org/10.1016/0012-821X(82)90047-4
Harford, C.L., Pringle, M.S., Sparks, R.S.J., Young, S.R., 2002. The volcanic evolution of Montserrat using ^{40} Ar/ ^{39} Ar geochronology. Memoirs 21, 93–113. https://doi.org/10.1144/GSL.MEM.2002.021.01.05
Harrison, R.J., Putnis, A., 1998. The Magnetic Properties and Crystal Chemistry of Oxide Spinel Solid Solutions. Surveys in Geophysics 19, 461–520. https://doi.org/10.1023/A:1006535023784
Hawkesworth, C., Turner, S., Peate, D., McDermott, F., Van Calsteren, P., 1997. Elemental U and Th variations in island arc rocks: implications for U-series isotopes. Chemical Geology 139, 207–221. https://doi.org/10.1016/S0009-2541(97)00036-3
Hawkesworth, C.J., Hergt, J., Ellam, R., McDermott, F., 1991. Element fluxes associated with subduction related magmatism. Phil. Trans. R. Soc. Lond. A 335, 393–405. https://doi.org/10.1098/rsta.1991.0054
Heap, M.J., Troll, V.R., Kushnir, A.R.L., Gilg, H.A., Collinson, A.S.D., Deegan, F.M., Darmawan, H., Seraphine, N., Neuberg, J., Walter, T.R., 2019. Hydrothermal alteration of andesitic lava domes can lead to explosive volcanic behaviour. Nat Commun 10, 5063. https://doi.org/10.1038/s41467-019-13102-8
Heath, E., 1997. Genesis and evolution of calc-alkaline magmas at Soufriere volcano, St. Vincent, Lesser Antilles arc. (PhD Thesis). Lancaster University.
Heath, E., Macdonald, R., Belkin, H., Hawkesworth, C., Sigurdsson, H., 1998a. Magmagenesis at Soufrière Volcano, St Vincent, Lesser Antilles Arc. Journal of Petrology 39, 1721–1764. https://doi.org/10.1093/petroj/39.10.1721
Heath, E., Turner, S.P., Macdonald, R., Hawkesworth, C.J., Van Calsteren, P., 1998b. Long magma residence times at an island arc volcano (Soufriere, St. Vincent) in the Lesser Antilles: evidence from 238U–230Th isochron dating. Earth and Planetary Science Letters 160, 49–63. https://doi.org/10.1016/S0012-821X(98)00084-3
Hedge, C.E., Lewis, J.F., 1971. Isotopic composition of strontium in three basalt-andesite centers along the Lesser Antilles arc. Contr. Mineral. and Petrol. 32, 39–47. https://doi.org/10.1007/BF00372232
Hekinian, R., 1982. Chapter 11 Deuteric Alteration, in: Elsevier Oceanography Series. Elsevier, pp. 329–331. https://doi.org/10.1016/S0422-9894(08)70953-X
Hicks, S.P., Bie, L., Rychert, C.A., Harmon, N., Goes, S., Rietbrock, A., Wei, S.S., Collier, J.S., Henstock, T.J., Lynch, L., Prytulak, J., Macpherson, C.G., Schlaphorst, D., Wilkinson, J.J., Blundy, J.D., Cooper, G.F., Davy, R.G., Kendall, J.-M., VoiLA Working Group, 2023. Slab to back-arc to arc: Fluid and melt pathways through the mantle wedge beneath the Lesser Antilles. Sci. Adv. 9, eadd2143. https://doi.org/10.1126/sciadv.add2143
Higgins, O., Sheldrake, T., Caricchi, L., 2022. Machine learning thermobarometry and chemometry using amphibole and clinopyroxene: a window into the roots of an arc volcano (Mount Liamuiga, Saint Kitts). Contrib Mineral Petrol 177, 10. https://doi.org/10.1007/s00410-021-01874-6
Hildreth, W., Moorbath, S., 1988. Crustal contributions to arc magmatism in the Andes of Central Chile. Contr. Mineral. and Petrol. 98, 455–489. https://doi.org/10.1007/BF00372365
Hogan, J.P., 1993. Monomineralic Glomerocrysts: Textural Evidence for Mineral Resorption during Crystallization of Igneous Rocks. The Journal of Geology 101, 531–540. https://doi.org/10.1086/648245
Holland, T., Blundy, J., 1994. Non-ideal interactions in calcic amphiboles and their bearing on amphibole-plagioclase thermometry. Contr. Mineral. and Petrol. 116, 433–447. https://doi.org/10.1007/BF00310910
Holloway, J.R., 2004. Redox reactions in seafloor basalts: possible insights into silicic hydrothermal systems. Chemical Geology 210, 225–230. https://doi.org/10.1016/j.chemgeo.2004.06.009
Holloway, J.R., Burnham, C.W., 1972. Melting Relations of Basalt with Equilibrium Water Pressure Less Than Total Pressure. Journal of Petrology 13, 1–29. https://doi.org/10.1093/petrology/13.1.1

Holness, M.B., 2018. Melt segregation from silicic crystal mushes: a critical appraisal of possible mechanisms and their microstructural record. Contrib Mineral Petrol 173, 48. https://doi.org/10.1007/s00410-018-1465-2
Holtz, F., 2001. The water-undersaturated and dry Qz-Ab-Or system revisited. Experimental results at very low water activities and geological implications. Contrib Mineral Petrol 141, 347–357. https://doi.org/10.1007/s004100100245
Hort, M., 1998. Abrupt Change in Magma Liquidus Temperature because of Volatile Loss or Magma Mixing: Effects on Nucleation, Crystal Growth and Thermal History of the Magma. Journal of Petrology 39, 1063–1076. https://doi.org/10.1093/petroj/39.5.1063
Hou, T., Botcharnikov, R., Moulas, E., Just, T., Berndt, J., Koepke, J., Zhang, Z., Wang, M., Yang, Z., Holtz, F., 2021. Kinetics of Fe–Ti Oxide Re-equilibration in Magmatic Systems: Implications for Thermo-oxybarometry. Journal of Petrology 61, egaa116. https://doi.org/10.1093/petrology/egaa116
Hu, H., Lentz, D., Li, J.-W., McCarron, T., Zhao, X.-F., Hall, D., 2015. REEQUILIBRATION PROCESSES IN MAGNETITE FROM IRON SKARN DEPOSITS. Economic Geology 110, 1–8. https://doi.org/10.2113/econgeo.110.1.1
Huebner, J.S., Lipin, B.R., Wiggins, L.B., 1976. Partitioning of chromium between silicate crystals and melts. Lunar and Planetary Science Conference Proceedings 1, 1195–1220.
Humphreys, M.C.S., Blundy, J.D., Sparks, R.S.J., 2006b. Magma Evolution and Open-System Processes at Shiveluch Volcano: Insights from Phenocryst Zoning. Journal of Petrology 47, 2303–2334. https://doi.org/10.1093/petrology/egl045
Humphreys, M.C.S., Kearns, S.L., Blundy, J.D., 2006a. SIMS investigation of electron-beam damage to hydrous, rhyolitic glasses: Implications for melt inclusion analysis. American Mineralogist 91, 667–679. https://doi.org/10.2138/am.2006.1936
Humphris, S.E., 1976. The hydrothermal alteration of oceanic basalts by seawater. Massachusetts Institute of Technology and Woods Hole Oceanographic Institution, Woods Hole, MA. https://doi.org/10.1575/1912/1351
Hunter, Blake, 1995. Petrogenetic Evolution of a Transitional Tholeiitic—Calc-alkaline Series: Towada Volcano, Japan. Journal of Petrology k. https://doi.org/10.1093/oxfordjournals.petrology.a037266
Huppert, H.E., Shepherd, J.B., Haraldur Sigurdsson, R., Sparks, S.J., 1982. On lava dome growth, with application to the 1979 lava extrusion of the Soufrière of St. Vincent. Journal of Volcanology and Geothermal Research 14, 199–222. https://doi.org/10.1016/0377-0273(82)90062-2
Husen, A., Almeev, R.R., Holtz, F., 2016. The Effect of H2O and Pressure on Multiple Saturation and Liquid Lines of Descent in Basalt from the Shatsky Rise. Journal of Petrology 57, 309–344. https://doi.org/10.1093/petrology/egw008
Iddings, J.P., 1892. The Origin of Igenous Rocks. Bull. Phil. Soc., Washington 12, 89–214.
Jackson, M.D., Blundy, J., Sparks, R.S.J., 2018. Chemical differentiation, cold storage and remobilization of magma in the Earth's crust. Nature 564, 405–409. https://doi.org/10.1038/s41586-018-0746-2
Jakobsson, S., 2012. Oxygen fugacity control in piston-cylinder experiments. Contrib Mineral Petrol 164, 397–406. https://doi.org/10.1007/s00410-012-0743-7
Jakobsson, S., Blundy, J., Moore, G., 2014. Oxygen fugacity control in piston-cylinder experiments: a re-evaluation. Contrib Mineral Petrol 167, 1007. https://doi.org/10.1007/s00410-014-1007-5
Jerram, D.A., Martin, V.M., 2008. Understanding crystal populations and their significance through the magma plumbing system. SP 304, 133–148. https://doi.org/10.1144/SP304.7
Jicha, B.R., Singer, B.S., Sobol, P., 2016. Re-evaluation of the ages of 40Ar/39Ar sanidine standards and supereruptions in the western U.S. using a Noblesse multi-collector mass spectrometer. Chemical Geology 431, 54–66. https://doi.org/10.1016/j.chemgeo.2016.03.024
Johnson, J.A., 2014. A Geochemical Study of Crustal Plutonic Rocks from the Southern Mariana Trench Forearc: Relationship to Volcanic Rocks Erupted during Subduction Initiation (Doctor of Philosophy Geosciences). Florida International University. https://doi.org/10.25148/etd.FI14040840
Johnston, A.D., Draper, D.S., 1992. Near-liquidus phase relations of an anhydrous high-magnesia basalt from the Aleutian Islands: Implications for arc magma genesis and ascent. Journal of Volcanology and Geothermal Research 52, 27–41. https://doi.org/10.1016/0377-0273(92)90131-V
Johnston, A.D., Stout, J.H., 1984. Development of orthopyroxene-Fe/Mg ferrite symplectites by continuous olivine oxidation. Contr. Mineral. and Petrol. 88, 196–202. https://doi.org/10.1007/BF00371423
Joseph, E.P., Camejo-Harry, M., Christopher, T., Contreras-Arratia, R., Edwards, S., Graham, O., Johnson, M., Juman, A., Latchman, J.L., Lynch, L., Miller, V.L., Papadopoulos, I., Pascal, K., Robertson, R., Ryan, G.A., Stinton, A., Grandin, R., Hamling, I., Jo, M.-J., Barclay, J., Cole, P., Davies, B.V., Sparks, R.S.J., 2022. Responding to eruptive transitions during the 2020–2021 eruption of La Soufrière volcano, St. Vincent. Nat Commun 13, 4129. https://doi.org/10.1038/s41467-022-31901-4
Juriček, M.P., Keppler, H., 2023. Amphibole stability, water storage in the mantle, and the nature of the lithosphere-asthenosphere boundary. Earth and Planetary Science Letters 608, 118082. https://doi.org/10.1016/j.epsl.2023.118082
Kagi, R., 2005. Piston-cylinder experiments on H2O undersaturated Fe-bearing systems: An experimental setup approaching fO2 conditions of natural calc-alkaline magmas. American Mineralogist 90, 708–717. https://doi.org/10.2138/am.2005.1663
Kawai, N., Kume, S., Sasajima, S., 1954. Magnetism of Rocks and Solid Phase Transformation in Ferromagnetic Minerals. Proceedings of the Japan Academy 30, 588–593. https://doi.org/10.2183/pjab1945.30.588
Kawamoto, T., 1996. Experimental constraints on differentiation and H2O abundance of calc-alkaline magmas. Earth and Planetary Science Letters 144, 577–589. https://doi.org/10.1016/S0012-821X(96)00182-3
Kawamoto, T., Hirose, K., 1994. Au-Pd sample containers for melting experiments on iron and water bearing systems. ejm 6, 381–386. https://doi.org/10.1127/ejm/6/3/0381
Kay, S.M., Kay, R.W., Citron, G.P., 1982. Tectonic controls on tholeiitic and calc-alkaline magmatism in the Aleutian Arc. J. Geophys. Res. 87, 4051–4072. https://doi.org/10.1029/JB087iB05p04051
Kelfoun, K., Santoso, A.B., Latchimy, T., Bontemps, M., Nurdien, I., Beauducel, F., Fahmi, A., Putra, R., Dahamna, N., Laurin, A., Rizal, M.H., Sukmana, J.T., Gueugneau, V., 2021. Growth and collapse of the 2018–2019 lava dome of Merapi volcano. Bull Volcanol 83, 8. https://doi.org/10.1007/s00445-020-01428-x
Kelley, K.A., Cottrell, E., 2012. The influence of magmatic differentiation on the oxidation state of Fe in a basaltic arc magma. Earth and Planetary Science Letters 329–330, 109–121. https://doi.org/10.1016/j.epsl.2012.02.010

Kelley, K.A., Cottrell, E., 2009. Water and the Oxidation State of Subduction Zone Magmas. Science 325, 605–607. https://doi.org/10.1126/science.1174156
Khisina, N.R., Khramov, D.A., Kleschev, A.A., Langer, K., 1998. Laihunitization as a mechanism of olivine oxidation. ejm 10, 229–238. https://doi.org/10.1127/ejm/10/2/0229
Khisina, N.R., Khramov, D.A., Kolosov, M.V., Kleschev, A.A., Taylor, LawrenceA., 1995. Formation of ferriolivine and magnesioferrite from Mg - Fe-olivine: Reactions and kinetics of oxidation. Phys Chem Minerals 22. https://doi.org/10.1007/BF00202257
Klaver, M., Matveev, S., Berndt, J., Lissenberg, C.J., Vroon, P.Z., 2017. A mineral and cumulate perspective to magma differentiation at Nisyros volcano, Aegean arc. Contrib Mineral Petrol 172, 95. https://doi.org/10.1007/s00410-017-1414-5
Klein, B.Z., Jagoutz, O., Schmidt, M.W., Kueter, N., 2023. A Global Assessment of the Controls on the Fractionation of Arc Magmas. Geochem Geophys Geosyst 24, e2023GC010888. https://doi.org/10.1029/2023GC010888
Knafelc, J., Filiberto, J., Ferré, E.C., Conder, J.A., Costello, L., Crandall, J.R., Dyar, M.D., Friedman, S.A., Hummer, D.R., Schwenzer, S.P., 2019. The effect of oxidation on the mineralogy and magnetic properties of olivine. American Mineralogist 104, 694–702. https://doi.org/10.2138/am-2019-6829
Koulakov, I., Abkadyrov, I., Al Arifi, N., Deev, E., Droznina, S., Gordeev, E.I., Jakovlev, A., El Khrepy, S., Kulakov, R.I., Kugaenko, Y., Novgorodova, A., Senyukov, S., Shapiro, N., Stupina, T., West, M., 2017. Three different types of plumbing system beneath the neighboring active volcanoes of Tolbachik, Bezymianny, and Klyuchevskoy in Kamchatka. JGR Solid Earth 122, 3852–3874. https://doi.org/10.1002/2017JB014082
Krawczynski, M.J., Grove, T.L., Behrens, H., 2012. Amphibole stability in primitive arc magmas: effects of temperature, H2O content, and oxygen fugacity. Contrib Mineral Petrol 164, 317–339. https://doi.org/10.1007/s00410-012-0740-x
Kress, V.C., Carmichael, I.S.E., 1991. The compressibility of silicate liquids containing Fe2O3 and the effect of composition, temperature, oxygen fugacity and pressure on their redox states. Contr. Mineral. and Petrol. 108, 82–92. https://doi.org/10.1007/BF00307328
Kuno, H., 1966. REVIEW OF PYROXENE RELATIONS IN TERRESTRIAL ROCKS IN THE LIGHT OF RECENT EXPERIMENTAL WORKS. Mineral. J. 5, 21–43. https://doi.org/10.2465/minerj1953.5.21
Kushiro, I., 1973. Origin of some magmas in oceanic and circum-oceanic regions. Tectonophysics 17, 211–222. https://doi.org/10.1016/0040-1951(73)90003-6
Laeger, K., Halama, R., Hansteen, T., Savov, I.P., Murcia, H.F., Cortés, G.P., Garbe-Schönberg, D., 2013. Crystallization conditions and petrogenesis of the lava dome from the ~900 years BP eruption of Cerro Machín Volcano, Colombia. Journal of South American Earth Sciences 48, 193–208. https://doi.org/10.1016/j.jsames.2013.09.009
Lanphere, M.A., 2000. Comparison of Conventional K–Ar and ^{40} Ar/^{39} Ar Dating of Young Mafic Volcanic Rocks. Quat. res. 53, 294–301. https://doi.org/10.1006/qres.1999.2122
Lattard, D., 1995. Experimental evidence for the exsolution of ilmenite from titaniferous spinel. American Mineralogist 80, 968–981. https://doi.org/10.2138/am-1995-9-1013
Laukert, G., Von Der Handt, A., Hellebrand, E., Snow, J.E., Hoppe, P., Klügel, A., 2014. High-pressure Reactive Melt Stagnation Recorded in Abyssal Pyroxenites from the Ultraslow-spreading Lena Trough, Arctic Ocean. Journal of Petrology 55, 427–458. https://doi.org/10.1093/petrology/egt073
Le Friant, A., Boudon, G., Arnulf, A., Robertson, R.E.A., 2009. Debris avalanche deposits offshore St. Vincent (West Indies): Impact of flank-collapse events on the morphological evolution of the island. Journal of Volcanology and Geothermal Research 179, 1–10. https://doi.org/10.1016/j.jvolgeores.2008.09.022
Leake, B.E., 1978. Nomenclature of amphiboles. American Mineralogist 63, 1023–1052.
Lee, J.-Y., Marti, K., Severinghaus, J.P., Kawamura, K., Yoo, H.-S., Lee, J.B., Kim, J.S., 2006. A redetermination of the isotopic abundances of atmospheric Ar. Geochimica et Cosmochimica Acta 70, 4507–4512. https://doi.org/10.1016/j.gca.2006.06.1563
Leeman, W.P., Hawkesworth, C.J., 1986. Open magma systems: Trace element and isotopic constraints. J. Geophys. Res. 91, 5901–5912. https://doi.org/10.1029/JB091iB06p05901
Lepage, L.D., 2003. ILMAT: an Excel worksheet for ilmenite–magnetite geothermometry and geobarometry. Computers & Geosciences 29, 673–678. https://doi.org/10.1016/S0098-3004(03)00042-6
Lewis, J.F., 1973. Petrology of the Ejected Plutonic Blocks of the Soufriere Volcano, St. Vincent, West Indies. Journal of Petrology 14, 81–112. https://doi.org/10.1093/petrology/14.1.81
Lewis, J.F., 1970. CHEMICAL COMPOSITION AND PHYSICAL PROPERTIES OF MAGNETITE FROM THE EJECTED PLUTONIC BLOCKS OF THE SOUFRIERE VOLCANO, ST. VINCENT, WEST INDIES. The American Mineralogist 55.
Liao, Y., 2023. Transport of melt, pressure and heat through a magma mush. Front. Earth Sci. 11, 1085897. https://doi.org/10.3389/feart.2023.1085897
Lilova, K.I., Pearce, C.I., Gorski, C., Rosso, K.M., Navrotsky, A., 2012. Thermodynamics of the magnetite-ulvospinel (Fe3O4-Fe2TiO4) solid solution. American Mineralogist 97, 1330–1338. https://doi.org/10.2138/am.2012.4076
Lindsley, D.H., 1991. Chapter 3.EXPERIMENTAL STUDIES OF OXIDE MINERALS, in: Lindsley, D.H. (Ed.), Oxide Minerals. De Gruyter, pp. 69–106. https://doi.org/10.1515/9781501508684-006
Lindsley, D.H., Andersen, D.J., 1983. A two-pyroxene thermometer. J. Geophys. Res. 88, A887. https://doi.org/10.1029/JB088iS02p0A887
Lissenberg, C.J., MacLeod, C.J., Bennett, E.N., 2018. Consequences of a crystal mush-dominated magma plumbing system: a mid-ocean ridge perspective. Phil. Trans. R. Soc. A. 377, 20180014. https://doi.org/10.1098/rsta.2018.0014
Lomax, A., Virieux, J., Volant, P., Berge-Thierry, C., 2000. Probabilistic Earthquake Location in 3D and Layered Models, in: Thurber, C.H., Rabinowitz, N. (Eds.), Advances in Seismic Event Location, Modern Approaches in Geophysics. Springer Netherlands, Dordrecht, pp. 101–134. https://doi.org/10.1007/978-94-015-9536-0_5
Longhi, J., Bertka, C.M., 1996. Graphical analysis of pigeonite-augite liquidus equilibria. American Mineralogist 81, 685–695. https://doi.org/10.2138/am-1996-5-616
Lowenstern, J., 2001. Carbon dioxide in magmas and implications for hydrothermal systems. Mineralium Deposita 36, 490–502. https://doi.org/10.1007/s001260100185

Ludlam, A.P., Frey, H.M., Manon, M.R.F., 2018. Decompression and heating induced amphibole breakdown in effusive volcanism on Dominica, Lesser Antilles. Presented at the 53rd Annual GSA Northeastern Section Meeting - 2018, Keck Geology Consortium, p. 311190. https://doi.org/10.1130/abs/2018NE-311190
Maccaferri, F., Richter, N., Walter, T.R., 2017. The effect of giant lateral collapses on magma pathways and the location of volcanism. Nat Commun 8, 1097. https://doi.org/10.1038/s41467-017-01256-2
Macdonald, R., Hawkesworth, C.J., Heath, E., 2000. The Lesser Antilles volcanic chain: a study in arc magmatism. Earth-Science Reviews 49, 1–76. https://doi.org/10.1016/S0012-8252(99)00069-0
Mallmann, G., O'Neill, H.St.C., 2013. Calibration of an Empirical Thermometer and Oxybarometer based on the Partitioning of Sc, Y and V between Olivine and Silicate Melt. Journal of Petrology 54, 933–949. https://doi.org/10.1093/petrology/egt001
Manconi, A., Longpre, M.-A., Walter, T.R., Troll, V.R., Hansteen, T.H., 2009. The effects of flank collapses on volcano plumbing systems. Geology 37, 1099–1102. https://doi.org/10.1130/G30104A.1
Mandler, B.E., Grove, T.L., 2016. Controls on the stability and composition of amphibole in the Earth's mantle. Contrib Mineral Petrol 171, 68. https://doi.org/10.1007/s00410-016-1281-5
Marxer, F., Ulmer, P., Müntener, O., 2023. Ascent-driven differentiation: a mechanism to keep arc magmas metaluminous? Contrib Mineral Petrol 178, 51. https://doi.org/10.1007/s00410-023-02035-7
Marxer, F., Ulmer, P., Müntener, O., 2022. Polybaric fractional crystallisation of arc magmas: an experimental study simulating trans-crustal magmatic systems. Contrib Mineral Petrol 177, 3. https://doi.org/10.1007/s00410-021-01856-8
Masotta, M., Freda, C., Paul, T.A., Moore, G.M., Gaeta, M., Scarlato, P., Troll, V.R., 2012. Low pressure experiments in piston cylinder apparatus: Calibration of newly designed 25mm furnace assemblies to P=150MPa. Chemical Geology 312–313, 74–79. https://doi.org/10.1016/j.chemgeo.2012.04.011
Mathez, E.A., 1984. Influence of degassing on oxidation states of basaltic magmas. Nature 310, 371–375. https://doi.org/10.1038/310371a0
Matjuschkin, V., Brooker, R.A., Tattitch, B., Blundy, J.D., Stamper, C.C., 2015. Control and monitoring of oxygen fugacity in piston cylinder experiments. Contrib Mineral Petrol 169, 9. https://doi.org/10.1007/s00410-015-1105-z
Matsumoto, K., Geshi, N., 2021. Shallow crystallization of eruptive magma inferred from volcanic ash microtextures: a case study of the 2018 eruption of Shinmoedake volcano, Japan. Bull Volcanol 83, 31. https://doi.org/10.1007/s00445-021-01451-6
Matthews, S.J., Jones, A.P., Beard, A.D., 1994. Buffering of melt oxygen fugacity by sulphur redox reactions in calc-alkaline magmas. JGS 151, 815–823. https://doi.org/10.1144/gsjgs.151.5.0815
McBirney, A.R., 1980. Mixing and umixing of magmas. J. Volcanol. Geotherm. Res.
McCarthy, A., Chelle-Michou, C., Blundy, J.D., Vonlanthen, P., Meibom, A., Escrig, S., 2020. Taking the pulse of volcanic eruptions using plagioclase glomerocrysts. Earth and Planetary Science Letters 552, 116596. https://doi.org/10.1016/j.epsl.2020.116596
McDade, P., Wood, B.J., Van Westrenen, W., Brooker, R., Gudmundsson, G., Soulard, H., Najorka, J., Blundy, J., 2002. Pressure corrections for a selection of piston-cylinder cell assemblies. Mineral. mag. 66, 1021–1028. https://doi.org/10.1180/0026461026660074
McKenzie, D., 1985. The extraction of magma from the crust and mantle. Earth and Planetary Science Letters 74, 81–91. https://doi.org/10.1016/0012-821X(85)90168-2
Médard, E., Le Pennec, J.-L., 2022. Petrologic imaging of the magma reservoirs that feed large silicic eruptions. Lithos 428–429, 106812. https://doi.org/10.1016/j.lithos.2022.106812
Médard, E., Schmidt, M.W., Schiano, P., Ottolini, L., 2006. Melting of Amphibole-bearing Wehrlites: an Experimental Study on the Origin of Ultra-calcic Nepheline-normative Melts. Journal of Petrology 47, 481–504. https://doi.org/10.1093/petrology/egi083
Melekhova, E., Annen, C., Blundy, J., 2013. Compositional gaps in igneous rock suites controlled by magma system heat and water content. Nature Geosci 6, 385–390. https://doi.org/10.1038/ngeo1781
Melekhova, E., Blundy, J., 2024. Generation of mantle-derived basaltic andesites in volcanic arcs. Earth and Planetary Science Letters 641, 118791. https://doi.org/10.1016/j.epsl.2024.118791
Melekhova, E., Blundy, J., Martin, R., Arculus, R., Pichavant, M., 2017. Petrological and experimental evidence for differentiation of water-rich magmas beneath St. Kitts, Lesser Antilles. Contrib Mineral Petrol 172, 98. https://doi.org/10.1007/s00410-017-1416-3
Melekhova, E., Blundy, J., Robertson, R., Humphreys, M.C.S., 2015. Experimental Evidence for Polybaric Differentiation of Primitive Arc Basalt beneath St. Vincent, Lesser Antilles. Journal of Petrology 56, 161–192. https://doi.org/10.1093/petrology/egu074
Melekhova, E., Camejo-Harry, M., Blundy, J., Wallis, S.R., Annen, C., Kunz, B.E., Jenner, F.E., Thirlwall, M., 2022. Arc Crust Formation of Lesser Antilles Revealed by Crustal Xenoliths from Petit St. Vincent. Journal of Petrology 63, egac033. https://doi.org/10.1093/petrology/egac033
Melekhova, E., Schlaphorst, D., Blundy, J., Kendall, J.-M., Connolly, C., McCarthy, A., Arculus, R., 2019. Lateral variation in crustal structure along the Lesser Antilles arc from petrology of crustal xenoliths and seismic receiver functions. Earth and Planetary Science Letters 516, 12–24. https://doi.org/10.1016/j.epsl.2019.03.030
Melnik, O., Lyakhovsky, V., Shapiro, N.M., Galina, N., Bergal-Kuvikas, O., 2020. Deep long period volcanic earthquakes generated by degassing of volatile-rich basaltic magmas. Nat Commun 11, 3918. https://doi.org/10.1038/s41467-020-17759-4
Mercer, C.N., Johnston, A.D., 2008. Experimental studies of the P–T–H2O near-liquidus phase relations of basaltic andesite from North Sister Volcano, High Oregon Cascades: constraints on lower-crustal mineral assemblages. Contrib Mineral Petrol 155, 571–592. https://doi.org/10.1007/s00410-007-0259-8
Mercury, J.M.R., Pena, P., De Aza, A.H., Sheptyakov, D., Turrillas, X., 2006. On the Decomposition of Synthetic Gibbsite Studied by Neutron Thermodiffractometry. Journal of the American Ceramic Society 89, 3728–3733. https://doi.org/10.1111/j.1551-2916.2006.01191.x
Metcalfe, A., Moune, S., Komorowski, J.-C., Robertson, R., Christopher, T.E., Joseph, E.P., Moretti, R., 2023. Diverse magma storage and major and volatile magma composition: What are the implications on the eruptive style across a volcanic arc? An example of the Lesser Antilles Arc. Earth-Science Reviews 241, 104440. https://doi.org/10.1016/j.earscirev.2023.104440

Miller, T.P., 1994. Dome growth and destruction during the 1989–1990 eruption of Redoubt Volcano. Journal of Volcanology and Geothermal Research 62, 197–212. https://doi.org/10.1016/0377-0273(94)90034-5
Mills, R.D., Glazner, A.F., 2013. Experimental study on the effects of temperature cycling on coarsening of plagioclase and olivine in an alkali basalt. Contrib Mineral Petrol 166, 97–111. https://doi.org/10.1007/s00410-013-0867-4
Min, K., Mundil, R., Renne, P.R., Ludwig, K.R., 2000. A test for systematic errors in 40Ar/39Ar geochronology through comparison with U/Pb analysis of a 1.1-Ga rhyolite. Geochimica et Cosmochimica Acta 64, 73–98. https://doi.org/10.1016/S0016-7037(99)00204-5
Mixon, E.E., Singer, B.S., Jicha, B.R., Ramirez, A., 2021. Calbuco, a monotonous andesitic high-flux volcano in the Southern Andes, Chile. Journal of Volcanology and Geothermal Research 416, 107279. https://doi.org/10.1016/j.jvolgeores.2021.107279
Miyashiro, A., 1978. Nature of alkalic volcanic rock series. Contr. Mineral. and Petrol. 66, 91–104. https://doi.org/10.1007/BF00376089
Miyashiro, A., 1974. Volcanic rock series in island arcs and active continental margins. American Journal of Science 274, 321–355.
Moore, G., Carmichael, I.S.E., 1998. The hydrous phase equilibria (to 3 kbar) of an andesite and basaltic andesite from western Mexico: constraints on water content and conditions of phenocryst growth. Contributions to Mineralogy and Petrology 130, 304–319. https://doi.org/10.1007/s004100050367
Moore, H.C., Carey, R.J., Houghton, B.F., Jutzeler, M., White, J.D.L., 2022. High-temperature oxidation of proximal basaltic pyroclasts, 1886 Tarawera, New Zealand. Bull Volcanol 84, 46. https://doi.org/10.1007/s00445-022-01549-5
Morrison-Evans, B., Melekhova, E., Blundy, J., 2024. Experimental insight into basaltic andesite lava dome oxidation textures at La Soufrière, St Vincent. SP 539, 121–152. https://doi.org/10.1144/SP539-2022-298
Moseley, D., 1984. Symplectic exsolution in olivine. American Mineralogist 69, 139–153.
Muan, A., Hauck, J., Löfall, T., 1972. Equilibrium studies with a bearing on lunar rocks. Lunar and Planetary Science Conference Proceedings 3, 185.
Mujin, M., Nakamura, M., Miyake, A., 2017. Eruption style and crystal size distributions: Crystallization of groundmass nanolites in the 2011 Shinmoedake eruption. American Mineralogist 102, 2367–2380. https://doi.org/10.2138/am-2017-6052CCBYNCND
Murch, A.P., Cole, P.D., 2019. Using microlites to gain insights into ascent conditions of differing styles of volcanism at Soufrière Hills Volcano. Journal of Volcanology and Geothermal Research 384, 221–231. https://doi.org/10.1016/j.jvolgeores.2019.07.022
Murphy, M.D., Sparks, R.S.J., Barclay, J., Carroll, M.R., Brewer, T.S., 2000. Remobilization of Andesite Magma by Intrusion of Mafic Magma at the Soufriere Hills Volcano, Montserrat, West Indies. Journal of Petrology 41, 21–42. https://doi.org/10.1093/petrology/41.1.21
Muth, M.J., Wallace, P.J., 2021. Slab-derived sulfate generates oxidized basaltic magmas in the southern Cascade arc (California, USA). Geology 49, 1177–1181. https://doi.org/10.1130/G48759.1
Nakada, S., Zaennudin, A., Yoshimoto, M., Maeno, F., Suzuki, Y., Hokanishi, N., Sasaki, H., Iguchi, M., Ohkura, T., Gunawan, H., Triastuty, H., 2019. Growth process of the lava dome/flow complex at Sinabung Volcano during 2013–2016. Journal of Volcanology and Geothermal Research 382, 120–136. https://doi.org/10.1016/j.jvolgeores.2017.06.012
Nakamura, M., 1995. Continuous mixing of crystal mush and replenished magma in the ongoing Unzen eruption. Geology 23, 807. https://doi.org/10.1130/0091-7613(1995)023<0807:CMOCMA>2.3.CO;2
Nakamura, N., 1974. Determination of REE, Ba, Fe, Mg, Na and K in carbonaceous and ordinary chondrites. Geochimica et Cosmochimica Acta 38, 757–775. https://doi.org/10.1016/0016-7037(74)90149-5
Nandedkar, R.H., Ulmer, P., Müntener, O., 2014. Fractional crystallization of primitive, hydrous arc magmas: an experimental study at 0.7 GPa. Contrib Mineral Petrol 167, 1015. https://doi.org/10.1007/s00410-014-1015-5
Neave, D.A., Bali, E., Guðfinnsson, G.H., Halldórsson, S.A., Kahl, M., Schmidt, A.-S., Holtz, F., 2019. Clinopyroxene–Liquid Equilibria and Geothermobarometry in Natural and Experimental Tholeiites: the 2014–2015 Holuhraun Eruption, Iceland. Journal of Petrology 60, 1653–1680. https://doi.org/10.1093/petrology/egz042
Nelson, S., Montanna, A., 1992. Sieve-textured plagioclase in volcanic rocks produced by rapid decompression 77, 1242–1249.
Newhall, C.G., Melson, W.G., 1983. Explosive activity associated with the growth of volcanic domes. Journal of Volcanology and Geothermal Research 17, 111–131. https://doi.org/10.1016/0377-0273(83)90064-1
Nicholls, I.A., Ringwood, A.E., 1973. Effect of Water on Olivine Stability in Tholeiites and the Production of Silica-Saturated Magmas in the Island-Arc Environment. The Journal of Geology 81, 285–300. https://doi.org/10.1086/627871
Nicholls, J., Stout, M., 1997. EPITACTIC OVERGROWTH AND INTERGROWTHS OF CLINOPYROXENE ON ORTHOPYROXE: IMPLICATIONS FOR PATHS OF CRYSTALLIZATION, 1881 LAVA FLOW MAUNA LOA VOLCANO, HAWAII. THE CANADIAN MINERALOGIST 35, 909–922.
Nickel, E.H., 1958. The composition and microtexture of an ulvoespinel-magnetite intergrowth [Quebec]. The Canadian Mineralogist 6, 191–199.
Nisbet, E.G., Pearce, J.A., 1977. Clinopyroxene composition in mafic lavas from different tectonic settings. Contrib. Mineral. and Petrol. 63, 149–160. https://doi.org/10.1007/BF00398776
Nitsan, U., 1974. Stability field of olivine with respect to oxidation and reduction. J. Geophys. Res. 79, 706–711. https://doi.org/10.1029/JB079i005p00706
Ogburn, S.E., Loughlin, S.C., Calder, E.S., 2015. The association of lava dome growth with major explosive activity (VEI ≥ 4): DomeHaz, a global dataset. Bull Volcanol 77, 40. https://doi.org/10.1007/s00445-015-0919-x
O'Hara, M.J., 1968. The bearing of phase equilibria studies in synthetic and natural systems on the origin and evolution of basic and ultrabasic rocks. Earth-Science Reviews 4, 69–133. https://doi.org/10.1016/0012-8252(68)90147-5
O'Neill, H.St.C., Wall, V.J., 1987. The Olivine--Orthopyroxene--Spinel Oxygen Geobarometer, the Nickel Precipitation Curve, and the Oxygen Fugacity of the Earth's Upper Mantle. Journal of Petrology 28, 1169–1191. https://doi.org/10.1093/petrology/28.6.1169
Osborn, E.F., 1959. Role of oxygen pressure in the crystallization and differentiation of basaltic magma. American Journal of Science 257, 609–647. https://doi.org/10.2475/ajs.257.9.609
Pallister, J.S., Thornber, C.R., Cashman, K.V., Clynne, M.A., Lowers, H.A., Mandeville, C.W., Brownfield, I.K., Meeker, G.P., 2008. Chapter 30: Petrology of the 2004–2006 Mount St. Helens Lava Dome—Implications for Magmatic

Plumbing and Eruption Triggering., in: A Volcano Rekindled: The Renewed Eruption of Mount St. Helens, 2004-2006.
Pan, R., Hou, T., Wang, X., Encarnación, J., Botcharnikov, R., 2022. Multiple Magma Storage Regions and Open System Processes Revealed by Chemistry and Textures of the Datong Tholeiitic Lavas, North China Craton. Journal of Petrology 63, egac034. https://doi.org/10.1093/petrology/egac034
Pang, K.-N., Zhou, M.-F., Lindsley, D., Zhao, D., Malpas, J., 2007. Origin of Fe-Ti Oxide Ores in Mafic Intrusions: Evidence from the Panzhihua Intrusion, SW China. Journal of Petrology 49, 295–313. https://doi.org/10.1093/petrology/egm082
Panjasawatwong, Y., Danyushevsky, L.V., Crawford, A.J., Harris, K.L., 1995. An experimental study of the effects of melt composition on plagioclase-melt equilibria at 5 and 10 kbar: implications for the origin of magmatic high-An plagioclase. Contr. Mineral. and Petrol. 118, 420–432. https://doi.org/10.1007/s004100050024
Parat, F., Streck, M.J., Holtz, F., Almeev, R., 2014. Experimental study into the petrogenesis of crystal-rich basaltic to andesitic magmas at Arenal volcano. Contrib Mineral Petrol 168, 1040. https://doi.org/10.1007/s00410-014-1040-4
Parkinson, I.J., Arculus, R.J., 1999. The redox state of subduction zones: insights from arc-peridotites. Chemical Geology 160, 409–423. https://doi.org/10.1016/S0009-2541(99)00110-2
Parkinson, I.J., Arculus, R.J., Eggins, S.M., 2003. Peridotite xenoliths from Grenada, Lesser Antilles Island Arc. Contributions to Mineralogy and Petrology 146, 241–262. https://doi.org/10.1007/s00410-003-0500-z
Pascal, M.-L., Fonteilles, M., Boudouma, O., Principe, C., 2011. QANDILITE FROM VESUVIUS SKARN EJECTA: CONDITIONS OF FORMATION AND MISCIBILITY GAP IN THE TERNARY SPINEL - QANDILITE - MAGNESIOFERRITE. The Canadian Mineralogist 49, 459–485. https://doi.org/10.3749/canmin.49.2.459
Pelton, A.D., 2001. Thermodynamics and Phase Diagrams of Materials, in: Kostorz, G. (Ed.), Phase Transformations in Materials. Wiley, pp. 1–80. https://doi.org/10.1002/352760264X.ch1
Pertermann, M., Lundstrom, C.C., 2006. Phase equilibrium experiments at 0.5 GPa and 1100–1300 °C on a basaltic andesite from Arenal volcano, Costa Rica. Journal of Volcanology and Geothermal Research 157, 222–235. https://doi.org/10.1016/j.jvolgeores.2006.03.043
Petersen, N., 1970. Calculation of diffusion coefficient and activation energy of titanium in titanomagnetite. Physics of the Earth and Planetary Interiors 2, 175–178. https://doi.org/10.1016/0031-9201(70)90005-1
Pichavant, M., Macdonald, R., 2007. Crystallization of primitive basaltic magmas at crustal pressures and genesis of the calc-alkaline igneous suite: experimental evidence from St Vincent, Lesser Antilles arc. Contrib Mineral Petrol 154, 535–558. https://doi.org/10.1007/s00410-007-0208-6
Pichavant, M., Martel, C., Bourdier, J., Scaillet, B., 2002b. Physical conditions, structure, and dynamics of a zoned magma chamber: Mount Pelée (Martinique, Lesser Antilles Arc). J. Geophys. Res. 107. https://doi.org/10.1029/2001JB000315
Pichavant, M., Mysen, B.O., Macdonald, R., 2002a. Source and H2O content of high-MgO magmas in island arc settings: an experimental study of a primitive calc-alkaline basalt from St. Vincent, lesser antilles arc. Geochimica et Cosmochimica Acta 66, 2193–2209. https://doi.org/10.1016/S0016-7037(01)00891-2
Pichavant, M., Poussineau, S., Lesne, P., Solaro, C., Bourdier, J.-L., 2018. Experimental Parametrization of Magma Mixing: Application to the ad 1530 Eruption of La Soufrière, Guadeloupe (Lesser Antilles). Journal of Petrology 59, 257–282. https://doi.org/10.1093/petrology/egy030
Plank, T., 2005. Constraints from Thorium/Lanthanum on Sediment Recycling at Subduction Zones and the Evolution of the Continents. Journal of Petrology 46, 921–944. https://doi.org/10.1093/petrology/egi005
Plank, T., Kelley, K.A., Zimmer, M.M., Hauri, E.H., Wallace, P.J., 2013. Why do mafic arc magmas contain ~4wt% water on average? Earth and Planetary Science Letters 364, 168–179. https://doi.org/10.1016/j.epsl.2012.11.044
Plank, T., Langmuir, C.H., 1993. Tracing trace elements from sediment input to volcanic output at subduction zones. Nature 362, 739–743. https://doi.org/10.1038/362739a0
Popp, R.K., Bryndzia, L.T., 1992. Statistical analysisof Fe3+,Ti, and oH in kaersutitefrom alkalic igneous rocks and mafic mantle xenoliths. American Mineralogist 77, 1250–1257.
Powell, R., 1985. Geothermometry and geobarometry: a discussion. JGS 142, 29–38. https://doi.org/10.1144/gsjgs.142.1.0029
Powell, R., Hergt, J., Woodhead, J., 2002. Improving isochron calculations with robust statistics and the bootstrap. Chemical Geology 185, 191–204. https://doi.org/10.1016/S0009-2541(01)00403-X
Powell, R., Holland, T., 1994. Optimal geothermometry and geobarometry. American Mineralogist 79, 120–133.
Preece, K., Barclay, J., Gertisser, R., Herd, R.A., 2013. Textural and micro-petrological variations in the eruptive products of the 2006 dome-forming eruption of Merapi volcano, Indonesia: Implications for sub-surface processes. Journal of Volcanology and Geothermal Research 261, 98–120. https://doi.org/10.1016/j.jvolgeores.2013.02.006
Preece, K., Gertisser, R., Barclay, J., Charbonnier, S.J., Komorowski, J.-C., Herd, R.A., 2016. Transitions between explosive and effusive phases during the cataclysmic 2010 eruption of Merapi volcano, Java, Indonesia. Bull Volcanol 78, 54. https://doi.org/10.1007/s00445-016-1046-z
Price, G.D., 1981. Diffusion in the titanomagnetite solid solution series. Mineral. mag. 44, 195–200. https://doi.org/10.1180/minmag.1981.044.334.13
Price, G.D., 1980. Exsolution microstructures in titanomagnetites and their magnetic significance. Physics of the Earth and Planetary Interiors 23, 2–12. https://doi.org/10.1016/0031-9201(80)90078-3
Price, G.D., Putnis, A., 1979. Oxidation phenomena in pleonaste bearing titanomagnetites. Contr. Mineral. and Petrol. 69, 355–359. https://doi.org/10.1007/BF00372261
Pushkar, P., Steuber, A.M., Tomblin, J.F., Julian, G.M., 1973. Strontium isotopic ratios in volcanic rocks from St. Vincent and St. Lucia, Lesser Antilles. J. Geophys. Res. 78, 1279–1287. https://doi.org/10.1029/JB078i008p01279
Putirka, K.D., 2008. Thermometers and Barometers for Volcanic Systems. Reviews in Mineralogy and Geochemistry 69, 61–120. https://doi.org/10.2138/rmg.2008.69.3
Putirka, K.D., 2005. Igneous thermometers and barometers based on plagioclase + liquid equilibria: Tests of some existing models and new calibrations. American Mineralogist 90, 336–346. https://doi.org/10.2138/am.2005.1449
Pyle, D.M., Barclay, J., Armijos, M.T., 2018. The 1902–3 eruptions of the Soufrière, St Vincent: Impacts, relief and response. Journal of Volcanology and Geothermal Research 356, 183–199. https://doi.org/10.1016/j.jvolgeores.2018.03.005

Rader, E.L., Larsen, J.F., 2013. Experimental phase relations of a low MgO Aleutian basaltic andesite at XH2O = 0.7–1. Contrib Mineral Petrol 166, 1593–1611. https://doi.org/10.1007/s00410-013-0944-8
Reagan, M.K., Gill, J.B., Malavassi, E., Garcia, M.O., 1987. Changes in magma composition at Arenal volcano, Costa Rica, 1968?1985: Real-time monitoring of open-system differentiation. Bull Volcanol 49, 415–434. https://doi.org/10.1007/BF01046634
Reiners, P.W., 2002. Temporal-compositional trends in intraplate basalt eruptions: Implications for mantle heterogeneity and melting processes. Geochem Geophys Geosyst 3, 1–30. https://doi.org/10.1029/2001GC000250
Richards, J.P., 2015. The oxidation state, and sulfur and Cu contents of arc magmas: implications for metallogeny. Lithos 233, 27–45. https://doi.org/10.1016/j.lithos.2014.12.011
Ridolfi, F., Renzulli, A., 2012. Calcic amphiboles in calc-alkaline and alkaline magmas: thermobarometric and chemometric empirical equations valid up to 1,130°C and 2.2 GPa. Contrib Mineral Petrol 163, 877–895. https://doi.org/10.1007/s00410-011-0704-6
Ridolfi, F., Renzulli, A., Puerini, M., 2010. Stability and chemical equilibrium of amphibole in calc-alkaline magmas: an overview, new thermobarometric formulations and application to subduction-related volcanoes. Contrib Mineral Petrol 160, 45–66. https://doi.org/10.1007/s00410-009-0465-7
Riel, N., Kaus, B.J.P., Green, E.C.R., Berlie, N., 2022. MAGEMin, an Efficient Gibbs Energy Minimizer: Application to Igneous Systems. Geochem Geophys Geosyst 23, e2022GC010427. https://doi.org/10.1029/2022GC010427
Righter, K., Sutton, S.R., Newville, M., Le, L., Schwandt, C.S., Uchida, H., Lavina, B., Downs, R.T., 2006. An experimental study of the oxidation state of vanadium in spinel and basaltic melt with implications for the origin of planetary basalt. American Mineralogist 91, 1643–1656. https://doi.org/10.2138/am.2006.2111
Ringwood, A.E., Lovering, J.F., 1970. Significance of pyroxene-ilmenite intergrowths among kimberlite xenoliths. Earth and Planetary Science Letters 7, 371–375. https://doi.org/10.1016/0012-821X(69)90052-1
Ringwood, A.E., 1974. The petrological evolution of island arc systems: Twenty-seventh William Smith Lecture. JGS 130, 183–204. https://doi.org/10.1144/gsjgs.130.3.0183
Robertson, R., 2002. The Volcanic Geology of the Pre- Soufrière Rocks of St. Vincent, West Indies (PhD Thesis). University of the West Indies.
Robertson, R.E.A., 2005. Volcanic hazard atlas of the Lesser Antilles: St. Vincent, in: Volcanic Hazard Atlas of the Lesser Antilles. Seismic Research Unit, The University of the West Indies, Trinidad and Tobago, pp. 239–261.
Robertson, R.E.A., Barclay, J., Joseph, E.P., Sparks, R.S.J., 2024. An overview of the eruption of La Soufrière Volcano, St Vincent 2020–21. SP 539, 1–24. https://doi.org/10.1144/SP539-2023-95
Rojas-Agramonte, Y., Williams, I.S., Arculus, R., Kröner, A., García-Casco, A., Lázaro, C., Buhre, S., Wong, J., Geng, H., Echeverría, C.M., Jeffries, T., Xie, H., Mertz-Kraus, R., 2017. Ancient xenocrystic zircon in young volcanic rocks of the southern Lesser Antilles island arc. Lithos 290–291, 228–252. https://doi.org/10.1016/j.lithos.2017.08.002
Roobol, M.J., Smith, A.L., 1975. A Comparison of the Recent Eruptions of Mt. Pelee, Martinique and Soufriere, St. Vincent.
Rowbotham, G., 1973. Hydrothermal synthesis and mineralogy of the alkali amphiboles (PhD Thesis). Durham University.
Rowley, K., 1978. Stratigraphy and geochemistry of the Soufriere volcano, St. Vincent, West Indies (PhD Thesis). University of the West Indies St. Augustine - Seismic Research Unit.
Ruprecht, P., Bachmann, O., 2010. Pre-eruptive reheating during magma mixing at Quizapu volcano and the implications for the explosiveness of silicic arc volcanoes. Geology 38, 919–922. https://doi.org/10.1130/G31110.1
Rutherford, M.J., Devine, J.D., 1988. The May 18, 1980, eruption of Mount St. Helens: 3. Stability and chemistry of amphibole in the magma chamber. J. Geophys. Res. 93, 11949–11959. https://doi.org/10.1029/JB093iB10p11949
Rutherford, M.J., Hill, P.M., 1993. Magma ascent rates from amphibole breakdown: An experimental study applied to the 1980–1986 Mount St. Helens eruptions. J. Geophys. Res. 98, 19667–19685. https://doi.org/10.1029/93JB01613
Sack, R.O., 1982. Spinels as petrogenetic indicators: Activity-composition relations at low pressures. Contr. Mineral. and Petrol. 79, 169–186. https://doi.org/10.1007/BF01132886
Safanda, J., Čermák, V., 2000. Subsurface Temperature Changes Due to the Crustal Magmatic Activity – Numerical Simulation. Studia Geophysica et Geodaetica 44, 327–335. https://doi.org/10.1023/A:1022127312875
Saito, T., Ishikawa, N., Kamata, H., 2007. Magnetic petrology of the 1991–1995 dacite lava of Unzen volcano, Japan: Degree of oxidation and implications for the growth of lava domes. Journal of Volcanology and Geothermal Research 164, 268–283. https://doi.org/10.1016/j.jvolgeores.2007.05.015
Saito, T., Ishikawa, N., Kamata, H., 2004a. Iron–titanium oxide minerals in block-and-ash-flow deposits: implications for lava dome oxidation processes. Journal of Volcanology and Geothermal Research 138, 283–294. https://doi.org/10.1016/j.jvolgeores.2004.07.006
Saito, T., Ishikawa, N., Kamata, H., 2004b. Magnetic Petrology of Unzen Volcano, Japan: Implications for Lava Dome Oxidation Processes (Annual Report No. 47). Disaster Prevention Research Institute, Kyoto University.
Sato, M., Wright, T.L., 1966. Oxygen Fugacities Directly Measured in Magmatic Gases. Science 153, 1103–1105. https://doi.org/10.1126/science.153.3740.1103
Saxena, S.K., Ekstrom, T.K., 1970. Statistical chemistry of calcic amphiboles. Contr. Mineral. and Petrol. 26, 276–284. https://doi.org/10.1007/BF00390076
Scaillet, S., Guillou, H., 2004. A critical evaluation of young (near-zero) K–Ar ages. Earth and Planetary Science Letters 220, 265–275. https://doi.org/10.1016/S0012-821X(04)00069-X
Schaen, A.J., Jicha, B.R., Hodges, K.V., Vermeesch, P., Stelten, M.E., Mercer, C.M., Phillips, D., Rivera, T.A., Jourdan, F., Matchan, E.L., Hemming, S.R., Morgan, L.E., Kelley, S.P., Cassata, W.S., Heizler, M.T., Vasconcelos, P.M., Benowitz, J.A., Koppers, A.P., Mark, D.F., Niespolo, E.M., Sprain, C.J., Hames, W.E., Turrin, B.D., Renne, P.R., Ross, J., Nomade, S., Guillou, H., Webb, L.E., Cohen, B.A., Calvert, A.T., Joyce, N., Ganerød, M., Wijbrans, J., Ishizuka, O., He, H., Ramirez, A., Pfänder, J.A., Lopez-Martínez, M., Qiu, H., Singer, B.S., 2020. Interpreting and reporting 40Ar/39Ar geochronologic data. Geological Society of America Bulletin 133.
Schiavi, F., Walte, N., Keppler, H., 2009. First in situ observation of crystallization processes in a basaltic-andesitic melt with the moissanite cell. Geology 37, 963–966. https://doi.org/10.1130/G30087A.1
Schilling, F., Wunder, B., 2004. Temperature distribution in piston-cylinder assemblies: Numerical simulations and laboratory experiments. ejm 16, 7–14. https://doi.org/10.1127/0935-1221/2004/0016-0007
Schlaphorst, D., Harmon, N., Kendall, J.M., Rychert, C.A., Collier, J., Rietbrock, A., Goes, S., the VoiLA Team, 2021. Variation in Upper Plate Crustal and Lithospheric Mantle Structure in the Greater and Lesser Antilles From Ambient Noise Tomography. Geochem Geophys Geosyst 22, e2021GC009800. https://doi.org/10.1029/2021GC009800

Schlaphorst, D., Kendall, J.-M., Collier, J.S., Verdon, J.P., Blundy, J., Baptie, B., Latchman, J.L., Massin, F., Bouin, M.-P., 2016. Water, oceanic fracture zones and the lubrication of subducting plate boundaries—insights from seismicity. Geophysical Journal International 204, 1405–1420. https://doi.org/10.1093/gji/ggv509
Schlaphorst, D., Melekhova, E., Kendall, J.-M., Blundy, J., Latchman, J.L., 2018. Probing layered arc crust in the Lesser Antilles using receiver functions. R. Soc. open sci. 5, 180764. https://doi.org/10.1098/rsos.180764
Schmidt, M.E., Grunder, A.L., 2011. Deep Mafic Roots to Arc Volcanoes: Mafic Recharge and Differentiation of Basaltic Andesite at North Sister Volcano, Oregon Cascades. Journal of Petrology 52, 603–641. https://doi.org/10.1093/petrology/egq094
Seaman, S.J., 2000. Crystal Clusters, Feldspar Glomerocrysts, and Magma Envelopes in the Atascosa Lookout Lava Flow, Southern Arizona, USA: Recorders of Magmatic Events. Journal of Petrology 41, 693–716. https://doi.org/10.1093/petrology/41.5.693
Shane, P., Cocker, K., Coote, A., Stirling, C.H., Reid, M.R., 2019. The prevalence of plagioclase antecrysts and xenocrysts in andesite magma, exemplified by lavas of the Tongariro volcanic complex, New Zealand. Contrib Mineral Petrol 174, 89. https://doi.org/10.1007/s00410-019-1626-y
Shearer, C.K., McKay, G., Papike, J.J., Karner, J.M., 2006. Valence state partitioning of vanadium between olivine-liquid: Estimates of the oxygen fugacity of Y980459 and application to other olivine-phyric martian basalts. American Mineralogist 91, 1657–1663. https://doi.org/10.2138/am.2006.2155
Shepherd, J.B., Aspinall, W.P., Rowley, K.C., Pereira, J., Sigurdsson, H., Fiske, R.S., Tomblin, J.F., 1979. The eruption of Soufrière volcano, St Vincent April–June 1979. Nature 282, 24–28. https://doi.org/10.1038/282024a0
Shepherd, J.B., Sigurdsson, H., 1982. Mechanism of the 1979 explosive eruption of soufriere volcano, St. Vincent. Journal of Volcanology and Geothermal Research 13, 119–130. https://doi.org/10.1016/0377-0273(82)90023-3
Sigurdsson, H., 1981. GEOLOGIC OBSERVATIONS IN THE CRATER OF SOUFRIFRE VOLCANO, ST. VINCENT. UNIVERSITY OF THE WEST INDIES SEISMIC RESEARCH UNIT SPECIAL PUBLICATION.
Sisson, T.W., Grove, T.L., 1993a. Experimental investigations of the role of H20 in calc-alkaline differentiation and subduction zone magmatism.
Sisson, T.W., Grove, T.L., 1993b. Temperatures and H20 contents of low-MgO high-alumina basalts. Contributions to Mineralogy and Petrology 167–184.
Sisson, T.W., Ratajeski, K., Hankins, W.B., Glazner, A.F., 2005. Voluminous granitic magmas from common basaltic sources. Contrib Mineral Petrol 148, 635–661. https://doi.org/10.1007/s00410-004-0632-9
Sisson, T.W., Salters, V.J.M., Larson, P.B., 2014. Petrogenesis of Mount Rainier andesite: Magma flux and geologic controls on the contrasting differentiation styles at stratovolcanoes of the southern Washington Cascades. Geological Society of America Bulletin 126, 122–144. https://doi.org/10.1130/B30852.1
Smith, A.L., Roobol, M.J., Gunn, B.M., 1980. The lesser antilles — A discussion of the Island arc magmatism. Bull Volcanol 43, 287–302. https://doi.org/10.1007/BF02598033
Smith, D.J., 2014. Clinopyroxene precursors to amphibole sponge in arc crust. Nat Commun 5, 4329. https://doi.org/10.1038/ncomms5329
Solano, J.M.S., Jackson, M.D., Sparks, R.S.J., Blundy, J., 2014. Evolution of major and trace element composition during melt migration through crystalline mush: Implications for chemical differentiation in the crust. American Journal of Science 314, 895–939. https://doi.org/10.2475/05.2014.01
Spandler, C., O'Neill, H.St.C., 2010. Diffusion and partition coefficients of minor and trace elements in San Carlos olivine at 1,300°C with some geochemical implications. Contrib Mineral Petrol 159, 791–818. https://doi.org/10.1007/s00410-009-0456-8
Sparks, R.S.J., Annen, C., Blundy, J.D., Cashman, K.V., Rust, A.C., Jackson, M.D., 2019. Formation and dynamics of magma reservoirs. Phil. Trans. R. Soc. A. 377, 20180019. https://doi.org/10.1098/rsta.2018.0019
Sparks, S.R.J., Sigurdsson, H., Wilson, L., 1977. Magma mixing: a mechanism for triggering acid explosive eruptions. Nature 267, 315–318. https://doi.org/10.1038/267315a0
Speidel, D.H., 1967. Phase Equilibria in the System MgO-FeO-Fe2O3: The 1300oC Isothermal Section and Extrapolations to Other Temperatures. J American Ceramic Society 50, 243–248. https://doi.org/10.1111/j.1151-2916.1967.tb15096.x
Stamper, C.C., Blundy, J.D., Arculus, R.J., Melekhova, E., 2014a. Petrology of Plutonic Xenoliths and Volcanic Rocks from Grenada, Lesser Antilles. Journal of Petrology 55, 1353–1387. https://doi.org/10.1093/petrology/egu027
Stamper, C.C., Melekhova, E., Blundy, J.D., Arculus, R.J., Humphreys, M.C.S., Brooker, R.A., 2014b. Oxidised phase relations of a primitive basalt from Grenada, Lesser Antilles. Contrib Mineral Petrol 167, 954. https://doi.org/10.1007/s00410-013-0954-6
Stein, S., Engeln, J.F., Wiens, D.A., Fujita, K., Speed, R.C., 1982. Subduction seismicity and tectonics in the Lesser Antilles Arc. J. Geophys. Res. 87, 8642–8664. https://doi.org/10.1029/JB087iB10p08642
Stinton, A., Sparks, R.S.J., Huppert, H.E., 2024. Analysis of magma rheology from lava spreading and explosive activity during the 2020–21 eruption of La Soufrière, St Vincent, with implications for eruption dynamics. SP 539, 153–169. https://doi.org/10.1144/SP539-2022-284
Stinton, A.J., 2024. Growth and evolution of the lava dome and coulée during the 2020–21 eruption of La Soufrière, St Vincent. SP 539, 25–39. https://doi.org/10.1144/SP539-2022-304
Stock, M.J., Geist, D., Neave, D.A., Gleeson, M.L.M., Bernard, B., Howard, K.A., Buisman, I., Maclennan, J., 2020. Cryptic evolved melts beneath monotonous basaltic shield volcanoes in the Galápagos Archipelago. Nat Commun 11, 3767. https://doi.org/10.1038/s41467-020-17590-x
Streck, M.J., 2008. Mineral Textures and Zoning as Evidence for Open System Processes. Reviews in Mineralogy and Geochemistry 69, 595–622. https://doi.org/10.2138/rmg.2008.69.15
Streck, M.J., Dungan, M.A., Bussy, F., Malavassi, E., 2005. Mineral inventory of continuously erupting basaltic andesites at Arenal volcano, Costa Rica: implications for interpreting monotonous, crystal-rich, mafic arc stratigraphies. Journal of Volcanology and Geothermal Research 140, 133–155. https://doi.org/10.1016/j.jvolgeores.2004.07.018
Streck, M.J., Dungan, M.A., Malavassi, E., Reagan, M.K., Bussy, F., 2002. The role of basalt replenishment in the generation of basaltic andesites of the ongoing activity at Arenal volcano, Costa Rica: evidence from clinopyroxene and spinel. Bull Volcanol 64, 316–327. https://doi.org/10.1007/s00445-002-0209-2
Sun, S. -s., McDonough, W.F., 1989. Chemical and isotopic systematics of oceanic basalts: implications for mantle composition and processes. SP 42, 313–345. https://doi.org/10.1144/GSL.SP.1989.042.01.19

Swanson, D.A., Dzurisin, D., Holcomb, R.T., Iwatsubo, E.Y., Chadwick, W.W., Casadevall, T.J., Ewert, J.W., Heliker, C.C., 1987. Growth of the lava dome at Mount St. Helens, Washington, (USA), 1981–1983, in: Geological Society of America Special Papers. Geological Society of America, pp. 1–16. https://doi.org/10.1130/SPE212-p1
Szramek, L., Gardner, J.E., Larsen, J., 2006. Degassing and microlite crystallization of basaltic andesite magma erupting at Arenal Volcano, Costa Rica. Journal of Volcanology and Geothermal Research 157, 182–201. https://doi.org/10.1016/j.jvolgeores.2006.03.039
Tan, W., Liu, P., He, H., Wang, C.Y., Liang, X., 2016. Mineralogy and Origin of Exsolution In Ti-Rich Magnetite From Different Magmatic Fe-Ti Oxide-Bearing Intrusions. Can Mineral 54, 539–553. https://doi.org/10.3749/canmin.1400069
Tarney, J., 1969. Epitaxic relations between coexisting pyroxenes. Mineral. mag. 37, 115–122. https://doi.org/10.1180/minmag.1969.037.285.11
Tatsumi, Y., Furukawa, Y., Yamashita, S., 1994. Thermal and geochemical evolution of the mantle wedge in the northeast Japan arc: 1. Contribution from experimental petrology. J. Geophys. Res. 99, 22275–22283. https://doi.org/10.1029/94JB00283
Tatsumi, Y., Sakuyama, M., Fukuyama, H., Kushiro, I., 1983. Generation of arc basalt magmas and thermal structure of the mantle wedge in subduction zones. J. Geophys. Res. 88, 5815–5825. https://doi.org/10.1029/JB088iB07p05815
Thirlwall, M.F., Graham, A.M., 1984. Evolution of high-Ca, high-Sr C-series basalts from Grenada, Lesser Antilles: the effects of intra-crustal contamination. JGS 141, 427–445. https://doi.org/10.1144/gsjgs.141.3.0427
Thirlwall, M.F., Smith, T.E., Graham, A.M., Theodorou, N., Hollings, P., Davidson, J.P., Arculus, R.J., 1994. High Field Strength Element Anomalies in Arc Lavas: Source or Process? Journal of Petrology 35, 819–838. https://doi.org/10.1093/petrology/35.3.819
Thy, P., Lofgren, G.E., 1994. Experimental constraints on the low-pressure evolution of transitional and mildly alkalic basalts: the effect of Fe-Ti oxide minerals and the origin of basaltic andesites. Contr. Mineral. and Petrol. 116, 340–351. https://doi.org/10.1007/BF00306502
Tollan, P.M.E., Bindeman, I., Blundy, J.D., 2012. Cumulate xenoliths from St. Vincent, Lesser Antilles Island Arc: a window into upper crustal differentiation of mantle-derived basalts. Contrib Mineral Petrol 163, 189–208. https://doi.org/10.1007/s00410-011-0665-9
Tomblin, J.F., 1975. The Lesser Antilles and Aves Ridge, in: Nairn, A.E.M., Stehli, F.G. (Eds.), The Gulf of Mexico and the Caribbean. Springer US, Boston, MA, pp. 467–500. https://doi.org/10.1007/978-1-4684-8535-6_11
Tomiya, A., Takahashi, E., Furukawa, N., Suzuki, T., 2010. Depth and Evolution of a Silicic Magma Chamber: Melting Experiments on a Low-K Rhyolite from Usu Volcano, Japan. Journal of Petrology 51, 1333–1354. https://doi.org/10.1093/petrology/egq021
Toplis, M.J., Corgne, A., 2002. An experimental study of element partitioning between magnetite, clinopyroxene and iron-bearing silicate liquids with particular emphasis on vanadium. Contrib Mineral Petrol 144, 22–37. https://doi.org/10.1007/s00410-002-0382-5
Tsuchiyama, A., 1985. Dissolution kinetics of plagioclase in the melt of the system diopside-albite-anorthite, and origin of dusty plagioclase in andesites. Contr. Mineral. and Petrol. 89, 1–16. https://doi.org/10.1007/BF01177585
Turner, M.B., Cronin, S.J., Stewart, R.B., Bebbington, M., Smith, I.E.M., 2008. Using titanomagnetite textures to elucidate volcanic eruption histories. Geol 36, 31. https://doi.org/10.1130/G24186A.1
Turner, S.J., Langmuir, C.H., 2022. Sediment and ocean crust both melt at subduction zones. Earth and Planetary Science Letters 584, 117424. https://doi.org/10.1016/j.epsl.2022.117424
Turner, S.J., Langmuir, C.H., 2015. What processes control the chemical compositions of arc front stratovolcanoes? Geochem Geophys Geosyst 16, 1865–1893. https://doi.org/10.1002/2014GC005633
Turnock, A.C., Eugster, H.P., 1962. Fe-Al Oxides: Phase Relationships below 1,000 C. Journal of Petrology 3, 533–565. https://doi.org/10.1093/petrology/3.3.533
Ueda, H., Shibuya, T., Sawaki, Y., Shozugawa, K., Makabe, A., Takai, K., 2021. Chemical Nature of Hydrothermal Fluids Generated by Serpentinization and Carbonation of Komatiite: Implications for H_2 -Rich Hydrothermal System and Ocean Chemistry in the Early Earth. Geochem Geophys Geosyst 22. https://doi.org/10.1029/2021GC009827
Ueki, K., Inui, M., Matsunaga, K., Okamoto, N., Oshio, K., 2020. Oxidation during magma mixing recorded by symplectites at Kusatsu–Shirane Volcano, Central Japan. Earth Planets Space 72, 68. https://doi.org/10.1186/s40623-020-01192-4
Ulmer, P., 2001. Partial melting in the mantle wedge — the role of H2O in the genesis of mantle-derived 'arc-related' magmas. Physics of the Earth and Planetary Interiors 127, 215–232. https://doi.org/10.1016/S0031-9201(01)00229-1
Ulmer, P., Kaegi, R., Müntener, O., 2018. Experimentally Derived Intermediate to Silica-rich Arc Magmas by Fractional and Equilibrium Crystallization at 1·0 GPa: an Evaluation of Phase Relationships, Compositions, Liquid Lines of Descent and Oxygen Fugacity. Journal of Petrology 59, 11–58. https://doi.org/10.1093/petrology/egy017
Utami, S.B., Andujar, J., Costa, F., Scaillet, B., Humaida, H., 2021. The Role of Magma Storage Conditions and Excess Fluids in the Effusive to Explosive Eruption Styles (preprint). Geology. https://doi.org/10.1002/essoar.10508062.1
Vance, J.A., 1969. On synneusis. Contr. Mineral. and Petrol. 24, 7–29. https://doi.org/10.1007/BF00398750
Venezky, D.Y., Rutherford, M.J., 1999. Petrology and Fe–Ti oxide reequilibration of the 1991 Mount Unzen mixed magma. Journal of Volcanology and Geothermal Research 89, 213–230. https://doi.org/10.1016/S0377-0273(98)00133-4
Verhoogen, J., 1962. Oxidation of Iron-Titanium Oxides in Igneous Rocks. The Journal of Geology 70, 168–181. https://doi.org/10.1086/626806
Villiger, S., 2004. The Liquid Line of Descent of Anhydrous, Mantle-Derived, Tholeiitic Liquids by Fractional and Equilibrium Crystallization--an Experimental Study at 1{middle dot}0 GPa. Journal of Petrology 45, 2369–2388. https://doi.org/10.1093/petrology/egh042
Villiger, S., Ulmer, P., Muntener, O., 2007. Equilibrium and Fractional Crystallization Experiments at 0{middle dot}7 GPa; the Effect of Pressure on Phase Relations and Liquid Compositions of Tholeiitic Magmas. Journal of Petrology 48, 159–184. https://doi.org/10.1093/petrology/egl058
Vincent, E.A., Wright, J.B., Chevallier, R., Mathieu, S., 1957. Heating experiments on some natural titaniferous magnetites. Mineral. mag. j. Mineral. Soc. 31, 624–655. https://doi.org/10.1180/minmag.1957.31.239.03

Voight, B., Constantine, E.K., Siswowidjoyo, S., Torley, R., 2000. Historical eruptions of Merapi Volcano, Central Java, Indonesia, 1768–1998. Journal of Volcanology and Geothermal Research 100, 69–138. https://doi.org/10.1016/S0377-0273(00)00134-7
Von Gruenewaldt, G., Klemm, D.D., Henckel, J., Dehm, R.M., 1985. Exsolution features in titanomagnetites from massive magnetite layers and their host rocks of the upper zone, eastern Bushveld Complex. Economic Geology 80, 1049–1061. https://doi.org/10.2113/gsecongeo.80.4.1049
Walker, D., Shibata, T., DeLong, S.E., Laboratory, H., 1979. Abyssal tholeiites from the Oceanographer Fracture Zone 111–125.
Walker, G.P.L., Huntingdon, A.T., Sanders, A.T., Dinsdale, J.L., 1973. Lengths of Lava Flows [and Discussion]. Philosophical Transactions of the Royal Society of London. Series A, Mathematical and Physical Sciences 274, 107–118.
Wang, J., Wang, Q., Dan, W., Yang, J.-H., Yang, Z.-Y., Sun, P., Qi, Y., Hu, W.-L., 2019. The role of clinopyroxene in amphibole fractionation of arc magmas: Evidence from mafic intrusive rocks within the Gangdese arc, southern Tibet. Lithos 338–339, 174–188. https://doi.org/10.1016/j.lithos.2019.04.013
Waters, L.E., Andrews, B.J., Lange, R.A., 2015. Rapid Crystallization of Plagioclase Phenocrysts in Silicic Melts during Fluid-saturated Ascent: Phase Equilibrium and Decompression Experiments. Journal of Petrology 56, 981–1006. https://doi.org/10.1093/petrology/egv025
Waters, L.E., Cottrell, E., Coombs, M.L., Kelley, K.A., 2020. Generation of Calc-Alkaline Magmas during Crystallization at High Oxygen Fugacity: An Experimental and Petrologic Study of Tephras from Buldir Volcano, Western Aleutian Arc, Alaska, USA. Journal of Petrology 62, egaa104. https://doi.org/10.1093/petrology/egaa104
Weber, G., Blundy, J., 2024. A Machine Learning-Based Thermobarometer for Magmatic Liquids. Journal of Petrology 65, egae020. https://doi.org/10.1093/petrology/egae020
Weber, G., Blundy, J., Barclay, J., Pyle, D.M., Cole, P., Frey, H., Manon, M., Davies, B.V., Cashman, K., 2024. Petrology of the 2020–21 effusive to explosive eruption of La Soufrière Volcano, St Vincent: insights into plumbing system architecture and magma assembly mechanism. SP 539, 171–200. https://doi.org/10.1144/SP539-2022-177
Weber, R.M., Wallace, P.J., Dana Johnston, A., 2012. Experimental insights into the formation of high-Mg basaltic andesites in the trans-Mexican volcanic belt. Contrib Mineral Petrol 163, 825–840. https://doi.org/10.1007/s00410-011-0701-9
Wells, P.R.A., 1977. Pyroxene thermometry in simple and complex systems. Contr. Mineral. and Petrol. 62, 129–139. https://doi.org/10.1007/BF00372872
White, W.M., Dupré, B., 1986. Sediment subduction and magma genesis in the Lesser Antilles: Isotopic and trace element constraints. J. Geophys. Res. 91, 5927–5941. https://doi.org/10.1029/JB091iB06p05927
Wieser, P.E., Edmonds, M., Gansecki, C., Maclennan, J., Jenner, F.E., Kunz, B., Antoshechkina, P., Trusdell, F., Lee, R.L., Eimf, 2022. Explosive Activity on Kīlauea's Lower East Rift Zone Fueled by a Volatile-Rich, Dacitic Melt. Geochem Geophys Geosyst 23, e2021GC010046. https://doi.org/10.1029/2021GC010046
Wieser, P.E., Kent, A.J.R., Till, C.B., 2023. Barometers Behaving Badly II: a Critical Evaluation of Cpx-Only and Cpx-Liq Thermobarometry in Variably-Hydrous Arc Magmas. Journal of Petrology 64, egad050. https://doi.org/10.1093/petrology/egad050
Wilke, M., Behrens, H., 1999. The dependence of the partitioning of iron and europium between plagioclase and hydrous tonalitic melt on oxygen fugacity. Contributions to Mineralogy and Petrology 137, 102–114. https://doi.org/10.1007/s004100050585
Wilson, L., Head, J.W., 1981. Ascent and eruption of basaltic magma on the Earth and Moon. J. Geophys. Res. 86, 2971–3001. https://doi.org/10.1029/JB086iB04p02971
Woermann, E., Brezney, B., Muan, A., 1969. Phase equilibria in the system MgO–iron oxide—TiO2 in air. American Journal of Science 267, 463–479.
Wood, B.J., Bryndzia, L.T., Johnson, K.E., 1990. Mantle Oxidation State and Its Relationship to Tectonic Environment and Fluid Speciation. Science 248, 337–345. https://doi.org/10.1126/science.248.4953.337
Wood, B.J., Henderson, C.M.B., 1978. Compositions andunit-cellparameters of syntheticnon-stoichiometric tschermakitic clinopyroxene. American Mineralogist 63, 66–72.
Wyllie, P.J., 1984. Constraints imposed by experimental petrology on possible and impossible magma sources and products. Phil. Trans. R. Soc. Lond. A 439–456.
Yagi, K., Onuma, K., 1967. The Join CaMgSi_2O_6-CaTiAl_2O_6 and its bearing on the Titanaugites. Journal of the Faculty of Science, Hokkaido University, Series 4, Geology and mineralogy, 13(4), 463-483.
Yoder, H.S., Tilley, C.E., 1962. Origin of Basalt Magmas: An Experimental Study of Natural and Synthetic Rock Systems. Journal of Petrology 3, 342–532. https://doi.org/10.1093/petrology/3.3.342
Zellmer, G.F., 2021. Gaining acuity on crystal terminology in volcanic rocks. Bull Volcanol 83, 78. https://doi.org/10.1007/s00445-021-01505-9
Zellmer, G.F., Iizuka, Y., Straub, S.M., 2024. Origin of Crystals in Mafic to Intermediate Magmas from Circum-Pacific Continental Arcs: Transcrustal Magmatic Systems Versus Transcrustal Plutonic Systems. Journal of Petrology 65, egae013. https://doi.org/10.1093/petrology/egae013
Zen, E., 1966. Construction of pressure-temperature diagrams for multicomponent systems after the method of Schreinemakers - a geometric approach. https://doi.org/10.3133/b1225
Zenk, M., Schulz, B., 2004. Zoned Ca-amphiboles and related *P-T* evolution in metabasites from the classical Barrovian metamorphic zones in Scotland. Mineral. mag. 68, 769–786. https://doi.org/10.1180/0026461046850218
Zhang, J., Humphreys, M.C.S., Cooper, G.F., Davidson, J.P., Macpherson, C.G., 2017. Magma mush chemistry at subduction zones, revealed by new melt major element inversion from calcic amphiboles. American Mineralogist 102, 1353–1367. https://doi.org/10.2138/am-2017-5928
Zharinov, N.A., Demyanchuk, Yu.V., 2013. Large explosive eruptions of shiveluch volcano, kamchatka resulting in partial destruction of the extrusive dome (February 28, 2005 and October 27, 2010). J. Volcanolog. Seismol. 7, 131–144. https://doi.org/10.1134/S0742046313020061
Ziberna, L., 2021. Geothermobarometry of Mafic and Ultramafic Xenoliths: Examples From Hualalai and Mauna Kea Volcanoes, Hawaii, in: Masotta, M., Beier, C., Mollo, S. (Eds.), Geophysical Monograph Series. Wiley, pp. 1–18. https://doi.org/10.1002/9781119564485.ch1

Zimmer, M.M., Plank, T., Hauri, E.H., Yogodzinski, G.M., Stelling, P., Larsen, J., Singer, B., Jicha, B., Mandeville, C., Nye, C.J., 2010. The Role of Water in Generating the Calc-alkaline Trend: New Volatile Data for Aleutian Magmas and a New Tholeiitic Index. Journal of Petrology 51, 2411–2444. https://doi.org/10.1093/petrology/egq062

Appendices

All appendices are attached as an electronic supplementary file and include:

Chapter 2

S2.1 Plateau age spectrums and inverted isochrons for $^{40}Ar/^{39}Ar$ dated lava samples.

S2.2 New trace element data for La Soufrière magmas

Chapter 3

S3.1 Mineral compositional data for La Soufrière lava and dyke samples

S3.2 Additional St. Vincent xenolith mineral data collected by J. Blundy

Chapter 4

S4.1 One atmosphere experimental run table

S4.2 Epma standards

S4.3 AuPdFe data

S4.4 Piston cylinder experimental mineral compositional data

S4.5 OP calibration

S4.6 SIMS calibration

S4.7 Cpx-opx equilibrium pairs

Chapter 5

S5.1 2020-2021 dome and scoria mineral data

S5.2 One atmosphere experimental data